

## University of Southampton Research Repository ePrints Soton

Copyright © and Moral Rights for this thesis are retained by the author and/or other copyright owners. A copy can be downloaded for personal non-commercial research or study, without prior permission or charge. This thesis cannot be reproduced or quoted extensively from without first obtaining permission in writing from the copyright holder/s. The content must not be changed in any way or sold commercially in any format or medium without the formal permission of the copyright holders.

When referring to this work, full bibliographic details including the author, title, awarding institution and date of the thesis must be given e.g.

AUTHOR (year of submission) "Full thesis title", University of Southampton, name of the University School or Department, PhD Thesis, pagination

UNIVERSITY OF SOUTHAMPTON

FACULTY OF ENGINEERING AND THE ENVIRONMENT

BIOENGINEERING SCIENCES AND ENGINEERING MATERIALS RESEARCH GROUPS

MICROMECHANICAL CHARACTERISATION OF FATIGUE FAILURE IN  
ACRYLIC BONE CEMENT

BY

**Natalie Shearwood-Porter**

A thesis submitted in partial fulfillment of  
the requirements for the degree of

**Doctor of Philosophy**

JUNE 2013



UNIVERSITY OF SOUTHAMPTON

ABSTRACT

FACULTY OF ENGINEERING AND THE ENVIRONMENT

BIOENGINEERING SCIENCES AND ENGINEERING MATERIALS RESEARCH GROUPS

Doctor of Philosophy

MICROMECHANICAL CHARACTERISATION OF FATIGUE FAILURE IN ACRYLIC BONE  
CEMENT

**Natalie Shearwood-Porter**

Acrylic bone cement has been used for fixation of load-bearing orthopaedic implants for over five decades, and continues to be the 'gold standard' for elderly patients and those with systemic disease. Aseptic loosening remains a major indication for revision of cemented hip implants, and has been associated with mechanical degradation of the cement mantle via the initiation and coalescence of fatigue micro-cracks. Microstructural defects such as voids and agglomerates of radiopacifier particles have been implicated in this damage accumulation process. Improved understanding of the relative effects of these features on the mechanisms of fatigue crack initiation and failure within the cement is required in order to inform the development of more robust cement formulations and thus increase the longevity of the cement mantle *in vivo*.

The present study utilised micro-computed tomography ( $\mu$ -CT) and scanning electron microscopy (SEM), in conjunction with mechanical testing, to provide a systematic, quantitative assessment of the effect of cement formulation and microstructure (including voids and radiopacifiers) on the *in vitro* fatigue failure of four commercial, vacuum-mixed cement formulations. Results were compared with  $\mu$ -CT data and fractographic analysis of an *ex vivo* cement specimen. This novel 'data rich' methodology enabled non-destructive, three-dimensional analysis of defect populations in terms of the size, morphology and spatial density of individual microstructural features, and the identification and characterisation of crack-initiating defects.

The inclusion of barium sulphate as a radiopacifier was found to have a negative effect on the fatigue life of cement; radiopacifier particles showed a tendency to form numerous large agglomerates, which readily initiated fatigue cracks; furthermore, fatigue life scaled consistently with initiating defect size. In contrast, cement containing zirconium dioxide as a radiopacifier demonstrated superior fatigue performance, and failure in these cement formulations was dominated by crack initiation from voids. In all four cement formulations, void populations were found to be bi-modal, and the largest voids (> 0.5 mm equivalent spherical diameter) were surrounded by secondary satellite voids in both *in vitro* and *ex vivo* cement specimens. Extensive void formation was also noted in both moulded specimens and cement mixing gun stubs, in addition to *ex vivo* cement. Optimisation of cement formulations and vacuum-mixing techniques may therefore be advantageous in order to reduce the formation of barium sulphate agglomerates and large voids, and thus minimise their potential crack initiation effects *in vivo*.



## CONTENTS

Contents .....	i
List of Figures.....	v
List of Tables .....	xiii
Nomenclature .....	xv
Declaration of Authorship .....	xvii
Acknowledgements .....	xix
Chapter 1. Introduction .....	1
1.1    Motivation.....	1
1.2    Objectives.....	3
Chapter 2. Literature Review .....	5
2.1    Total Hip Replacement .....	5
2.1.1    Introduction.....	5
2.1.2    Implant Characteristics.....	6
2.1.3    Patient Characteristics .....	9
2.1.4    Service Conditions .....	10
2.1.5    Failure of Total Hip Replacement.....	11
2.2    Bone Cement Characteristics .....	14
2.2.1    Chemical Composition.....	14
2.2.2    Curing and Handling Properties.....	15
2.2.3    Biological properties.....	16
2.2.4    Microstructure.....	18
2.2.5    Mechanical Properties.....	19
2.2.6    Cementing Techniques.....	20
2.3    Fatigue Failure .....	23
2.3.1    Introduction.....	23
2.3.2    Microstructural Aspects of Fatigue Failure .....	24

2.3.3	Effect of Defect Size.....	24
2.3.4	Effect of Defect Shape and Orientation.....	28
2.3.5	Effect of Defect Location .....	30
2.3.6	Effect of Defect Clustering.....	32
2.3.7	Consideration of Test Parameters .....	33
2.3.8	Summary .....	34
2.4	Bone Cement Fatigue and Failure .....	35
2.4.1	Introduction.....	35
2.4.2	Effect of Porosity.....	36
2.4.3	Effect of Radiopacifying agent.....	37
2.4.4	Effect of Sterilisation Technique .....	39
2.4.5	Effect of Curing and Aging Conditions .....	40
2.4.6	Results of <i>In vitro</i> testing of Cemented Constructs.....	42
2.4.7	Results of <i>Ex Vivo</i> Studies.....	44
2.4.8	Summary .....	46
Chapter 3	Materials, Techniques and Experimental Procedure .....	47
3.1	Materials .....	47
3.2	Specimen Preparation.....	49
3.3	Mechanical Testing.....	51
3.4	Microstructural Imaging .....	54
3.4.1	Computed Tomography (CT).....	54
3.4.2	Scanning Electron Microscopy (SEM) .....	55
3.5	Image Analysis.....	56
3.5.1	Segmentation of Microstructural Features .....	56
3.5.2	CT Artefacts.....	61
3.5.3	Microstructural Feature Quantification .....	63
Chapter 4	The Effect of Barium Sulphate as a Radiopacifier .....	65
4.1	Introduction .....	65
4.2	Materials and Methods.....	68

4.3	Results .....	70
4.3.1	Defect Population Characterisation.....	70
4.3.2	Micromechanisms of Failure .....	75
4.3.3	Effect of Agglomerate Size on Fatigue Life of CMW-1 .....	80
4.4	Discussion .....	82
4.5	Conclusion.....	87
Chapter 5. The Effect of Zirconium Dioxide as a Radiopacifier .....		89
5.1	Introduction .....	89
5.2	Materials and Methods .....	91
5.3	Results .....	93
5.3.1	Defect Population Characterisation.....	93
5.3.2	Micromechanisms of Failure .....	99
5.4	Discussion .....	107
5.4.1	Effect of Microstructure on Crack Initiation Processes .....	107
5.4.2	Effect of Cement Formulation on Fatigue Life.....	109
5.5	Conclusion.....	112
Chapter 6. Characterisation of Porosity in Vacuum-Mixed Cement.....		113
6.1	Introduction .....	113
6.2	Materials and Methods .....	115
6.2.1	Moulded coupons for Void Population Characterisation.....	115
6.2.2	Mixing Gun Stubs for Void Population Characterisation.....	116
6.2.3	Specimens Containing Large Voids.....	117
6.3	Results .....	118
6.3.1	Characterisation of Void Populations in Moulded Coupons.....	118
6.3.2	Characterisation of Void Populations in Mixing Gun Stubs .....	123
6.3.3	Fractographic Analysis of Void Morphology.....	126
6.4	Discussion .....	129
6.5	Conclusion.....	134
Chapter 7. Fatigue Processes in the <i>In Vivo</i> Cement Mantle.....		135

---

7.1	Introduction .....	135
7.2	Materials and Methods.....	137
7.3	Results.....	141
7.3.1	Defect Population Characterisation .....	141
7.3.2	Fractographic Analysis of <i>Ex Vivo</i> Cement.....	145
7.3.3	Comparison with <i>In Vitro</i> Fracture Surface Characteristics .....	151
7.4	Discussion .....	154
7.5	Conclusion.....	158
Chapter 8. Conclusions and Further Work.....		159
8.1	Summary and Conclusions .....	159
8.2	Further Work.....	161
8.2.1	Microstructural Characterisation of Bone Cement.....	161
8.2.2	Development of Bone Cement with Improved Clinical Longevity .....	162
References .....		165
Appendix A. List of Publications.....		183
Appendix B. Validation of Particle Analysis Plug-in.....		185
Appendix C. Further Characterisation of Cement Microstructure .....		187
Appendix D. Anatomical Terms of Location .....		193
Appendix E. Statistical Analysis of Defect Size Distributions.....		195

---



---

LIST OF FIGURES

---



---

Figure 2-1: Schematic illustration of (a) osteoarthritis of the hip and (b) total hip replacement.....	6
Figure 2-2: Schematic diagram of (a) cemented and (b) uncemented total hip replacement.....	7
Figure 2-3: Primary hip replacement procedures undertaken between 2005 and 2011, by fixation type (after NJR 2012).....	8
Figure 2-4: Survival rates for cemented and uncemented femoral stems in Sweden 1992-2010 (Garrelick <i>et al.</i> 2010).....	13
Figure 2-5: Structure of PMMA.....	14
Figure 2-6: Working times for Palacos R cement, mixed manually at 55 % relative humidity (Heraeus Medical 2008). ....	16
Figure 2-7: SEM image of CMW-1 cement showing (a) pre-polymerised PMMA beads and (b) BaSO <sub>4</sub> filled matrix (adapted from Sinnett-Jones 2007).....	18
Figure 2-8: SRCT Image of porosity in a sample of hand-mixed cement taken from a knee implant (Sinnett-Jones 2007).....	19
Figure 2-9: Typical S-N curve showing variation of stress amplitude for fully reversed fatigue loading of nominally smooth specimens as a function of number of cycles to failure (Suresh 1998).....	23
Figure 2-10: SEM micrograph showing fatigue cracks originating from a void in a Sr-modified A356 cast Al alloy (Wang <i>et al.</i> 2001). ....	24
Figure 2-11: The fatigue life of a sand-cast A356 Al alloy as a function of the void size (Wang <i>et al.</i> 2001). A void size of zero was recorded for specimens that failed from slip bands. ....	25
Figure 2-12: The effect of surface void size on the fatigue life of LP PM319-F and A356-T6 cast Al alloys (Ammar <i>et al.</i> 2008).....	26
Figure 2-13: The effect of void size on the fatigue life on bone cement (Hoey and Taylor 2009b).....	28
Figure 2-14: Finite element model showing the stress distribution around a shrinkage void in a cast Al alloy subjected to a nominal stress of 90 MPa (Tijani <i>et al.</i> 2013). Void geometry was obtained from $\mu$ -CT data. ....	29

Figure 2-15: Computational finite element model of the stress concentration factor $K_t$ around a spherical void as a function of the void diameter and distance from surface (Tijani <i>et al.</i> 2013).....	31
Figure 2-16: Interaction effect between adjacent cracks (Murakami 2002).....	32
Figure 2-17: Fatigue strength predictions of the clustering effects of porosity, showing the effect of void separation on fatigue strength at $10^5$ cycles for three different void diameters (Hoey and Taylor 2009a).....	33
Figure 2-18: S-N curves for a PMMA-based bone cement (Palacos R), highlighting the dependency of the fatigue performance on the specimen geometry and method of loading (Kuehn <i>et al.</i> 2005b).....	34
Figure 2-19: SRCT image of a fatigue crack (highlighted in red) initiating from a void in a sample of bone cement (Sinnott-Jones 2007).....	36
Figure 2-20: FEG-SEM image of fatigue cracks initiating from a barium sulphate agglomerate (Sinnott-Jones 2007).....	38
Figure 2-21: Optical micrograph of fatigue striations originating from a pore (P) at the stem-cement interface (Jeffers <i>et al.</i> 2007).....	44
Figure 2-22: SEM micrograph of fracture surface of an <i>ex vivo</i> cement mantle, showing cracking and fatigue striations surrounding a large void (Jasty <i>et al.</i> 1991).....	45
Figure 3-1: Photographs of (a) Instron actuator and load frame; (b) custom self-aligning four-point bend test rig.....	52
Figure 3-2: Schematic diagram of specimen geometry and loading conditions; the shaded region corresponds to the 1mm region of interest referred to in subsequent chapters.....	53
Figure 3-3: Histograms showing grey values (attenuation coefficients) for a typical CMW-1 specimen: (a) identification of the three grey-value intervals - the first, very small peak corresponds to void attenuation and the second peak to attenuation of the bulk PMMA construct; (b) magnification of the small peak corresponding to attenuation of voids.....	57
Figure 3-4: Effect of median filtering on image quality of reconstructed CT slice: (a) original image; (b) image processed using 3 x 3 median filter; (c) image processed using 5 x 5 median filter.....	58
Figure 3-5: Slice showing (a) voids and radiopacifier agglomerates and (b) same slice with features selected according to the grey value thresholds defined in Figure 3-3....	58
Figure 3-6: Relationship between threshold attenuation coefficient and volume fraction of void interval.....	60

Figure 3-7: Relationship between threshold attenuation coefficient and volume fraction of radiopacifier interval..... 60

Figure 3-8: Computed tomography images showing (a) ring artefact and (b) localised beam hardening, indicated by yellow arrows. .... 61

Figure 3-9: Schematic showing the effect of partial volume averaging on attenuation coefficient – both voxels may be represented by the same average grey value, though their material compositions are entirely different..... 62

Figure 4-1: Representative CT slices highlighting variation in microstructure between cement formulations: (a) CMW-1, (b) CMW Original..... 70

Figure 4-2: Distribution of microstructural defects within the 1mm section of a ‘typical’ specimen: (a) CMW-1 and (b) CMW Original. Gridlines are 1mm apart..... 71

Figure 4-3: SEM micrograph of clusters of individual barium sulphate particles on CMW-1 fracture surface. Note the poor adhesion to the polymer matrix and evidence of plastic deformation during fracture. .... 71

Figure 4-4: Size distribution of microstructural features in 1mm gauge sections of CMW-1 and CMW Original specimens..... 73

Figure 4-5: S-N data for all CMW Original and CMW-1 specimens tested. .... 75

Figure 4-6: SEM micrograph of CMW-1 fracture surface, showing (1) initiation site, (2) ‘halo’ region of early crack growth, (3) region of short crack growth and (4) region of long crack growth. Arrow indicates overall direction of crack propagation..... 76

Figure 4-7: SEM micrograph of CMW Original fracture surface, showing (1) initiation site, (2) region of short crack growth and (3) region of long crack growth. Arrow indicates overall direction of crack propagation. .... 76

Figure 4-8: Multiple fatigue cracks initiating from a BaSO<sub>4</sub> agglomerate in CMW-1. Black arrow indicates overall direction of crack propagation. Discontinuous growth bands are evident in the surrounding polymer, as indicated by the yellow arrows. .... 77

Figure 4-9: SEM micrographs of a CMW-1 fracture surface, showing a crack-initiating agglomerate surrounded by pre-polymerised beads. Note the poor adhesion between the radiopacifier and polymer matrix, with pull-out of barium sulphate particles indicated by the arrow..... 78

Figure 4-10: Discontinuous growth bands in a pre-polymerised bead in CMW-1. Arrow indicates overall direction of crack propagation. .... 78

Figure 4-11: 20x optical micrograph of CMW Original specimen showing fatigue cracks initiating from a void. Black arrow indicates overall direction of crack propagation. Discontinuous growth bands are evident in the surrounding pre-polymerised beads, as indicated by the yellow arrow. .... 79

Figure 4-12: Secondary cracks initiating from a void in CMW Original. ....	80
Figure 4-13: Relationship between the equivalent spherical diameter (ESD) of crack-initiating agglomerates in CMW-1 and the corresponding number of cycles to failure (N <sub>f</sub> ).....	81
Figure 5-1: Representative CT slices highlighting microstructure of (a) Palacos R and (b) Smartset HV, prior to the application of a 3 x 3 median filter (as described in Section 3.5).....	93
Figure 5-2: Distribution of (a) voids and (b) ZrO <sub>2</sub> particles in Palacos R. ....	94
Figure 5-3: Distribution of (a) voids and (b) ZrO <sub>2</sub> particles in Smartset HV. ....	94
Figure 5-4: Size distribution of microstructural features in 1mm sections of Palacos R and Smartset HV. ....	98
Figure 5-5: Size distribution of ZrO <sub>2</sub> particles measured in one matchstick (2 x 2 x 2 mm) specimen of Palacos R using synchrotron radiation CT (“ESRF”) at 1.8 μm resolution and CT 160Xi (“Benchtop”) at 8.3 μm resolution.....	98
Figure 5-6: SEM micrograph of Palacos R fracture surface, showing (1) initiation site, (2) ‘halo’ region of early crack growth, (3) region of short crack growth and (4) region of long crack growth. Arrow indicates overall direction of crack propagation.....	99
Figure 5-7: Discontinuous growth bands surrounding crack initiation sites in (a) Palacos R and (b) Smartest HV, as indicated by the yellow arrows. Black arrows show overall direction of crack propagation. ....	100
Figure 5-8: Crack initiating voids in (a-b) Palacos R and (c) Smartset HV.....	100
Figure 5-9: Multiple cracks initiating from a agglomerate of ZrO <sub>2</sub> particles in Palacos R. Arrow indicates overall direction of crack propagation. ....	101
Figure 5-10: Discontinuous growth bands indicating multiple crack initiation sites in Smartset HV. Arrows indicate local direction of crack propagation ( $\sigma = 50$ MPa, $N_f = 2.2$ million).....	102
Figure 5-11: Discontinuous growth bands in a pre-polymerised bead at the edge of a crack-initiating void on the fracture surface of a Smartset HV specimen.....	102
Figure 5-12: Particles of zirconium dioxide on the fracture surface of (a) Palacos R and (b) Smartset HV at 1000 x magnification. ....	103
Figure 5-13: Particles of zirconium dioxide on the fracture surface of (a) Palacos R and (b) Smartset HV at 250x magnification.....	103
Figure 5-14: Zirconium dioxide agglomerates close to the crack initiation site in (a) Palacos R and (b) Smartset HV, highlighting local deformation at the ZrO <sub>2</sub> /matrix interface.....	104

Figure 5-15: Fatigue test results for all failed specimens of all four cement formulations.....	110
Figure 6-1: Schematic diagram of four-point bend specimen, highlighting central 10mm region of interest (shaded) for void population characterisation. ....	115
Figure 6-2: Examples of void distributions in CMW Original specimens: (a) specimen with 1.5 voids per mm <sup>3</sup> and bulk porosity of 0.007%; (b) specimen with 0.5 voids per mm <sup>3</sup> , bulk porosity of 0.289% and 2 macro-voids. The upper views are transverse, and the lower views longitudinal, with respect to the direction of injection of the cement into the moulds. Gridline spacing is 1mm.....	119
Figure 6-3: Mean size distribution of voids in 10mm sections of CMW-1 and CMW Original.....	120
Figure 6-4: Example images of large voids in Palacos R cement with secondary satellite voids. Gridline spacing is 1mm. ....	120
Figure 6-5: Relationship between the equivalent spherical diameter of the primary void and the corresponding number of satellite voids in CMW-1 (blue) and CMW Original (red).....	122
Figure 6-6: Relationship between the volume of the primary void and the total volume of surrounding satellite voids in CMW-1 (blue) and CMW Original (red).....	122
Figure 6-7: Distribution of voids (shown in red) in cement mixing gun stubs.....	124
Figure 6-8: Mean size distribution of voids in cement stub and moulded specimens fabricated from one charge of CMW Original cement. ....	125
Figure 6-9: SEM micrographs showing examples of type 1 voids in (a) CMW Original and (b) Palacos R.....	126
Figure 6-10: SEM micrographs showing examples of type 2 voids in CMW Original...	126
Figure 6-11: SEM micrographs showing examples of type 3 voids in (a) CMW-1, (b-d) Palacos R and (e-f) Smartset HV. ....	127
Figure 6-12: Type 1 satellite void in the vicinity of a large type 3 void in Smartset HV. ....	128
Figure 6-13: SEM micrograph showing crack initiation from type 2 satellite voids in CMW-1. ....	128
Figure 7-1: (a) Zimmer CPT® femoral stem retrieved at revision; (b) schematic diagram of a cemented Zimmer CPT® Primary Hip construct, indicating likely origin of retrieved cement specimen.....	138
Figure 7-2: CT slice through width of retrieved cement specimen ( <i>i.e.</i> transverse view). The arrow indicates the location of the main pre-existing crack.....	139

Figure 7-3: CT reconstructions of (a) coronal view of retrieved cement specimen; (b) coronal view of distribution of voids (coloured red) within specimen; (c) transverse view of distribution of voids, showing position of pre-existing crack indicated by black arrow. ....143

Figure 7-4: Size distribution of voids in specimen of retrieved cement.....143

Figure 7-5: P-P plot showing the fit between the observed cumulative distribution function and the theoretical cumulative distribution predicted by the GEV distribution function. ....144

Figure 7-6: (a) Photograph showing *ex vivo* cement fracture surface – letters A-C indicate regions referred to in subsequent figures; (b) corresponding CT slice through crack plane. Note the presence of a secondary crack in the bottom right corner of both images. ....145

Figure 7-7: (a) SEM micrograph (x25) of region D on the cement fracture surface; (b) enlargement of corresponding CT slice through main crack plane. A secondary crack is evident in both images, indicated by yellow arrows. ....146

Figure 7-8: SEM micrograph (x950) of region A, showing: (a) cluster of ZrO<sub>2</sub> radiopacifier; (b) red blood cells; (c) pre-polymerised bead; (d) indent indicating ZrO<sub>2</sub> pull-out; (e) void.....146

Figure 7-9: SEM micrographs (x250) indicating different void types identified on *ex vivo* fracture surface .....148

Figure 7-10: SEM micrograph (x370) of region C, showing secondary ‘satellite’ voids around a shrinkage void close to the cement-stem interface. ....148

Figure 7-11: SEM micrograph (x50) of region C, highlighting different morphologies of smooth fast fracture region and roughened surface of pre-existing crack. ....149

Figure 7-12: SEM Micrographs of region B, showing fatigue striations on fracture surface: (a) x25; (b) x250; (c) x500; (d) x2500. ....149

Figure 7-13: SEM Micrograph (x3,500) of region B, showing opened-up craze on fracture surface. ....150

Figure 7-14: SEM Micrographs (x250) of (a) *ex vivo* region A and (b) *in vitro* fractures surfaces, highlighting stepped morphology, clusters of ZrO<sub>2</sub> particles (black arrows) and ZrO<sub>2</sub> pull-out (white arrows).....151

Figure 7-15: SEM micrographs (x2,500) of (a) *ex vivo* region A and (b) *in vitro* fracture surfaces, highlighting morphology of ZrO<sub>2</sub> particles and limited bonding to surrounding polymer, with evidence of localised plastic deformation during fracture (yellow arrows). ....152

Figure 7-16: SEM Micrographs of void morphology on fracture surfaces of (a) *ex vivo* region B (x200) and (b) *in vitro* (x250) specimens. Pre-polymerised beads, identified by yellow arrows, are visible on the internal surfaces of the voids. ....153



---



---

LIST OF TABLES

---



---

Table 2-1: Patient characteristics for primary total hip replacement in 2011 (NJR 2012).....	10
Table 2-2: Recommended loads for the testing of hip implants (Bergmann <i>et al.</i> 2010) .....	11
Table 2-3: Indications for revision hip surgery in 2011, for all fixation types. Indications are not mutually exclusive (NJR 2012). .....	11
Table 2-4: Short to medium term revision rates for primary THR, by fixation type (NJR 2012). .....	12
Table 2-5: Compositions of six commercial bone cement formulations (Lewis 1997)..	15
Table 2-6: Comparison of the mechanical properties of three commercial bone cement brands (Lewis and Mladi 2000). .....	20
Table 2-7: Evolution of cementing techniques (Breusch and Malchau 2005, Haydon <i>et al.</i> 2004) .....	21
Table 3-1: Composition of the four cement formulations selected for use in this work. ....	47
Table 3-2: Theoretical attenuation coefficients for selected materials at 40 kV (Hubbell and Seltzer 2004). .....	57
Table 4-1: Characteristics of microstructural features in 1x 8 x 10mm gauge sections of CMW-1 and CMW Original.....	72
Table 4-2: Characteristics of BaSO <sub>4</sub> agglomerate populations in 1 x 8 x 10mm gauge sections of CMW-1. ....	74
Table 4-3: Characteristics of crack-initiating agglomerates in CMW-1. ....	81
Table 5-1: CT acquisition parameters.....	92
Table 5-2: Characteristics of microstructural features in 1 x 8 x 10mm gauge sections of Palacos R and Smartset HV.....	97
Table 5-3: Results of mechanical testing – Palacos R.....	105
Table 5-4: Results of mechanical testing – Smartset HV .....	105
Table 5-5: Characteristics of crack-initiating voids .....	106
Table 6-1: CT acquisition parameters – moulded cement coupons .....	116
Table 6-2: CT acquisition parameters – cement gun stubs.....	116
Table 6-3: Bulk porosity for each of the four cement types (8 x 8 x 10 mm sections). ..	119
Table 6-4: Characteristics of void populations in cement stubs.....	123

Table 7-1: Composition of Palacos R and Palacos R+G cements..... 140  
Table 7-2: Void population characteristics..... 144

---

---

## NOMENCLATURE

---

---

ASA	American Society of Anaesthesiologists
AOA	Australian Orthopaedic Association
ASTM	American Society for Testing and Materials
BaSO <sub>4</sub>	Barium sulphate
BEI	Backscattered Electron Image
BMI	Body Mass Index
BPO	Benzoyl peroxide
BW	Bodyweight
CT	Computed Tomography
DCG	Discontinuous Crack Growth
DGB	Discontinuous Growth Band
$\Delta K$	Stress intensity factor range
DMPT	Dimethylparatoludeine
EDX	Energy Dispersive X-ray spectroscopy
ESD	Equivalent spherical diameter
ESRF	European Synchrotron Research Facility
EtO	Ethylene oxide
FCP	Fatigue Crack Propagation
FEG-SEM	Field Emission Gun Scanning Electron Microscopy
HA	Hydroxyapatite
ISO	International Organisation for Standardization
Micro-CT	Micro-Computed Tomography
$\mu$ -CT	Micro-Computed Tomography
$\mu$ m	Micrometre
MMA	Methyl methacrylate

MW	Molecular Weight
<i>N</i>	Number
NAR	Norwegian Arthroplasty Register
<i>N<sub>f</sub></i>	Number of cycles to failure
NJR	National Joint Registry for England and Wales
<i>N,N</i> -DMPT	<i>N,N</i> -dimethylparatoluidine
OA	Osteoarthritis
PMMA	Poly(methyl methacrylate)
P(MMA/MA)	Poly(methyl methacrylate/ methyl acrylate)
P(MMA/ST)	Poly(methyl methacrylate/ styrene)
ppm	Parts per million
R	Ratio of minimum to maximum stress
RH	Relative Humidity
$\sigma$	Applied stress
SD	Standard Deviation
SEI	Secondary Electron Image
SEM	Scanning Electron Microscopy
SHAR	Swedish Hip Arthroplasty Register
SiC	Silicon carbide
S-N	Stress vs. Number of cycles to failure
SRCT	Synchrotron Radiation Computed Tomography
<i>T<sub>g</sub></i>	Glass transition temperature
THA	Total Hip Arthroplasty
THR	Total Hip Replacement
TJR	Total Joint Replacement
WOF	Work of Fracture
w/w	Weight/weight
ZrO <sub>2</sub>	Zirconium dioxide

---

---

## DECLARATION OF AUTHORSHIP

---

---

I, Natalie Shearwood-Porter, declare that this thesis entitled '*Micromechanical Characterisation of Fatigue Failure in Acrylic Bone Cement*' is an account of the work carried out within the Bioengineering Sciences and Engineering Materials Research Groups, Faculty of Engineering and the Environment, University of Southampton, under the supervision of Prof. Martin Browne and Prof. Ian Sinclair. The work presented in the thesis is my own, and has been generated by me as the result of my own original research.

No part of this thesis has previously been submitted for a degree at this University or any other institution. Where the work of others has been drawn upon, due acknowledgement and/or appropriate referencing has been included in the text. Parts of this work have been published prior to submission and a list of journal and conference publications are given in Appendix A.

Signed: .....

Date: .....



---

---

## ACKNOWLEDGEMENTS

---

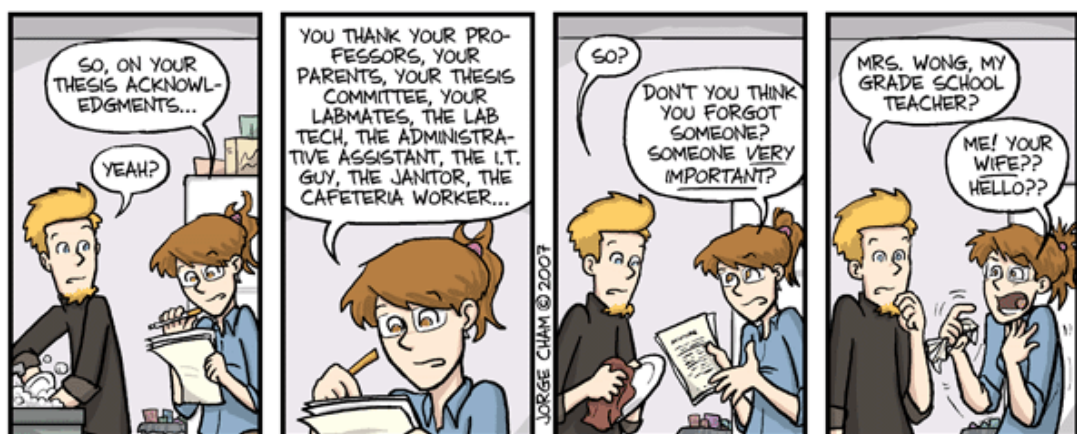
---

*The first mention must go to my supervisors, Professors Martin Browne and Ian Sinclair; without their intellectual and financial support this thesis would not have been possible. Special thanks to the Boss, for his endless patience, sense of humour, and for 'saving' me from a military career by extolling the virtues of academia.*

*Thank you to my fellow post-grads and post-docs for keeping me sane for the last ... ahem ... four years: Jack (putting the world to rights), Liam (chai breaks), Kath (my doppelganger), Prammy (humour and biscuits), Richard (employment opportunities), Alex (mechanical testing guru and Parisian tour guide) and all the occupants of 3021, past and present.*

*Thank you to the group secretaries, Gwyneth and Sue, for acting as the researcher's equivalent of directory enquiries; to the technicians, Chris, Dave and Bob; to Shuncaï, for assistance with SEM; and to the  $\mu$ -VIS fellows (Anna, Mav, Rich and Dmitry) for their invaluable help with all things CT related.*

*Finally, thank you to my parents, for supporting my seemingly endless academic folly, and to my long-suffering husband Joe. This one's for you:*





---

---

## 1. INTRODUCTION

---

---

### 1.1 MOTIVATION

Total joint replacement is an established procedure, with good long-term survivorship for the hip and knee joints. Indicated for the treatment of conditions such as end-stage osteoarthritis, hip dysplasia and avascular necrosis (NJR 2012), the aims of joint replacement surgery are to relieve pain and improve the function and mobility of the affected joint. In developed countries, total joint replacement is one of the most common elective surgeries of the modern era, with many thousands of operations conducted each year in England and Wales alone (NJR 2012). Furthermore, rising incomes in countries such as Brazil, India and China have led to increasing demand for joint arthroplasty procedures in these emerging markets as uptake of private health insurance has increased (Gagnon 2011).

The latest National Joint Registry data for England and Wales shows that over the last eight years, the average body mass index of arthroplasty patients has been steadily increasing (NJR 2012). In 2011, seventy-seven percent of hip replacement patients were classified as overweight or obese. In addition, longer patient life expectancies, higher activity levels and greater functional expectations are placing ever greater demands on the sustained load-bearing capabilities of implants. Acrylic bone cement is routinely used for fixation of orthopaedic implants (Garellick *et al.* 2010, NAR 2010, NJR 2012), and remains the 'gold standard' for elderly patients and those with existing medical conditions who cannot rely on bone in-growth to achieve stable cementless fixation. Arguably, it is these vulnerable patient groups who are also least capable of undergoing multiple successful revision surgeries. Therefore, there is a need to improve the performance of cemented fixation in order to maximize the longevity of the cemented construct.

Aseptic loosening remains the predominant cause of failure in cemented total hip arthroplasty (NJR 2012). Damage accumulation due to initiation and coalescence of micro-cracks within the cement mantle and at its interfaces with the stem and bone has been implicated in the loosening process (Jeffers *et al.* 2007, Race *et al.* 2011, for example). It has been shown that the microstructure of the cement, including pre-polymerised beads, matrix, radiopacifier particles and voids, is a factor in the development of fatigue cracks (Lewis 1997). While the impact of porosity on *in vitro*

failure has been extensively researched, leading to the development of improved mixing methods, the relative effects of other microstructural features, such as radiopacifier particles, has largely been ignored despite evidence linking particle agglomerates to crack initiation (Sinnott-Jones 2007). Furthermore, there is a lack of clinical evidence to validate these experimental findings, leading to some controversy over the effect of porosity on cement fatigue *in vivo* (Ling and Lee 1998, Janssen *et al.* 2005a, 2005b). A greater understanding of the micromechanics of the damage accumulation process is therefore required to aid the development of more robust cement formulations can be developed.

Until recently, characterisation of microstructural features in acrylic bone cement has been limited to two-dimensional stereological methods, which typically involved sectioning, staining and optical examination (e.g. Jasty *et al.* 1990, Wang *et al.* 1993, Dunne *et al.* 2003 and Mau *et al.* 2004). Such techniques are destructive, time-consuming and limited in resolution by the number of sections that can reasonably be examined. The use of non-destructive, high-resolution micro-computed tomography ( $\mu$ -CT) is therefore advantageous for three-dimensional volume assessment of cement, offering enhanced repeatability (Cox *et al.* 2005). Although  $\mu$ -CT has been applied by other researchers in this field, studies have generally been limited to qualitative observation of cement microstructure (Kurtz *et al.* 2005, Sinnott-Jones 2007) and calculation of bulk porosity values (Cox *et al.* 2005, Hoey and Taylor 2009b). A detailed, quantitative comparison of the size, morphology and distribution of microstructural features such as radiopacifiers and pores, exploiting the capabilities of advanced  $\mu$ -CT combined with SEM for failure characterisation, would therefore be a valuable additional contribution to the existing literature.

## 1.2 OBJECTIVES

This project aims to use a combination of high-resolution interrogative techniques to determine the relative effects of microstructural features and cement formulation on the fatigue performance of conventional bone cements. The work described exploits the three-dimensional volume imaging capabilities of  $\mu$ -CT for the microstructural characterisation of four commercial cement formulations. This is complemented by four-point bend fatigue testing and fractographic analysis using scanning electron microscopy. Particular emphasis is placed on the impact of radiopacifier particles (i.e. zirconium dioxide and barium sulphate) and voids of differing morphologies on the initiation of fatigue cracks *in vitro*. Experimental fracture surfaces are then compared and contrasted with the microstructure and fractographic characteristics of an *ex vivo* cement specimen retrieved during revision hip arthroplasty surgery.

The main objectives of this research are:

- i. To develop a 'data rich' method for the systematic, quantitative characterisation of cement microstructure and fatigue failure mechanisms in low volume, high value specimens;
- ii. To investigate the relative influence of different microstructural features (i.e. voids and radiopacifier particles) on cement fatigue and failure *in vitro*;
- iii. To compare microstructural and fractographic characteristics of *in vitro* and *ex vivo* cement specimens.

It is hoped that a greater understanding of the microstructural characteristics of fatigue crack initiation in acrylic bone cement will ultimately inform the development of more robust cement formulations, improved mixing methods and enhanced *in vitro* testing regimes that better capture *in vivo* failure methods, in order to improve the longevity of cemented fixation.



---

---

## 2. LITERATURE REVIEW

---

---

### 2.1 TOTAL HIP REPLACEMENT

#### 2.1.1 INTRODUCTION

Early attempts to replace the 'ball and socket' of the hip joint date back to the late 19<sup>th</sup> Century, when joints damaged by tuberculosis were implanted with prostheses made from ivory (Reynolds and Tansey 2007). The first clinically successful total hip replacements were developed in the 1950s and 1960s; today, total hip replacement is an established procedure, with nearly 80,000 operations conducted in 2011 in the UK alone (NJR 2012).

The main indication for primary total hip replacement (THR) is osteoarthritis, which accounted for 93% of all hip replacement operations in 2011, although the procedure is also used to treat other conditions, including avascular necrosis (2%), fracture of the femoral neck (2%), congenital hip dysplasia (2%) and rheumatoid arthritis (1%). Osteoarthritis is a degenerative joint disease, resulting from wear of the articular cartilage of the affected joint, which leads to inflammation, bony spur growth and deformity (Figure 2-1 (a)), causing pain and stiffness. An estimated 8.5 million people have osteoarthritis in the UK; approximately 12% of the population aged over 65 suffers from hip pain due to the condition (NHS 2012). THR aims to reduce this pain and restore function and range of motion (Wroblewski *et al.* 2005) by replacing the articulating surfaces of the diseased joint with artificial femoral and acetabular implants (Figure 2-1 (b)).

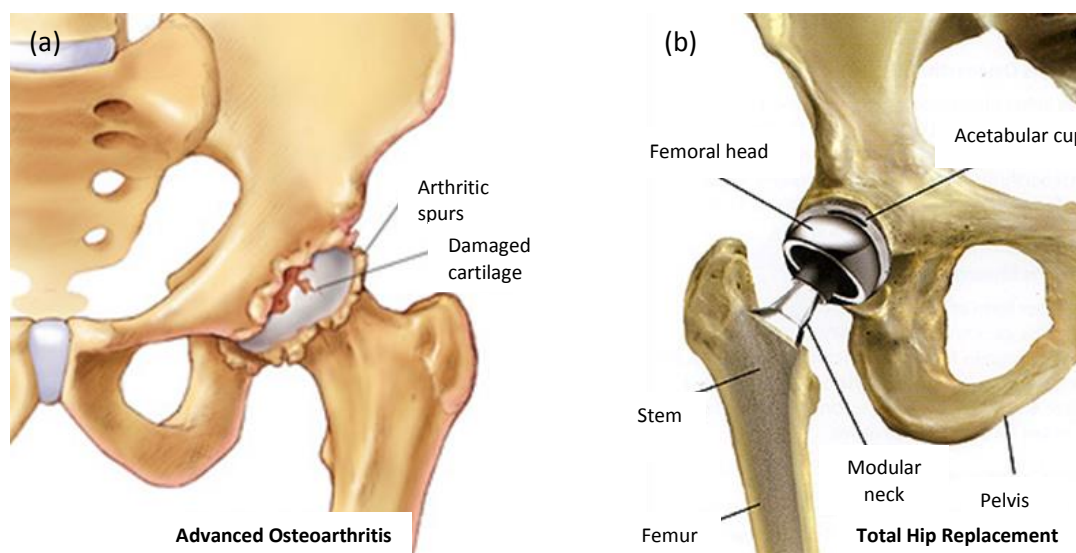


Figure 2-1: Schematic illustration of (a) osteoarthritis of the hip<sup>1</sup> and (b) total hip replacement<sup>2</sup>.

### 2.1.2 IMPLANT CHARACTERISTICS

Although the general principle of total hip arthroplasty remains consistent (comprising a femoral stem and head paired with an acetabular cup), there are a wide variety of total hip prostheses on the market that vary in choice of bearing surface and method of fixation. Bearing surface combinations include, in order of popularity, a metal head articulating on a polyethylene cup (MoP), ceramic head on ceramic cup (CoC), ceramic-on-polyethylene (CoP), metal-on-metal (MoM) and rarely, ceramic-on-metal (CoM). The femoral stem is most commonly manufactured from cobalt-chrome (NJR 2012). The femoral implant may be modular (*i.e.* with separate stem and head components), collared or collarless, and the surface finish may be matte or polished; polished collarless tapered stem designs currently dominate the domestic market (NJR 2012). One or both of the femoral and acetabular implants may be fixed to the surrounding bone using acrylic bone cement, or the THR may be cementless (Figure 2-2).

<sup>1</sup> <http://www.zimmer.com/web/images/anatomy/hips/OsteoarthritisHip1.jpg>

<sup>2</sup> <http://www.orthoteam.com/wp-content/uploads/2010/12/hipTotalHipReplacement.jpg>

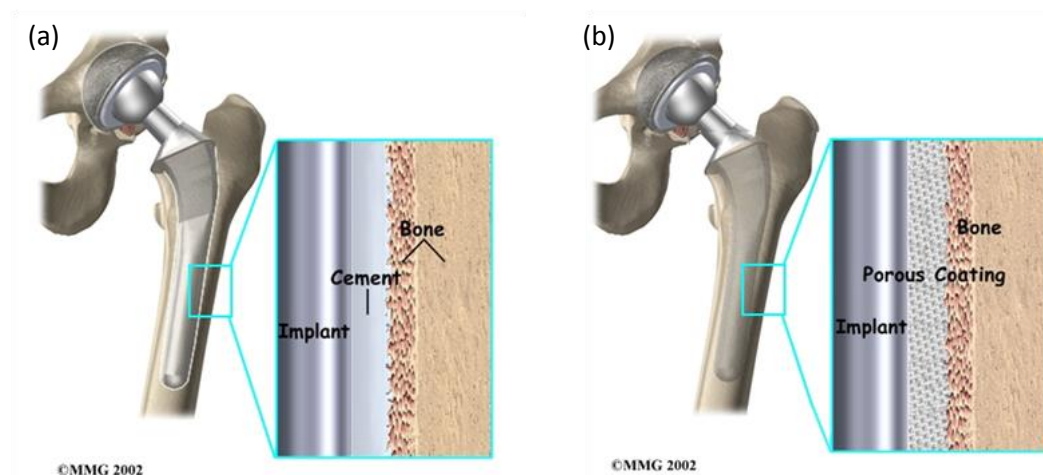


Figure 2-2: Schematic diagram of (a) cemented and (b) uncemented total hip replacement<sup>1</sup>.

Poly(methylmethacrylate) (PMMA) acrylic bone cement is routinely used in total hip arthroplasty for implant fixation: in 2011, over 40,000 total hip procedures involving cement were recorded in the National Joint Registry (NJR 2012). Bone cement acts as a grout, providing a mechanical interlock between the implant and the bone (Figure 2-2 (a)). As with all fixation types, the cement functions to transfer bodyweight and service loads from the implant to the bone, and increase the load-bearing capacity of the construct (Lewis 1997).

However, concerns over the integrity of bone cement, and high rates of loosening in some hospitals in the 1960s and 1970s, led to the development of cementless methods of fixation, which rely on bone in-growth to achieve biological fixation and mechanical interlock between the implant and the host bone (Pilliar 2005). Original cementless designs incorporated porous surfaces designed to encourage bone formation between pores; metallic, trabecular-structured porous coatings have since been developed to mimic the physical and mechanical properties of bone, with up to 80% porosity to encourage enhanced osseointegration (Levine *et al.* 2006). A major development in fixation technology took place with the introduction of calcium hydroxyapatite (HA) coatings, to induce osteoconduction (HA is the predominant mineral constituent of bone). HA coatings can either be used alone or in conjunction with a porous surface, thus providing stronger fixation than metallic porous coatings alone (Coathup *et al.* 2005). Cementless fixation requires a high degree of precision in the surgical

<sup>1</sup> <http://www.eorthopod.com/content/hip-replacement>

preparation of the bone cavity, to achieve adequate initial stability of press-fit components (Bellemans *et al.* 2005b).

Hybrid total hip arthroplasty involves the use of both cemented and cementless components, most commonly consisting of a cemented femoral stem combined with a cementless acetabular cup (NJR 2012). Hybrid procedures accounted for 17% of all primary hip replacements conducted in England and Wales in 2011.

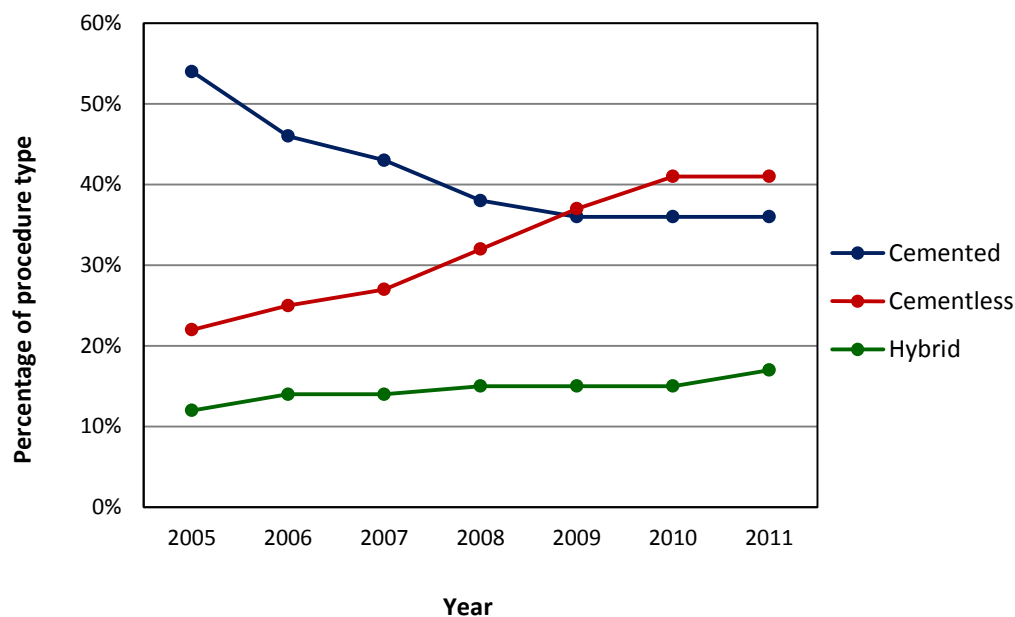


Figure 2-3: Primary hip replacement procedures undertaken between 2005 and 2011, by fixation type (after NJR 2012).

The long-term survivorship of cemented implants is high, with success rates in excess of 90% reported after 15 years (Lewis 1997, Berger 2001). Bone cement was previously considered the 'gold standard' in fixation (Bauer and Schils 1999, Bellemans *et al.* 2005a), although it has suffered a reduction in popularity in recent years, according to joint registry data (NJR 2012, NAR 2010, Garrelick *et al.* 2010); in England and Wales, cementless hip procedures outnumbered fully cemented replacements for the first time in 2009 (Figure 2-3). This may be partly attributed to concern over so called 'cement disease', in which cement debris was thought to induce adverse biological effects, contributing to loosening and failure of implants (Goodman 2005). It was later discovered, however, that particles of polyethylene generated through wear at the articulating surfaces were predominantly responsible for this effect (Agarwal

2004). However, 'cement disease' has arguably led to increased interest, development and uptake of cementless fixation, and the long-term survivorship of cementless methods of fixation has improved over the last two decades (Garrelick *et al.* 2010).

### 2.1.3 PATIENT CHARACTERISTICS

The average age for a primary hip arthroplasty patient in England and Wales has remained static since the inception of the National Joint Registry in 2003. This trend is replicated in the data from the Swedish and Norwegian national joint registers. In all three countries, female patients outnumbered males; sixty percent of primary hip replacement patients in England and Wales in 2011 were female. The mean age for female patients was two years higher than for male patients (NJR 2012).

The Body Mass Index (BMI) measurements of hip replacement patients have been steadily increasing over the last decade. Mean patient BMI rose from 27.4 to 28.6 between 2004 and 2011, while the percentage of obese patients (*i.e.* those presenting with a BMI of 30 or above) increased from 29% to 37% over the same period (NJR 2012). The Swedish Hip Arthroplasty Register reported that obese patients had an increased risk of failure of primary hip replacement within the first two years after surgery. Increasing the strength and stability of fixation may therefore be beneficial, to ensure hip replacements are capable of sustaining this greater loading.

In addition to the trend of increasing BMI, the health of patients undergoing hip replacement has been declining in recent years. Health and fitness is classified in the National Joint Registry according to the American Society of Anesthesiologists' (ASA) grading system, where grade P1 represents a normal healthy patient and P5 a moribund patient who is not expected to survive (NJR 2012). Since 2003, the percentage of hip replacement patients graded otherwise fit and healthy (P1) has dropped from 37% to 15%, while the number of patients with mild systemic disease (P2) has increased from 53% to 70% and those with incapacitating systemic disease (P3) from 9% to 15%.

Typical patient characteristics vary for the different methods of implant fixation, as highlighted in Table 2-1. Patients undergoing hip replacements involving the use of bone cement tend to be older and less healthy than those undergoing cementless procedures. This is consistent with the notion that bone cement remains the 'gold standard' for patients with poor bone stock, either due to age or underlying medical conditions, who cannot rely on bone in-growth to achieve stable cementless fixation.

Table 2-1: Patient characteristics for primary total hip replacement in 2011 (NJR 2012).

	Primary THR (cemented)	Primary THR (hybrid)	Primary THR (uncemented)
No. procedures	25,789	12,794	31,307
Mean patient age	72.8	69.6	65.4
Mean patient BMI	28.3	28.6	28.8
Patient physical status: P1	10%	14%	19%
Patient physical status: P2	70%	70%	70%
Patient physical status: P3	19%	16%	11%

Physical status grades: P1 (fit and healthy); P2 (mild systemic disease, not incapacitating); P3 (incapacitating systemic disease).

#### 2.1.4 SERVICE CONDITIONS

Total hip replacement implants are known to experience cyclic loading during normal daily activities such as walking and stair climbing. Research using specially instrumented prostheses has been conducted by Bergmann and co-workers (2001, 2004 and 2010) to measure the magnitude of the contact forces in patients with total hip replacements. Cyclic loading of up to 300% bodyweight was reported during general activity, with higher loads (in excess of 800% bodyweight) measured during untoward events such as trips and falls. Peak loads may be higher in patients with disturbed gait patterns (Bergmann *et al.* 2001). Based on this analysis, recommendations were made for realistic loads for the testing of hip implants (Table 2-2).

Estimates of the number of gait cycles per year for implanted patients range from 0.5 – 13 million cycles (cited in Fischer *et al.* 2009) and will of course vary greatly depending on the activity level of the individual patient. According to Bergmann *et al.* (2010), active patients may accumulate 10 million loading cycles in 3.9 years; based on this assumption, an implant designed to last 15 years may experience approximately 40 million cycles during its lifetime.

Table 2-2: Recommended loads for the testing of hip implants (Bergmann *et al.* 2010)

Activity	Average Peak Force (N)	Highest Peak Force (N)
Walking	1,800	3,900
Stair climbing	1,900	4,200
Stumbling	-	11,000

### 2.1.5 FAILURE OF TOTAL HIP REPLACEMENT

Clinical failure of a THR is usually defined as the point at which revision surgery is necessitated to replace one or both components (Söderman 2000). The main indications for revision surgery in England and Wales are presented in Table 2-3. The predominant cause of failure in THR is aseptic loosening, cited as an indication for 42% of recent hip revisions in England and Wales, 48% in Norway and 56% in Australia (AOA 2009, NAR 2010 & NJR 2012).

Table 2-3: Indications for revision hip surgery in 2011, for all fixation types. Indications are not mutually exclusive (NJR 2012).

Indication for revision	Percentage of patients
Aseptic loosening	42%
Pain	24%
Dislocation	13%
Lysis	13%
Infection	12%
Wear	12%
Peri-prosthetic fracture	8%
Malalignment	5%

Aseptic loosening may occur due to a reduction in bone density at the implant site caused by stress shielding (as a result of the increased stiffness of implant materials compared to the host bone) or osteolysis (dissolution of bone due to disease, infection or inadequate blood supply). In the case of cemented implants, chemical or thermal necrosis of peri-prosthetic bone may also occur due to leaching of unreacted monomer

from the bone cement or high peak curing temperatures respectively (Stanczyk and van Rietbergen 2004). In addition to causing failure by aseptic loosening, osteolysis at the implant site may contribute to peri-prosthetic fracture, and complicate revision surgery by increasing the difficulty of achieving stable implant fixation, necessitating the use of a bone graft to restore bone stock (Gross 2005).

Osteolysis may occur as an auto-immune response to the presence of small particles (<7 µm) of wear debris (Agarwal 2004). Particles are phagocytised (digested) by specialist white blood cells called macrophages, which then secrete enzymes to induce bone resorption or inhibit bone formation. Macrophages may also differentiate into osteoclasts (bone-removing cells) leading to more rapid bone resorption at the cement-bone or implant-bone interface. Osteolysis was initially observed in cemented implants and was thought to be induced solely by cement debris, leading to the term 'cement disease'. It is now more correctly termed 'particulate disease' and is known to occur as a result of wear particles from both cement and implant materials, predominantly polyethylene, which accounts for 70-90% of wear debris volume; the size of this debris is in the range most likely to induce macrophage response (Agarwal 2004, Goodman 2005).

Table 2-4: Short to medium term revision rates for primary THR, by fixation type (NJR 2012).

Fixation Type	Risk of revision (%)		
	Year 3	Year 5	Year 8
Cemented	0.98	1.46	2.29
Hybrid	1.24	1.92	2.95
Reverse hybrid	1.52	2.19	3.30
Cementless	2.20	3.56	5.10

Survival rates and indications for revision vary according to the method of fixation of the primary THR and time since implantation. The use of bone cement is associated with a lower risk of revision in the first eight years (Table 2-4), but a higher revision rate in the longer term, particularly for aseptic loosening (Figure 2-4). According to NJR data, the main causes of failure for cemented implants at 8 years were infection (24%) and dislocation (24%) compared to aseptic loosening (20%) and dislocation (20%) in uncemented implants. High rates of early aseptic loosening in uncemented procedures may be attributed to peri-prosthetic osteolysis and failure of the implant-bone

interface (Lewis 1997), which relies on osseointegration of porous metal and/or HA coated implants, while late aseptic loosening of cemented implants may be attributed to degradation of the cement mantle (Williams and McQueen 1992).

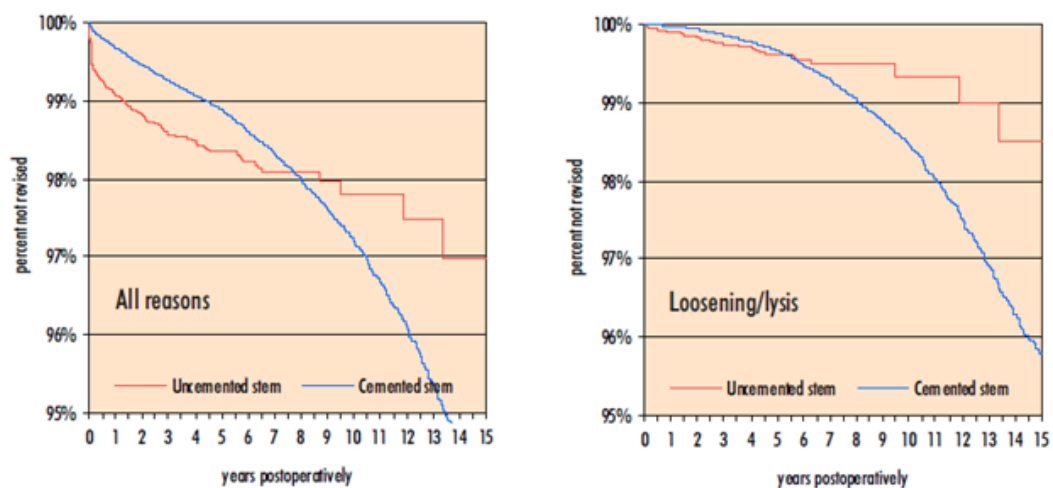


Figure 2-4: Survival rates for cemented and uncemented femoral stems in Sweden 1992-2010 (Garrellick *et al.* 2010).

## 2.2 BONE CEMENT CHARACTERISTICS

### 2.2.1 CHEMICAL COMPOSITION

The predominant constituent of acrylic bone cement is poly(methylmethacrylate) (PMMA), synthesized by free-radical chain polymerisation (Young and Lovell 1991). The chemical composition of PMMA is shown in Figure 2-5.

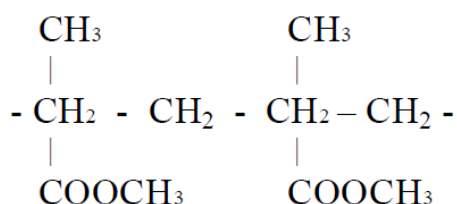


Figure 2-5: Structure of PMMA.

Commercial bone cement has two components, a liquid and a powder, which are mixed together in theatre prior to implantation. The liquid component comprises the methylmethacrylate (MMA) monomer, an inhibitor (hydroquinone) and an activator (*N-N*-dimethylparatoluidine). The powder component consists predominantly of pre-polymerised PMMA beads, with an initiator (benzoyl peroxide) and in most formulations, a radio-pacifying agent such as barium sulphate ( $\text{BaSO}_4$ ) or zirconium dioxide ( $\text{ZrO}_2$ ). The compositions of six popular cement brands are given in Table 2-5.

The inhibitor stabilises the liquid component, preventing polymerisation during storage. When the two components are mixed together, the activator in the liquid reacts with the initiator in the powder to produce free radicals, thus starting the chain polymerisation process. The reaction is terminated when the ends of two polymer chains combine to form an inert molecule.

Table 2-5: Compositions of six commercial bone cement formulations (Lewis 1997).

Constituent	CMW-1	CMW-3	Palacos R	Simplex P	Zimmer Regular	Zimmer LVC	
<b>Powder</b>	BPO	2.60	2.20	0.5-1.6	1.19	0.75	0.75
	BaSO <sub>4</sub>	9.10	10.00	-	10.00	10.00	10.00
	ZrO <sub>2</sub>	-	-	14.85	-	-	-
	Chlorophyll (ppm)	-	-	200	-	-	-
	PMMA	88.30	87.80	-	16.55	89.25	89.25
	P(MMA/MA)	-	-	83.55-84.65	-	-	-
	P(MMA/ST)	-	-	-	82.26	-	-
<b>Liquid</b>	<i>N,N</i> -DMPT	0.40	0.99	2.13	2.48	2.73	2.75
	Hydroquinone (ppm)	15-20	15-20	64	75	75	75
	MMA	98.66	98.07	97.87	97.51	97.27	97.25
	Ethanol	0.92	0.92	-	-	-	-
	Ascorbic acid	0.02	0.02	-	-	-	-
	Chlorophyll (ppm)	-	-	267	-	-	-

Compositions are given in % (w/w) unless otherwise stated.

In addition to the above constituents, commercial cement formulations may contain antibiotics such as gentamicin or tobramycin, which are blended into the powder component. Antibiotic laden versions of most major cement brands are now available, including Palacos R+G (Heraeus Medical, Germany), Smartset GHV (Depuy CMW, UK) and Simplex P with Tobramycin (Stryker Orthopaedics, USA), which became the first FDA-approved antibiotic-impregnated cement in 2003. The use of antibiotic-laden cement in primary THR has become standard clinical practice, accounting for 87% bone cement used in England and Wales in 2011 (NJR 2012).

### 2.2.2 CURING AND HANDLING PROPERTIES

The cement polymerisation process can be divided into four phases: mixing, waiting (commonly referred to as 'dough time'), application and setting. The 'dough time' is defined as the period between the end of mixing and the point at which the cement no longer sticks to an unpowdered surgical glove (Kuehn *et al.* 2005a). The duration of each phase is dependent on the cement formulation and mixing method employed (Lewis 1997). High viscosity cements such as CMW-1, Simplex P and Palacos R

generally have a shorter waiting phase but longer application and setting times than low viscosity cements such as Palacos LV (Heraeus Medical 2008).

The rate of the polymerisation reaction is also dependent on temperature and humidity; the effect of operating theatre temperature on the working times for a particular cement type (Palacos R, Heraeus Medical) is shown in Figure 2-6. Standard conditions of  $23 \pm 2^\circ\text{C}$  and  $50 \pm 10\%$  relative humidity are specified for the production of cement specimens for mechanical testing (ASTM F451, ISO 5833).

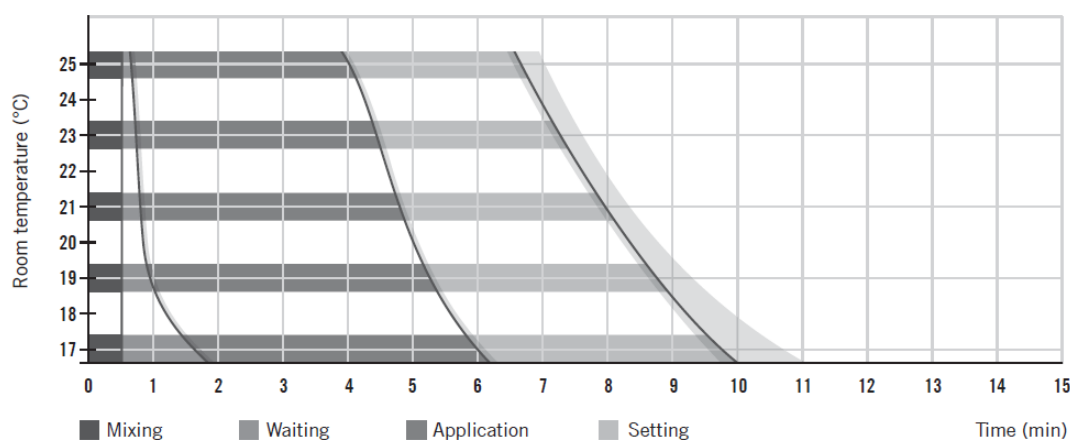


Figure 2-6: Working times for Palacos R cement, mixed manually at 55 % relative humidity (Heraeus Medical 2008).

### 2.2.3 BIOLOGICAL PROPERTIES

New cement formulations must undergo rigorous biocompatibility testing to ensure safety prior to clinical trials (ISO 10993); however, a number of potential concerns exist over the biological effects of cement constituents. Cytotoxicity of cell replication and damage to chromosomes may occur due to high residual levels of *N-N*-DMPT accelerator, while high initial concentrations of BPO in the cement formulation have been linked to inflammatory and genotoxic effects (Lewis 2008).

The inclusion of  $\text{BaSO}_4$  or  $\text{ZrO}_2$  in the cement formulation may have a significant impact on the biological properties of the cement. The presence of these particles can increase macrophage-osteoclast differentiation, causing increased bone resorption and osteolysis (Ingham *et al.* 2000). Barium sulphate has a more detrimental effect than

zirconium dioxide (Ginebra *et al.* 2002). Cement wear debris particles generated at the cement-prosthesis or cement-bone interfaces are small enough to be phagocytised, initiating macrophage response and leading to osteolysis. It has been found that this inflammatory response is also heightened by the presence of barium sulphate particles (Lewis 2008).

Unreacted MMA monomer is toxic to humans - exposure can cause irritation of skin and mucous membranes, while inhalation of high levels of MMA (>150 ppm) can cause central nervous system effects (Dart 2004). Ambient monomer levels of up to 225 ppm have been reported when open-air mixing is used in theatre (Dart 2004), hence the desire to reduce monomer levels within the clinical environment to minimise any potential effects of long-term exposure among staff (see Section 2.2.6). In addition, leaching of unreacted monomer from the cured cement into surrounding tissues may result in inflammation and chemical necrosis (Stanczyk and van Rietbergen 2004).

Cement polymerisation is an exothermic reaction, generating 57 kJ energy per mole of MMA monomer. Theoretically, the cement may reach temperatures of up to 80°C during the curing process, although the maximum temperature *in vivo* is lower due to blood circulation and heat dissipation into the adjacent prosthesis and tissue (Kuehn *et al.* 2005a). However, temperatures generated are still considered to be sufficient to cause thermal necrosis of peri-prosthetic tissue (Stanczyk and van Rietbergen 2004).

Efforts have been made to reduce the detrimental biological effects associated with the use of acrylic bone cement. Monomer toxicity and thermal necrosis led to the development of Bone loc cement (Biomet Inc., Warsaw, USA), released in 1991; it was formulated with a lower monomer content to reduce peak curing temperature and release of unreacted monomer, and was purported to have improved mechanical properties compared to conventional PMMA cements. However, clinical results were poor with high rates of aseptic loosening in the early post-operative period; up to 42% revision and 65% loosening rates were reported after 4 years (Riegels-Nielsen *et al.* 1995). It was found that Bone loc was prone to debonding of the prosthesis-cement interface, subsidence of the stem and cement fracture (Abdel-Kader 2001), in addition to excessive femoral osteolysis (Walczak 2000). Consequentially, the cement was withdrawn from the market in 1995.

### 2.2.4 MICROSTRUCTURE

The overall microstructure of radiopaque acrylic bone cement is characterised by the presence of pre-polymerised beads contained within a polymer matrix loaded with radiopacifier particles (see Figure 2-7). Voids of varying sizes are also major features of the cement microstructure; fine voids ranging from 2-20  $\mu\text{m}$  diameter have been found within a small fraction of PMMA beads (Sinnott-Jones 2007), while larger voids of up to 2 mm diameter are not uncommon in the cement volume (Murphy and Prendergast 2000). The bulk porosity of the cement and the size and spatial density of voids is dependent on the mixing method, which is discussed further in Section 2.2.6. An example of the void distribution in a specimen of hand-mixed cement is presented in Figure 2-8.

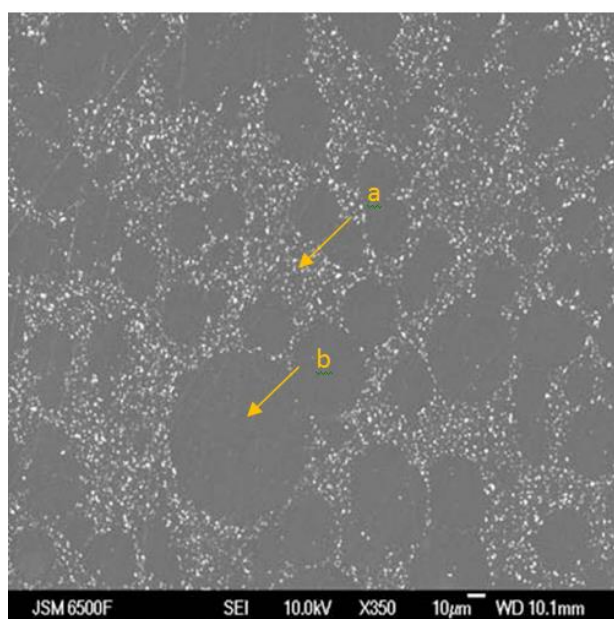


Figure 2-7: SEM image of CMW-1 cement showing (a) pre-polymerised PMMA beads and (b) BaSO<sub>4</sub> filled matrix (adapted from Sinnott-Jones 2007).

Commercial cements typically contain either barium sulphate or zirconium dioxide particles as radiopacifying agents. The size and morphology of radiopacifier particles is dependent on the cement formulation and varies between brands. Ginebra *et al.* (2002) obtained SEM images of radiopacifier particles on the fracture surfaces of cement samples prepared using custom formulations. The authors remarked that the ZrO<sub>2</sub> particles in their cement were cauliflower-like in shape and approximately 10  $\mu\text{m}$  in

diameter, while the BaSO<sub>4</sub> particles were found to be egg-shaped and mostly sub-micron in size, with a few larger particles in the order of 5-10 μm. However, it has been widely reported that barium sulphate has a tendency to form agglomerates of up to 200 μm diameter in the cement construct (Ginebra *et al.* 2002, Kurtz *et al.* 2005, Sinnett-Jones 2007, Topoleski *et al.* 1990).

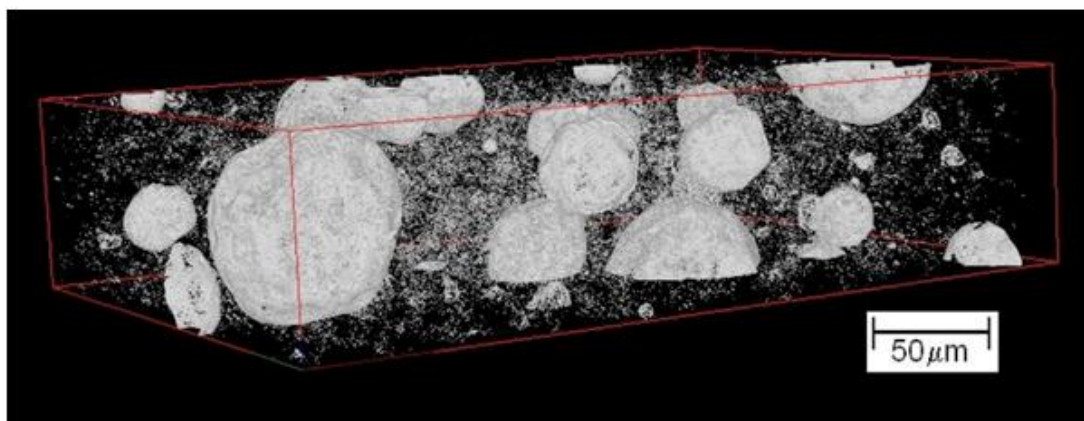


Figure 2-8: SRCT Image of porosity in a sample of hand-mixed cement taken from a knee implant (Sinnett-Jones 2007).

### 2.2.5 MECHANICAL PROPERTIES

Minimum standards for the compressive strength (70 MPa), bending strength (50 MPa) and bending modulus (1800 MPa) of bone cement are specified in ISO 5833. Kuehn *et al.* (2005) conducted a comprehensive test regime on a range of commercial bone cements according to these standards, and additionally measured the tensile strength and fatigue life of selected cements. They reported tensile strengths of 50-60 MPa, including 54 MPa for Palacos R cement, with no significant differences between cement brands. However, another study by Lewis and Mdlasi (2000) reported a lower value of 40 MPa for the same cement, highlighting the inherent variability of the mechanical properties of bone cement and the dependence on the preparation and testing conditions. The basic mechanical properties of three commercial bone cements as measured by Lewis and Mdlasi (2000) are presented in Table 2-6, while the effect of different variables on the mechanical properties and fatigue performance of cement is discussed further in Section 2.3.

Table 2-6: Comparison of the mechanical properties of three commercial bone cement brands (Lewis and Mladsi 2000).

	Simplex P	Palacos R	CMW-1
Fracture toughness/MPa m <sup>½</sup> [3]	1.45	1.85	-
Impact strength/kJ m <sup>-2</sup> [3]	3.08	4.05	-
Shear strength/MPa [1]	69.9	50.0	63.0
Ultimate Tensile strength/MPa [1]	46.0	40.0	47.0
Ultimate Compressive strength/MPa [2]	96.0	97.0	96.0
Flexural strength/MPa [2]	72.0	72.0	67.0

The cements were prepared under the following conditions: [1] Chilled prior to vacuum mixing at 20 kPa (absolute), then aged and tested in water at 37°C; [2] Chilled prior to vacuum mixing at 20 kPa (absolute), then cured at RT for 24 hours in air (Lewis 1997), [3] Hand-mixed at 1Hz then cured at RT in air.

## 2.2.6 CEMENTING TECHNIQUES

The use of acrylic cement for fixation of orthopaedic implants was pioneered by Sir John Charnley in the 1960s. The chemical composition of commercial cement brands has remained relatively unchanged since that time, with the exception of widespread addition of antibiotics for prophylaxis and treatment of peri-prosthetic infection, as previously noted in Section 2.2.1. However, the mechanical properties of cured acrylic bone cement are dependant not only on the chemical composition of the constituents but also on the method of preparation utilized in theatre, and in particular the mixing method (Lewis 1997). Since the 1960s, mixing and delivery techniques have developed significantly in an attempt to improve the quality of the cement mantle and reduce the effects of monomer toxicity on clinical staff; these changes are summarised in Table 2-7.

Table 2-7: Evolution of cementing techniques (Breusch and Malchau 2005, Haydon *et al.* 2004)

	1 <sup>st</sup> Generation (Pre-1980)	2 <sup>nd</sup> Generation (1980-1990)	3 <sup>rd</sup> Generation (Post-1990)
Bone bed preparation	Limited preparation	Some preparation (irrigation/drying)	Thorough preparation (pulsatile lavage)
Cement mixing	Mixing by hand	Open atmosphere mixing by hand	Vacuum mixing/centrifugation
Cement delivery	Stiff, doughy cement introduced by hand	Retrograde cement application via cement gun	Retrograde cement application via cement gun Stem centralizers/cement spacers
Pressurisation	Digital pressurization	Femoral and acetabular cement pressurisation	Femoral pressuriser Acetabular pressuriser
Distal Cement restriction	Unplugged femur	Distal cement restrictor (bone/plastic)	Improved distal cement restrictor

First generation cement mixing was conducted by hand using a spatula and an open bowl at 1-2 Hz for 45-120 seconds (Lewis 1997). The cement was then manually packed into the joint space and cured under thumb pressure. This hand-mixed cement typically had a high degree of porosity due to the inclusion of air bubbles during the mixing process. The quality of hand-mixed cement was heavily dependent on mixing skill, and thus the results were variable (Lindén 1988, Dunne and Orr 2001). In addition, open-air mixing exposed operators to high levels of hazardous MMA vapours.

Second generation mixing techniques involved the use of open atmosphere mixing in specially designed mixing bowls; the cement was then transferred into a cement gun for retrograde injection into the femoral canal, reducing the incidence of large defects in the cement mantle (Rice *et al.* 1998).

In response to the limitations of the first two generations of mixing methods, modified mixing bowls were developed that allowed the cement to be mixed using centrifugation and/or vacuum pressure (-30 kPa), reducing the amount of monomer vapour released into the operating room and the amount of air included in the cement (Dunne and Orr 2001). However, voids were still introduced into the cement during transfer from the mixing device to the cement gun (Lewis 1997). Integrated mixing and delivery systems

were later developed that reduced cement porosity in comparison to separate devices (Wang *et al.* 1993, for example).

Modern third generation mixing systems utilise lower pressure (-70 kPa) to further reduce the porosity of the cured cement and exposure to monomer fumes (Dunne and Orr 2001). There are several brands available commercially; each differs slightly in design and operation but with essentially the same principle (Wang *et al.* 1996). The monomer and powder constituents of the cement are placed into an evacuated mixing chamber and agitated under vacuum for 30-150 seconds (Lewis 1997) depending on the mixing system and cement formulation. The chamber is removed and placed into a cement gun, which is used to inject the cement into the joint space. The need for handling of the cement, and the potential for release of monomer vapour, is thus minimized.

Integrated mixing systems have been reported to significantly reduce cement porosity in comparison to previous systems. Dunne and Orr (2000) produced specimens of conventional bone cement using three types of mixing systems. Specimens prepared at atmospheric pressure using the open bowl technique yielded a porosity of 16.4%; vacuum mixing in a modified bowl at -39 kPa produced specimens of 10.3% porosity, while porosity as low as 1.44% was recorded in specimens mixed at -86 kPa in conventional integrated mixing and delivery systems. In addition, for a given mixing system, a greater pressure reduction was found to yield a higher density (*i.e.* less porous) cement (Wang *et al.* 1996, Dunne and Orr 2000). For example, cement mixed in a Summit Hi Vac syringe at -72 kPa and -86 kPa was reported to contain 3.17% and 1.70% porosity respectively (Dunne and Orr 2000). While vacuum mixing reduces the total void fraction of the cement in comparison to hand mixing (Davies and Harris 1990, Wang *et al.* 1993, Lewis 1999b), vacuum-mixed cement has often been found to contain large, isolated macro-voids 1-2mm in diameter (Murphy and Prendergast 2000, Hoey and Taylor 2009b), while hand-mixed cement is characterised by the presence of multiple smaller voids in clusters (Sinnott-Jones *et al.* 2007, Hoey and Taylor 2009b).

## 2.3 FATIGUE FAILURE

### 2.3.1 INTRODUCTION

The fatigue life of a material is defined as the number of stress cycles a specimen can sustain before failure occurs. The total fatigue life comprises the crack initiation phase, *i.e.* the number of cycles to initiate a fatigue crack, and the crack propagation phase, *i.e.* the number of cycles to propagate the crack to failure. The relative importance of the two phases to the total fatigue life of a specimen is dependent on the applied stress; at high stress levels, fatigue cracks can be expected to initiate readily and thus the number of cycles to initiate a fatigue crack is considered negligible. For high cycle fatigue ( $>10^6$  cycles) at low applied stresses, the number of cycles taken to initiate a fatigue crack will generally be longer and the total fatigue life will be more dependent on the presence of stress concentrations within the specimen.

The total fatigue life of a material can be characterised using a stress-life (S-N) curve, as shown in Figure 2-9. Some materials, such as mild steels, exhibit a critical stress ( $\sigma_e$ ), termed the 'fatigue limit' or 'endurance limit', below which the material can be cycled indefinitely without failure (as represented by the solid horizontal line at  $> 10^5$  cycles in Figure 2-9). For other materials, such as high strength steel and aluminium alloys, no such plateau is shown (as represented by the dashed line in Figure 2-9) and the endurance limit is then defined as the cyclic stress at which the material will sustain a sufficiently large number of cycles (usually  $10^7$ ) before failure occurs (Suresh 1998).

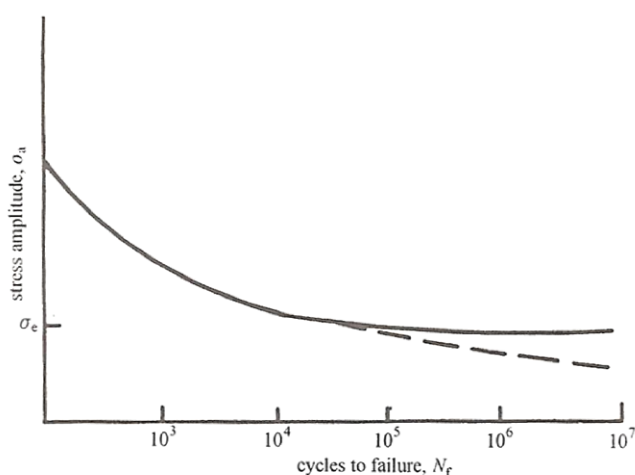


Figure 2-9: Typical S-N curve showing variation of stress amplitude for fully reversed fatigue loading of nominally smooth specimens as a function of number of cycles to failure (Suresh 1998).

### 2.3.2 MICROSTRUCTURAL ASPECTS OF FATIGUE FAILURE

Most fatigue cracks initiate from microstructural features and inhomogeneities within a material that act as stress concentrations (Murakami 2002); the mechanisms of crack initiation are therefore dependent on the microstructure of the material. In metallic materials, crack initiation has been associated with persistent slip bands, grain boundaries, second phase particles and corrosion pits. More generally, cracks may initiate at gas or shrinkage voids (Figure 2-10), inclusions, processing defects (*e.g.* scratches or machining marks), geometrical features (*e.g.* holes or notches) and other microscopic stress concentrations (Suresh 1998, Mbuya 2011). As bone cement contains voids and inclusions (*i.e.* radiopacifier particles), further consideration of the particular effects of these microstructural features on crack initiation will be considered in more detail.

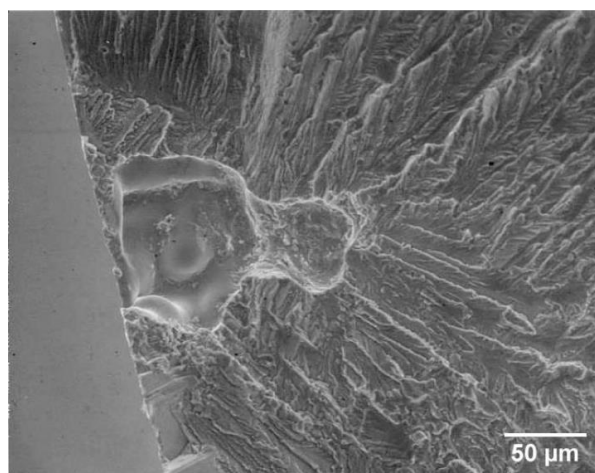


Figure 2-10: SEM micrograph showing fatigue cracks originating from a void in a Sr-modified A356 cast Al alloy (Wang *et al.* 2001).

### 2.3.3 EFFECT OF DEFECT SIZE

The effect of macroscopic defects on fatigue life may be considered using theories of notch effect, *i.e.* the decrease in fatigue strength of a material due to the presence of stress concentrations (Murakami 2002). If the effect of a stress concentration in a large volume is evaluated only in terms of the maximum stress, *i.e.* the stress concentration factor ( $K_t$ ), it is found to be independent of the defect size. For example, a circular hole in an infinite plate has stress concentration factor  $K_t = 3$ . For a spherical cavity in an infinite volume, the stress concentration factor is given by:

$$K_t = \frac{27 - 5\nu}{2(7 - 5\nu)}$$

where  $\nu$  is the Poisson's ration of the material.

However, the influence of defect size on fatigue life has been reported by numerous authors (Ammar *et al.* 2008, Nadot *et al.* 2004, Murakami 2002, Mbuya 2011 & Wang *et al.* 2001, for example). Zhu *et al.* (2007) investigated the high cycle fatigue behaviour of a cast Al alloy and found that cracks initiated from single shrinkage voids at the upper tail of the void size distribution, while Gao and co-workers (2004) reported that the largest voids initiated fatigue cracks in a cast Al-Si alloy. Wang *et al.* (2001) and Ammar *et al.* (2008) identified a relationship between increased void size and reduced fatigue life in various cast Al alloys, as shown in Figure 2-11 and Figure 2-12.

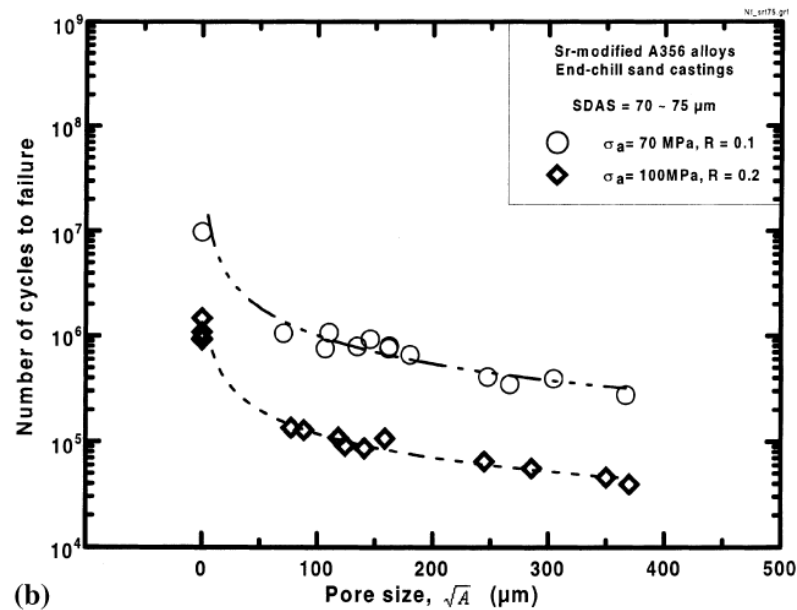


Figure 2-11: The fatigue life of a sand-cast A356 Al alloy as a function of the void size (Wang *et al.* 2001). A void size of zero was recorded for specimens that failed from slip bands.

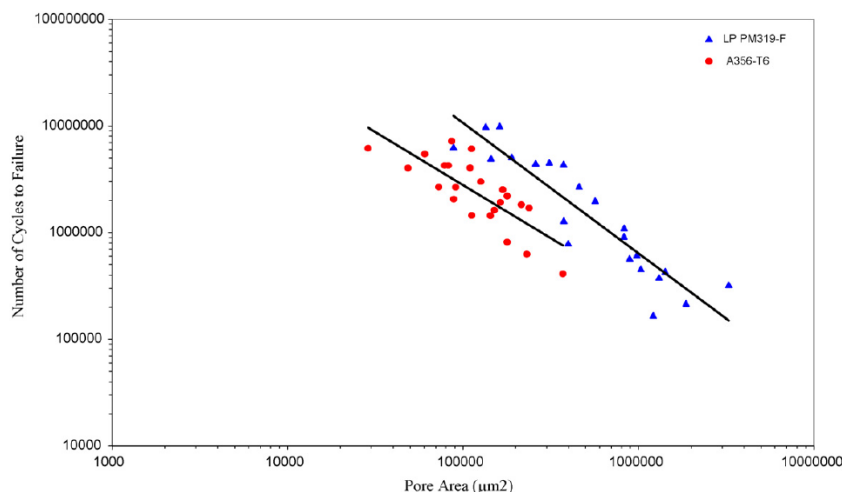


Figure 2-12: The effect of surface void size on the fatigue life of LP PM319-F and A356-T6 cast Al alloys (Ammar *et al.* 2008).

Yi *et al.* (2006) found that, while larger crack-initiating voids resulted in reduced fatigue life, smaller voids influenced fatigue life in low stress, high cycles fatigue regimes, but had no effect on fatigue performance at higher stresses. Indeed, it has been acknowledged that, for a given stress, voids below a certain 'critical void size' are non-damaging and will not affect the fatigue life of the material (Murakami 2002). In this scenario, fatigue performance will be controlled by other competing microstructural features, such as inclusions (Mbuya 2011, Wang *et al.* 2001). Computational studies, summarised by Mbuya (2011), have shown that the critical void size increases with increasing stress amplitude, which is consistent with the findings of Yi and co-authors (2006) as described above. This may be explained by considering the fatigue limit in terms of the threshold stress required for propagation of an existing crack, rather than the critical stress required for crack initiation (Murakami 2002). Thus stress concentrations below the critical size do not affect fatigue life because a crack may initiate but not propagate to failure if the stress intensity factor range ( $\Delta K$ ) is too low. In addition, for low cycle, high stress fatigue regimes, in which the fatigue life is expected to be dominated by the crack propagation phase, a larger initiating defect will result in a greater effect crack length, larger  $\Delta K$  and thus faster crack propagation.

The effect of defect size highlights that the stress concentration factor is not the critical parameter when determining the effect of stress concentrations on fatigue life. In addition, the behaviour of microscopic defects is different to that of macroscopic defects, and must be considered in terms of short-crack behaviour (Taylor 1989).

Murakami (2002) proposed that small defects, of the order of 5-500  $\mu\text{m}$ , may be treated as small cracks of equivalent length and characterised in terms of the stress intensity factor ( $K_I$ ) according to the equation:

$$K_{I_{max}} \propto \sigma_0 \sqrt{\pi \sqrt{\text{area}}}$$

This approach considers that the maximum stress intensity factor for small defects is dependent on the size of the defect, in terms of the  $\sqrt{\text{area}}$  of the defect projected along the loading axis, but is independent of the defect shape; *i.e.* a small notch will have the same maximum stress intensity factor as a crack of equivalent area, but a very different stress concentration factor. The effect of defect shape will be discussed in more detail in the following section.

Another model that can be applied to examine the size effect of stress concentrations is the theory of critical distances (TCD). This is a group of related methods that rely on a critical length  $L$  to predict small-crack behaviour. For fatigue problems,  $L$  is defined by the equation:

$$L = \frac{1}{\pi} \left( \frac{\Delta K_{th}}{\Delta \sigma_o} \right)^2$$

where  $\Delta K_{th}$  is the crack propagation threshold and  $\Delta \sigma_o$  is the critical stress range, *i.e.* the fatigue limit (Taylor 2008). The model predicts that if the crack or defect is much smaller than  $L$ , it will not conform to linear elastic fracture mechanics and will have no effect on the fatigue strength. The TCD has been successfully applied to a variety of engineering materials, including metals, ceramics, composite materials and brittle polymers (see Susmel 2008 and Taylor 2008 for an overview of these studies).

Hoey and Taylor (2007, 2009a, 2009b) used the point method of the TCD to examine the size effect of stress concentrations in bone cement. The point method states that a crack will propagate from a defect if the stress at a certain distance  $r_c$  from the defect is equal to the critical stress; the critical value of  $r_c$  has been shown to be equal to  $L/2$  (Taylor 2008). Both the critical distance  $L/2$  and critical stress range  $\Delta \sigma_o$  are dependent on the ratio of maximum to minimum applied stress (the  $R$  ratio) and the number of cycles to failure (Hoey and Taylor 2009a). For bone cement tested at  $R = 0.1$  with a fatigue life of  $10^5$  cycles, the critical distance and critical stress range were reported to be 0.1 mm and 25 MPa respectively. Based on these parameters, Hoey and

Taylor (2009b) modelled the effect of void size on the fatigue life of the cement (Figure 2-13).

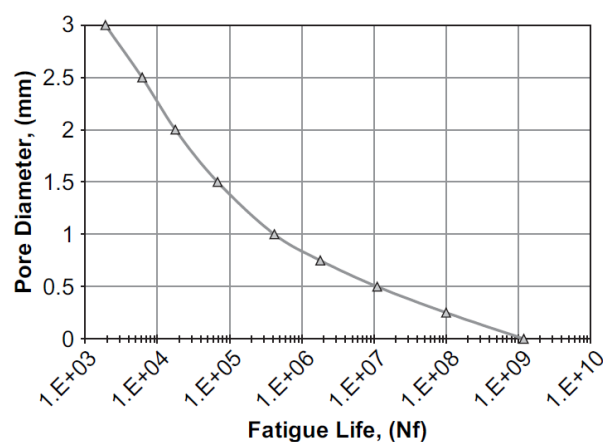


Figure 2-13: The effect of void size on the fatigue life on bone cement (Hoey and Taylor 2009b).

#### 2.3.4 EFFECT OF DEFECT SHAPE AND ORIENTATION

The shape of a defect is expected to influence the fatigue life of a material because a 'sharper' geometry with smaller local notch root radius will generate higher stress concentration and thus more readily initiate fatigue cracks. Voids formed due to natural phenomena do not have the same effect on fatigue life as artificially created defects (Nadot *et al.* 2004). Shrinkage voids in particular often have a complex, tortuous shape and thus stress concentration factor may deviate significantly from that of an idealised spherical void. Nicoletto *et al.* (2010) computed  $K_t$  values of 3 - 3.5 for naturally occurring shrinkage and gas voids in a cast Al-Si alloy; despite very different morphologies, the stress concentration factors of the two void types were reported to be comparable due to the similar local minimum radii on the void surfaces. For complex void geometries, the stress concentration factor is also found to be dependent on the orientation of the void with respect to the loading axis (Nicoletto *et al.* 2010).

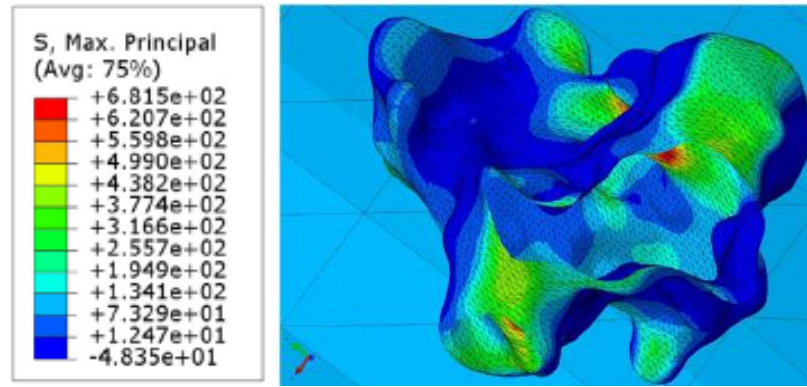


Figure 2-14: Finite element model showing the stress distribution around a shrinkage void in a cast Al alloy subjected to a nominal stress of 90 MPa (Tijani *et al.* 2013). Void geometry was obtained from  $\mu$ -CT data.

Tijani *et al.* (2013) evaluated the effect of void shape on the stress concentration factor using finite element analysis based on realistic void geometry obtained from computed tomography data (Figure 2-14). They developed a theoretical model for the stress concentration factor  $K_t$  based on the deviation of the void shape ( $M_{dev}$ ) from a sphere<sup>1</sup>:

$$K_t = \left( 2.74 + 0.6R - \frac{0.71R}{\sqrt{R} - \frac{1.1}{\sqrt{R}}} + \frac{0.31}{\sqrt{R}} - 2.21\sqrt{R} \right) M_{dev}$$

where  $M_{dev} = \frac{\text{Maximum Feret Diameter}}{\left(\frac{6 \cdot \text{Volume}}{\text{Area}}\right)}$  and  $R = \frac{\text{void distance to surface}}{\text{void diameter}}$ ,  $R \neq 0$

This is a different approach to the method of Murakami (2002), as discussed in the previous section, which utilises  $\sqrt{\text{area}}$  as a parameter to determine the effect of void shape and size on the stress intensity factor,  $K_{max}$ . For irregularly shaped crack and defects, Murakami recommended the calculation of *effective* projected area based on a smooth contour encompassing the original shape of the defect.

While complex void geometries with smaller local notch root radii generate higher stress concentrations, this effect does not necessarily result in a significant reduction in fatigue life. A study by Gao *et al.* (2004) compared tensile specimens of cast Al-Si alloys

<sup>1</sup> Erroneously, however, the equation for  $M_{dev}$  yields a value of 0.25 (rather than 1) for an idealised spherical defect.

containing shrinkage voids with a finite element model containing an ideal spherical pore, and found good agreement between the experimental and computational fatigue lives; the effect of defect shape on the fatigue life was found to be relatively small (approximately 10%). This was considered to be due to the occurrence of localised plastic deformation around the voids, which limited the maximum local stresses.

In summary, the high stress concentration generated at the local minimum radius on the surface of a complex shaped void will create favourable conditions for crack initiation, but as the stress intensity for small defects may be considered dependent only on the projected area and not the void shape, this will have a limited effect on the fatigue life.

### 2.3.5 EFFECT OF DEFECT LOCATION

In section 2.3.3, it was shown that, for a spherical defect in an infinite volume, the stress concentration factor is independent of the void size. Near a free surface, however, local stresses are magnified due to reduced constraint, and the stress concentration factor increases significantly as a function of the void size (Gao *et al.* 2004, Tijani *et al.* 2013), as shown in Figure 2-15. The location of a defect relative to the specimen surface has therefore been shown to exert considerable influence on the fatigue life of a specimen. Nadot and co-workers (2004) found that, for a given size, internal shrinkage voids were less damaging than surface voids in a nodular cast iron; the internal crack-initiating void in one specimen was ten times larger than the surface crack-initiating void in another specimen with similar fatigue life. Another study (Zhu *et al.* 2007) reported that 70% specimens failed from a shrinkage defect at or close to the specimen surface.

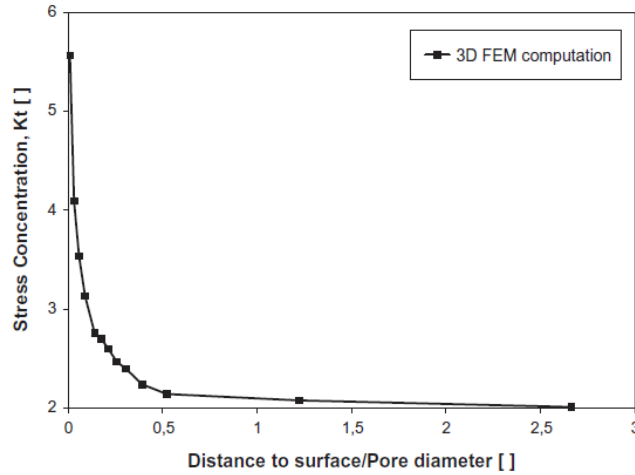


Figure 2-15: Computational finite element model of the stress concentration factor  $K_t$  around a spherical void as a function of the void diameter and distance from surface (Tijani *et al.* 2013).

Murakami (2002) defined internal and surface defects in terms of the ratio of the defect diameter ( $d$ ) to the distance between the centre of the defect and the free surface ( $h$ ). If  $d/h < 1.6$ , the defect is classified as an internal defect and the interaction between defect and free surface may be considered negligible. At  $d/h = 1.6$ , the value of  $K_{I_{max}}$  is found to be only 11% larger than for a penny shaped crack in an infinite solid. The effect of depth from the free surface can therefore be modelled for crack, voids and inclusions by incorporating an additional term into the equation for  $K_{I_{max}}$ :

$$K_{I_{max}} = f \sigma_0 \sqrt{\pi \sqrt{area}}$$

where  $f = 0.65$  for a surface defect and 0.5 for an internal defect.

The effect of defect location is particularly applicable to flexural fatigue testing methods, such as four point bending, where the applied stress decreases with distance from the surface of the specimen, and thus free surface effects are magnified by the stress gradient. Murakami (2002) considered the critical volume for location of crack initiation sites in a specimen subjected to bending to be the region in which stress is  $\geq 90\%$  of the nominal stress.

### 2.3.6 EFFECT OF DEFECT CLUSTERING

Two or more defects in close proximity are more detrimental to fatigue performance than a single defect of the same size. Multiple defects will interact, causing an increase in stress concentration and promoting crack initiation. If the defects are considered as cracks of equivalent  $\sqrt{\text{area}}$  as proposed by Murakami (2002) and discussed in section 2.3.3, the following rule may be applied: if the distance between the two defects is greater than the diameter of the smaller defect, the interaction may be considered negligible; otherwise, the two defects may be modelled as a single defect with an effective area equal to the sum of the defect areas and the space between, as shown in Figure 2-16 (Murakami 2002).



Figure 2-16: Interaction effect between adjacent cracks (Murakami 2002).

Figure 2-17 shows the fatigue strength of bone cement as a function of the distance between two voids, predicted using a finite element method (Hoey and Taylor 2009a). It can be seen that the maximum separation distance at which interaction occurs increases with increasing void size. Hoey and Taylor (2009b) modelled the effect of void clustering using the TCD as described in section 2.3.3. In these studies, voids were considered to be clustered if the distance between the two voids was less than the critical length  $L$ . If this criterion was met, the clustered voids were approximated as a single void with diameter equivalent to the radii of the two voids plus the distance between them.

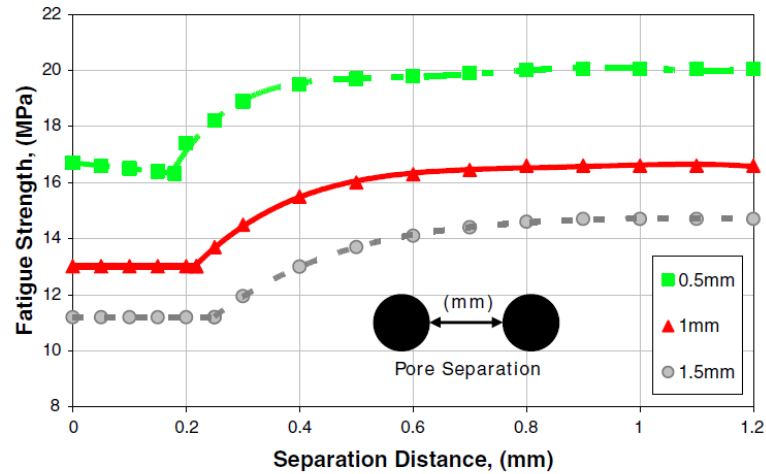


Figure 2-17: Fatigue strength predictions of the clustering effects of porosity, showing the effect of void separation on fatigue strength at  $10^5$  cycles for three different void diameters (Hoey and Taylor 2009a).

### 2.3.7 CONSIDERATION OF TEST PARAMETERS

When characterised experimentally, the fatigue life of a material may be dependent on a number of test parameters, including environmental conditions, specimen geometry, maximum applied stress, ratio of maximum to minimum applied stress (the  $R$  ratio) and method of loading (*e.g.* tension, tension-compression or bending, as shown in Figure 2-18). The fatigue life of polymeric materials is also dependent on the test frequency; smooth specimens exhibit a reduction in fatigue resistance with increasing cyclic frequency (typically  $>10$  Hz) that may be attributed to hysteretic heating and thermal softening of the polymer (Hertzberg *et al.* 1975, Suresh 1998). In addition, prolonged testing may result in viscoelastic creep deformation of the polymer, alleviating stresses and extending the fatigue life (Kuehn *et al.* 2005b). Careful consideration of the parameters used for fatigue testing is therefore required when investigating the effect of microstructure on fatigue life.

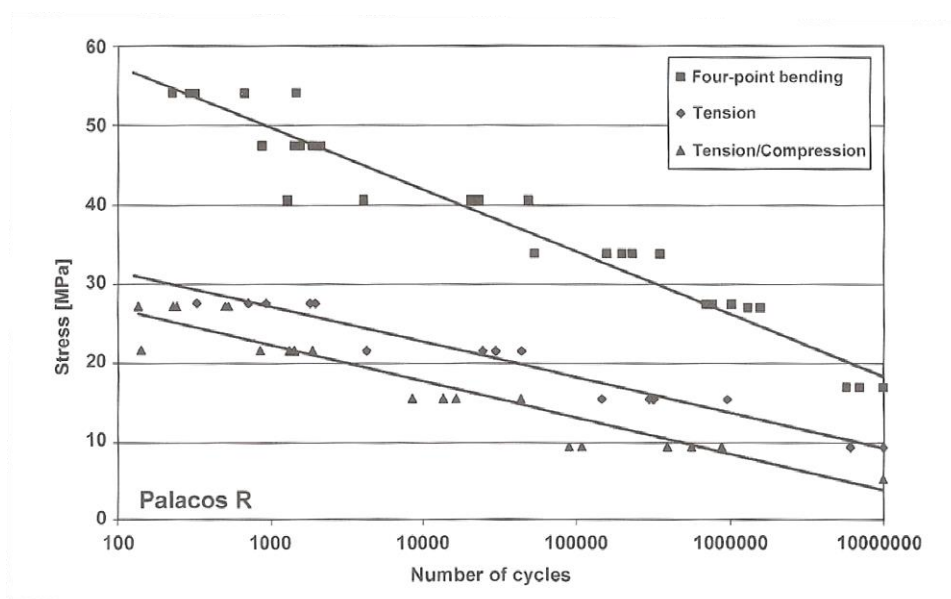


Figure 2-18: S-N curves for a PMMA-based bone cement (Palacos R), highlighting the dependency of the fatigue performance on the specimen geometry and method of loading (Kuehn *et al.* 2005b).

### 2.3.8 SUMMARY

Fatigue cracks may initiate from microstructural defects within a material that act as stress concentrations, such as voids and inclusions. The influence of these microstructural features on crack initiation is dependent on the size, shape, location, spatial distribution and, in the case of inclusions, the elastic constants of the matrix and inclusion and the strength of adhesion at the interface. Of these factors, size and location appear to be the most significant. Surface defects are more damaging to the fatigue life of a material than internal defects of equivalent size. Larger defects are more likely to initiate fatigue cracks, and large initiating defects may reduce fatigue life in comparison to smaller defects. Defects below a critical size may initiate fatigue cracks but not affect the fatigue life of the material; thus a reduction in the size and density of voids or inclusions within a material will not always yield an improvement in the fatigue strength. These observations are of relevance to the fatigue performance of bone cement due to the presence of voids and radiopacifier particles within the cement that may act as stress concentrations and potential fatigue crack initiation sites.

## 2.4 BONE CEMENT FATIGUE AND FAILURE

### 2.4.1 INTRODUCTION

Numerous studies have been published on the effect of different variables on the mechanical and fatigue properties of commercial cements (see Lewis 1997 for a summary of these studies). The mechanical properties of cement are known to be dependent on the cement formulation, sterilization method of the components, mixing method, and curing and aging conditions (Lewis 1997), which are discussed further in Section 2.3. In addition, the choice of radiopacifier agent has been shown to affect the mechanical properties of the cement (Ginebra *et al.* 2002), in particular tensile strength, fracture toughness and fatigue crack propagation resistance. However, a major limitation of the published *in vitro* data is the variation in preparation, mixing, curing, aging and testing conditions, and specimen geometry utilised, despite the development of ISO and ASTM standard conditions for pre-clinical testing of cement (Lewis 1997). Furthermore, many studies only investigate the properties of one or two brands of cement (*e.g.* Graham *et al.* 2000, Dunne and Orr 2001, Baleani *et al.* 2003, Evans 2007). Although survivorship data from national joint registries gives an indication of the relative performance of different cements *in vivo*, a larger-scale comparative characterisation of the cement formulations currently in use may be beneficial in order to maximise fatigue performance.

A number of studies have also been published examining the mechanisms leading to failure of the cemented femoral constructs of hip replacements, which may result from damage accumulation within the bulk cement (Topoleski *et al.* 1990, Jasty *et al.* 1991, McCormack and Prendergast 1999, Jeffers *et al.* 2007). Some authors have examined explanted cement mantles, retrieved either at revision or post-mortem (Topoleski *et al.* 1990, Jasty *et al.* 1991), while others have conducted *in vitro* mechanical testing on representative constructs (McCormack and Prendergast 1999, Lennon *et al.* 2002, Jeffers *et al.* 2007). There is also an abundance of literature relating to finite element computational modelling of cemented hip stems, which is beyond the scope of this review (Verdonschot and Huiskes 1997a, Stolk *et al.* 2003, 2004, Jeffers *et al.* 2007).

### 2.4.2 EFFECT OF POROSITY

The importance of porosity effects on fatigue of cement is widely reported in the literature (Murphy and Prendergast 2000, Dunne *et al.* 2003, Jeffers *et al.* 2005a, Hoey and Taylor 2009). Voids act as crack initiation sites, as shown in Figure 2-19 (*e.g.* McCormack and Prendergast 1999, Murphy and Prendergast 2000, Jeffers *et al.* 2005a, Sinnett-Jones 2007, Hoey and Taylor 2008, Coultrup *et al.* 2009); large voids, of 1-2mm diameter, are purported to initiate a greater number and size of fatigue cracks than small voids (James *et al.* 1992, Cristofolini *et al.* 2000). The number and distribution of voids can also have a significant effect on fatigue cracking; Hoey and Taylor (2008) found that crack initiation sites usually contained two or more voids in a cluster, while Murphy and Prendergast (2000) reported crack initiation in the region of stress concentration between two voids.

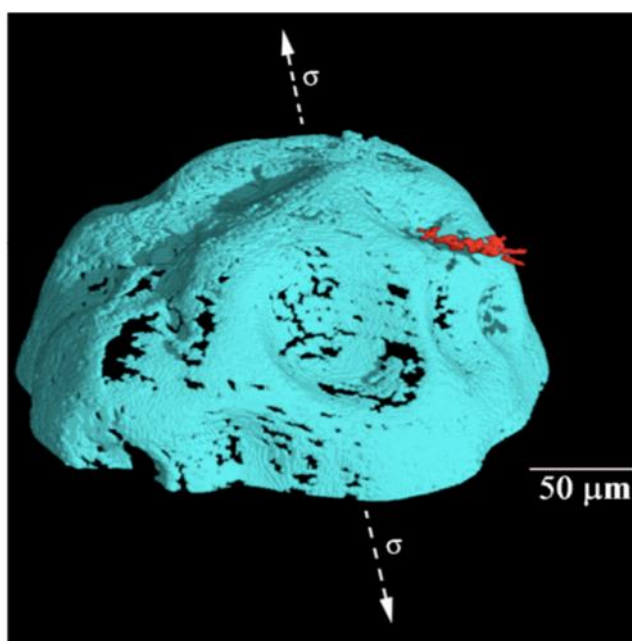


Figure 2-19: SRCT image of a fatigue crack (highlighted in red) initiating from a void in a sample of bone cement (Sinnett-Jones 2007).

It is widely accepted that hand-mixed cement has a greater degree of porosity than vacuum-mixed cement, as discussed in Section 2.2.6. *In vitro* testing has shown that a reduction in porosity corresponds to an increase in fatigue life (Murphy and Prendergast 2000, Lewis *et al.* 2005). Vacuum-mixed cement has been reported to

demonstrate greater variability in fatigue life than hand-mixed cement; this is attributed to the presence of occasional large voids in contrast to the small, well distributed voids typically found in hand-mixed cement (Murphy and Prendergast 2000). It should be noted, when investigating factors affecting the fatigue life of the cement, that some studies have discarded specimens containing voids exceeding 1mm diameter (Lewis *et al.* 1999, Kurtz *et al.* 2005, for example), despite the presence of large voids in *ex vivo* cement mantles (Topoleski *et al.* 1990, Jasty *et al.* 1991); according to Murphy and Prendergast (2000), this practice significantly affects the variability of the results and therefore “should not be tolerated”.

While the relationship between porosity and fatigue life of cement *in vitro* is well established, *in vivo* results remain controversial. Ling and Lee (1998) compared the survivorship of hip replacements with different cement porosities and concluded “porosity reduction is clinically irrelevant”. Indeed, vacuum mixing may increase the risk of premature failure in the first few years, as reported in the SHAR (Kärrholm *et al.* 2007). The variability in porosity and the tendency for fewer, larger voids in vacuum-mixed cement, which are thought to cause significant stress concentrations, may explain the propensity for early failure in some cases (Murphy and Prendergast 2000). Variations in stress distribution, caused in part by implant geometry, have been suggested as one possible explanation for the lack of clinical evidence to support porosity reduction (Janssen *et al.* 2005a).

### 2.4.3 EFFECT OF RADIOPACIFYING AGENT

Radiopacifier particles have also been shown to act as stress raisers in the cement mantle and as potential fatigue crack initiation sites (Ginebra *et al.* 2002). Kurtz and co-workers (2005) investigated the effect of barium sulphate on fatigue of cement, using high-resolution SEM imaging and mechanical testing. They reported that preparing commercial bone cement (Simplex P, Stryker Orthopaedics, NJ) with elevated barium sulphate content (36%) caused a reduction in tensile strength and fatigue life in comparison to plain cement. In the same study, addition of barium sulphate in quantities typical of commercial radiopaque cement (~10% w/w) was also shown to reduce tensile strength. Agglomerates of barium sulphate particles have been found to initiate fatigue cracks (Kurtz *et al.* 2005, Sinnott-Jones 2007 & Coultrup *et al.* 2009); one example is shown in Figure 2-20.

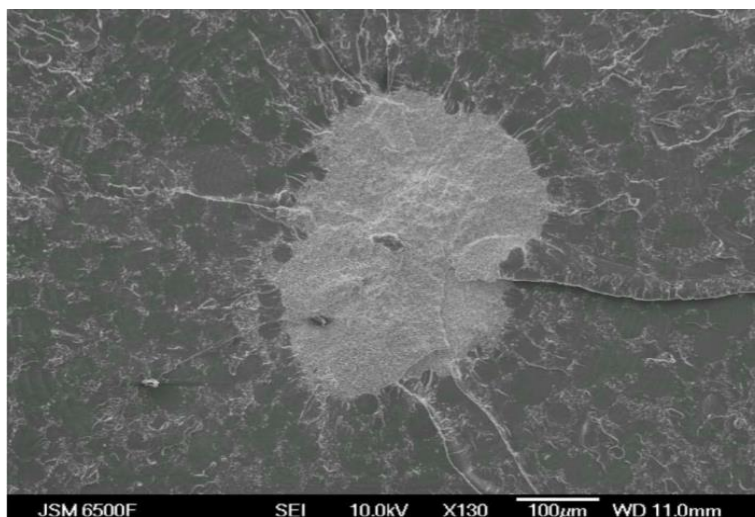


Figure 2-20: FEG-SEM image of fatigue cracks initiating from a barium sulphate agglomerate (Sinnett-Jones 2007).

However, there have been conflicting arguments regarding the benefits or otherwise of radiopacifier particles on the fatigue life of cemented implants. The addition of zirconium dioxide has been reported to improve the tensile strength and fracture toughness of bone cement (Ginebra *et al.* 2002), while the presence of barium sulphate or zirconium dioxide particles has been linked to improved fatigue crack propagation resistance in PMMA (Ginebra *et al.* 2002) and Simplex cement (Molino and Topoleski 1996). This characteristic is not observed in Palacos cement. It has been suggested that the influence of the radiopacifier on fatigue of cement thus depends on the cement brand and, in particular, the molecular weight of the base polymer (Ginebra *et al.* 2002), which has been shown to influence fatigue cracking in PMMA (Kim *et al.* 1977).

Coultrup *et al.* (2009) conducted experimental tensile fatigue testing of dog-bone specimens of vacuum-mixed CMW-1 bone cement, and analysed the populations of pores and radiopacifier agglomerates within the specimens using  $\mu$ -CT. This data was used as the input for predictive finite element modelling of the effect of these defects on the fatigue life of the cement. The authors reported that the best fit between experimental and computational fatigue life was found when the agglomerates were modelled with the same material properties as the surrounding polymer matrix. Barium sulphate agglomerates were identified on the fracture surfaces of 30% of specimens, and were therefore considered to influence the location of damage accumulation in the cement, but to have a negligible effect on the fatigue life.

#### 2.4.4 EFFECT OF STERILISATION TECHNIQUE

As with all biomaterials designed for *in vivo* use, the sterilization of bone cement is necessary prior to use. Commercial cement powder is sterilized during manufacture, either using ethylene oxide (EtO) gas or gamma irradiation at 25 kGy, while the monomer is sterilized using membrane filtration (Lewis 1997). However, irradiation of PMMA using high energy gamma radiation has been reported to cause chain scission and thus a reduction in molecular weight (Pratt *et al.* 2006, Lewis and Mladsı 1997, Harper *et al.* 1997, Graham *et al.* 2000). The use of gamma sterilization may therefore have significant implications for fatigue performance, as the mechanical properties of bone cement are known to be dependent on the molecular weight of the base polymer (Lewis and Mladsı 1997). It is recognised that a reduction in molecular weight reduces the ability of polymer fibrils to bridge craze formations, therefore reducing fatigue resistance (Graham *et al.* 2000, Lampman 2003).

A number of studies have investigated the relative effects of gamma and EtO sterilisation on mechanical properties and fatigue performance of PMMA cements. Lewis and Mladsı (1997) reported a marked decrease in the molecular weight and fatigue resistance of Palacos R cement sterilised by Gamma irradiation, in comparison to the EtO gas method. A study led by Graham (2000) investigated the effect of increased radiation dose on vacuum-mixed Palacos R cement, which was sterilised using 25, 50 or 100 kGy gamma radiation. It was found that a 61% reduction in molecular weight occurred when a clinically applicable dose of 25 kGy was used, compared to sterilization with EtO gas. A decrease in fracture toughness of vacuum-mixed specimens with increased radiation dose was reported, but this trend was not observed for hand-mixed cement, nor for cements sterilised using EtO. Fatigue life was found to be inversely proportional to radiation dose in the vacuum-mixed specimens, but there was no significant difference in the fatigue life of cement sterilised using 25 kGy gamma radiation compared to EtO in hand-mixed specimens. It was postulated that the fatigue life of hand-mixed cement is limited by the higher degree of porosity and thus degradation of the base polymer has little effect.

Harper *et al.* (1997) investigated the effect of gamma radiation dose on a range of experimental cements, including a formulation comparable to commercial Palacos R cement. Static and dynamic tensile testing was conducted on hand-mixed specimens of a methylmethacrylate/methylacrylate copolymer cement containing 10% zirconium dioxide, and exposed to 25 kGy gamma radiation. This study reported a reduction in

molecular weight and a corresponding deterioration of mechanical properties; a 4.5% reduction in tensile strength and 64% reduction in fatigue life were observed following sterilisation.

Harper and co-workers (1997) also highlighted the importance of conducting dynamic, as well as static, testing of cements prior to clinical use, and the significant reduction in performance associated with the use of gamma radiation sterilisation. Graham *et al.* (2000) cited the work of Pelletier *et al.* (1999) suggesting the degradation in molecular weight resulting from gamma irradiation of PMMA may continue after sterilisation and implantation, thus impacting on the long-term performance of the cement *in vivo*. However, the findings of Harper *et al.* (1997) and Graham *et al.* (2000) are contradictory with regard to the effect of clinically relevant exposure to gamma radiation on the fatigue life of cement. In the absence of conclusive evidence of the significance of gamma radiation to cement use *in vivo*, it has been recommended that the method of sterilisation of cement preparations should be considered when investigating the effect of other variables on the fatigue life of cement (Lewis 1997).

#### 2.4.5 EFFECT OF CURING AND AGING CONDITIONS

There is a large volume of literature on the mechanical properties of acrylic bone cement, in which various curing and aging conditions have been described (Lewis 1997). These include curing at room temperature in air, or at 37°C in air, water or saline; aging has been conducted at room temperature in air, or at body temperature in saline or Ringer's solution, for a period of between 1 day and 18 months (Lewis 1997). It is therefore important to consider the effects of curing and aging environments on the mechanical properties of cements if comparisons of the published results are to be made.

Watson *et al.* (1990) conducted an investigation into the effect of curing time and environment on the fracture properties of hand-mixed Simplex P. After mixing, the cement dough was packed into silicon moulds and cured in either air or distilled water, at 21°C or 37°C for 7 or 21 days. The fracture resistance was significantly higher for cement cured at 21°C compared to 37°C in either medium. There was no significant difference in the fracture resistance over time when specimens were cured in air; however, work of fracture (WOF; J/m<sup>2</sup>) of cement cured in water at 21°C and 37°C was

found to have increased by 43% and 141% respectively after 21 days compared to 7 days storage.

These findings are corroborated by the work of Hailey *et al.* (1994) who studied the influence of environment and storage time on properties of Simplex P over a longer time period of 2 years. An increase in WOF for cement cured in water-based media (distilled water or Ringer's solution) was observed for the first 18 months, after which the fracture resistance of the cement began to decline. The fracture properties of specimens cured in air continued to deteriorate over time, though the most significant embrittlement occurred over an initial 3 week period.

Arnold and Venditti (2001) explored the effect of environment on the creep properties of poly(ethylmethacrylate) (PEMA) cement. Samples were aged in air, water, lipid or Ringer's solution at 24°C for between 7 and 28 days. Further specimens were aged for 3 days in each environment maintained at 24°C, 30°C, 40°C or 50°C. It was found that the effect of environment on creep behaviour diminished at higher temperatures. The largest creep rates occurred for samples aged in water or Ringer's solution, while air yielded the lowest creep rate. There was no appreciable difference in the results for water and Ringer's solution. A similar study was conducted by Kuzmychov *et al.* (2009) on the effect of physical aging on creep of two commercial cements, Palacos R+G and Smartset GHV, both high viscosity PMMA cements with added gentamicin. Hand-mixed specimens were aged in distilled water at 37° for between 45 minutes and 2.5 years. Creep compliance was found to diminish significantly over time.

The effect of aging temperature and environment on compressive strength of bone cement was reported by Baleani *et al* (2001). No significant difference in compressive strength was found when cement was aged in water at 37°C; however; when aged in air at room temperature (23°C) there was a statistical increase in compressive strength over time when the cement was aged for up to 21 days. However, as cement fatigue and failure is not dominated by compressive forces *in vivo*, the clinical relevance of this data is limited.

Water-based aging environments have been found to have a plasticizing effect on bone cement, increasing the fracture resistance of the material (Watson *et al.* 1990, Hailey *et al.* 1994). Solvent-induced plasticization is a common behaviour in amorphous polymers such as PMMA, lowering the glass transition temperature and thus promoting ductile behaviour (Scheirs 2000). The plasticizing effect is time-dependent (due to rate of liquid uptake) and for bone cement is considered to be most significant

at up to 21 days aging, after which time the cement is saturated (Lee *et al.* 1978, Arnold and Venditti 2001). Regardless of storage medium, fracture resistance is greater when cement is cured and aged at room temperature rather than body temperature (Watson *et al.* 1990, Hailey *et al.* 1994).

#### 2.4.6 RESULTS OF *IN VITRO* TESTING OF CEMENTED CONSTRUCTS

While an understanding of the fatigue behaviour of acrylic bone cement at coupon level is useful for optimisation of cement formulations, the interaction of the cement mantle with the prosthesis and surrounding bone has significant implications for the clinical life of a total joint replacement. The stem-cement and cement-bone interfaces play a critical role in the stability and functionality of fixation (Jones *et al.* 2005), while stem geometry and surface finish also impact heavily on the performance of the construct as a whole (Howell 2003). Failure of the interfaces and degradation of the cement mantle can lead to loosening of the prosthesis, resulting in pain and loss of function and necessitating revision (Jones *et al.* 2005).

Cement shrinkage during curing leads to residual stress in the cement that may be great enough to initiate damage within the cement mantle in the immediate post-implantation period (Lennon and Prendergast 2002, Race *et al.* 2003, Roques *et al.* 2004). In addition, the implanted cement mantle contains defects such as voids and agglomerates even before loading commences. Damage accumulation occurs as micro-cracks initiate at the stem-cement interface and from defects within the cement, propagating and coalescing to form larger cracks through the entire thickness of the cement mantle (Jasty *et al.* 1991). Debonding at the stem-cement and bone-cement interfaces may also occur. If the implanted stem is roughened, debonding will result in accelerated wear of the cement mantle at the stem-cement interface, due to micro-motion between the materials as the implant is cyclically loaded (Jones *et al.* 2005).

*In vitro* testing of representative cement constructs has been conducted to investigate the interaction between bone, cement and stem under simulated loading conditions, and may be used for pre-clinical testing of implants (*e.g.* Hua and Walker 1994, Cristofolini *et al.* 2007), investigation of the micromechanical causes of fixation failure in cemented prostheses (*e.g.* Mann *et al.* 2004) and for validation of finite element models (*e.g.* McCormack and Prendergast 1999, Jeffers *et al.* 2007).

There is wide variation in the materials and techniques used for *in vitro* testing of cement constructs published in the literature. Typically, Charnley-type femoral stems have been utilised (McCormack and Prendergast 1999, Race *et al.* 2003, Jeffers *et al.* 2007), presumably due to widespread clinical use and excellent long-term results (Lewis 1997), though alternative prostheses have also been tested (Mann *et al.* 2004). Femoral prostheses have been implanted into human cadavers (Race *et al.* 2003, Mann *et al.* 2004), bovine rib bone (McCormack and Prendergast 1999, Lennon *et al.* 2003) and artificial bone constructed from polyurethane foam (Jeffers *et al.* 2007). Reported loading regimes include sinusoidal compressive loading of 1.8 kN at 2 Hz for 300,000 cycles (Mann *et al.* 2004), 2.2 kN at 2 Hz for 300,000 cycles (Race *et al.* 2003), 2.5 kN at 7 Hz for 5 million cycles (Jeffers *et al.* 2007) and 2.9 kN at 5 Hz for 2 million cycles (McCormack and Prendergast 1999, Lennon *et al.* 2003).

Race *et al.* (2003) found evidence of micro-cracks in non-loaded control specimens; these are likely to have been induced by thermal and shrinkage stresses during curing, though it should be noted that maximum curing temperatures may have been artificially high due to lack of blood circulation and heat transfer to viable tissue (Kuehn *et al.* 2005a). The presence of pre-load cracks in the *in vitro* cement mantle has also been reported by other investigators (McCormack and Prendergast 1999, Lennon and Prendergast 2002, Mann *et al.* 2004).

Propagation rates after 5 million cycles were found to be the same for pre-existing and load-induced cracks (McCormack and Prendergast 1999); this suggests that pre-load cracks will typically be longer after a given number of cycles and may therefore dominate the loosening process (McCormack and Prendergast 1999). In addition, the rate of new crack formation was found to diminish as cyclic loading progressed; the authors propose that this is because cracks initiate readily at regions of high local stress intensity after relatively few loading cycles. This is consistent with the results of experimental testing by Jeffers *et al.* (2007), in which complete cement mantle fracture in the highly-stressed distal region occurred after only 300 cycles.

There is disagreement within the literature in terms of the locations from which micro-cracks develop in the cement mantle; McCormack and Prendergast (1999) identified cracks initiating primarily at voids within the cement mantle, while Race *et al.* (2003) found early cracks were most likely to occur at the cement-bone interface, and in general did not involve voids. Jeffers *et al.* (2007) reported evidence of fatigue failure

originating from defects at the stem-cement interface (Figure 2-21) and from voids within the cement mantle.

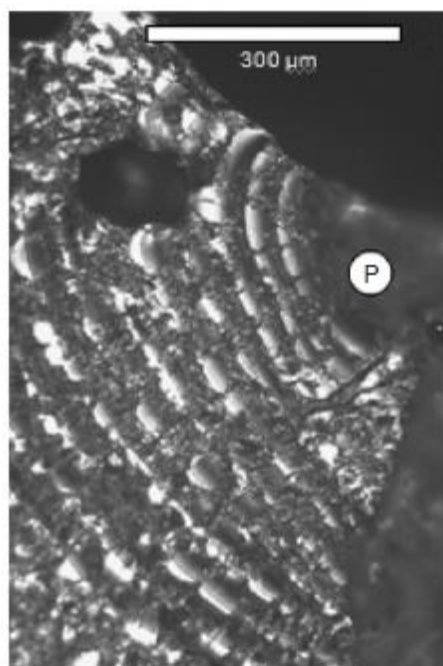


Figure 2-21: Optical micrograph of fatigue striations originating from a pore (P) at the stem-cement interface (Jeffers *et al.* 2007).

It should be highlighted that the cement utilised by McCormack and Prendergast (1999) was radiolucent and mixed by hand, while Race *et al.* (2003) and Jeffers *et al.* (2007) used vacuum-mixed Simplex-P and CMW-1 cements respectively, both of which contain barium sulphate as a radiopacifier. This discrepancy in cement formulation and mixing method almost certainly resulted in differences in defect population characteristics (*i.e.* type, size, number and distribution) between studies, although the micromechanical impact of these variables is still relatively unexplored.

#### 2.4.7 RESULTS OF *EX VIVO* STUDIES

A study by Jasty *et al.* (1991) examined 16 explanted cemented femoral prostheses retrieved at post mortem; time *in vivo* ranged from 2 weeks to 17 years. Some debonding of the stem-cement interface was evident in all cases, while complete cement mantle fractures had occurred in specimens with implantation periods of greater than 10 years. Cracks appeared to initiate at the stem-cement interface and

from voids within the cement, and propagate radially through the cement mantle; fatigue striations were seen around a large (0.2 mm) void in one fractured cement mantle (Figure 2-22). A greater number of cracks were evident in older specimens, supporting the theory of progressive damage accumulation in the cement mantle over time. Cement mantle fractures were observed even in specimens with no clinical or radiographic evidence of loosening.

Culleton *et al.* (1993) performed a microscopic evaluation of a cemented femoral stem retrieved at revision, and found evidence of fatigue cracking originating from defects within the cement mantle, and rapid, brittle fracture of the cement, though some uncertainty was associated with the small sample size and the possibility of damage being introduced during retrieval.

Topoleski *et al.* (1990) conducted fractographic analysis of *ex vivo* cement specimens, retrieved at revision from femoral components of total hip arthroplasties, using scanning electron microscopy. Fracture surfaces were found to have a rough, irregular morphology consistent with observations of *in vitro* fatigue surfaces. In addition, cracks appeared to propagate preferentially through the barium sulphate filled matrix, and through voids in the cement. In one specimen, crack initiation occurred at a large defect, several millimetres in length, which spanned over 50% of the cement mantle thickness.

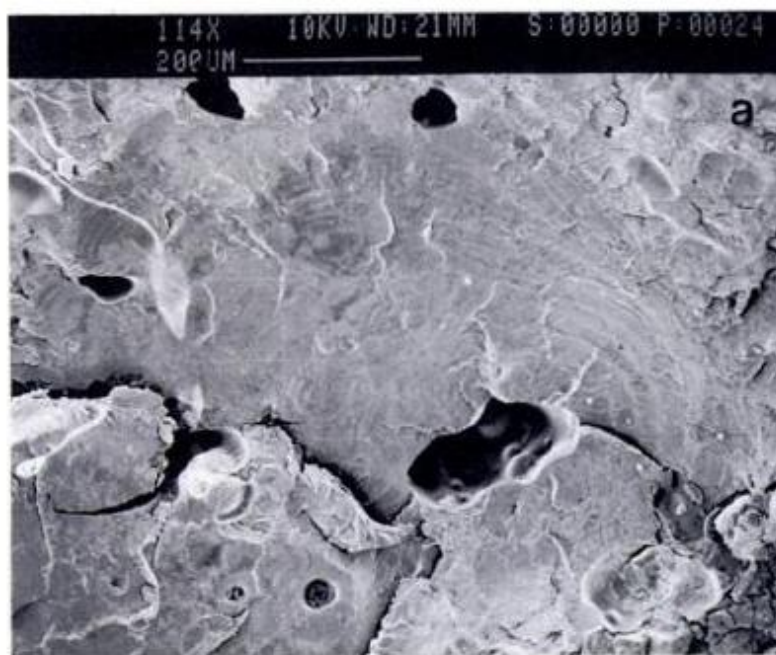


Figure 2-22: SEM micrograph of fracture surface of an *ex vivo* cement mantle, showing cracking and fatigue striations surrounding a large void (Jasty *et al.* 1991).

Although data gained from explanted cement mantles is useful in assessing the effect of complex loading and biological conditions on the performance of bone cement *in vivo*, retrieval studies have a number of limitations: the retrieval of human tissue must adhere to strict ethical guidelines (Human Tissue Act 2004) and analysis requires specialised laboratory facilities and practices (McCaskie *et al.* 1995), availability of *ex vivo* cement mantles is restricted, and damage may be incurred during removal (Topoleski *et al.* 1990). Observations of crack formation in *ex vivo* bone cement must therefore be interpreted with caution, particularly for specimens retrieved during revision surgery, when patient welfare is a priority, as cracks and artefacts may be introduced due to instrument damage during the retrieval process. The most convincing evidence of crack initiation within the cement mantle comes from studies using cement fragments that could be easily removed at the time of revision (*e.g.* Topoleski *et al.* 1990) or intact femurs that were sectioned after retrieval at post-mortem (*e.g.* Jasty *et al.* 1991).

#### 2.4.8 SUMMARY

The microstructural characteristics of failure in acrylic bone cement are dependent on a range of factors. Mixing method has been found to have a profound effect on the porosity of cement and therefore its mechanical performance. As a result, significant attention has been directed towards development of mixing techniques to reduce porosity, as described in Section 2.6.2. However, the effect of radiopacifying agent on cement fatigue remains unclear; a systematic study of cement composition and radiopacifier agglomeration would be beneficial to quantify the relative effects of different radiopacifying agents to the *in vitro* fatigue performance of PMMA cements.

Following the experience with Bone loc, greater importance was given to pre-clinical characterisation of new cement formulations; ISO 5833: 1992 (revised 2002) and ASTM F451 - 99a (revised 2008) standards have since been developed to regulate the mechanical properties of acrylic bone cements. However, clinicians are likely to be reluctant to accept new cement formulations in the future due to the poor performance of Bone loc cement. A thorough micromechanical understanding of failure in bone cement is therefore necessary; the development of a methodology to characterise existing and proposed cements would potentially result in increased confidence in new formulations, if *in vitro* results could be assured.

### 3. MATERIALS, TECHNIQUES AND EXPERIMENTAL PROCEDURE

#### 3.1 MATERIALS

Four standard, commercially available brands of acrylic bone cement were selected for the preparation of specimens used in this work.

- i. CMW Original (Depuy-CMW, Blackpool, UK), a high viscosity, PMMA based radiolucent cement;
- ii. CMW-1 (Depuy-CMW, Blackpool, UK), a similar formulation to CMW Original with the addition of barium sulphate as a radiopacifier;
- iii. Palacos R (Heraeus Medical, Hanau, Germany), a high viscosity, PMMA/PMA based radiopaque cement containing zirconium dioxide radiopacifier;
- iv. Smartset HV (Depuy-CMW, Blackpool, UK), a high viscosity, PMMA /PMA based radiopaque cement containing zirconium dioxide radiopacifier.

The compositions of these cements, according to the specifications detailed in the manufacturers' packaging inserts, are given in Table 3-1.

Table 3-1: Composition of the four cement formulations selected for use in this work.

		CMW Original	CMW-1	Palacos R	Smartset HV
<b>Powder</b>	PMMA	97.75	88.85		
	P(MA/MMA)			84.5	84.0
	Benzyl Peroxide	2.25	2.05	0.75	1.00
	Barium Sulphate	-	9.10	-	-
	Zirconium Dioxide	-	-	14.75	15.00
<b>Liquid</b>	Methyl Methacrylate	99.18	98.50	97.87	97.50
	N,N-DMPT	<0.82	< 1.50	2.13	<2.50
	Hydroquinone (ppm)	25	75	trace	75

Compositions in % (w/w) unless otherwise stated.

The method of sterilization of the cement powder should be noted when comparing the performance of these cements, as sterilization by gamma irradiation is known to reduce the molecular weight of the base polymer, as previously discussed (Harper *et al.* 1997). CMW-1 and CMW Original powders are sterilized using gamma radiation, while Palacos R and Smartset HV powders are sterilized by ethylene oxide (EtO) gas. All four liquid monomers are sterilized by membrane filtration.

### 3.2 SPECIMEN PREPARATION

The powder and liquid components of each cement brand were pre-chilled at 4°C for 24 hours prior to mixing. This practice is recommended by Heraeus Medical, the manufacturer of Palacos R, to increase the working time of the cement, and was conducted for all cements to maintain consistent preparation conditions.

Mixing and moulding of the cement was conducted under standard atmospheric conditions ( $23 \pm 1^\circ\text{C}$  and relative humidity (RH)  $\geq 40\%$ ) as specified in ISO 5833. For each batch of specimens, one charge of cement (40g powder and 20ml liquid) was mixed according to the manufacturer's instructions in a CemVac (Depuy, Leeds, UK) integrated mixing and delivery system for 30 seconds at a vacuum pressure of -70 kPa, and then injected into a polyethylene mould backed by sheets of PTFE using a cement gun. The cement was initially injected towards the end of the waiting phase (i.e. early application) and then finger-packed during the application phase, to facilitate adequate filling of the mould. The mould and PTFE sheets were clamped between two steel plates and the cement was allowed to cure under clamping pressure for 24 hours before the cement blocks were removed. A maximum of eight specimens, measuring 8 x 8 x 45 mm, were moulded from each charge of cement; specimens that had failed to fill the mould were discarded at this stage.

After removal from the mould, the specimens were each ground using 120 grade silicon carbide (SiC) paper to remove burrs and extra material resulting from the moulding process. Further grinding and edge-rounding of the four longitudinal faces of each specimen was then conducted with 800, 1200 and 4000 grade SiC papers to produce a smooth, consistent surface finish. The aim of this preparation process was to ensure that, during testing, fatigue cracks were most likely to initiate from intrinsic microstructural features of the cement, rather than from surface defects arising during specimen preparation.

Previous studies, such as that conducted by Graham *et al.* (2000) have discarded any individual specimens found to contain macro-voids, but there is significant evidence in the literature to suggest that voids in the range of 1-2mm diameter are typically found in vacuum-mixed cement specimens (Wang *et al.* 1996, Murphy and Prendergast 2000, for example). It was therefore considered of clinical relevance to retain, prepare and test all specimens regardless of the presence of voids in this size range. However, specimens found to contain larger defects (>2mm length) in pre-test  $\mu$ -CT imaging (see Section 3.4.1) were excluded from the mechanical testing described in Chapter 4 and

Chapter 5 due to their significantly reduced cross-sectional area; the failure characteristics of these specimens are examined separately in Chapter 6.

### 3.3 MECHANICAL TESTING

Four-point bending was selected for the fatigue testing conducted in this study. This facilitated the straightforward preparation of specimens to the required geometry (i.e. plain rectangular bars) and surface finish, with no requirement for machining. In addition, as the ideal geometry for CT specimens is cylindrical (resulting in uniform beam path lengths and efficient use of scan volumes), long, thin rectangular specimens with square cross sections were considered a satisfactory compromise between the ideal requirements for specimen preparation, mechanical testing and CT imaging (see Section 3.4).

The cement construct is known to experience cyclic bending forces *in vivo* (Bergmann *et al.* 2001). The tensile strength of PMMA cements has been reported to be approximately half the compressive strength (see Section 2.2.5) so specimens subjected to cyclic bending could reasonably be expected to fail at or close to the tensile surface. Although no standard fatigue test is specified in ISO 5833, a method of four-point bend testing is described for the determination of flexural strength. A modified version of this test is recommended for the investigation of cement fatigue life by Kuehn *et al.* (2005b), and has been adopted by other researchers (Lewis 2003). The use of a four-point, rather than three-point, bend test allows a larger volume of interrogation and is thus better able to capture the effect of critical defects (Vallo *et al.* 2002a, 2002b); careful selection of test parameters ensures the applied stress is evenly distributed across the distance between the two inner rollers (Zhai *et al.* 1999).

Testing of the prepared specimens was conducted using an Instron 8874 servo-hydraulic system (Instron, High Wycombe, UK) fitted with a custom built load frame and a 1KN load cell (Figure 3-1(a)). Due to the small specimen size and corresponding accuracy required in positioning and loading, a self-aligning rig was designed and manufactured. A number of key features were incorporated into the design (similar to that used by Lefebvre (2003)) to minimise the effect of alignment errors on test results (Figure 3-1(b)). Two curved bearing surfaces were used to minimise horizontal misalignment, ensuring the specimen was uniformly loaded during testing. In addition, there were four corresponding notches on the upper and lower grips between which the specimen was placed. During initial setup of the equipment, the actuator framework was aligned horizontally using a spirit level, to ensure the actuator movement, and thus the applied load, was truly vertical. The lower grip was then bolted to the base of the testing machine, and the load cell connector with attached

alignment block was bolted to the load cell. Two four-point bend rollers were placed into the notches of the lower grip, 40 mm apart, and the specimen positioned centrally on the rollers. The specimen was marked up with the required roller positions to facilitate this process. The upper grip and rollers (10 mm apart) were then lowered into place. Relative alignment of the upper and lower grips was verified using engineers' parallels, before a small tensile load (approximately 20 N) was gradually applied. A final visual inspection of the assembly was then conducted before commencement of fatigue testing.

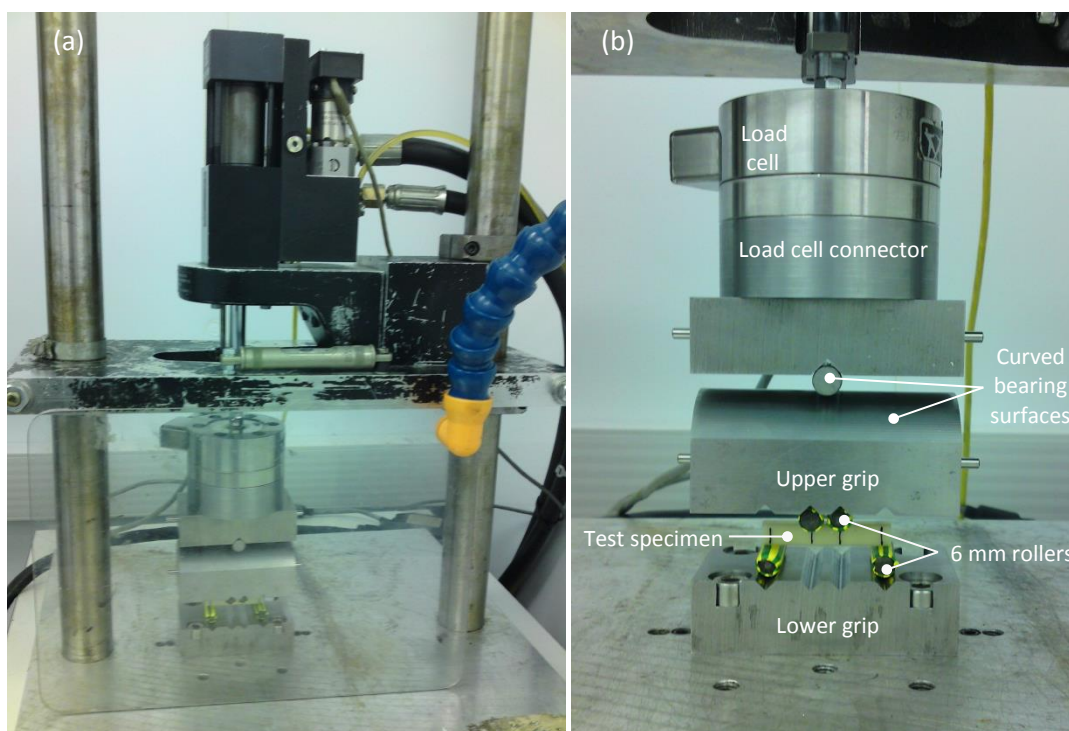


Figure 3-1: Photographs of (a) Instron actuator and load frame; (b) custom self-aligning four-point bend test rig.

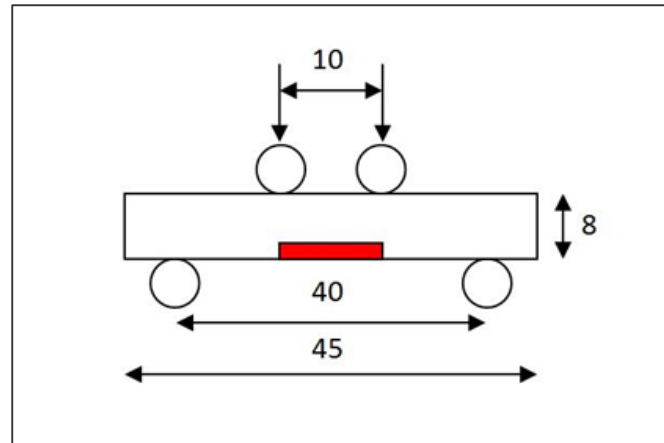


Figure 3-2: Schematic diagram of specimen geometry and loading conditions; the shaded region corresponds to the 1mm region of interest referred to in subsequent chapters.

Testing was conducted under load control (as recommended by Soltész 1994) at an R-ratio of 0.1 and frequency of 3 Hz, selected to expedite testing. Although this frequency is higher than could be expected during normal gait (Bergmann *et al.* 2001), Lewis *et al.* (2003) found no significant difference in fatigue life when specimens were tested at frequencies of 1 and 10 Hz. Maximum applied stress was determined for each cement type, informed by previous work (Sinnott-Jones 2007) and the results of preliminary tests, to ensure consistent failure occurred within  $10^5$  fatigue cycles due to machine time constraints. The applied stress varied from 25-60 MPa and the values for each cement formulation are detailed in Sections 4.2 and 5.2. All fatigue tests in this study were conducted in air at room temperature ( $23\pm 1^\circ\text{C}$ ), as specified in ISO 5833 for static four-point bend tests. Specimens were cured in air at room temperature for a minimum of 3 weeks prior to testing, to allow full evaporation of residual monomer (Kuehn *et al.* 2005a).

## 3.4 MICROSTRUCTURAL IMAGING

### 3.4.1 COMPUTED TOMOGRAPHY (CT)

The computed tomography imaging acquisition described in this thesis was conducted using either a 160kV Benchtop  $\mu$ -CT system (CT 160Xi, X-Tek systems, Tring, UK) with a Hamamatsu C7943CA-02 1248 x 1248 pixel CMOS flat panel, or a 225kV cabinet  $\mu$ -CT system (Custom HMX-ST, Nikon Metris, Tring, UK) with a PE1621 2048 x 2048 CMOS flat panel. Both systems utilise a reflection source with molybdenum target, and have a maximum resolution capability of  $\sim 3 \mu\text{m}$  (based on emission spot size) at an accelerating potential of 80kV and beam current of  $80\mu\text{A}$ .

For the assessment of fatigue performance, only the central 10 mm of each specimen was imaged, corresponding to the section between the inner four-point bend rollers at which maximum stress was applied. Small polymeric markers were applied to this section to facilitate accurate positioning of the specimen within the scanner cabinet. Specimens were positioned centrally to enable maximum geometrical magnification and scanned at a resolution of  $\sim 10 \mu\text{m}$ . Beam conditions were optimised to ensure the whole specimen was penetrated with no saturation of the image; typically, an accelerating voltage of  $\sim 80\text{kV}$  and beam current of  $\sim 100\mu\text{A}$  were utilised. The accelerating voltage and current selected were dependent on the equipment operating conditions and the material microstructure, but were consistent for each batch of cement specimens; exact values are given in Chapters 4-7. A digital camera gain of 1 and exposure time of 2134 ms was utilised, unless otherwise stated. Prior to each scan, the beam was focused at high magnification using the chip interconnect wires in a standard integrated circuit; black, white, bad pixel and centre of rotation correction images were also obtained. The specimens were rotated through  $360^\circ$  in either 1905 increments (CT 160 Xi) or 3142 increments (HMX-ST) during scanning, optimised for the panel size and specimen dimensions.

CT volumes were reconstructed using a standard FDK filtered-back projection algorithm (Feldkamp *et al.* 1984) implemented for commodity GPUs, in CT Pro Client 2008 (Nikon Metrology, Belgium). Centre of rotation was found using the automatic function at standard accuracy and with dual slice selection for tilt correction, with manual optimisation if necessary. A modest correction was applied to reduce the effect of beam hardening at the corners of the specimen without compromising the clarity of the edges. Beam hardening is discussed further in Section 3.5.2.

The CT data was examined using commercial processing, visualisation and analysis package, V.G. Studio Max 2.1 (Volume Graphics GmbH, Germany). Segmentation of voids and radiopacifier particles was performed to allow statistical quantification of the characteristics of the internal microstructure, for example total void fraction, void size and void distribution. Quantitative analysis of particle populations was performed using Image J 1.41 (National Institutes of Health, Bethesda, USA). Further details of the data processing methodology are given in Section 3.5

### 3.4.2 SCANNING ELECTRON MICROSCOPY (SEM)

Post-failure microstructural imaging of specimen fracture surfaces was conducted using a JEOL JSM6500F FEG-SEM. As acrylic bone cement is non-conductive, it was necessary to coat the specimens with a thin layer (~15 nm) of gold prior to imaging, to prevent charging. This was achieved using a Hummer 6.2 Sputter Coater (Anatech USA, California) on pulse deposition mode for 2 minutes.

PMMA is sensitive to beam damage and may undergo chain scission in the presence of high-energy electrons (Scheirs 2000). Low accelerating voltages were therefore utilised to minimise beam-induced degradation – either 5 or 10 kV for secondary electron (SEI) or 15 kV for back-scattered electron (BEI) modes. It was noted that degradation of the polymer surface occurred at greater than 5000 x magnification at 10 kV, which manifested as a crack or hole-like artefact with a melted appearance. Very high magnifications were therefore avoided and analysis was conducted with caution to ensure that morphological features identified on SEM micrographs were not attributable to beam damage.

### 3.5 IMAGE ANALYSIS

CT volumes of intact cement specimens were obtained to characterise the microstructure (particularly the surface and near surface conditions of the test faces) and for referral at the post-failure analysis stage. Additional scans were subsequently conducted after testing to identify microstructural defects implicated in crack initiation processes. In order to quantify these microstructural features and their relative influence on cement failure, an optimised image processing and feature segmentation methodology was developed as detailed below. The process is described only for CMW-1 cement, though the techniques developed were equally applicable to CT image processing for the other cement formulations.

#### 3.5.1 SEGMENTATION OF MICROSTRUCTURAL FEATURES

Segmentation and feature extraction was performed using VG Studio Max 2.1. Initially, specimen volumes were isolated from the surrounding air using the adaptive rectangle tool: an iterative segmentation procedure that uses specified depth (number of iterations) and threshold ISO (grey value iso-surface) parameters to determine the edges of an object within a rectangular search volume (Volume Graphics 2010).

The grey value of each voxel is related to the attenuation coefficient of that voxel, i.e. the amount of radiation absorbed or attenuated by the material. The theoretical attenuation coefficients for air and the major constituents of the cement formulation are presented in Table 3-2, assuming the mean photon energy is 40 kV. A histogram of the grey values of the voxels in a typical CMW-1 specimen is shown in Figure 3-3. There is a small peak corresponding to attenuation in the voids, and another, much larger peak due to the PMMA beads and matrix that form the bulk of the material. Barium sulphate has a much higher attenuation coefficient than either air or PMMA, allowing it to function as a radiopacifier, and so appears distinctly 'bright' in the CT images.

The extracted cement volumes were processed using a median filter, which sorts the grey values of a selected grid of voxels into ascending order, and then assigns the median grey value to all voxels within the grid (Nixon and Aguado 2008). The effect of image processing using 3 x 3 and 5 x 5 median filters is shown in Figure 3-4. The application of a median filter characteristically reduces noise in the image (potentially compromising segmentation), whilst maintaining a degree of edge retention. A 3 x 3 median filter was qualitatively judged to offer a useful compromise between noise reduction and sharpness for ease of subsequent segmentation and feature extraction.

Table 3-2: Theoretical attenuation coefficients for selected materials at 40 kV (Hubbell and Seltzer 2004).

Material	Attenuation Coefficient (g/cm <sup>3</sup> )
Air	0.2485
PMMA	0.2350
BaSO <sub>4</sub>	1.5991
ZrO <sub>2</sub>	0.8767

Values for BaSO<sub>4</sub> and ZrO<sub>2</sub> calculated from elemental data in Hubbell and Seltzer (2004) according to the rule of mixtures.

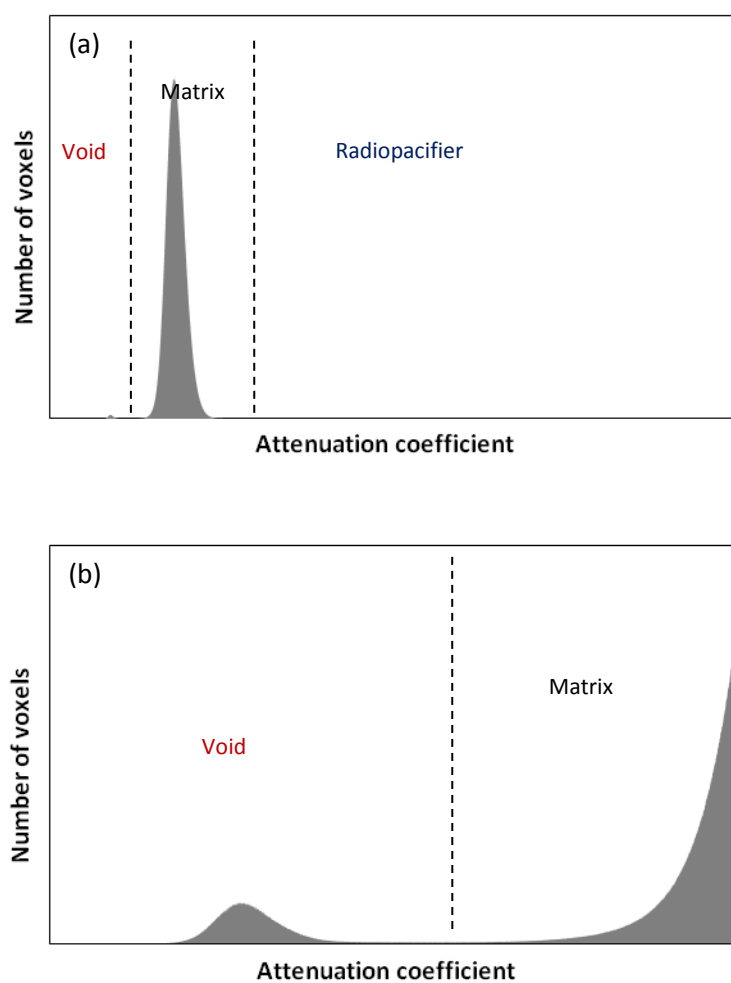


Figure 3-3: Histograms showing grey values (attenuation coefficients) for a typical CMW-1 specimen: (a) identification of the three grey-value intervals - the first, very small peak corresponds to void attenuation and the second peak to attenuation of the bulk PMMA construct; (b) magnification of the small peak corresponding to attenuation of voids.

Grey value thresholding was used to segment significant microstructural features (i.e. voids and agglomerates of radiopacifier particles, highlighted in Figure 3-5(a)) from the surrounding matrix, according to the interval thresholds defined in Figure 3-3. The application of false colour corresponding to grey value interval (red for voids, blue for radiopacifier particles), as shown in Figure 3-5(b), allowed the defects to be clearly visualised within the cement volume.

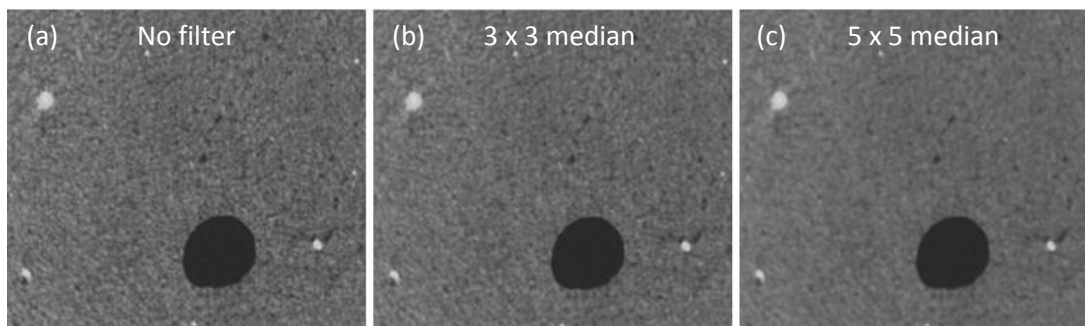


Figure 3-4: Effect of median filtering on image quality of reconstructed CT slice: (a) original image; (b) image processed using 3 x 3 median filter; (c) image processed using 5 x 5 median filter.

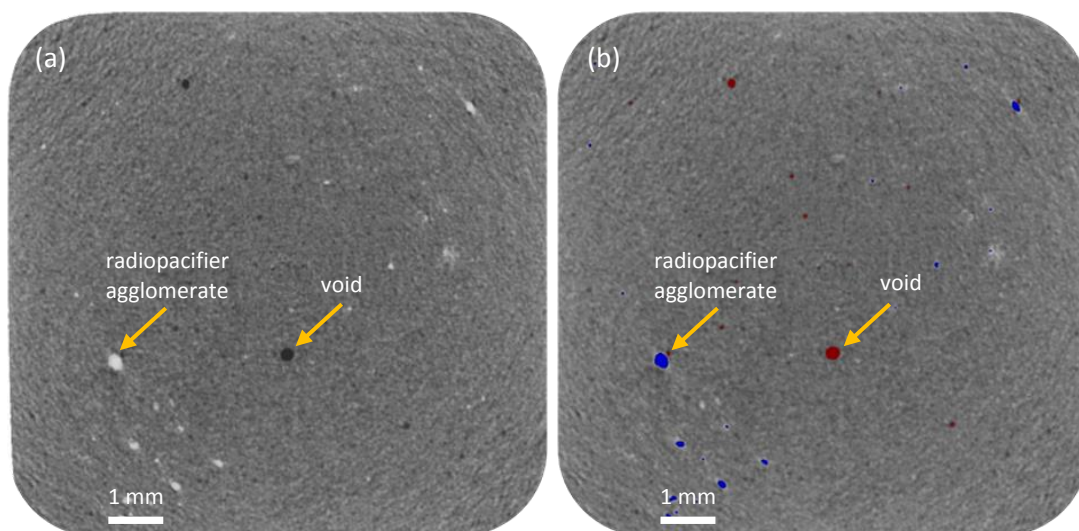


Figure 3-5: Slice showing (a) voids and radiopacifier agglomerates and (b) same slice with features selected according to the grey value thresholds defined in Figure 3-3.

Grey value thresholds were carefully defined to ensure accurate, repeatable segmentation of voids and agglomerates was performed. The selection of a threshold grey value for each feature impacts on the measured volume fraction for that feature, particularly in the case of voids for which attenuation is relatively close to that of the matrix. The effect of interval definitions on volume fractions for voids and radiopacifier agglomerates are plotted in Figure 3-6 and Figure 3-7 respectively. The black markers correspond to the threshold values shown in Figure 3-3. Plotting a range of attenuation coefficients of  $\pm 800$  shows the influence of the selected values on defect feature volume fractions (Figure 3-6 and Figure 3-7); Figure 3-6 particularly shows an upper threshold level beyond which 'spill' into surrounding material occurs and volume fraction rises rapidly (see below).

Although grey levels amongst different specimens, and different cement formulations, were found to differ to some extent (due to variation in imaging conditions), the pattern of attenuation within specimens of the same formulation was very similar. The threshold value for the void interval was selected mid-way between the void and matrix peaks, so that partially filled voxels were attributed to their dominant material (see Section 3.5.2). Selection of a threshold value for the radiopacifier particles was more difficult, as the material spanned a wide grey value range, and no obvious plateau was evident in the histogram data (Figure 3-3). As such, threshold grey values for the radiopacifier interval were chosen with reference to the gradient of the threshold value vs. volume fraction curve (Figure 3-7) to give reasonable selection of radiopacifier agglomerates by visual inspection, as in Figure 3-5(b). However, the threshold definitions (based on grey value histogram shape and visual inspection) chosen in this work can be seen to provide comparable upper bound estimates of feature volume fractions between specimens; the sensitivity-based thresholding criterion used here (Figure 3-6 & Figure 3-7) is therefore considered to provide a good compromise between representation of the features of interest, comparability between specimens and ease of use.

Finally, the defined intervals were extracted to form separate volumes for the voids and radiopacifier particles within each CMW-1 cement specimen. Defect characterisation was performed using a particle analysis plug-in, as described in Section 3.5.3.

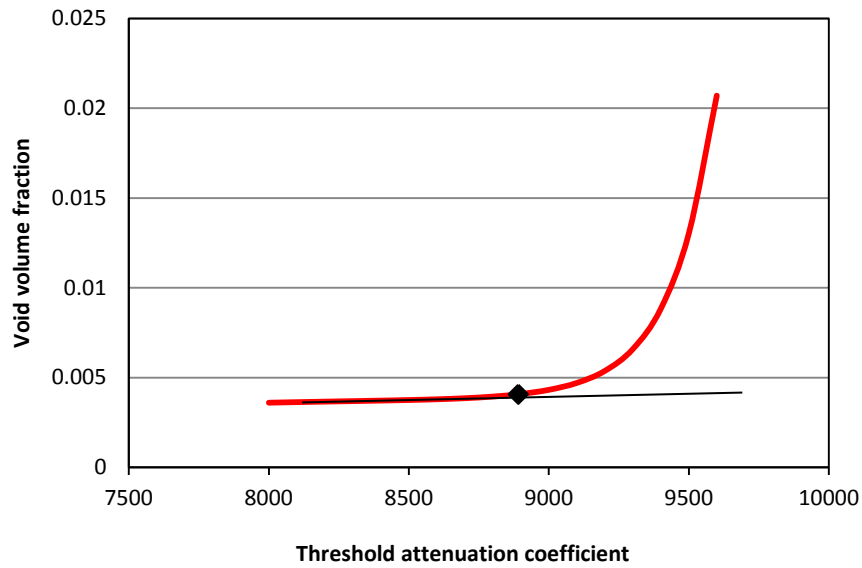


Figure 3-6: Relationship between threshold attenuation coefficient and volume fraction of void interval.

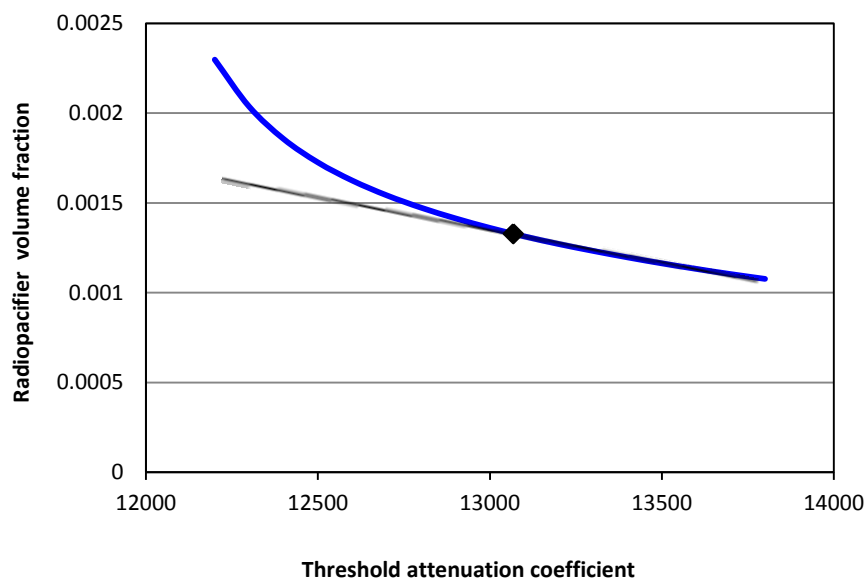


Figure 3-7: Relationship between threshold attenuation coefficient and volume fraction of radiopacifier interval.

## 3.5.2 CT ARTEFACTS

Computed tomography imaging may be distorted by the presence of artefacts, which arise due to discrepancies between the measured and actual attenuation coefficients during acquisition and reconstruction of the CT data. Two types of artefact were evident in the data obtained for this work: ring artefacts and localised beam hardening (Figure 3-8).

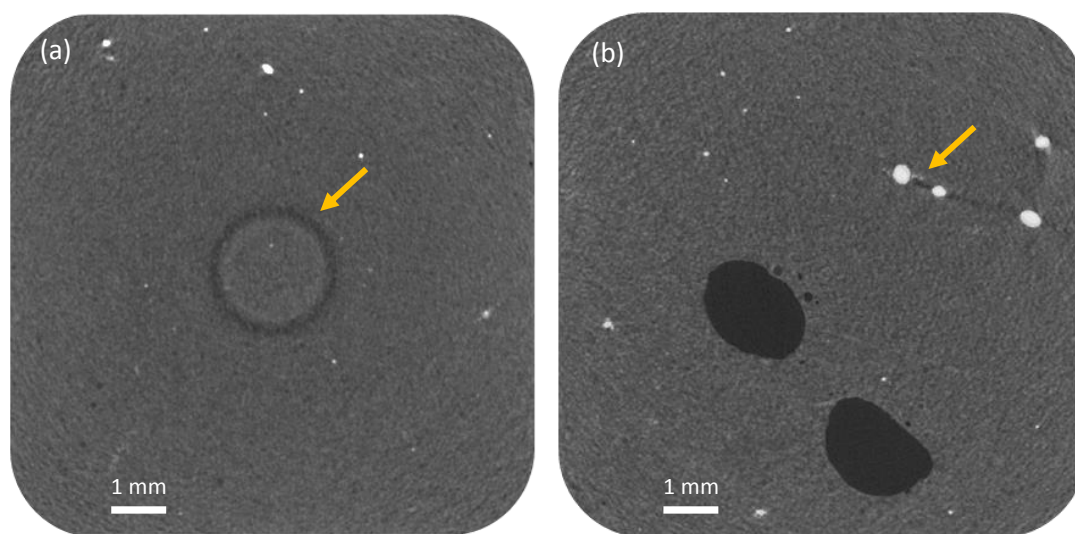


Figure 3-8: Computed tomography images showing (a) ring artefact and (b) localised beam hardening, indicated by yellow arrows.

Ring artefacts arise either due to defective or badly corrected pixels, or because the specimen has not been placed in the centre of the rotation axis during image acquisition (Vidal et al. 2005). They appear as a circular structures centered on the rotation axis of the scan (Figure 3-8(a)). Ring artefacts can be minimized during acquisition by displacing the rotation stage laterally in small known increments during the scan, to average out the non-ideal behaviour of any single element (known as 'shuttling'). Whilst shuttling increases scan times, this method is an effective solution to the problem of ring artefacts, avoiding potential corruption of real image data when post-scanning ring reduction methods are employed (Ketcham and Carlson 2001).

Laboratory-based micro-computed tomography necessarily uses a polychromatic light source and thus photons with a range of energies are encountered (Vidal et al. 2005). As the beam passes through the specimen, lower energy photons are

attenuated preferentially, leading to the phenomenon of 'beam hardening' that causes a reduction in the brightness of the image towards the centre of the specimen. The attenuation coefficient of internal material is interpreted as being low, as the higher energy photons reaching the interior of the specimen are more penetrating. In Figure 3-8(b), dark streaks can be seen between the large radiopacifier agglomerates, again attributable to beam hardening, but in this case specifically arising in paths between the highly attenuating particles.

In addition to the presence of artefacts, CT imaging may be distorted due to partial volume averaging effects, which occur when two or more materials of different densities are present in the same voxel. The assigned grey value represents the average attenuation of all the materials within the voxel, and therefore a voxel containing only a small fraction of high density material (such as barium sulphate), may yield the same grey value as a voxel consisting entirely of a lower density material (PMMA, for example), as demonstrated in Figure 3-9. This averaging process results in a loss of radiographic contrast at the edges of features within CT volumes, particularly for small round objects such as voids (Plewes and Dean 1981).

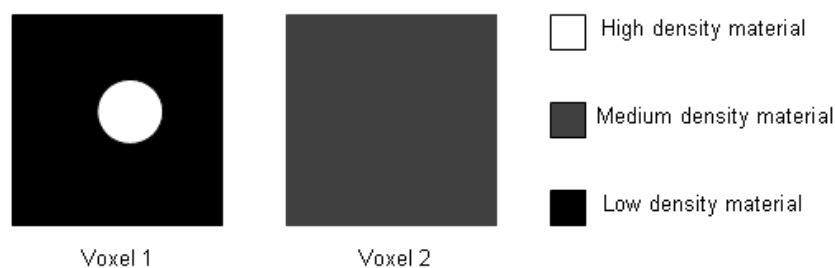


Figure 3-9: Schematic showing the effect of partial volume averaging on attenuation coefficient – both voxels may be represented by the same average grey value, though their material compositions are entirely different.

The effect of partial volume averaging on segmentation of voids in the present work was considered to be negligible, except in the case of very small defects with volumes of only a few voxels, as the attenuation of air is relatively close to that of the matrix and thus a large percentage of a voxel must be occupied by air for it to be approximated as a void. However, segmentation of radiopacifier particles is more susceptible to errors arising from partial volume averaging, as the very high contrast between matrix and

radiopacifier means that only a small percentage of a voxel needs to be occupied by the radiopacifier for the average grey value of the voxel to potentially be placed in the radiopacifier interval. Sub-voxel interpolation methods may be considered (e.g. ASTM E-1441 2005) to augment accuracy at small feature sizes, but are subject to significant errors themselves due to angle and microstructure dependant phenomena such as localized beam hardening, as previously discussed.

### 3.5.3 MICROSTRUCTURAL FEATURE QUANTIFICATION

Image J 1.41 (National Institutes of Health, USA), an open-access Java image processing program, was used to quantify microstructural features within the cement specimens. The features of interest (voids and radiopacifier particles) were segmented using the methodology described in the previous section. The data was then imported to Image J in RAW format and the resulting image stack was binarised. An open-access particle analysis plug-in (Eric Maire, Université de Lyon, INSA-Lyon, MATEIS CNRS, Villeurbanne, France) was run, first to label each feature within the image stack and subsequently to return the characteristics of each feature, including  $x$ ,  $y$  and  $z$  coordinates; dimensions in  $x$ ,  $y$  and  $z$  planes; particle volume and geometric shape. Accuracy of the plug-in was checked against synthetic test images (Appendix B).



---

---

## 4. THE EFFECT OF BARIUM SULPHATE AS A RADIOPACIFIER

---

---

### 4.1 INTRODUCTION

Fatigue failure of bone cement has been reported to lead to debonding at the cement-prosthesis interface and aseptic loosening of the components, ultimately requiring revision (Topoleski *et al.* 1990). It has been shown that the microstructure of the cement construct, including pre-polymerised beads, matrix, radiopacifier particles and voids, is a factor in the development of fatigue cracks (Lewis 1997). Quantification of the effects of each of these microstructural elements is therefore desirable if cement failure is to be minimised, whether by improved cement manufacturing, mixing method, or physically-based performance prediction at the design stage.

The influence of porosity on the fatigue behaviour of cement is widely reported in the literature (Dunne *et al.* 2003, Jeffers *et al.* 2005, Hoey and Taylor 2009, Murphy and Prendergast 2000, for example). Pores are of course significant stress concentration sites, readily initiating fatigue cracks (Cristofolini *et al.* 2000, James *et al.* 1992, McCormack and Prendergast 1999). The number and distribution of pores within the cement volume can have a significant effect on fatigue cracking; Hoey and Taylor (2008) found crack initiation sites usually contained two or more pores in a cluster, while Murphy and Prendergast (2000) reported crack initiation in the region of stress concentration between two pores. *In vitro* testing has demonstrated that a reduction in porosity corresponds to an increase in fatigue life (Lewis *et al.* 2005, Murphy and Prendergast 2000). Indeed, the negative influence of porosity on the mechanical performance of the cement *in vitro* led to the development of reduced pressure, vacuum-mixing methods in an attempt to minimise pore formation during clinical application (Alkire *et al.* 1987, Wixson *et al.* 1987).

While the relationship between porosity and fatigue life of cement *in vitro* is well established, *in vivo* results remain controversial. Ling and Lee (1998) compared the survivorship of hip replacements with different cement porosities and concluded “porosity reduction is clinically irrelevant”. Indeed, vacuum mixing may increase the risk of premature failure in the first five years, as reported in the results of the Swedish National Hip Arthroplasty Register (Malchau *et al.* 2000). Variations in stress distribution within the cement mantle, caused in part by implant geometry, have been

suggested as one possible explanation (Janssen *et al.* 2005a) for the lack of clinical evidence to support porosity reduction. In addition, the variability in porosity and the tendency for fewer, larger pores to be present in vacuum-mixed cement, which are likely to cause significant stress concentrations, may explain the propensity for early failure in some cases (Murphy and Prendergast 2000).

It has been suggested that, in the absence of critical porosity, other microstructural defects such as radiopacifier particles may initiate fatigue failure (Sinnott-Jones *et al.* 2009). Barium sulphate particles, for instance, have shown a tendency to form agglomerates up to 200  $\mu\text{m}$  wide in bone cement (Ginebra *et al.* 2002, Kurtz *et al.* 2005, Sinnott-Jones 2007). These agglomerates are reported to act as stress concentration sites within the cement mantle (Ginebra *et al.* 2002) and to initiate fatigue cracks (Kurtz *et al.* 2005, Sinnott-Jones *et al.* 2009). Kurtz and co-workers (2005) investigated the effect of elevated barium sulphate content on fatigue of cement, using optical and scanning electron microscopy and mechanical testing. They reported that preparing commercial bone cement (Simplex P, Stryker Orthopaedics, NJ) with elevated barium sulphate content (36% w/w) caused a reduction in tensile strength and fatigue life in comparison to radiolucent cement. Addition of barium sulphate in quantities typical of commercial radiopaque cement ( $\sim 10\%$  w/w) has also been shown to reduce tensile strength (Endogan *et al.* 2009) and fatigue strength (Baleani *et al.* 2003) for certain cement formulations.

Despite this evidence, there are conflicting arguments regarding the benefits or otherwise of barium sulphate particles within cement. A study of Norwegian Arthroplasty Registry data (Espehaug *et al.* 2002) highlighted a significant difference in failure rates between different cements containing similar quantities of barium sulphate. It is therefore expected that the effect of barium sulphate particles on the mechanical properties of the cement will be dependent on several factors, including particle size, morphology and base polymer, rather than quantity alone.

To date, micromechanical investigation of bone cement has largely been confined to post-failure fractographic analysis using SEM and optical microscopy. Recent advances in the accessibility and performance of lab-based CT systems now enable detailed, non-destructive characterisation of microstructure and defect populations to be conducted prior to testing. In particular, three-dimensional morphology of critical, crack-initiating defects can be assessed by comparing pre- and post-failure CT data. This chapter thus describes a 'data rich' approach using high resolution  $\mu\text{-CT}$  and SEM techniques to

quantify the relative influence of barium sulphate radiopacifier dispersal on cement fatigue *in vitro*.

## 4.2 MATERIALS AND METHODS

Test specimens were prepared using two standard commercial cement formulations, CMW-1 and CMW Original (both Depuy CMW, Blackpool, UK). Both are high-viscosity PMMA cements designed for fixation of load-bearing orthopaedic implants by syringe or digital application. CMW-1 is radiopaque, containing 9.10 % by weight barium sulphate radiopacifier in the powder component (according to the manufacturer's specification). Commercially, CMW Original was supplied with 2 bags, each containing 2.5g barium sulphate powder, to be added at the mixing stage if the surgeon so wished<sup>1</sup>. However, no barium sulphate was added to the CMW Original cement for the purposes of this study, rendering the cement radiolucent. Apart from the radiopacifier constituent, the two cement formulations are identical in composition and sterilization method (as previously detailed in Section 3.1) and thus provide a reasonable comparison to assess the relative effect of barium sulphate on fatigue failure of the cement.

Thirteen specimens of CMW-1 and eleven specimens of CMW Original were prepared and tested under four point bend loading as previously described (Sections 3.2 & 3.1). Tests were conducted in air at room temperature at a maximum applied stress of either 25 MPa or 30 MPa for CMW-1 and 35 MPa for CMW Original, informed by previous work (Sinnott-Jones 2007) and the results of preliminary tests, to ensure consistent failure occurred within  $10^5$  fatigue cycles due to machine time constraints.

The central 10 mm gauge section of each specimen was imaged prior to testing and post-failure using a laboratory  $\mu$ -CT scanner (CT 160Xi, X-Tek Systems, Tring, UK) at a current of 98  $\mu$ A and accelerating voltage of 86 kV, achieving a resolution of  $\sim 10$   $\mu$ m. Volume images of the specimens were generated in CT Pro Client 2008 (Nikon Metrology, Belgium) using a standard Feldkamp, Davis and Kress (FDK) back projection approach (Feldkamp *et al.* 1984); analysis of defects within the specimens was conducted using VG Studio Max 2.1 (Volume Graphics GmbH, Germany) and ImageJ 1.41 (National Institutes of Health, USA). Characterisation of defect populations within the defined region of interest was conducted using  $\mu$ -CT data obtained prior to testing. Defects were segmented from the reconstructed CT volumes, enabling three-dimensional visualisation of the internal cement microstructure. This defect quantification was performed to a depth of 1 mm from the free surface loaded in tension (i.e. region of maximum fibre stress levels in bend), as previously highlighted in

---

<sup>1</sup> CMW Original (also marketed as CMW-1 Original) has now been withdrawn from the market

Figure 3.2, due to preliminary studies showing that crack initiation always occurred at defects present within this region.

Fracture surfaces were imaged using a JEOL JSM6500F FEG-SEM. Specimens were sputter-coated with a thin layer (~15 nm) of gold prior to SEM imaging. A low accelerating voltage of 5 or 10 kV was used to minimise beam-induced polymer degradation.

## 4.3 RESULTS

### 4.3.1 DEFECT POPULATION CHARACTERISATION

The two cement formulations had distinct microstructures, as demonstrated in Figure 4-1. Two types of microstructural defect were identified in the  $\mu$ -CT data: voids and agglomerates of barium sulphate particles. Small voids were evident in all specimens, but were most easily distinguishable in CMW Original due to the homogeneity of the polymer and absence of a radiopacifier phase. No distinction was evident between the pre-polymerised beads and matrix in CMW Original at the resolution shown ( $\sim 10\mu\text{m}$ ). Conversely, the polymer beads were clearly visible as darker regions in CMW-1, surrounded by the matrix which appeared brighter due to the presence of fine barium sulphate radiopacifier particles. The larger, bright spots in Figure 4-1(a) were evident in all specimens of CMW-1, but not in the radiolucent CMW Original cement, and indicate the presence of agglomerates of barium sulphate particles ( $>10\mu\text{m}$  diameter). A 'typical' defect distribution for each cement type is shown in Figure 4-2.

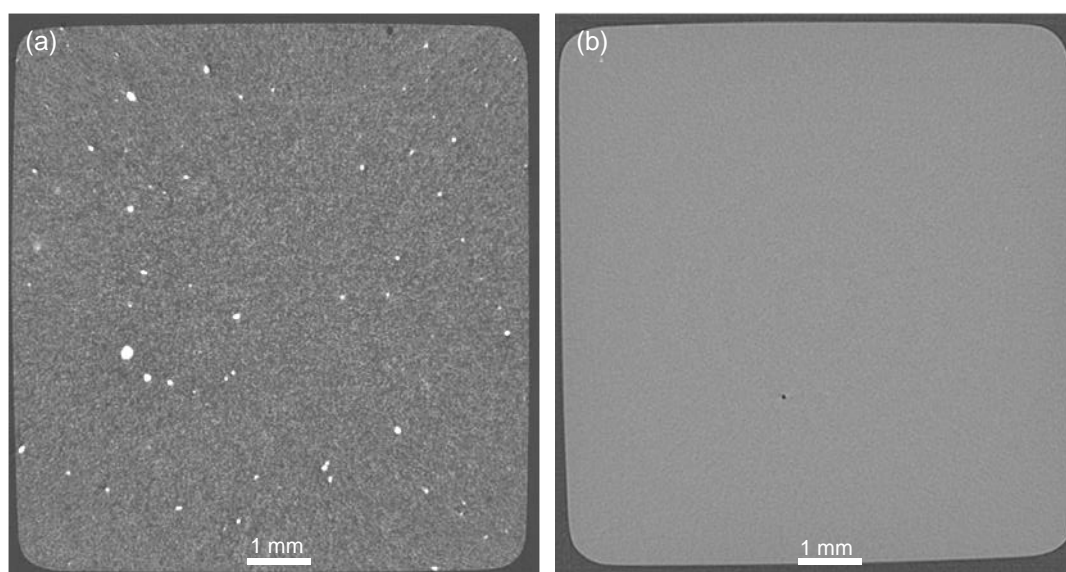


Figure 4-1: Representative CT slices highlighting variation in microstructure between cement formulations: (a) CMW-1, (b) CMW Original.

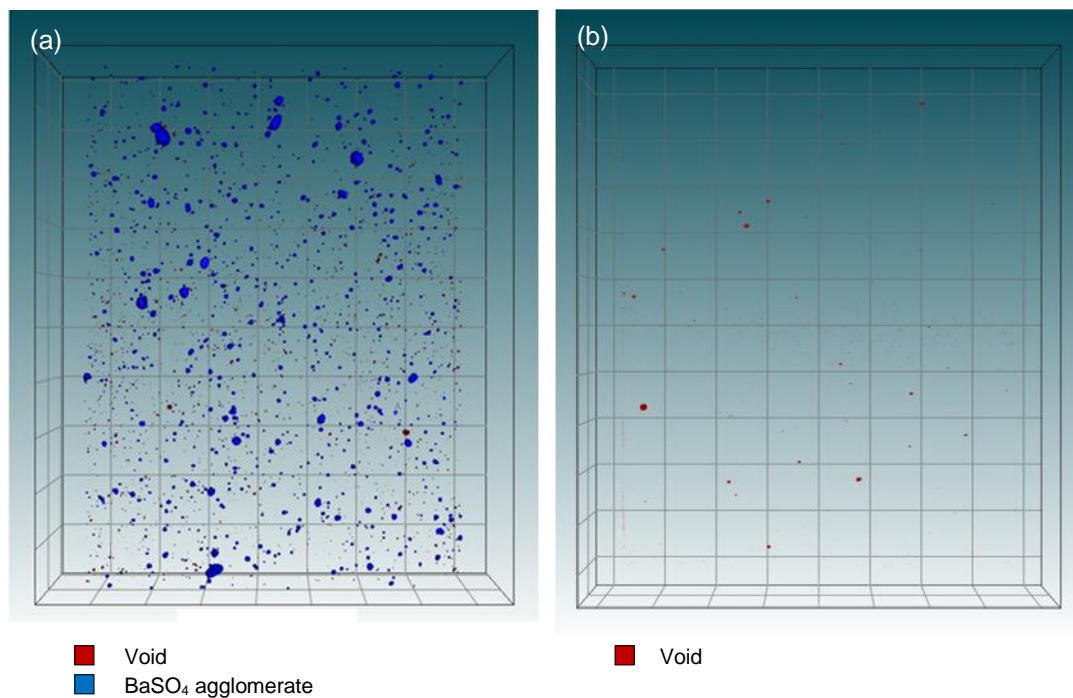


Figure 4-2: Distribution of microstructural defects within the 1mm section of a 'typical' specimen: (a) CMW-1 and (b) CMW Original. Gridlines are 1mm apart.

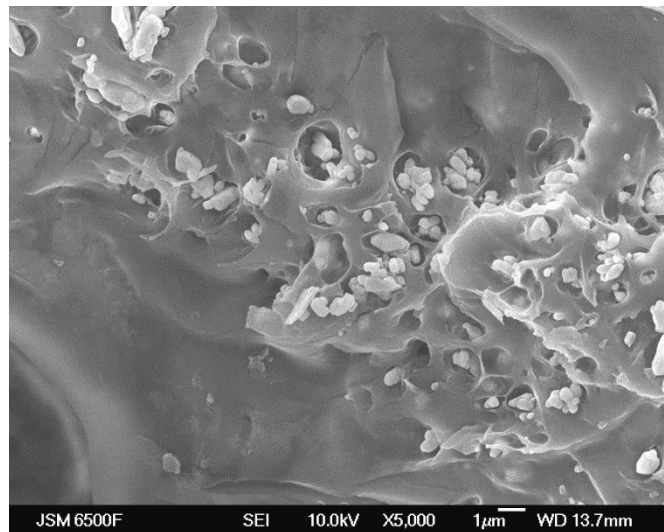


Figure 4-3: SEM micrograph of clusters of individual barium sulphate particles on CMW-1 fracture surface. Note the poor adhesion to the polymer matrix and evidence of plastic deformation during fracture.

SEM fractographic imaging revealed that even barium sulphate particles dispersed throughout the polymer matrix, rather than in large agglomerates, tended to form small clusters measuring a few microns in diameter (Figure 4-3). For the purpose of this study, barium sulphate agglomerates were therefore defined in terms of a distinctly larger group of identifiable structures with diameters of at least 10 microns. Agglomerates were present in the 1mm region of interest of each CMW-1 specimen at spatial densities of 4.6 – 22.0 per mm<sup>3</sup>; several agglomerates had an equivalent spherical diameter (ESD) of over 0.3 mm, the largest of which was 0.37 mm ESD. In comparison, the largest void present within the examined sections of all CMW-1 specimens was 0.25 mm ESD, while the largest void identified in the CMW Original specimens was 0.13 mm ESD. There was no first order correlation evident between the number of voids and number of agglomerates within any given CMW-1 specimen, *i.e.* the local presence of these two features does not appear to be related. However, significantly higher numbers of voids were identified in CMW-1 compared to CMW Original specimens, though the voids were similar in size (Table 4-1, Figure 4-4). The variation in global void populations between the two cement formulations is examined in more detail in Chapter 6.

Table 4-1: Characteristics of microstructural features in 1x 8 x 10mm gauge sections of CMW-1 and CMW Original

		CMW-1 voids	CMW-1 BaSO <sub>4</sub> agglomerates	CMW Original voids
Feature volume percentage	Mean	0.05	0.25	<0.01
	Standard deviation	0.05	0.10	<0.01
	Range	0.04 - 0.15	0.11-0.39	<0.01
No. features per mm <sup>3</sup>	Mean	22.6	13.2	0.60
	Standard deviation	23.2	7.1	0.23
	Range	0.9 - 50.9	4.6 - 22.0	0.35 - 0.97
Mean feature ESD (mm)	Mean	0.04	0.07	0.05
	Standard deviation	0.01	0.01	0.01
	Range	0.03 – 0.07	0.06 – 0.09	0.03 – 0.06
Largest feature ESD (mm)	Mean	0.16	0.30	0.10
	Standard deviation	0.05	0.04	0.02
	Range	0.10-0.25	0.25-0.37	0.08 – 0.13

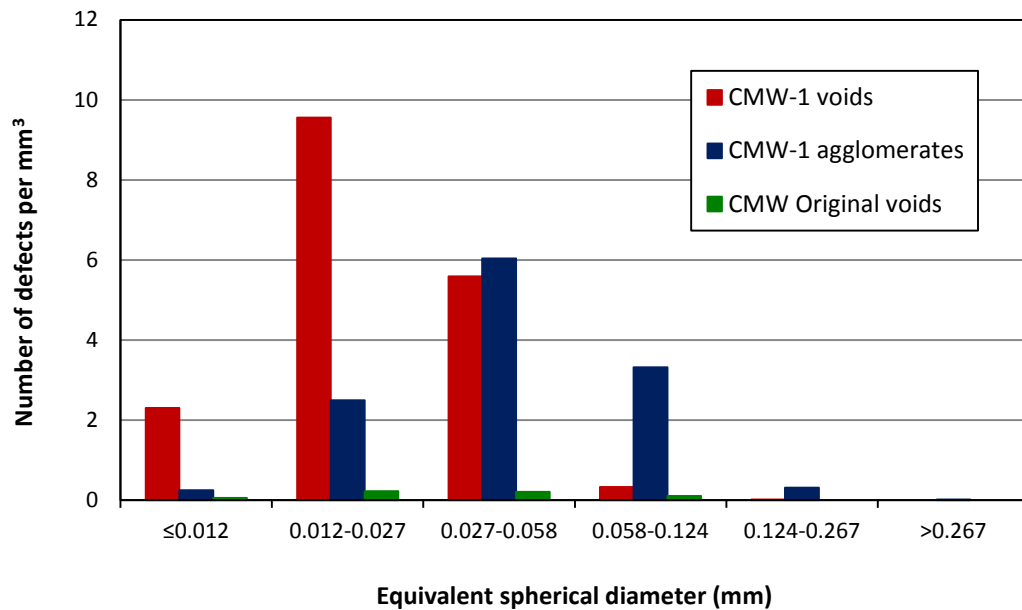


Figure 4-4: Size distribution of microstructural features in 1mm gauge sections of CMW-1 and CMW Original specimens

The mean size distribution, plotted in terms of the equivalent spherical diameter, for microstructural defects within the highly stressed regions of the specimens is presented in Figure 4-4. Both defect types (voids and BaSO<sub>4</sub> agglomerates) appear to demonstrate a log-normal distribution, with peak frequency occurring in the 0.012-0.027 mm ESD (1,001-10,000 μm<sup>3</sup>) interval for voids and 0.027-0.058 mm ESD (10,001-100,000 μm<sup>3</sup>) interval for agglomerates. The lower end of the defect population (by size), in CMW-1 was clearly dominated by voids, while larger sizes of agglomerates were seen at the upper tail of the distribution; agglomerates were the only defect type present in CMW-1 at greater than 0.27 mm ESD (corresponding to a volume of 0.01 mm<sup>3</sup>).

Statistical analysis of the size distribution for each defect type was conducted and the results are detailed in Appendix E. It was found that the distribution of CMW Original and CMW-1 voids can be approximated by a 3-parameter log-normal distribution function, although the fit is relatively poor at the lower tail of the size distribution due to the sensitivity of small defect volume measurements to the voxel size. The size distribution function of CMW-1 agglomerates can be described by a 2-parameter log-normal distribution as detailed in Appendix E.

Variation in the mean size and spatial density of agglomerates was noted between batches of CMW-1 cement specimens, as detailed in Table 4-2. The first batch (specimens 1-6) had fewer agglomerates per mm<sup>3</sup> (mean 6.2, SD 1.6) compared to the second batch (specimens 7-13) (mean 19.3, SD 2.4); the agglomerates in batch 1 were also typically larger (mean ESD 0.078 mm) than in batch 2 (mean ESD 0.070 mm). Statistical analysis using a two-tailed Welch's t-test (unpaired, unequal variance) found these differences were statistically significant (*p* values <0.0001 and 0.0236 respectively).

Table 4-2: Characteristics of BaSO<sub>4</sub> agglomerate populations in 1 x 8 x 10mm gauge sections of CMW-1.

Specimen number	Agglomerate volume percentage	No. agglomerates per mm <sup>3</sup>	Mean agglomerate ESD/mm	Mean agglomerate sphericity	Largest agglomerate ESD/mm	Largest agglomerate sphericity
1	0.16	5.4	0.083	0.86	0.31	0.56
2	0.19	5.6	0.087	0.87	0.37	0.85
3	0.13	6.6	0.072	0.84	0.29	0.49
4	0.12	4.6	0.078	0.84	0.32	0.80
5	0.23	9.4	0.076	0.82	0.35	0.31
6	0.11	5.4	0.074	0.88	0.28	0.75
7	0.39	22.0	0.070	0.90	0.26	0.77
8	0.27	21.1	0.063	0.89	0.28	0.72
9	0.31	17.0	0.073	0.89	0.29	0.78
10	0.37	14.9	0.078	0.89	0.34	0.80
11	0.29	19.4	0.066	0.89	0.26	0.92
12	0.37	21.6	0.069	0.89	0.28	0.85
13	0.32	19.1	0.069	0.90	0.25	0.82

## 4.3.2 MICROMECHANISMS OF FAILURE

Eleven specimens of each cement type (CMW-1 and CMW Original) were tested to failure, while two further specimens of CMW-1 were declared ‘run-outs’ as failure had not occurred within 1 million cycles. S-N data for all specimens tested is shown in

Figure 4-5. CMW Original demonstrated superior fatigue performance to CMW-1 in this study, as evidenced by the higher stress (30 MPa, compared to 20-25 MPa) needed to initiate failure within  $10^5$  cycles.

Fractographic imaging via SEM identified four key regions of crack initiation and propagation on the fracture surfaces of CMW-1 specimens, highlighted in Figure 4-6. In addition, there was a clearly identifiable final failure region, characterized by a smooth, glassy appearance, and often accompanied by a shear lip. The fracture surfaces of CMW Original specimens showed somewhat different characteristics (Figure 4-7); the length scale of surface features was coarser, and the halo region surrounding the initiation site was less evident. However, a similar trend in surface roughness was observed between the two cement types, *i.e.* increasing surface roughness as fatigue crack growth extends from the initiation site, followed by a flatter final failure region.

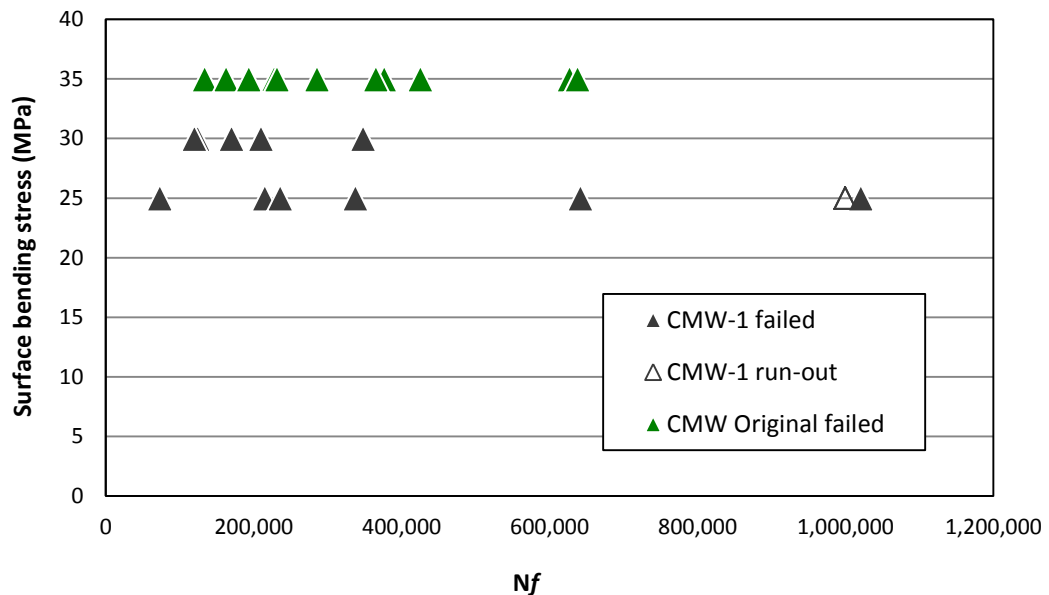


Figure 4-5: S-N data for all CMW Original and CMW-1 specimens tested.

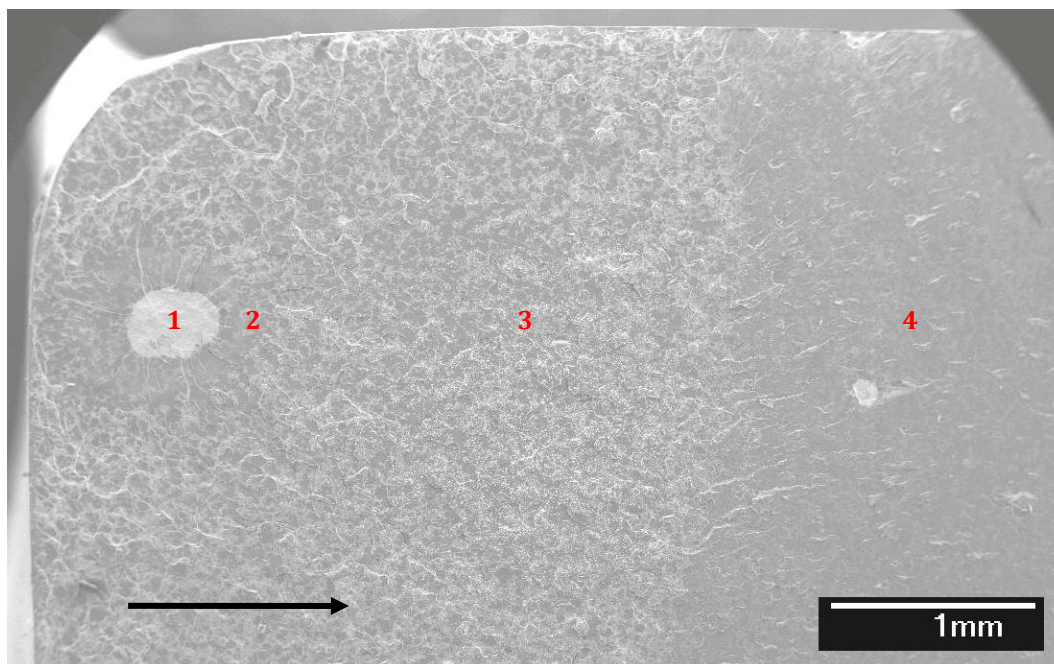


Figure 4-6: SEM micrograph of CMW-1 fracture surface, showing (1) initiation site, (2) 'halo' region of early crack growth, (3) region of short crack growth and (4) region of long crack growth. Arrow indicates overall direction of crack propagation.

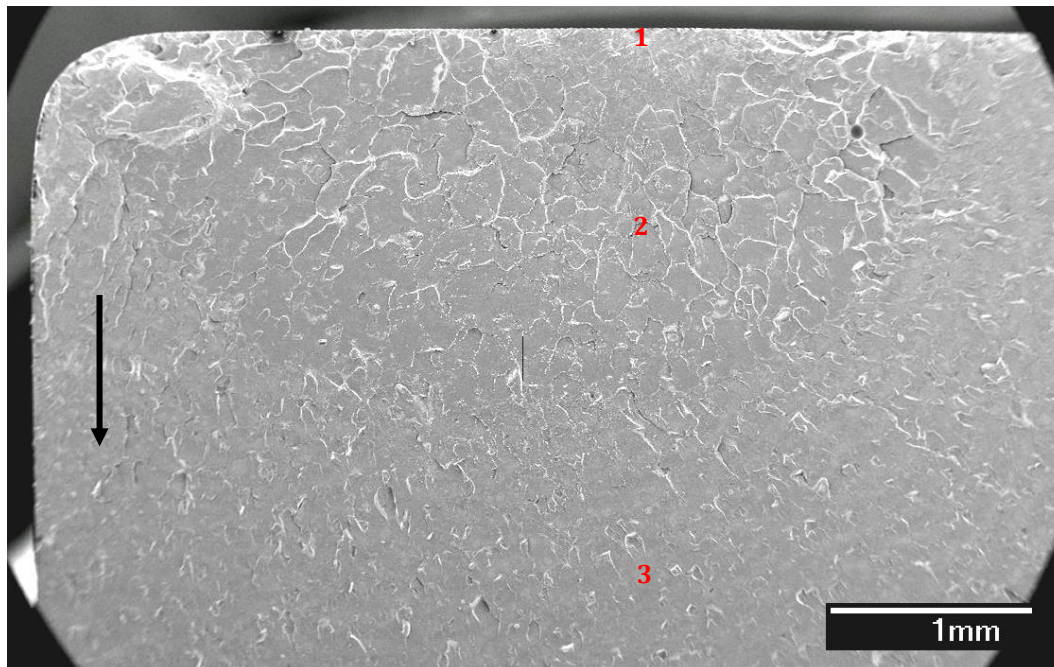


Figure 4-7: SEM micrograph of CMW Original fracture surface, showing (1) initiation site, (2) region of short crack growth and (3) region of long crack growth. Arrow indicates overall direction of crack propagation.

SEM imaging confirmed the presence of multiple large agglomerates on the fracture surfaces of CMW-1, formed primarily from small particles of  $\text{BaSO}_4$  interspersed with PMMA (Figure 4-6, Figure 4-8, and Figure 4-9). The chemical composition of these features was verified using energy dispersive x-ray spectroscopy (EDX). At the macro-scale, these agglomerates appeared to be essentially spherical (measured sphericity values were typically 0.8-0.9, Table 4-3). However, closer inspection revealed the edges of agglomerates were roughened at length scales of the order of  $10\ \mu\text{m}$ , with poor bonding between barium sulphate particles and PMMA at the agglomerate/matrix interface (Figure 4-9).

In all CMW-1 specimens, crack initiation was found to have occurred at large barium sulphate agglomerates, within 1mm of the free surface loaded in tension. Initiation was not found to occur at the locations of the bending rollers, nor from the corners of the specimens, thus confirming the efficacy of the self-aligning loading rig used in this study. Fractographic analysis using SEM indicated the initiation of multiple fatigue cracks in various directions at individual agglomerates, with classical 'ratchet marks' running back towards the agglomerate (Figure 4-8). Discontinuous fatigue crack growth bands, with a spacing of  $2\text{-}5\ \mu\text{m}$ , were also evident, particularly in pre-polymerised beads surrounding the initiation sites (Figure 4-10).

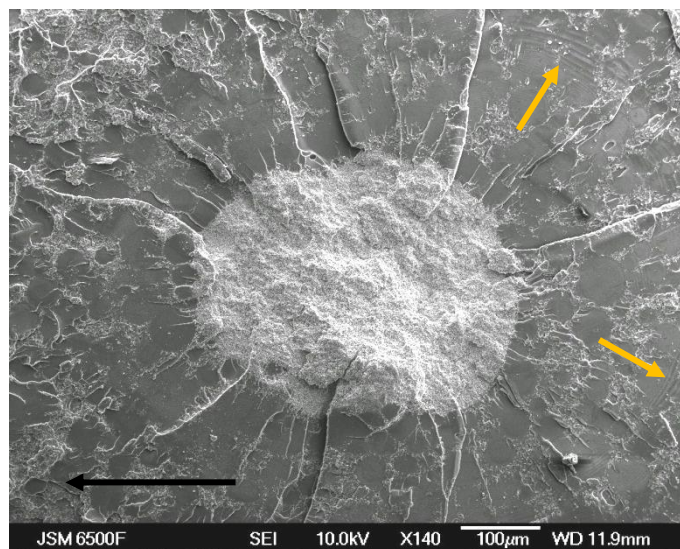


Figure 4-8: Multiple fatigue cracks initiating from a  $\text{BaSO}_4$  agglomerate in CMW-1. Black arrow indicates overall direction of crack propagation. Discontinuous growth bands are evident in the surrounding polymer, as indicated by the yellow arrows.

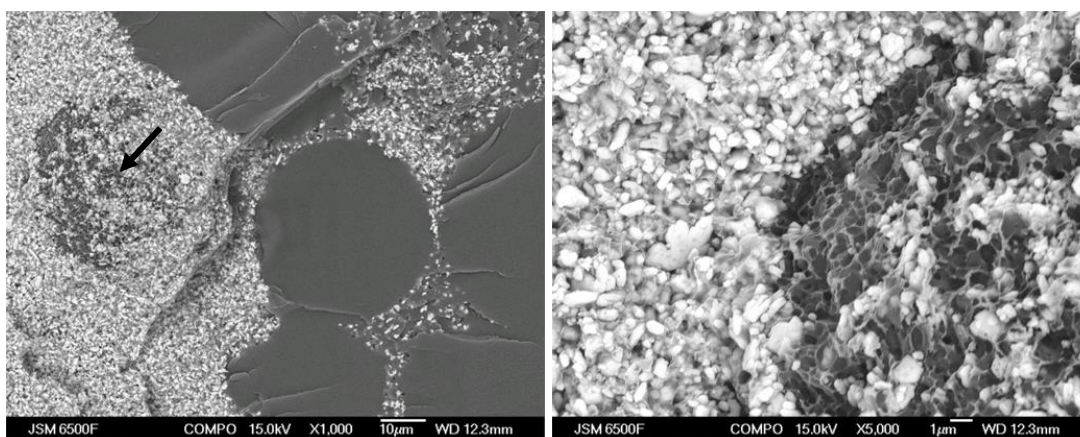


Figure 4-9: SEM micrographs of a CMW-1 fracture surface, showing a crack-initiating agglomerate surrounded by pre-polymerised beads. Note the poor adhesion between the radiopacifier and polymer matrix, with pull-out of barium sulphate particles indicated by the arrow.

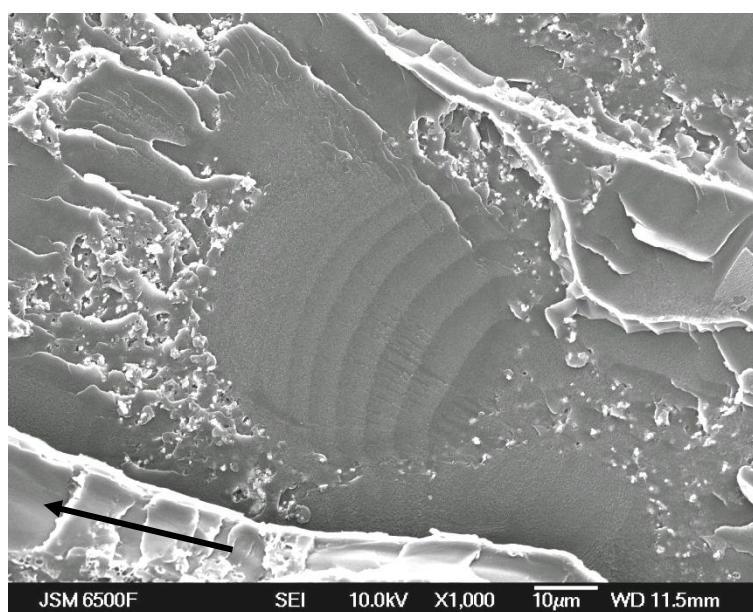


Figure 4-10: Discontinuous growth bands in a pre-polymerised bead in CMW-1. Arrow indicates overall direction of crack propagation.

While failure in CMW-1 was dominated by crack initiation from barium sulphate agglomerates, no major microstructural features were found to dominate failure in CMW Original. The region in which fatigue crack(s) had originated was easily identifiable due to the presence of semi-elliptical ‘thumbnail’ markings on the fracture surfaces, as evident in Figure 4-7. However, no primary crack-initiating defects could

be identified in ten of the eleven specimens, even under SEM examination. Crack initiation appeared to have occurred at or very close to the tensile surface in these specimens, and may therefore have originated at surface defects that were too small to be removed during polishing. In the remaining specimen, the primary fatigue crack was found to have initiated at an elliptical void with a mean diameter of 70  $\mu\text{m}$  (Figure 4-11). Secondary crack initiation was also identified at a void of similar size ( $\sim 80\mu\text{m}$  diameter) in one specimen (Figure 4-7, Figure 4-12), approximately 0.5 mm from the tensile surface and highlighted by the presence of ratchet marks running back towards the origin. Voids of this magnitude were the largest defects present in CMW Original, but only occurred at very low spatial densities ( $<1$  per  $\text{mm}^3$ , Table 4-1), which may account for the lack of identifiable crack-initiation sites in the majority of CMW Original specimens.

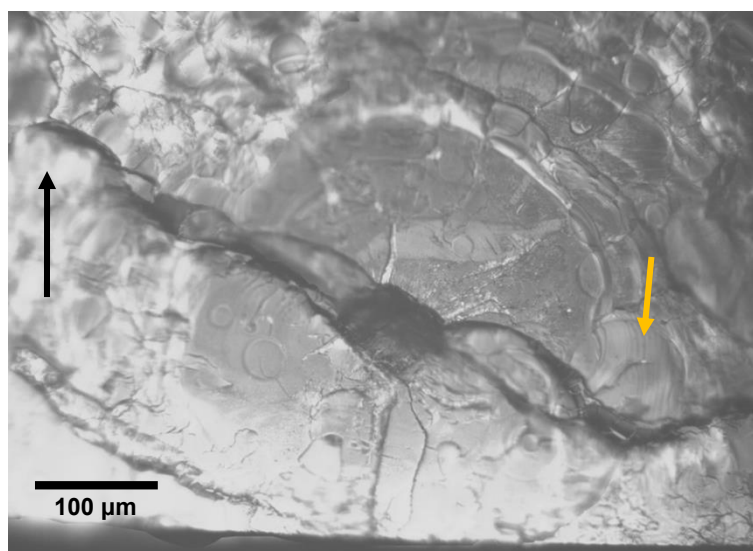


Figure 4-11: 20x optical micrograph of CMW Original specimen showing fatigue cracks initiating from a void. Black arrow indicates overall direction of crack propagation. Discontinuous growth bands are evident in the surrounding pre-polymerised beads, as indicated by the yellow arrow.

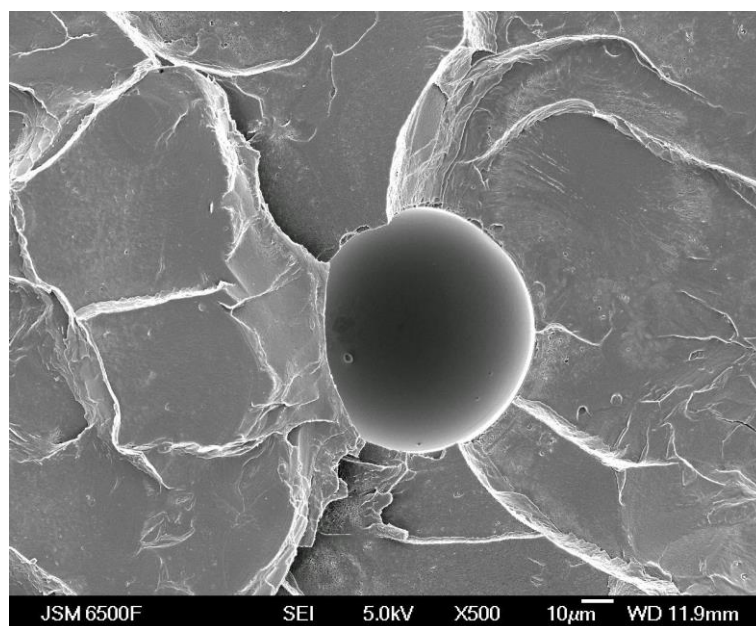


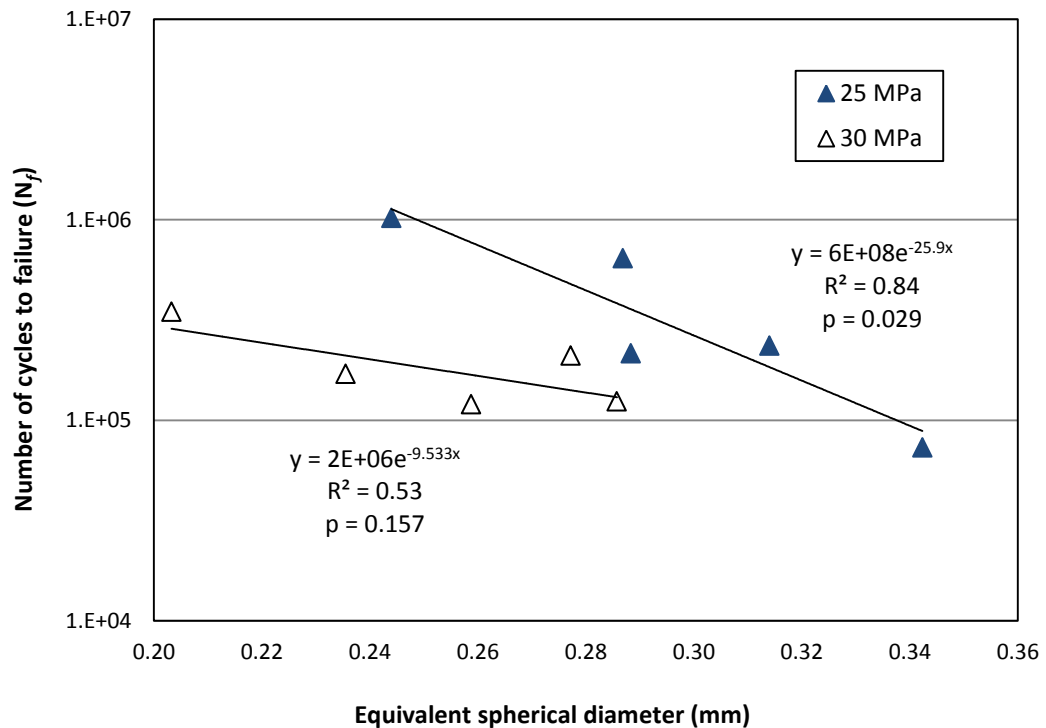
Figure 4-12: Secondary cracks initiating from a void in CMW Original.

#### 4.3.3 EFFECT OF AGGLOMERATE SIZE ON FATIGUE LIFE OF CMW-1

CT data obtained from CMW-1 specimens prior to testing and post-failure was correlated in order to identify and characterise the specific crack-initiating agglomerates (Table 4-3) noted in the post-failure FEG-SEM images. In each specimen, the crack-initiating agglomerate was always found to be one of the three largest agglomerates within the defined region of interest. Fatigue life was plotted against agglomerate volume, expressed as equivalent spherical diameter, and analysed using a simple linear regression method in Microsoft Excel (Figure 4-13). The figure highlights that increasing initiating defect volume correlated with reduced fatigue life for specimens tested at either stress level, although the proportion of the variance explained was appreciably greater at the lower stress level ( $R^2 = 0.84$  vs.  $0.53$  for a stress range of 30 and 25 MPa respectively). At 25 MPa, the  $p$  value (*i.e.* the probability that the result occurred by chance)  $< 0.05$ , and the relationship may be considered statistically significant. At the higher stress level,  $p > 0.05$  and thus the null hypothesis cannot be rejected, although the dependency of fatigue life on defect size should not be disregarded, due to the limited number of specimens and hence low power of the study.

Table 4-3: Characteristics of crack-initiating agglomerates in CMW-1.

Specimen number	Applied stress/MPa	No. cycles to failure/1000s	Agglomerate ESD/mm	$\sqrt{\text{Area}}$ in axial plane/mm	Distance from tensile surface/mm
1	25	641	0.29	0.30	0.0
2	25	73	0.34	0.31	0.0
3	25	215	0.29	0.29	0.0
4	25	236	0.31	0.29	0.0
7	25	1021	0.24	0.22	0.2
8	30	210	0.28	0.22	0.2
9	30	124	0.29	0.25	0.0
10	30	348	0.20	0.17	0.1
11	30	120	0.26	0.22	0.0
12	30	170	0.24	0.22	0.3

Figure 4-13: Relationship between the equivalent spherical diameter (ESD) of crack-initiating agglomerates in CMW-1 and the corresponding number of cycles to failure ( $N_f$ ).

#### 4.4 DISCUSSION

The tendency of barium sulphate radiopacifier particles to form large agglomerates within the cement is in agreement with the findings of other researchers (Ginebra *et al.* 2002, Kurtz *et al.* 2005, Jeffers *et al.* 2005, Sinnett-Jones 2007), although, to the author's knowledge, no previous work has been reported detailing the frequency of these structures.

It should be noted that although voids were the most frequent defect type observed in this study, BaSO<sub>4</sub> agglomerates were the most significant defect type by size, and dominated the upper tail of the defect size distribution. The agglomerate length scales found to initiate fatigue cracks in CMW-1 in this study (> 0.2 mm ESD) are of a similar magnitude to crack-initiating voids reported in *ex vivo* cement mantles (Jasty *et al.* 1991) and experimental constructs (Jeffers *et al.* 2007); furthermore, these agglomerates were significantly larger than the two crack-initiating voids identified in the CMW Original specimens. This finding is significant when viewed in terms of competition between stress concentration sites. As improved mixing methods are employed to inhibit void formation, alternative microstructural features, such as large agglomerates of barium sulphate particles, are likely to dominate failure, as previously suggested (Sinnett-Jones *et al.* 2009). The consistent initiation of fatigue cracks from agglomerates, and the scaling of fatigue life with agglomerate size, confirms that in this study barium sulphate agglomerates were the controlling defects in terms of the fatigue performance of the CMW-1 cement.

Fatigue cracks were found to initiate from the largest agglomerates within a specimen, especially when these defects were located close to the specimen surface. Adopting Murakami's definition of a surface defect (*i.e.* ratio of defect diameter to distance from surface > 1.6, Murakami 2002), 60% of the crack-initiating agglomerates in this study were considered to be surface defects. All crack-initiating agglomerates were located less than 0.8 mm from the free surface, *i.e.* within the critical volume for bending described by Murakami (2002). Free surface effects are expected to be more significant for the four-point bend testing conducted in this study than for tensile tests at equivalent stress, due to the more pronounced stress distribution as a function of the specimen cross-section.

The effect of agglomerate size on fatigue life observed in this study is consistent with experimental evidence of the effect of increasing pore size on the fatigue life of other materials such as cast aluminium alloys (Ammar *et al.* 2008, Nadot *et al.* 2004,

Murakami 2002, Mbuya 2011 & Wang *et al.* 2001, for example), as previously discussed in section 2.3.3. Fatigue life was found to scale with agglomerate size for defects 0.20 – 0.35 mm ESD; *i.e.* a larger crack-initiating agglomerate resulted in a shorter fatigue life. This is due to the greater effective crack length or  $\sqrt{\text{area}}$  of a crack initiating from a larger defect, which results in a higher stress intensity factor  $K$  and thus an increased rate of crack propagation for a given extent of physical crack growth from the void. Based on observations of the effect of casting voids in aluminium alloys (Ammar *et al.* 2008, Gao *et al.* 2004 & Wang *et al.* 2001), the dependency of fatigue life on initiating-defect size at low applied stress is expected to be linear for agglomerates exceeding the critical defect size. Below this size, however, a crack may initiate from a BaSO<sub>4</sub> agglomerate but this will not affect the fatigue life of the cement. This is because the fatigue limit may be considered as the threshold stress for crack propagation rather than initiation. As the maximum stress intensity factor is a function of the  $\sqrt{\text{area}}$ , if the agglomerate is below the critical size  $\Delta K$  will be insufficient for crack propagation and failure will not occur. Hoey and Taylor (2009a, 2009b) reported that the critical defect size for bone cement tested at 25MPa and R=0.1, expressed in terms of the critical length  $L$ , was 0.2 mm.

In this study, barium sulphate agglomerates are considered to act as stress concentrations and to facilitate crack initiation. The effect of an inclusion on fatigue performance is dependent not only on the size and location, but on the shape, stiffness and adhesion to the matrix (Murakami 2002). Agglomerates were found to be non-spherical at the micro-scale, with local minimum notch root radii of the order of 10  $\mu\text{m}$  and ‘sharp’ features at the interface between polymer beads. This geometry is likely to cause high local stress concentration, which may create favourable conditions for crack initiation (Sinnott-Jones *et al.* 2009).

If an inclusion is debonded, the interface between the inclusion and the matrix will be unable to sustain stress, and the inclusion may be regarded as mechanically equivalent to a stress free pore (Murakami 2002). However, SEM imaging showed no evidence of debonding at the agglomerate/matrix interface in this study, and cracks were found to initiate from within the agglomerates and propagate through the microstructure, as demonstrated in Figure 4-8, suggesting that agglomerates do not simply act as voids. Coultrup *et al.* (2009) modelled barium sulphate agglomerates in tensile specimens under four different boundary conditions: zero stiffness (*i.e.* as a void) and 10%, 100% and 1,000% Young’s modulus of bone cement. The best fit between experimental and computational fatigue lives was found when the agglomerates were modelled with the

same properties as the cement, implying they do not act as stress concentrations. Nonetheless, agglomerates were identified as initiation sites in 5/16 specimens in the study, confirming that cracks were able to initiate at the defects and then propagate through the surrounding microstructure.

Previous research has highlighted the tendency of barium sulphate within the matrix to form small clusters of particles (Ginebra *et al.* 2002, for example). These clusters have typically been observed on fracture surfaces, where they appear to be loosely contained within small voids, [Beaumont 1977, Harper and Bonfield 2000, Topoleski *et al.* 1990], consistent with the morphology seen in Figure 4-3. Several authors have implied that these voids are inherent in the cured cement (Ginebra *et al.* 2002, Molino and Topoleski 1996). However, SEM examination of a polished, untested CMW-1 specimen showed no evidence of voids around barium sulphate particles, either within the polymer matrix or at the edges of agglomerates (Appendix C); this is in agreement with synchrotron radiation computed tomography (SCRT) imaging of CMW-1 cement at a resolution of 0.7  $\mu\text{m}$  (Sinnott-Jones 2007). The voids seen around barium sulphate particles in this study (Figure 4-3, Figure 4-8) are therefore considered to be due to localised plastic deformation of the matrix during fracture.

Kurtz *et al.* (2005) reported that the addition of barium sulphate powder to Simplex P, hand-mixed in air, reduced the tensile and fatigue properties of the cement. Large  $\text{BaSO}_4$  agglomerates were observed in all specimens and were reported to initiate fatigue cracks in some cases. This detrimental effect on fatigue performance was not noted in a commercial formulation that contained a similar elevated barium sulphate content, but more homogenous distribution of particles. Although other factors, such as the molecular weight of the polymer, must be considered, these findings suggest that the dispersion of barium sulphate particles within the cement may be more significant to the mechanical properties than radiopacifier content alone.

A similar size distribution for  $\text{BaSO}_4$  particles, including the presence of large agglomerates, was identified in samples of unmixed CMW-1 cement powder in addition to the cured cement (Appendix C). This is perhaps unsurprising; during cement preparation, mixing is only conducted for a short period ( $\sim 30$  seconds), which is likely to be insufficient to effectively disperse the radiopacifier particles within the cement and break down the large agglomerates. The microstructure of the powder is therefore likely to be an important factor in determining the microstructure and radiopacifier

dispersion in the cured cement, and will thus impact upon the mechanical properties of the cemented construct.

In order to improve the dispersal of barium sulphate particles in future cement formulations, it is important to consider the underlying mechanisms contributing to particle agglomeration. The presence of agglomerates in both the polymer powder and cured cement, and the variation in agglomeration of barium sulphate particles in different cement formulations, suggests the formation of agglomerates relates to the manufacturing method of the cement powder. Barium sulphate is produced by mining barium sulphide or chloride from barite ore, and then reacting with sodium sulphate or sulphuric acid to form a solid  $\text{BaSO}_4$  precipitate. Precipitation of barium sulphate is a complex, multi-factorial process which has been the focus of numerous theoretical and experimental investigations in the field of chemical engineering (Cheng *et al.* 2009). The particle size of the precipitate is at least partially dependent on manufacturing parameters such as the feed location, feed concentration and mixing speed (Cheng *et al.* 2009). Wong *et al.* (2001), for example, found that, during precipitation of barium sulphate from barium chloride and sodium sulphate, agitation speed had a limited effect on particle size and morphology, but varying the ionic ratios gave some degree of particle size control. Marchisio *et al.* (2004) also found that high ion concentration resulted in particle agglomeration. This agglomeration occurs due to attractive van der Waals forces between colliding particles, and is therefore dependent on the rate of particle collisions, which may occur due to Brownian motion, thermal convection and shear forces (Wang *et al.* 2002). Attempts have been made to improve the dispersal of barium sulphate by precipitating nanoparticles (*e.g.* Li *et al.* 2012) or by coating the particles with a dispersal agent that inhibits agglomeration (*e.g.* Amirzadeh-Asl *et al.* 2010 & Hardinghaus *et al.* 2012).

There were a number of limitations in this study that should be acknowledged. While the experimental testing sought to correlate *in vivo* failure mechanisms, it did not accurately represent physiological loading conditions, environment or cement mantle geometry. A cemented implant may have a clinical life of 10-15 years (NJR 2010), corresponding to 40 million gait cycles for an active patient (Bergmann *et al.* 2010), at frequencies of 0.5 – 1Hz (Wykman and Olsson 1992). To the author's knowledge, there is no published data on the stresses induced in the cement mantle during *in vivo* loading, although instrumented hip implants have recorded hip contact forces of over 2.5 times bodyweight during normal activities (Bergmann *et al.* 2001). Based on this data, Lennon and Prendergast (2001) conducted a finite element simulation of a

cemented construct, which predicted peak tensile stresses of 7.6 MPa in the cement mantle, increasing to 38 MPa for a de-bonded stem. In the current study, machine time constraints necessitated accelerated fatigue testing; peak stresses (25, 30 or 35 MPa) were selected to produce failure within 1 million cycles, at a frequency of 3 Hz, consistent with fatigue testing of cement conducted by other researchers, as reviewed by Lewis (1997).

High dose ionizing radiation is known to adversely affect the tensile strength of PMMA (Tynny *et al.* 1967), and discolouration of bone cement has been observed after extended exposure to synchrotron radiation, indicating a reduction in molecular weight (Sinnott-Jones 2007). The exposure of cement specimens to ionizing radiation in this study exceeds the radiation dose an arthroplasty patient could be expected to receive from medical x-ray imaging equipment. However, fatigue tests conducted on specimens that were not irradiated resulted in similar fatigue lives and fracture surface characteristics to the specimens in this study. The potential effect of CT imaging on the results of this investigation is therefore considered to be negligible.

The study investigated the morphology and effect of barium sulphate agglomerates in CMW-1 mixed under vacuum using the CemVac mixing system. The presence of agglomerates has been identified in other cements, including Simplex P (Kurtz *et al.* 2005) and custom formulations (Ginebra *et al.* 2002, Kurtz *et al.* 2005) mixed by hand. However, the effect of barium sulphate agglomeration on the fatigue performance of these cements cannot be conclusively inferred from the results presented in this study. Furthermore, the relative influence of barium sulphate agglomerates on *in vivo* crack initiation processes is likely to be dependent on a number of factors, including interfacial strength, stem geometry and contamination of the cement mantle with biological debris, which may produce competing stress concentrations. Further investigation is therefore required to determine whether (a) the effect of barium sulphate agglomeration is consistent across all cement brands and cement mixing systems; (b) the crack initiation processes observed in this *in vitro* study are representative of *in vivo* failure mechanisms.

#### 4.5 CONCLUSION

Agglomerates of BaSO<sub>4</sub> radiopacifier particles in CMW-1 bone cement were observed to be large (up to 0.37 mm ESD) and numerous (up to 22 per mm<sup>3</sup>), and were the most significant microstructural defect type by size. The largest agglomerates consistently initiated fatigue cracks, and the fatigue life of CMW-1 specimens scaled with agglomerate size. The tendency of barium sulphate to form large agglomerates adversely affected the fatigue life of the cement *in vitro*, compared to radiolucent CMW Original cement. Barium sulphate agglomerates are therefore likely to have a negative impact on clinical performance if present in regions of high stress within the cement mantle. Optimisation of mixing techniques and/or cement formulations containing barium sulphate may therefore be advantageous in order to reduce the formation of agglomerates and their potential effects *in vivo*.



---

## 5. THE EFFECT OF ZIRCONIUM DIOXIDE AS A RADIOPACIFIER

---

### 5.1 INTRODUCTION

Since the early development of bone cement for use in load-bearing orthopaedic applications, radiopacifiers have been an important constituent of cement formulations to allow surgeons to visualize the cement mantle in post-operative x-rays. Commercial acrylic bone cements use either barium sulphate or zirconium dioxide as the x-ray contrast medium, and have done since the original 'heritage' cements (CMW-1 and Palacos R, for example) were produced in the late 1950s. The rationale for the choice of radiopacifier in these early bone cement formulations is unclear, although both compounds were already in general medical use (Barrs 2006); cost and availability of constituents may have been a factor (Schulze 2012).

Comparative studies of the performance of cement formulations containing BaSO<sub>4</sub> vs. ZrO<sub>2</sub> have been inconclusive. Zirconium dioxide has been reported to improve tensile strength and fracture toughness, but reduce compressive strength and fatigue crack propagation resistance in comparison to barium sulphate (Ginebra *et al.* 2002). While both radiopacifiers have been linked to abrasive wear of metallic implants (Isaac *et al.* 1987), and particles of each have been identified in peri-prosthetic tissue (Keen *et al.* 1992), barium sulphate has been hypothesized to increase osteolysis compared to radiolucent and ZrO<sub>2</sub> cements (Wimhurst *et al.* 2001, Sabokbar *et al.* 1997). Furthermore, the value of these comparative studies have been

Due to the reported limitations of BaSO<sub>4</sub> and ZrO<sub>2</sub> (as discussed in Sections 2.2.3 and 2.3.3) several attempts have been made to replace these inorganic compounds with an organic contrast medium in the form of an iodine-containing monomer (Ginebra *et al.* 2002, Artola *et al.* 2003, van Hooy-Corstjens *et al.* 2004, for example). While the mechanical properties of these experimental cements have been considered acceptable, none have yet progressed to commercial development, perhaps due to concerns over iodine sensitivity (Breusch and Malchau 2005).

In the absence of conclusive evidence supporting the use of one radiopacifier over the other, and in view of the widespread use of ZrO<sub>2</sub> as a radiopacifier in both established cement brands (e.g. Palacos R, Heraeus Kulzer GmbH, Hanau, Germany) and newer

formulations (e.g. Smartset HV, Depuy CMW, Blackpool, UK), further investigation of the effect of ZrO<sub>2</sub> particles on the mechanical properties of bone cement would be beneficial.

The micro-mechanisms of failure in zirconium dioxide containing cements have largely been ignored in the literature, with a few notable exceptions (Ginebra *et al.* 2002, Harper and Bonfield 2000). While barium sulphate has shown a tendency to form agglomerates that can initiate fatigue cracks, as previously discussed (Chapter 4), to the author's knowledge there is no published evidence of ZrO<sub>2</sub> particles forming large agglomerates (greater than tens of μm in diameter), or initiating fatigue cracks. The aim of this study was therefore to characterize the morphology and spatial distribution of microstructural features (i.e. voids and ZrO<sub>2</sub> particles) within two ZrO<sub>2</sub> containing commercial cement formulations, and to investigate the relative effects of these features on fatigue crack initiation processes.

## 5.2 MATERIALS AND METHODS

Two standard commercial cement formulations were selected for this study: Palacos R (Heraeus Kulzer GmbH, Hanau, Germany) and Smartset HV (Depuy CMW, Blackpool, UK). Both are high viscosity poly(methylmethacrylate)/ poly(methylacrylate) (PMMA/PMA) based cements indicated for load-bearing orthopaedic applications. The powder component of each cement is sterilised using EtO gas, while the liquid component is sterilised via membrane filtration. Palacos R contains 14.75% (w/w) zirconium dioxide ( $ZrO_2$ ) radiopacifier in the powder component, while Smartset HV contains 15.00% (w/w), according to the manufacturers' specifications. Detailed compositions of the two cements have been given in Chapter 3 (Table 3.1).

Twelve specimens of Palacos R and six specimens of Smartset HV were prepared and tested under four point bend loading as previously described (Chapter 3). Tests were conducted in air at room temperature at a maximum applied stress of 25 MPa to 50 MPa (in 5 MPa increments) for Palacos R and either 50 MPa or 60 MPa for Smartset HV. Maximum stresses were selected in an effort to ensure consistent failure occurred within  $10^5$  fatigue cycles, due to machine time constraints. The large scatter in fatigue life observed for Palacos R specimens, and the high percentage of run-outs at the lower stress levels, necessitated testing at progressively greater loads in order to produce sufficient fracture surface specimens for micromechanical analysis.

The central 10 mm gauge section of each specimen was imaged prior to testing and post-failure using a laboratory  $\mu$ -CT scanner (CT 160Xi or HMX-ST, Nikon-Metris, Tring, UK); the acquisition parameters for each pre-test scan are detailed in Table 5-1. Additionally, one specimen of Palacos R was sectioned after testing to produce a 2 mm x 2 mm x 10 mm matchstick coupon for examination using synchrotron radiation computed tomography (SRCT), at a resolution of 1.8  $\mu$ m. CT image analysis was conducted using VG Studio Max 2.1 and Image J software, according to the methodology outlined in Section 3.5.

Fracture surfaces were imaged using a JEOL JSM6500F FEG-SEM. Specimens were sputter-coated with a thin layer (~15 nm) of gold prior to SEM imaging. A low accelerating voltage of 10 kV was used to minimise beam-induced polymer degradation, while magnifications exceeding 5,000 x were avoided.

Table 5-1: CT acquisition parameters.

Cement type	Specimen no.	Scanner	Beam current ( $\mu\text{A}$ )	Accelerating voltage (kV)	Exposure time (ms)	No. projections	Voxel resolution ( $\mu\text{m}$ )
Palacos	1	CT160Xi	98	86	2134	1905	8.5
Palacos	2-4	CT160Xi	98	86	2134	1905	8.3
Palacos	5	CT160Xi	98	86	2134	1905	8.6
Palacos	6	CT160Xi	98	86	2134	1905	8.1
Palacos	7-8	HMX ST	90	100	2134	3142	12.3
Palacos	9	CT160Xi	55	85	2134	1905	9.8
Palacos	10	CT160Xi	60	80	2134	1905	9.8
Palacos	11-12	HMX ST	90	100	2134	3142	12.3
Smartset	1-6	HMX ST	135	100	500	3142	10.2

## 5.3 RESULTS

### 5.3.1 DEFECT POPULATION CHARACTERISATION

Palacos R and Smartset HV were found to have similar microstructures when examined using  $\mu$ -CT. In both formulations, pre-polymerised beads were indistinguishable from the polymer matrix at  $\sim 10 \mu\text{m}$  resolution; the zirconium dioxide radiopacifier appeared to be evenly dispersed through the cement with no large (i.e.  $>100 \mu\text{m}$  diameter) agglomerates (Figure 5-1).

Two microstructural features of potential relevance to fatigue crack initiation were identified: voids and radiopacifier particles; both were present in all specimens. Feature morphology and distribution varied between the two cement formulations, and between individual specimens from the same batch of cement. Examples of feature distributions for each cement type are shown in Figure 5-2 and Figure 5-3.

Although both cements contain similar quantities of zirconium dioxide radiopacifier by weight, Palacos R appeared to contain a significantly greater number of radiopacifier particles than Smartset HV when segmented from the CT data (Figure 5-2 & Figure 5-3). However, particles were found to be evenly dispersed and of a similar size in both cements. This suggests the radiopacifier phase in Palacos R is typically coarser and thus more readily detected at the resolution utilized here ( $8\text{-}12 \mu\text{m}$ ).

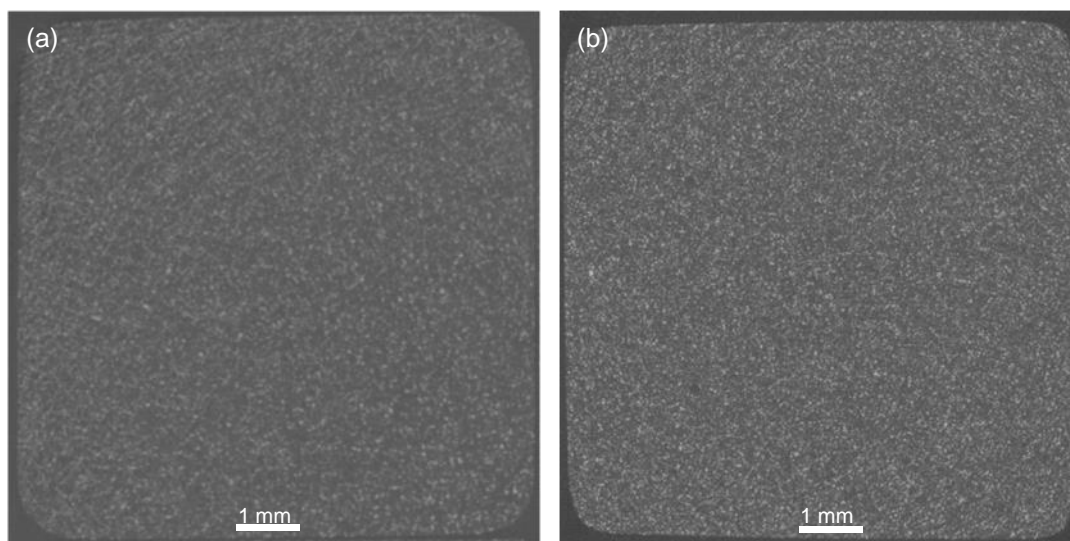


Figure 5-1: Representative CT slices highlighting microstructure of (a) Palacos R and (b) Smartset HV, prior to the application of a  $3 \times 3$  median filter (as described in Section 3.5).

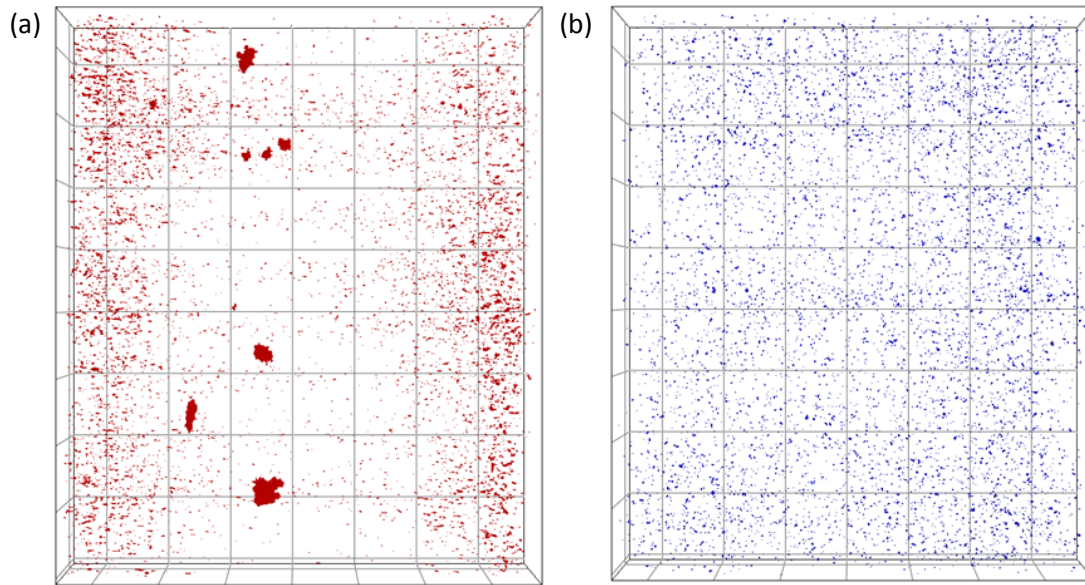


Figure 5-2: Distribution of (a) voids and (b) ZrO<sub>2</sub> particles in Palacos R.

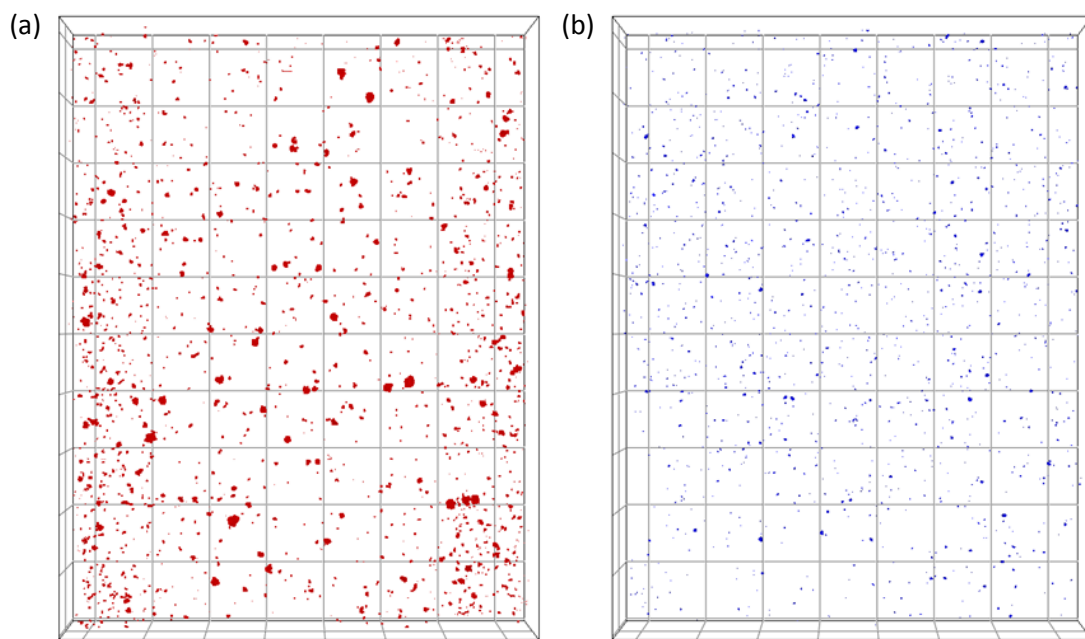


Figure 5-3: Distribution of (a) voids and (b) ZrO<sub>2</sub> particles in Smartset HV.

The void content in Palacos R was found to be bi-modal – most specimens contained many small voids (< 100  $\mu\text{m}$  ESD), concentrated towards the surface, while a few specimens contained one or more larger voids (> 100  $\mu\text{m}$  ESD) with a more random location (Figure 5-2 (a)). These large voids typically had a roughened, granulated surface morphology with a lower sphericity than the global void population; the mean sphericity of the large voids was 0.31 compared to 0.75 for all the voids in each specimen of Palacos R.

Quantitative analysis revealed that the zirconium dioxide populations in the two cement formulations demonstrated similar characteristics in terms of the size of detectable particles (Table 5-2). Mean particle size was found to be 0.027 mm ESD in Palacos R and 0.028 mm ESD in Smartset HV, while the mean of the largest particle within each specimen was comparable for both cement types (0.09 mm ESD, range 0.07-0.12 and 0.08-0.11, respectively). Of the particles detected at the given resolutions,  $\text{ZrO}_2$  in Palacos R had a significantly higher spatial density (mean 185 per  $\text{mm}^3$  vs. 30 per  $\text{mm}^3$ ) and volume percentage (0.16 vs. 0.04) than Smartset HV.

The mean volume distribution for voids and radiopacifier particles within the 1mm region of interest of all samples measured is presented in Figure 5-4. Both voids and  $\text{ZrO}_2$  particles appeared to demonstrate an exponential distribution, with peak frequency occurring in the 0.012 – 0.027 mm ESD (1,001-10,000  $\mu\text{m}^3$ ) interval. At the upper tail of the size distribution, voids were the only defect type present at volumes greater than 0.124 mm ESD (corresponding to  $1 \times 10^6 \mu\text{m}^3$ ). All Smartset HV specimens contained voids larger than 0.2 mm ESD, while two Palacos R specimens contained voids greater than 0.3 mm ESD.

Statistical analysis of the defect size distributions was conducted as detailed in Appendix E. Attempts were made to fit normal, log-normal, exponential and general extreme value (GEV) distribution functions to the data shown in Figure 5-4. It was found that the size distributions were best described by 3-parameter log-normal distribution functions for both voids and agglomerates, though the fit was poor. For larger voids, the size distribution was better approximated by an exponential or GEV function, but in all cases the statistical models did not pass Anderson-Darling or Chi-squared goodness of fit tests.

Significant variation in the spatial density of radiopacifier particles was noted when imaging was conducted at higher resolution using SRCT compared to  $\mu\text{-CT}$  for the same specimen of Palacos R (Figure 5-5). Peak frequency was found to occur in the 0.021-

0.025 mm ESD interval at 1.8  $\mu\text{m}$  resolution, with only 0.09% particles larger than 50  $\mu\text{m}$  in diameter. The specimen volume occupied by  $\text{ZrO}_2$  particles was measured as 2.59% at 1.8  $\mu\text{m}$  compared to 0.14% at 8.3  $\mu\text{m}$  resolution.

Table 5-2: Characteristics of microstructural features in 1 x 8 x 10mm gauge sections of Palacos R and Smartset HV.

		Palacos R voids	Palacos R ZrO <sub>2</sub> particles	Smartset HV voids	Smartset HV ZrO <sub>2</sub> particles
Feature volume percentage	Mean	0.33	0.16	0.54	0.04
	SD	0.17	0.07	0.28	0.01
	Range	0.09 – 0.55	0.09 – 0.26	0.29 – 1.04	0.02 – 0.05
No. features per mm <sup>3</sup>	Mean	189	185	132	30
	SD	90	113	85	8
	Range	62 – 342	49 – 402	9 – 235	19-38
Mean feature ESD	Mean	0.033	0.027	0.050	0.028
	SD	0.010	0.004	0.019	0.002
	Range	0.025 – 0.055	0.022 – 0.032	0.034 – 0.086	0.025 – 0.030
Largest feature ESD	Mean	0.18	0.09	0.23	0.09
	SD	0.14	0.01	0.03	0.01
	Range	0.08 – 0.71	0.07 – 0.12	0.20 – 0.26	0.08 – 0.11
No. feature per mm <sup>3</sup> with ESD >0.05 mm	Mean	7	1.5	18	0.7
	SD	6	1.3	11	0.3
	Range	1 – 16	0.2 – 4.2	8 – 38	0.3 – 1.0

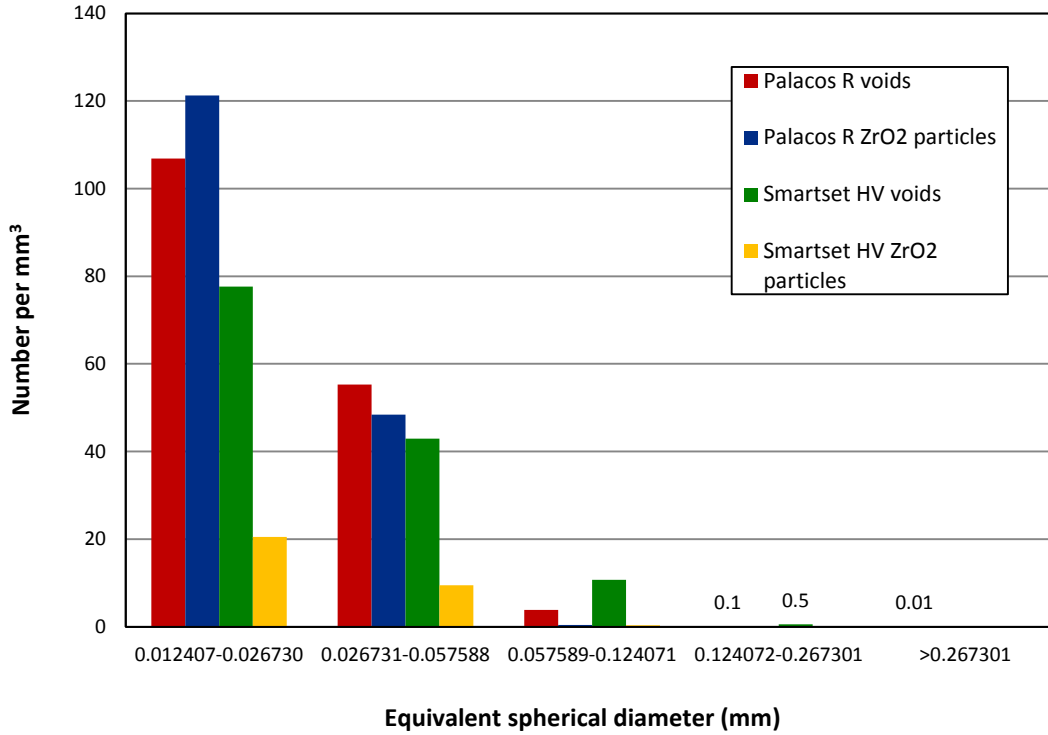


Figure 5-4: Size distribution of microstructural features in 1mm sections of Palacos R and Smartset HV.

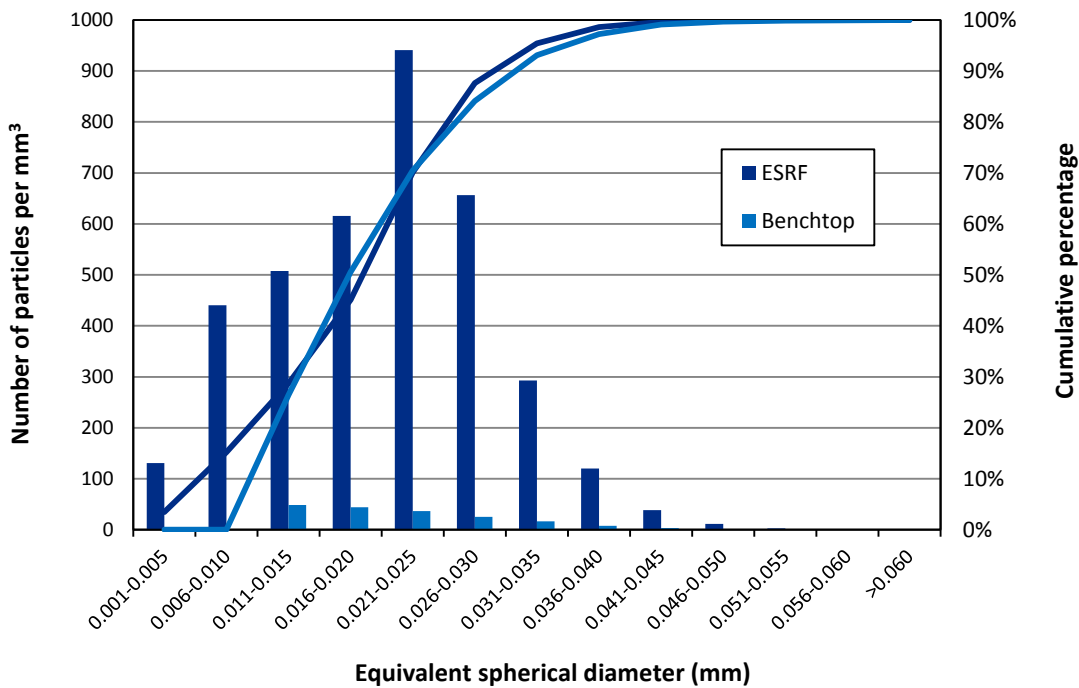


Figure 5-5: Size distribution of ZrO<sub>2</sub> particles measured in one matchstick (2 x 2 x 2 mm) specimen of Palacos R using synchrotron radiation CT (“ESRF”) at 1.8 μm resolution and CT 160Xi (“Benchtop”) at 8.3 μm resolution.

## 5.3.2 MICROMECHANISMS OF FAILURE

Eight Palacos R specimens and five Smartset HV specimens were tested to failure. The remaining specimens (4 Palacos R, 1 Smartset HV) were declared 'run-outs' at either 1 or 2 million cycles, depending on machine time constraints. One specimen of Palacos R and one specimen of Smartset HV failed before testing could be terminated, at 1.4 million and 2.2 million cycles respectively; the fractographic results of these specimens have therefore also been included in this study.

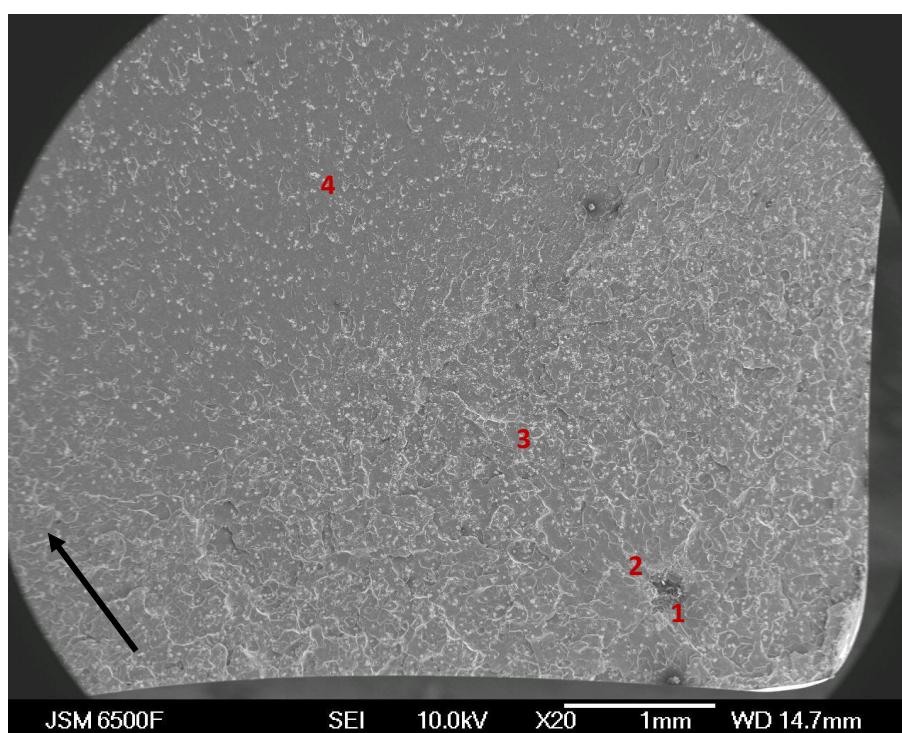


Figure 5-6: SEM micrograph of Palacos R fracture surface, showing (1) initiation site, (2) 'halo' region of early crack growth, (3) region of short crack growth and (4) region of long crack growth. Arrow indicates overall direction of crack propagation.

Several distinct regions were evident on the fracture surfaces of both cement types, as labelled in Figure 5-6. Regions 1 and 2 were not apparent on the fracture surfaces of all specimens. However, in specimens with a single, dominant fatigue crack origin, a 'halo' region of early crack growth through the beads and matrix was observed immediately surrounding the initiation site, resulting in a reasonably smooth fracture surface in this region. In all specimens, a 'thumbnail' region, indicating the advance of the crack front, was identified; this region was characteristically rough with a stepped morphology,

indicating propagation of a short fatigue crack relative to the microstructure. A clear transition was evident to micro-structurally independent, unstable crack growth, characterized by a reasonably smooth fracture surface.

Dominant crack initiation was observed at voids in specimens of both Palacos and Smartset cements. In these specimens, the fatigue origin was easily identified from the 'thumbnail' shape and direction of advance of the crack, and from the presence of discontinuous growth bands occurring in both pre-polymerised beads and polymer matrix surrounding the initiating void, indicating the local direction of crack advance (Figure 5-7). Crack-initiating voids were of the order of hundreds of  $\mu\text{m}$  in length (perpendicular to the loading direction) and had an irregular shape, with polymer beads protruding from the interior surfaces of the voids (Figure 5-8).

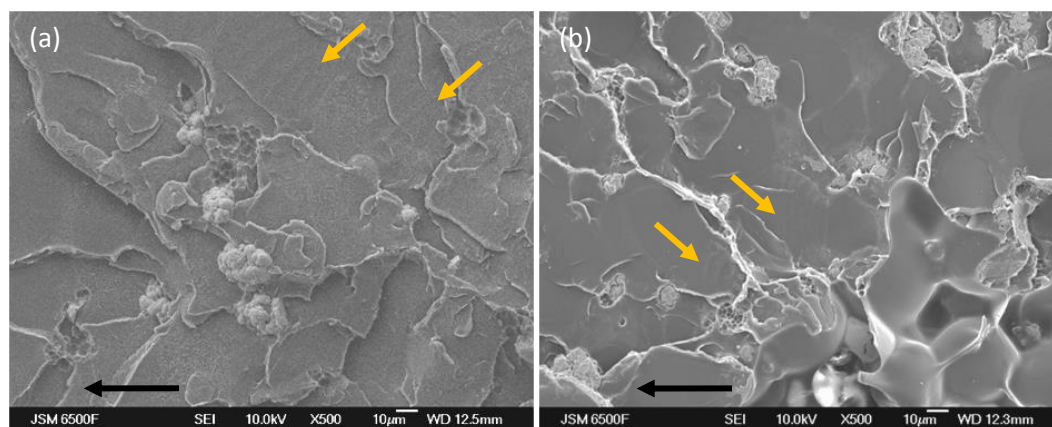


Figure 5-7: Discontinuous growth bands surrounding crack initiation sites in (a) Palacos R and (b) Smartest HV, as indicated by the yellow arrows. Black arrows show overall direction of crack propagation.

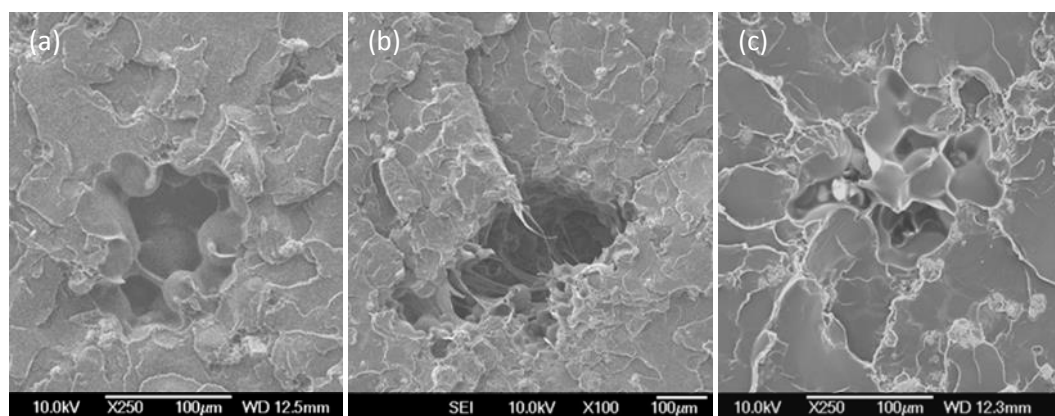


Figure 5-8: Crack initiating voids in (a-b) Palacos R and (c) Smartset HV.

In specimens in which no dominant fatigue origin was identified, the thumbnail region was generally longer, and ratchet marks were often present on the face of the specimen, indicative of multiple crack initiation sites. In one such specimen of Palacos R, multiple fatigue cracks were identified to have initiated from an agglomerate of radiopacifier particles close to the surface (Figure 5-9), while multiple separate crack initiation sites were identified in a specimen of Smartset HV, with cracks propagating in varying directions, as indicated by the discontinuous crack growth bands (DGBs) evident on the fracture surface (Figure 5-10). In one specimen of Smartset HV in which multiple fatigue cracks had initiated from a void (Figure 5-8(c)), DGBs appeared to originate from an agglomerate of  $ZrO_2$  particles at the edge of the void (Figure 5-11).

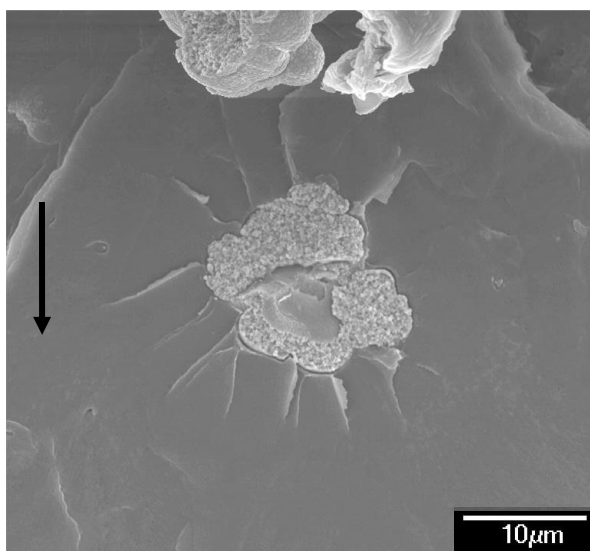


Figure 5-9: Multiple cracks initiating from a agglomerate of  $ZrO_2$  particles in Palacos R. Arrow indicates overall direction of crack propagation.

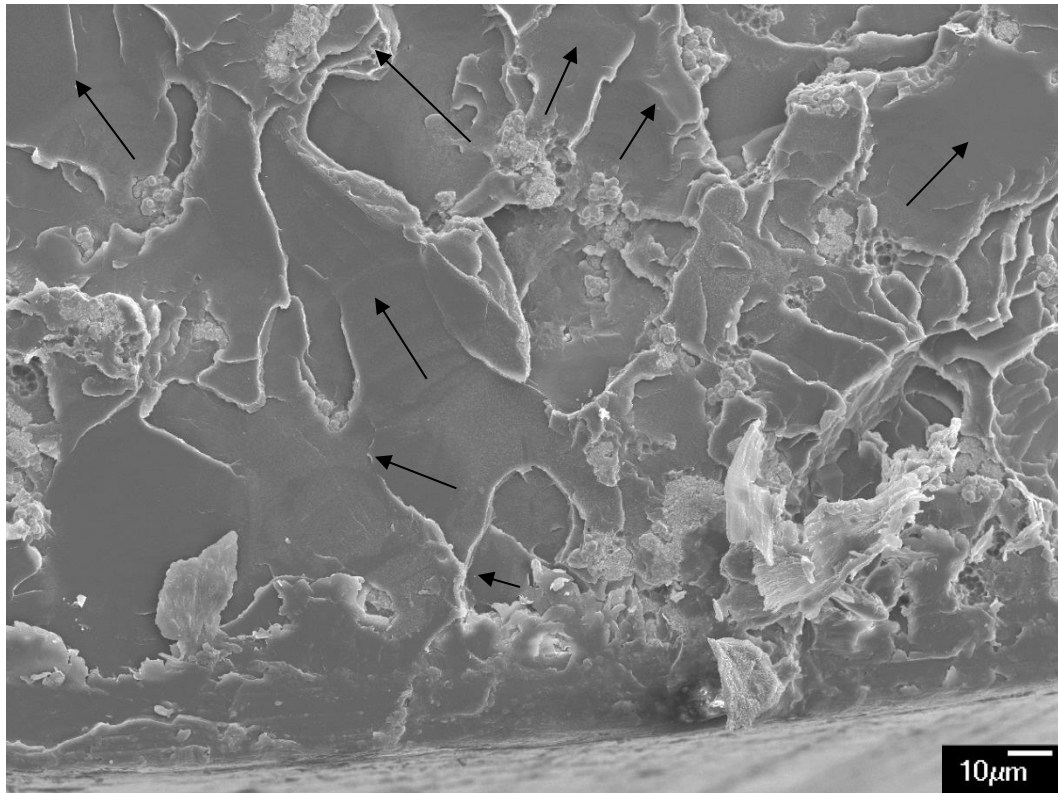


Figure 5-10: Discontinuous growth bands indicating multiple crack initiation sites in Smartset HV. Arrows indicate local direction of crack propagation ( $\sigma = 50$  MPa,  $N_f = 2.2$  million).

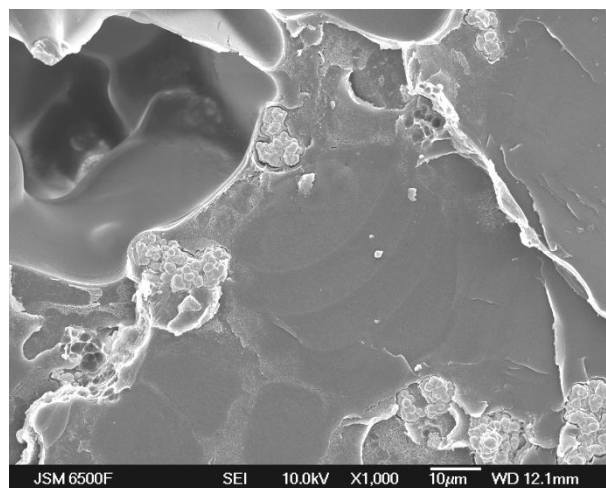


Figure 5-11: Discontinuous growth bands in a pre-polymerised bead at the edge of a crack-initiating void on the fracture surface of a Smartset HV specimen.

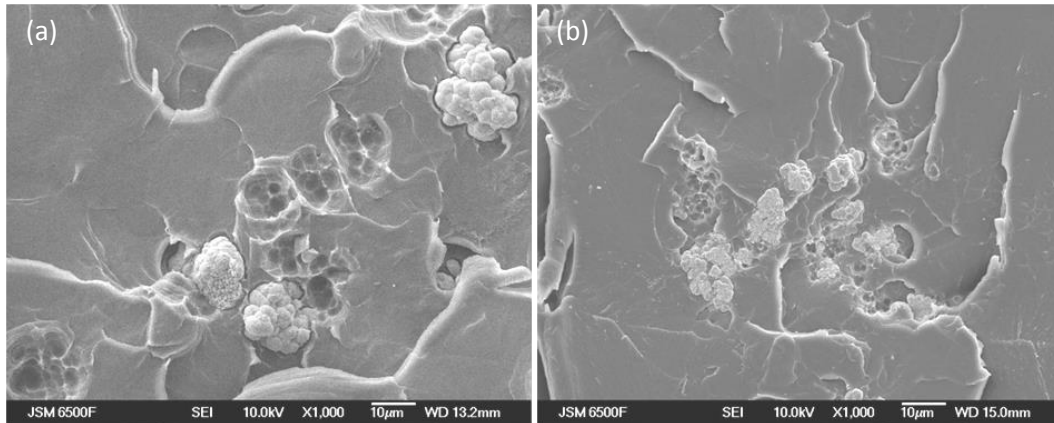


Figure 5-12: Particles of zirconium dioxide on the fracture surface of (a) Palacos R and (b) Smartset HV at 1000 x magnification.

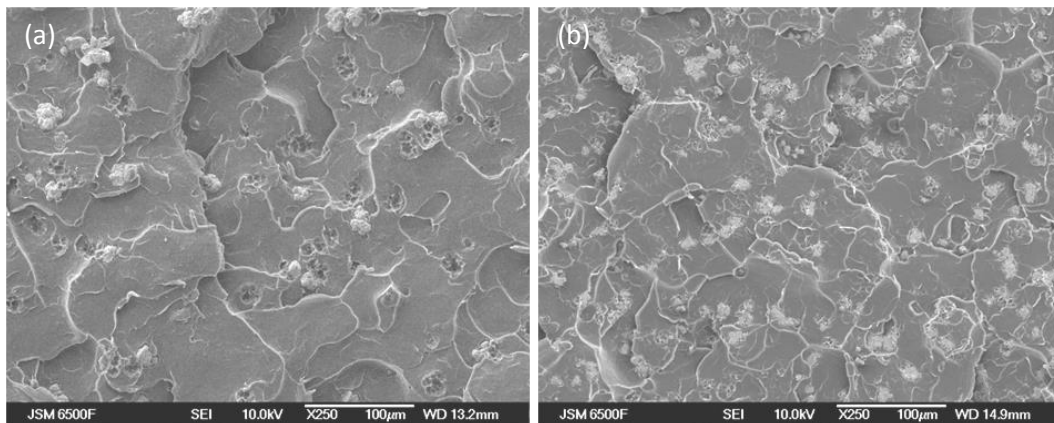


Figure 5-13: Particles of zirconium dioxide on the fracture surface of (a) Palacos R and (b) Smartset HV at 250x magnification.

Although limited fracture of  $ZrO_2$  agglomerates had occurred, many agglomerates were entirely separated from the surrounding matrix on one fracture surface (Figure 5-12).  $ZrO_2$  pull-out was observed more frequently in the early and short crack growth regions of Palacos specimens (*i.e.* regions 2 and 3 annotated on Figure 5-6), while fracture was observed more frequently in Smartset HV (Figure 5-13). A clear degree of matrix separation was identified around  $ZrO_2$  agglomerates in both cements, particularly in the early crack growth region (Figure 5-14), suggesting limited bonding between the radiopacifier and the polymer matrix. This voiding was not observed in SEM micrographs of polished cement surfaces (Appendix C).

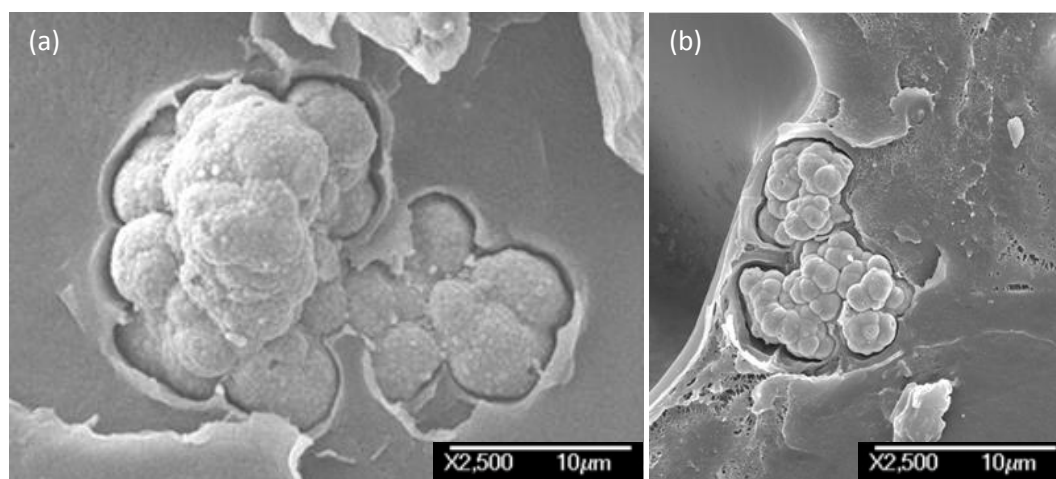


Figure 5-14: Zirconium dioxide agglomerates close to the crack initiation site in (a) Palacos R and (b) Smartset HV, highlighting local deformation at the  $ZrO_2$ /matrix interface.

The results of the fatigue tests for all specimens in this study are given in Table 5-3 and Table 5-4. Consistent failure occurred within  $10^6$  cycles at a peak stress of 50 MPa for Palacos R and 60 MPa for Smartset HV. Dominant cracks were identified to initiate at voids in 4/8 failed Palacos R specimens and 2/5 Smartset HV specimens, as evidenced by the presence of discontinuous growth bands (Figure 5-7) or river lines running back towards the defect. Of the remaining specimens, either no dominant crack initiation site could be identified, or multiple crack initiation sites were found (Figure 5-10).

Table 5-3: Results of mechanical testing – Palacos R

Palacos R specimen no.	Stress (MPa)	Number of cycles to failure (Nf)	Largest void ESD	Largest ZrO <sub>2</sub> particle ESD	Dominant defect *
1	25	Run-out (2 million)	0.71	0.09	-
2	30	Run-out (2 million)	0.08	0.09	-
3	35	37 200	0.27	0.07	V
4	35	198 400	0.34	0.07	V
5	35	1 389 900	0.08	0.08	V
6	35	Run-out (1 million)	0.08	0.08	-
7	45	512 900	0.13	0.12	U
8	45	Run-out (1 million)	-	0.09	-
9	50	22 600	0.18	0.09	U
10	50	25 200	0.14	0.09	M
11	50	85 300	0.24	0.07	V
12	50	598 600	-	0.09	U

\* M – multiple initiation sites identified at voids and/or ZrO<sub>2</sub> particles; V – dominant crack initiation at a void; U – no initiating features identified.

Table 5-4: Results of mechanical testing – Smartset HV

Smartset HV specimen no.	Stress (MPa)	Number of cycles to failure (Nf)	Largest void ESD	Largest ZrO <sub>2</sub> particle ESD	Dominant defect *
1	50	2 200 000	0.20	0.08	M
2	60	67 400	0.20	0.08	V
3	60	114 900	0.21	0.11	V
4	60	323 000	0.26	0.08	M
5	60	349 300	0.26	0.09	M
6	60	Run-out (1 million)	0.23	0.10	-

\* M – multiple initiation sites identified at voids and/or ZrO<sub>2</sub> particles; V – dominant crack initiation at a void; U – no initiating features identified.

No correlation was found between the sizes of the largest microstructural features in a given specimen and the number of cycles to failure, in either Palacos R or Smartset HV cements. In general, the individual crack initiating voids could not be definitively identified from computed tomography data, due to their size and morphology (<100  $\mu\text{m}$  diameter, and irregularly shaped with polymeric material protruding from void surface). However, the crack-initiating voids in three Palacos R specimens were identified in the pre-test volumes; the characteristics of these defects are shown in Table 5-5.

Table 5-5: Characteristics of crack-initiating voids

Specimen type and no.	Stress (MPa)	Number of cycles to failure ( $N_f$ )	Defect ESD (mm)	Defect sphericity	Defect root projected area (mm)
Palacos R - 3	35	37 200	0.21	0.47	0.21
Palacos R - 4	35	198 400	0.34	0.36	0.29
Palacos R - 11	50	85 300	0.24	0.40	0.21

## 5.4 DISCUSSION

### 5.4.1 EFFECT OF MICROSTRUCTURE ON CRACK INITIATION PROCESSES

In this study, voids were found to be the most significant defect type by size and the only defects to occur at sizes larger than 0.124 mm ESD, *i.e.* in the range previously found to initiate fatigue cracks in CMW-1 (Chapter 4). Spatial densities of voids in this size range in Palacos R (0.1 per mm<sup>3</sup>) and Smartset HV (0.5 per mm<sup>3</sup>) were comparable to the frequency of BaSO<sub>4</sub> agglomerates found in CMW-1 (0.3 per mm<sup>3</sup>).

Smartset HV was considered to demonstrate superior fatigue strength compared to Palacos R in this study due to the higher peak stress required to consistently initiate failure within 10<sup>6</sup> cycles. There was significant scatter in fatigue life for Palacos R specimens, particularly at lower stress levels, which may be explained by the size distribution of voids observed for this cement formulation. Voids were present at longer length scales in Palacos R than Smartset HV, as evidenced in Figure 5-2 – Figure 5-4; however, these larger voids were sparsely distributed and were not present in all Palacos R specimens. At the lower stresses (< 40 MPa), failure was initiated within approximately 10<sup>5</sup> fatigue cycles only if voids of sufficient magnitude were present close to the specimen surface (Table 5-3).

This may be explained by the concept of the fatigue limit as the threshold stress for propagation of a crack, as discussed in section 2.3. According to the model of root projected area proposed by Murakami (2002), the stress intensity factor may be approximated as a function of the root area of a smooth contour encompassing both the crack and initiating defect. If large voids are present in the highly-stressed region of the volume, the stress concentration will be sufficient to initiate a fatigue crack and the combined root area of the void and crack will result in sufficient stress intensity for the crack to propagate. However, in the absence of large voids, crack initiation may occur from smaller voids or inclusions, but below the critical defect size the stress intensity will be insufficient for the crack to propagate and failure will not occur. The decrease in fatigue life scatter with increasing stress level is consistent with the findings of Yi *et al.* (2006) for fine microstructure nodular cast iron, which was attributed to the sensitivity of the material to crack initiation and the dependency on the presence of crack-initiating defects.

In all specimens found to have a single dominant fatigue crack, initiation occurred at a void. Although these voids were of varying sizes, all were found to have a low

sphericity and irregular morphology. Exposed polymer beads were evident on the interior surface of the voids, consistent with fluid contraction in the surrounding matrix during the polymerisation process. The presence of fibrils within the voids suggests ductile tearing and shrinkage of a pre-existing defect. In this sense, the mechanism for void formation and growth in Palacos R and Smartset HV may be akin to solidification cracking in metallic welds and castings (Grasso *et al.* 2002).

In both Palacos R and Smartset HV cements, the zirconium dioxide radiopacifier phase formed cauliflower-like agglomerates of particles that were typically smaller than 50  $\mu\text{m}$  diameter, consistent with observations of  $\text{ZrO}_2$  morphology in the bone cement literature (Ginebra *et al.* 2002). In addition,  $\text{ZrO}_2$  particles occasionally formed larger agglomerates (up to 0.12 mm ESD in Palacos R and 0.11 mm ESD in Smartset HV), though none of these agglomerates initiated dominant fatigue cracks. However, in the absence of larger microstructural defects, multiple crack initiation and coalescence was observed around  $\text{ZrO}_2$  particles in both cement types tested at higher stresses. The ratchet marks observed on the fracture surfaces of these specimens are consistent with the notion of multiple crack initiation occurring across regions of high stress where no dominant stress concentrations are present. The clinical relevance of this finding is unclear, as the highest stresses utilized in this study (50 MPa and 60 MPa for Palacos R and Smartset HV, respectively) are much greater than would be expected in the *in vivo* cement mantle, as previously discussed in Chapter 4.

The morphological characteristics of fatigue fracture surfaces identified in this study are in agreement with the observations of previous researchers for both experimental (Ginebra *et al.* 2002) and commercial (Harper and Bonfield 2000) cement formulations containing zirconium dioxide as a radiopacifier. Harper and Bonfield (2000) identified pull-out of  $\text{ZrO}_2$  particles and roughened fracture surfaces surrounding initiating voids in tensile fatigue specimens of Palacos R, attributing this phenomenon to slow fracture; towards the edge of the specimen, the surface was noted to be smoother.  $\text{ZrO}_2$  pull-out was also observed by Ginebra *et al.* (2002) on the fracture surfaces of compact tension specimens (width 23 mm, initial crack length 11.35 mm, loaded at a cross-head speed of 1 mm/min). In both these studies, specimens were hand-mixed, aged and then tested in air at room-temperature.

The frequency of zirconium dioxide particles at lower length scales (i.e. < 50  $\mu\text{m}$  diameter) was found to be strongly dependent on the resolution of the computed tomography data, as highlighted in Figure 5-5.  $\text{ZrO}_2$  particle populations were therefore

significantly underestimated when assessed at the voxel size of 8-12  $\mu\text{m}$  achieved using laboratory  $\mu\text{-CT}$ . One possible explanation for this discrepancy is the use of median filtering to reduce noise in the computed tomography data, combined with partial volume effects due to the large contrast in attenuation between the radiopacifier and polymer phases, as previously discussed (Section 3.5.2). This may have reduced the reliability of the segmentation process due to the close proximity of the radiopacifier to the voxel size; individual particles typically occupied only a few voxels in the computed tomography data. However, this discrepancy is less significant for  $\text{ZrO}_2$  particles with diameters greater than 50  $\mu\text{m}$  (*i.e.* the largest 1-2% of particles measured), and thus analysis at lower resolution is considered satisfactory in assessing the frequency of larger particles that may have the potential to initiate fatigue cracks.

Differences were noted in the void populations between cement specimens, which may be attributed in part to normal variation introduced during the specimen fabrication process (Lindén 1988). However, difficulties were encountered when segmenting voids in both Palacos R and Smartset HV specimens, due to the lack of contrast between the voids and surrounding polymer. This limitation was not found when segmenting voids in CMW-1 cement (Chapter 4) due to the presence of small particles of radiopacifier which increased the attenuation of the polymer matrix. This may account for the apparent absence of small voids in a number of Palacos R specimens. While this limitation must be acknowledged, it is not considered to reduce the confidence of the void population data for the largest voids within each specimen, nor for the crack-initiating void data given in Table 5-5.

#### 5.4.2 EFFECT OF CEMENT FORMULATION ON FATIGUE LIFE

This work adopted a 'data rich' approach for the investigation of microstructural aspects of fatigue failure in bone cement. The limited number of specimens involved, and the different stress levels at which accelerated fatigue testing was conducted, precludes quantitative comparison of the fatigue data between cement types in this study. Nonetheless, evaluation of the stress levels required to consistently initiate failure allows qualitative comparison of the effect of cement formulation on the fatigue life of the cement. Fatigue data for the cements tested in this chapter have been amalgamated with results of the CMW cements investigated in the preceding chapter in Figure 5-15, for ease of reference. The cement formulation containing barium sulphate

(CMW-1) demonstrated the lowest fatigue strength of all the formulations in this study, while Smartset HV, containing zirconium dioxide as the radiopacifier, had the highest fatigue strength.

The superior fatigue performance of Palacos R relative to CMW-1 is in agreement with the findings of an *in vitro* study by Harper and Bonfield (2000), in which tensile fatigue tests of a number of hand-mixed commercial formulations were conducted in air at room temperature, at a peak stress of 22 MPa; Weibull median fatigue lives for Palacos R and CMW-1 cements were reported to be 27,982 and 4,407 cycles respectively. In addition, data from the Swedish Hip Registry analysed by Espehaug *et al.* (2002) identified a similar pattern in the failure rates of cemented THR, adjusted for patient and surgeon characteristics; the ten year revision rate for aseptic loosening of implants fixed with Palacos R was 4.2%, compared to 9.4% for CMW-1.

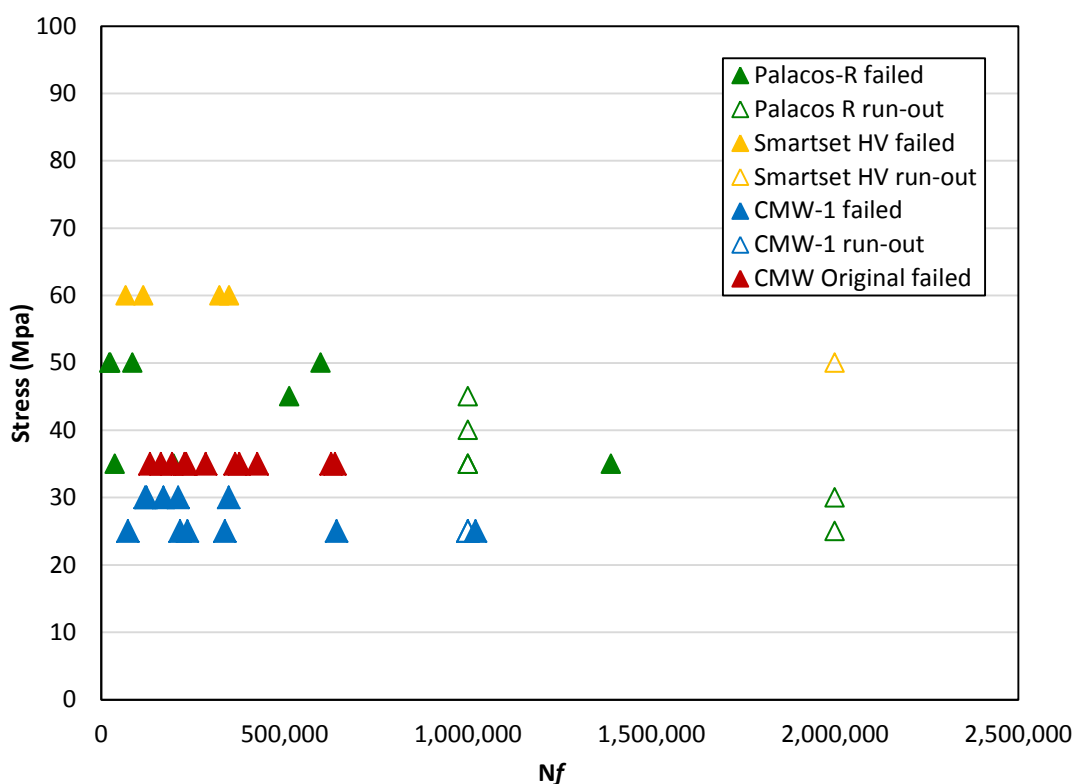


Figure 5-15: Fatigue test results for all failed specimens of all four cement formulations.

There are several possible explanations for the superior fatigue performance of Palacos R and Smartset HV compared to CMW-1 and CMW Original. The tendency of barium sulphate in CMW-1 to form agglomerates is clearly detrimental, as evidenced in Chapter 4; however, the crack-initiating behaviour of radiopacifier particles does not explain the difference between the zirconium-dioxide containing cements (Palacos R and Smartest HV) and radiolucent CMW Original.

Unlike the CMW cement formulations, in which the base polymer is PMMA, the predominant constituent of both the Palacos R and Smartset HV formulations is a P(MMA/MA) copolymer. In addition, the former cements are sterilised using gamma radiation, while the latter are sterilised using EtO gas. As a result, Palacos R and Smartset HV are expected to have significantly higher molecular weights (MW); a study by Kuehn *et al.* (2005a) reported MW values of approximately 270,000 g/mol for CMW-1, compared to 740,000 g/mol and 650,000 g/mol for Palacos R and Smartest HV respectively. The MW of the base polymer is known to affect the mechanical properties of the cement; in particular, higher MW is associated with a greater degree of polymer cross-linking and increased resistance to craze formation (Lewis & Mdlasi 1997), resulting in improved fatigue strength.

Despite higher molecular weight, both Palacos R and Smartest HV formulations are found to be more susceptible to creep than CMW-1; Liu *et al.* (2002) reported a higher creep rate for Palacos R compared to CMW-1, while Kuzmychov (2009) found no significant difference in the creep behaviour of Palacos R+G versus Smartset GHV (though both formulations contained Gentamicin). Certainly, visible deformation of Palacos R specimens was noted in the present study when specimens were loaded for in excess of 1 million cycles, which was attributed to creep. This may have had a beneficial effect on the fatigue performance of the cement, by creating a more favourable stress distribution. Verdonschot *et al.* (1997b) modelled the effect of creep on the cement mantle and found reduced stress at the cement-stem interface, while a similar simulation conducted by Waanders *et al.* (2010) reported that, at lower stress levels, cement creep reduced the incidence of fatigue cracks.

## 5.5 CONCLUSION

In this study, voids were found to be the dominant microstructural feature by size, and the controlling defect in terms of fatigue crack initiation. Considerable scatter in fatigue life was noted for Palacos R, attributed to the presence of occasional large voids (>0.27 mm ESD) with the potential to initiate fatigue cracks of sufficient stress intensity to propagate to failure. The ZrO<sub>2</sub> radiopacifier phase in Palacos R was typically coarser than in Smartset HV; 1.5 agglomerates per mm<sup>3</sup> in Palacos R and 0.7 per mm<sup>3</sup> in Smartset HV were found to exceed 50 μm diameter. The majority of ZrO<sub>2</sub> radiopacifier particles in both cement formulations were too small to be identified at a resolution of 10 μm. Multiple fatigue crack initiation and coalescence was identified from ZrO<sub>2</sub> agglomerates in both cement formulations in the absence of voids, but only at high applied stresses. At low stresses, it is anticipated that fatigue cracks may initiate at ZrO<sub>2</sub> agglomerates, but the stress intensity will be insufficient for the cracks to propagate to failure because the defects are below the critical size. Since bone cement *in vivo* is expected to operate in the low stress, high cycle regime *in vivo*, the presence of zirconium dioxide radiopacifier agglomerates at the length scales observed in this study is therefore not considered to be detrimental to the fatigue life of either cement formulation.

---

---

## 6. CHARACTERISATION OF POROSITY IN VACUUM-MIXED CEMENT

---

---

### 6.1 INTRODUCTION

The role of porosity in the mechanical performance of bone cement has been the focus of a large volume of literature, dating back over forty years to the pioneering work of Sir John Charnley. According to Ling and Lee (1998), Charnley himself believed porosity to be beneficial to the longevity of the cement mantle, and advocated maximum aeration of the cement mixture during the last thirty seconds of mixing in order to reduce the effect of shrinkage on the curing cement. However, subsequent *in vitro* mechanical testing (e.g. James *et al.* 1992) and examinations of explanted, hand-mixed cement (e.g. Jasty *et al.* 1991, Culleton *et al.* 1993, Topoleski *et al.* 1993) highlighted the role of voids in both rapid fracture and fatigue failure of the cement mantle. Furthermore, the practice of hand-mixing cement in open air was found to produce highly variable cement porosity, even between batches prepared by the same experienced operator (Lindén 1988). These findings led to the implementation of modern cementing techniques, including preparation of the cement under vacuum pressure using integrated mixing and delivery systems, in an effort to reduce porosity and improve the quality of the cement mantle.

Vacuum-mixing of cement has now been standard clinical practice for over ten years. Despite this, the effect of porosity and mixing method on fatigue failure of cement continues to be a source of discussion. *In vitro* testing has demonstrated that vacuum-mixing leads to an improvement in the mechanical properties of cement, including tensile and flexural strength (Lewis 1997), and results in a generally longer but more variable fatigue life (Lewis 1997, Lewis 1999b, Murphy and Prendergast 2000, Dunne *et al.* 2003). However, data from the Swedish Hip Registry indicates an increased risk of failure for vacuum-mixed cement mantles in the first 4-5 years after implantation (Malchau *et al.* 2000).

The effect of porosity on the fatigue life of the cement is likely to be dependent on the size, morphology and distribution of voids within the cement mantle (Murphy and Prendergast 2000, Dunne *et al.* 2003, Hoey and Taylor 2009). Vacuum-mixing has been found to decrease the overall porosity of *in vitro* cement coupons (Davies and Harris 1990, Wang *et al.* 1993, Lewis 1999b) but not of cemented constructs implanted into

cadaveric femurs (Messick *et al.* 2007), nor of specimens obtained from the nozzles of cement mixing stubs in theatre (Dunne *et al.* 2005). Moreover, there is disagreement regarding the effect of reduced pressure mixing methods on the size distribution of the largest voids within the cement: Lewis (1999b) found no difference between the numbers of macro-voids in hand-mixed vs. vacuum-mixed cement, while Wang *et al.* (1993) reported a reduction in frequency but an increase in the mean size of macro-voids when mixing pressure was reduced from 1 to 0.05 bar. Some uncertainty may be associated with the two-dimensional methods frequently employed to characterise cement porosity. Research by Cox *et al.* (2006) measured significantly higher porosity in cement specimens using radiography and microscopy in comparison to  $\mu$ -CT, concluding that imaging of a large proportion of each specimen would be required to reliably determine porosity.

The work presented in this chapter aims to characterise porosity in vacuum-mixed cement in terms of the size, morphology and spatial distribution of voids, using three-dimensional volume imaging and scanning electron microscopy of *in vitro* specimens prepared from four commercial cement formulations. By examining both moulded coupons and cement retained within the nozzles of vacuum-mixing systems, this study investigates potential mechanisms of void formation, focussing on the incidence of macro-voids and void clustering effects within the cement.

## 6.2 MATERIALS AND METHODS

### 6.2.1 MOULDED COUPONS FOR VOID POPULATION CHARACTERISATION

Specimens of all four cement types (CMW-1, CMW Original, Palacos R and Smartset HV), fabricated for the work described in Chapters 4-5, were used for this study. The central 10 mm sections of the specimens, corresponding to the distance between the inner four point bend rollers (Figure 6-1), were imaged as previously described (Section 3.4) using the CT acquisition parameters in Table 6-1. The resulting data was reconstructed and segmented using CT Pro Client 2008 (Nikon Metrology, Belgium) and VG Studio Max 2.1 (Volume Graphics GmbH, Germany), according to the method in Section 3.5. Bulk porosity values were calculated by dividing the number of voxels occurring within the threshold grayscale interval for voids by the total number of voxels in the cement volume. Additionally, the number of macro-voids (i.e. voids with a major axis length >1 mm approx.) present within the central section of each specimen was recorded. The void populations and macro-voids occurring in CMW-1 and CMW Original cement were then analysed further using Image J 1.41 (National Institutes of Health, USA) software to obtain quantitative data, including volume and sphericity, for individual voids.

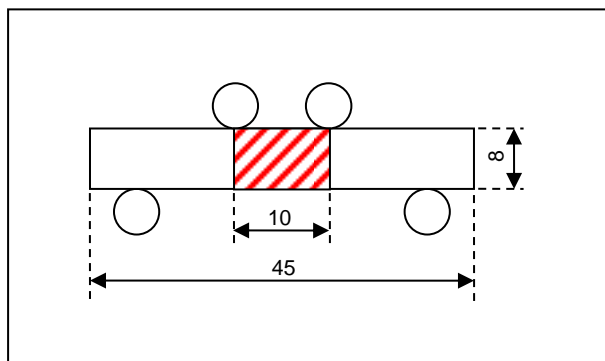


Figure 6-1: Schematic diagram of four-point bend specimen, highlighting central 10mm region of interest (shaded) for void population characterisation.

Table 6-1: CT acquisition parameters – moulded cement coupons

Cement	No. specimens	Scanner	Beam current ( $\mu\text{A}$ )	Accelerating voltage (kV)	Exposure time (ms)	No. projections	Voxel resolution ( $\mu\text{m}$ )
CMW-1	12	CT160Xi	98	86	2134	1905	8.6 – 10.9
CMW Original	7	CT160Xi	76	86	2134	1905	9.8
Palacos R	2	CT160Xi	98	86	2134	1905	8.3
Palacos R	4	HMX ST	90	100	2134	3142	12.3
Smartset HV	6	HMX ST	135	100	500	3142	10.2

### 6.2.2 MIXING GUN STUBS FOR VOID POPULATION CHARACTERISATION

Stubs from the nozzles of CemVac cement mixing systems (Depuy, Leeds, UK) were collected during fabrication of cement coupons for the four-point bend tests previously described. Two mixing stubs containing CMW Original cement, one stub containing Palacos R and one stub containing Smartset HV were collected. No mixing stub was available for CMW-1 cement as this study commenced after fabrication of CMW-1 cement coupons had been completed. The cement stubs were imaged using a CT 160Xi laboratory  $\mu$ -CT system (XTek systems, Tring, UK) according to the parameters in Table 6-2. Quantitative characterisation of void populations was then conducted as described above and in Section 3.5.

Table 6-2: CT acquisition parameters – cement gun stubs

Specimen type and no.	Accelerating voltage (kV)	Beam current ( $\mu\text{A}$ )	Exposure time (ms)	No. projections	Voxel resolution ( $\mu\text{m}$ )
CMW Original (1)	90	50	2134	1905	14.1
CMW Original (2)	90	50	2134	1905	14.1
Palacos R	90	50	2134	1905	11.6
Smartset HV	90	50	2134	1905	12.7

### 6.2.3 SPECIMENS CONTAINING LARGE VOIDS

Specimens of all cement types, fabricated for the characterisation and mechanical testing previously described in this thesis (Chapters 4 – 5), were screened using  $\mu$ -CT prior to inclusion in the aforementioned work. Specimens with very large voids ( $> 2$  mm diameter) were excluded from the previous studies due to the significant reduction in specimen cross-sectional area resulting from these voids. However, the excluded specimens were subjected to mechanical testing for the purposes of test rig alignment, and SEM examination of the resulting fracture surfaces is included in this chapter to allow qualitative investigation of different void morphologies and their potential effects.

## 6.3 RESULTS

### 6.3.1 CHARACTERISATION OF VOID POPULATIONS IN MOULDED COUPONS

All specimens were found to have some degree of porosity, although the size and spatial density of the voids differed even between specimens fabricated from the same charge of cement. The bulk porosity characteristics for the specimens of each of the four cement types are given in Table 6-1. Statistical analysis of these results using Welch's (unpaired, unequal variance) t-test indicates that only the difference in mean bulk porosity between CMW-1 vs. CMW Original and CMW-1 vs. Palacos R are significant at 95% confidence ( $p = 0.018$  and  $0.020$ , respectively). Smartset HV specimens demonstrated a higher mean porosity and greater variability than the other cement formulations, due to the presence of a very large defect in one specimen that accounted for  $\sim 2.5\%$  of the total specimen volume.

There was a bimodal aspect to void size distribution; while all specimens contained numerous small voids with diameters of a few microns, the majority of specimens also contained one or more very large, macro-voids. Examples of the global void populations in specimens of CMW Original cement with and without macro-voids are shown in Figure 6-2.

A comparison of the mean global void size distributions for two cement types (CMW Original and CMW-1) is presented in Figure 6-3. At the lower length scales, the spatial density of voids in CMW-1 cement specimens was far higher than in CMW Original cement. Peak void frequency occurred in the 0.012-0.027 mm ESD (1,001-10,000  $\mu\text{m}^3$ ) interval for CMW-1 and 0.027-0.058 mm ESD (10,001-100,000  $\mu\text{m}^3$ ) interval for CMW Original. As observed above, at the upper tail of the size distribution the largest voids present in the specimens had volumes greater than 1  $\text{mm}^3$ .

Table 6-3: Bulk porosity for each of the four cement types (8 x 8 x 10 mm sections).

Cement	No. specimens	No. specimens with macro voids	Mean % porosity	SD % porosity	Range % porosity
CMW-1	12	10	0.32	0.26	0.02 – 0.84
CMW Original	7	4	0.11	0.14	0.00 – 0.32
Palacos R	6	3	0.09	0.17	0.00 – 0.42
Smartset HV	6	3	0.60	0.92	0.09 – 2.48

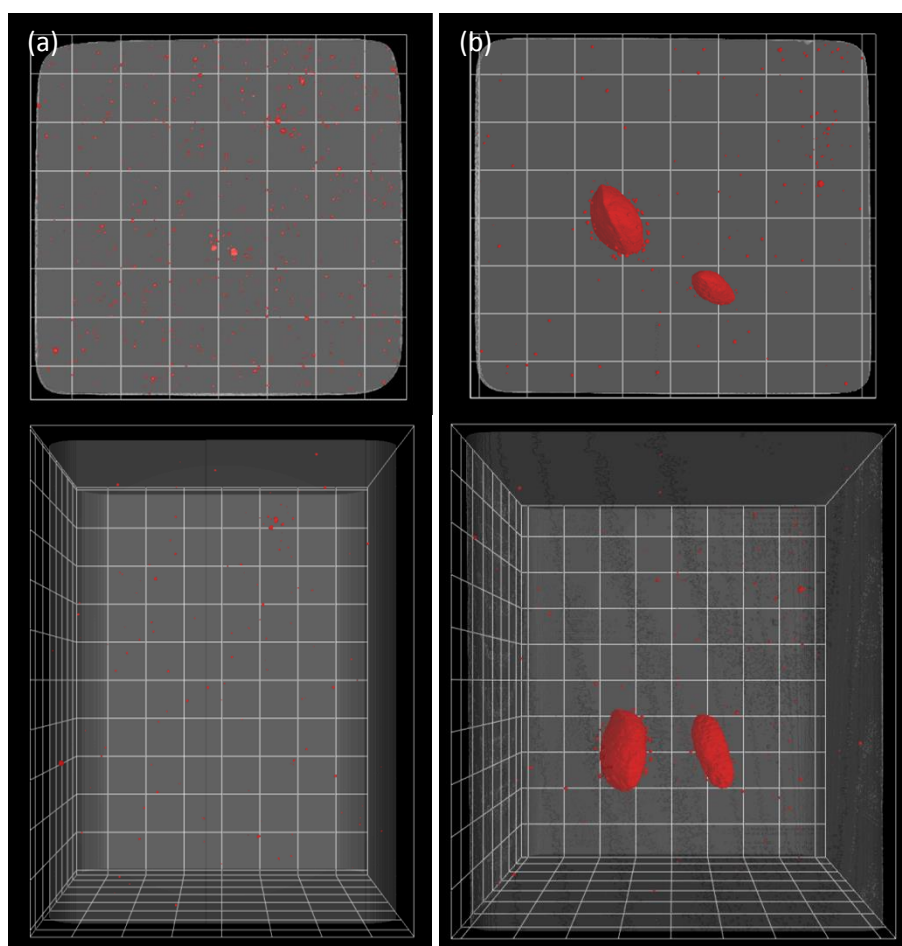


Figure 6-2: Examples of void distributions in CMW Original specimens: (a) specimen with 1.5 voids per  $\text{mm}^3$  and bulk porosity of 0.007%; (b) specimen with 0.5 voids per  $\text{mm}^3$ , bulk porosity of 0.289% and 2 macro-voids. The upper views are transverse, and the lower views longitudinal, with respect to the direction of injection of the cement into the moulds. Gridline spacing is 1mm.

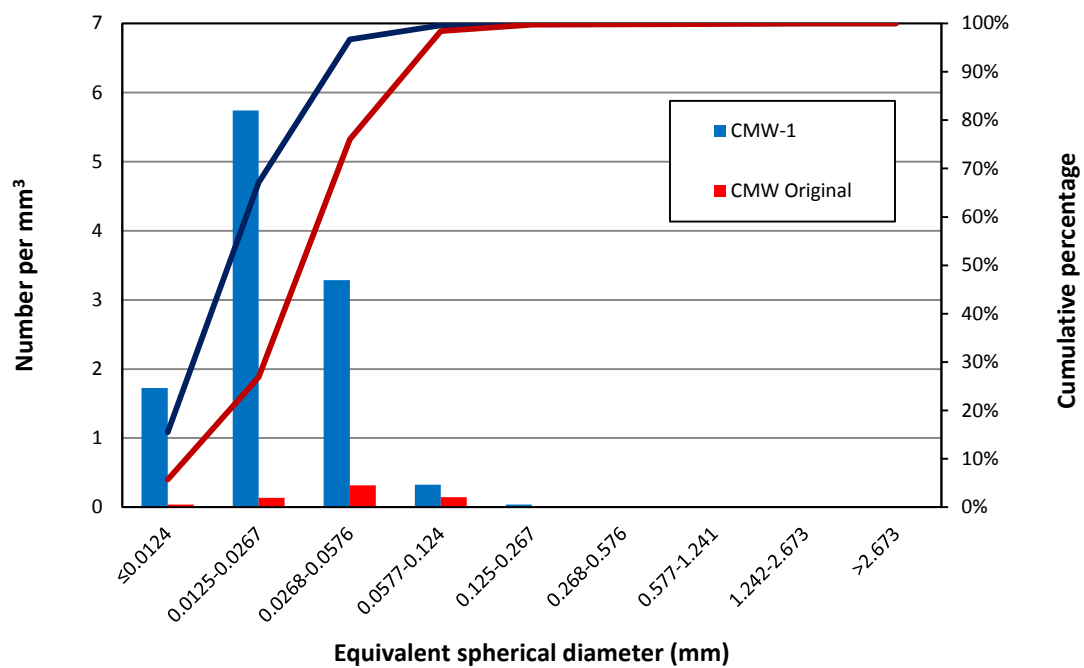


Figure 6-3: Mean size distribution of voids in 10mm sections of CMW-1 and CMW Original

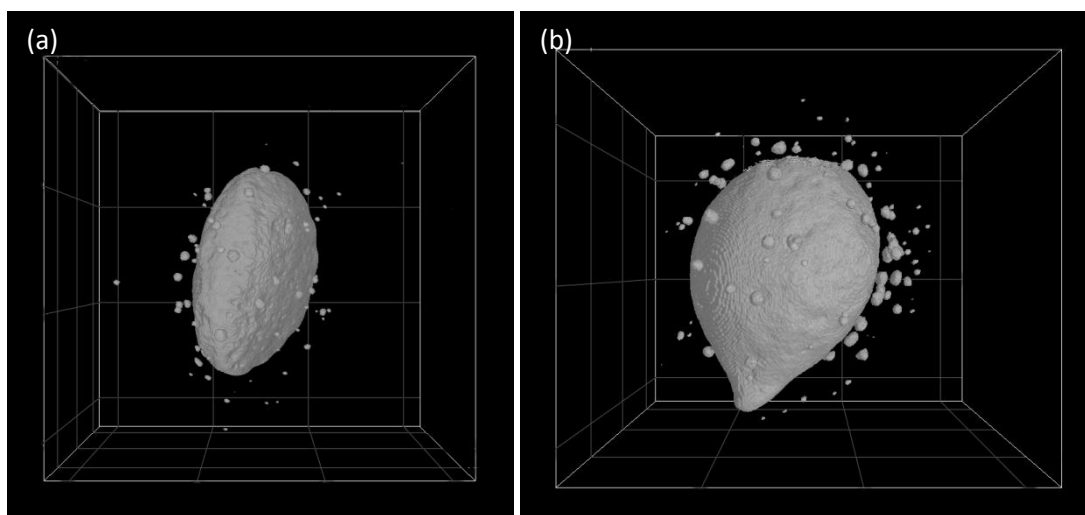


Figure 6-4: Example images of large voids in Palacos R cement with secondary satellite voids. Gridline spacing is 1mm.

The macro-voids were typically ellipsoidal, with a high degree of sphericity (mean value 0.81). Unlike the remainder of the void population, which was dispersed throughout the cement (Figure 6-2 (a)), the macro-voids were usually located towards the centre of the specimen (Figure 6-2 (b)). Furthermore, the major axis of each of these voids was usually oriented longitudinally (corresponding to the direction of injection of the cement into the moulds), and the voids often appeared to be flattened in the transverse direction (Figure 6-2 (b)).

In all cement types, macro-voids were often surrounded by clusters of smaller, satellite voids. A 'satellite' void was so classified if it was located within a bounding ellipsoid with dimensions double that of the primary macro-void. It should be noted, however, that this boundary was arbitrary, as the satellite voids were typically located very close to the surface of the primary void, and were easily distinguished from the surrounding global void population, as shown in Figure 6-4. The mean satellite void size across all cement types was 0.7 mm ESD (0.06 mm ESD and 0.08 mm ESD in CMW-1 and CMW Original cements, respectively). Even the satellite voids were therefore larger than the majority of the global void population (Figure 6-3).

The presence of satellite voids around a primary macro-void was found to be related to the size of the primary void; the 'cut-off' value for occurrence of secondary voids was approximately 0.5 mm ESD, and satellite voids were always identified for primary voids exceeding this size (Figure 6-5). In an attempt to elucidate the origin of satellite void formation, the relationship between the volume of the primary void and volume of surrounding satellite voids has been plotted for CMW Original and CMW-1, in addition to a simple exponential curve fit exhibiting an  $R^2$  value of 0.6 (Figure 6-6). There is evidence of increasing secondary void occurrence (by volume at least), although the fit is relatively poor for higher primary void sizes.

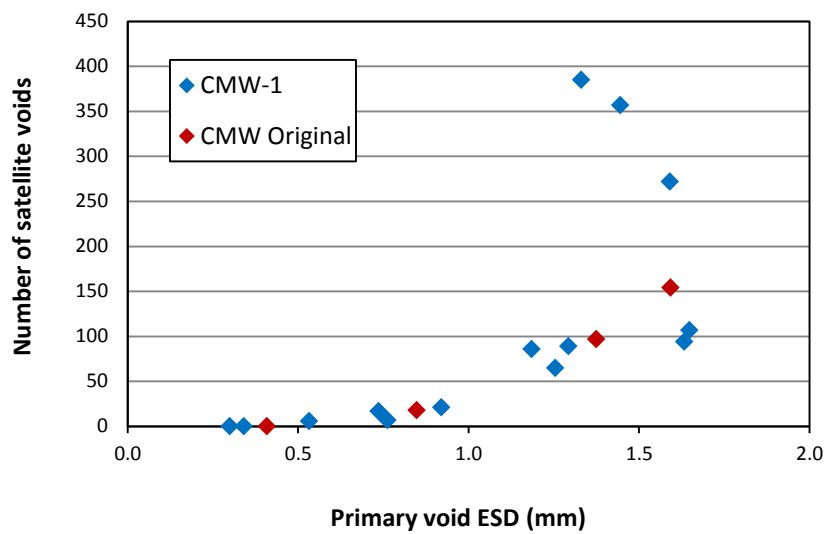


Figure 6-5: Relationship between the equivalent spherical diameter of the primary void and the corresponding number of satellite voids in CMW-1 (blue) and CMW Original (red).

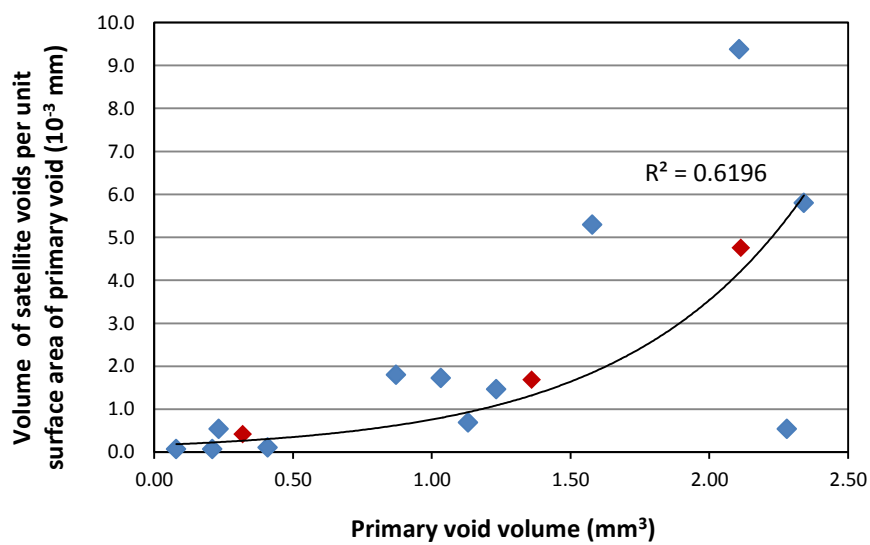


Figure 6-6: Relationship between the volume of the primary void and the total volume of surrounding satellite voids in CMW-1 (blue) and CMW Original (red).

## 6.3.2 CHARACTERISATION OF VOID POPULATIONS IN MIXING GUN STUBS

In order to assess the impact of injection and moulding of the polymer on the formation of macro-voids, the cement remaining in four of the mixing gun stubs was examined; the distribution of voids in each stub is shown in Figure 6-7. Large voids were evident in all stubs, located towards the centre of the specimens, and had a similar appearance to the macro-voids described in the previous section. Although secondary satellite void formation was seen in the CMW Original stubs, no satellite voids were evident in the Palacos stub, which contained multiple large voids representing nearly 40% of the total specimen volume (Table 6-4). Lines of large micro-voids were observed in both CMW Original cement stubs, but were not apparent in either the Palacos R or Smartset HV stubs, while the Smartset HV stub contained a large population of small micro-voids. With the exception of the top ends of the CMW Original 1 and Smartset HV stubs, which were open to the air, there was no indication of shrinkage of the cement away from the sides of the nozzle tubing; in addition, very little surface porosity was evident, unlike the moulded specimens (prior to polishing). These findings suggest that the curing cement was at least partly constrained by the mixing gun nozzles.

Table 6-4: Characteristics of void populations in cement stubs

Specimen type and number	% porosity	No. voids per mm <sup>3</sup>	Mean void ESD/mm	Mean void sphericity	Largest void ESD/mm	Largest void sphericity	No. voids per mm <sup>3</sup> >0.2 mm ESD
CMW Original (1)	1.8	1.5	0.05	0.80	2.64	0.76	0.03
CMW Original (2)	7.2	1.0	0.13	0.88	4.99	0.92	0.18
Palacos R	39.6	0.2	0.17	0.77	8.32	0.48	0.01
Smartset HV	6.3	4.5	0.07	0.78	4.39	0.68	0.09

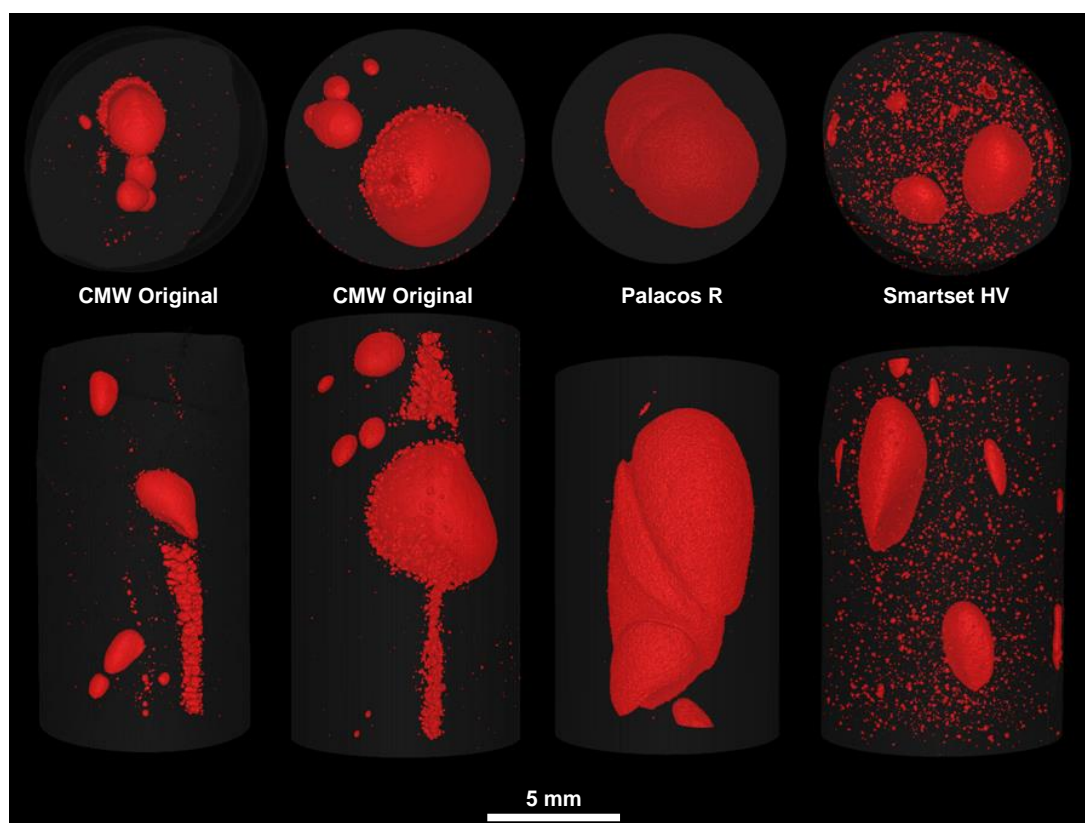


Figure 6-7: Distribution of voids (shown in red) in cement mixing gun stubs

Comparison of the bulk porosity values for CMW Original, Palacos R and Smartset HV in Table 6-3 and Table 6-4 reveals markedly higher percentage porosities in the cement stubs compared to the moulded specimens. Figure 6-8 shows the void size distribution data for the second CMW Original cement stub and the moulded specimens fabricated from the same charge of cement. While it is clear that the overall spatial density of voids in the cement stub is slightly higher (1.0 per  $\text{mm}^3$  compared to 0.6 per  $\text{mm}^3$  in the moulded specimens), the increased porosity in the cement stub is also attributable to the typically larger void size; the median ESD of the void population in the cement stub (0.085 mm) was found to be twice that of the voids in the moulded specimens (0.039 mm). It should be noted that, due to variation in the resolution of the  $\mu$ -CT data for the moulded specimens vs. cement stub, the cut-off value at the lower end of the size distribution has been adjusted in comparison to previous size distribution figures to prevent bias.

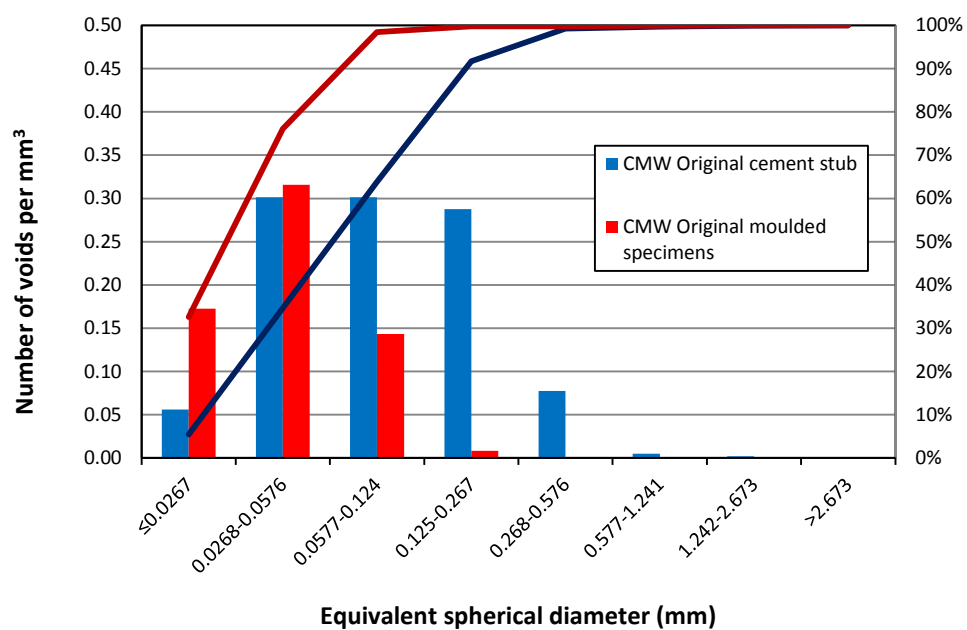


Figure 6-8: Mean size distribution of voids in cement stub and moulded specimens fabricated from one charge of CMW Original cement.

## 6.3.3 FRACTOGRAPHIC ANALYSIS OF VOID MORPHOLOGY

Voids identified on the fracture surfaces of cement specimens were classified into three types, according to their size and morphology:

- i. Type 1 voids were small (typically  $\sim 50 \mu\text{m}$  diameter) with an irregular shape and roughened surface (Figure 6-9);
- ii. Type 2 voids were also small, less than  $50 \mu\text{m}$  diameter, but very smooth and near-spherical in appearance (Figure 6-10);
- iii. Type 3 voids were much larger, from one hundred microns up to several millimeters in diameter, with pre-polymerised beads protruding from the interior surface of the voids (Figure 6-11). Type 3 voids in Palacos R and Smartset HV cement were bridged by intact and fractured fibrils, spanning the interiors of the voids.

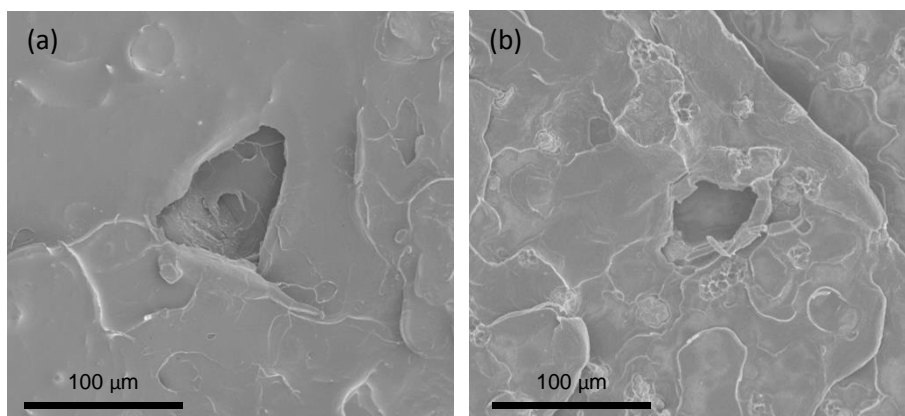


Figure 6-9: SEM micrographs showing examples of type 1 voids in (a) CMW Original and (b) Palacos R.

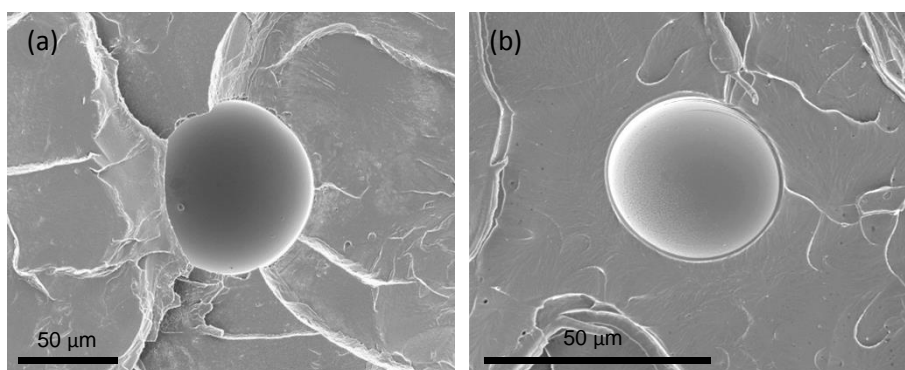


Figure 6-10: SEM micrographs showing examples of type 2 voids in CMW Original.

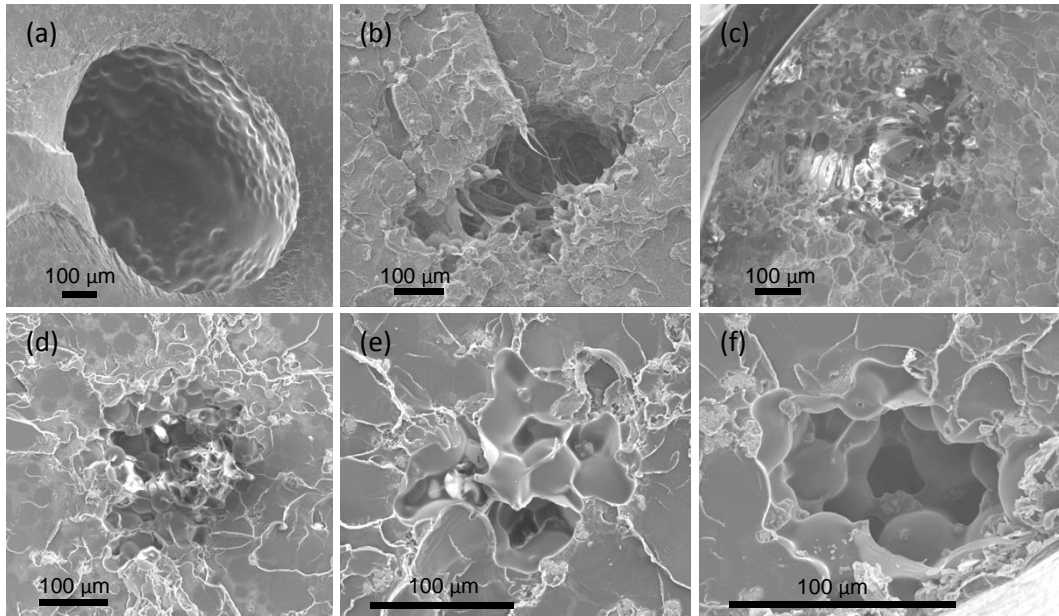


Figure 6-11: SEM micrographs showing examples of type 3 voids in (a) CMW-1, (b-d) Palacos R and (e-f) Smartset HV.

Four specimens containing large, non-surface breaking macro-voids were fatigue tested to failure at the same peak stress as other specimens of the same cement type (Chapters 4 – 5). The number of cycles recorded before failure occurred was found to be an order of magnitude lower than expected for an intact specimen (i.e.  $10^5$  cycles). Secondary ‘satellite’ voids, as noted in the  $\mu$ -CT data described in the previous section, were identified in the vicinity of the larger type 3 voids on the cement fracture surfaces (Figure 6-12 and Figure 6-13). Regardless of cement type, crack initiation in all four specimens was found to have occurred in the vicinity of these satellite voids; one such example is given in Figure 6-13, evidenced by a ‘halo’ region of relatively flat, early crack growth, as previously mentioned in Chapter 4.

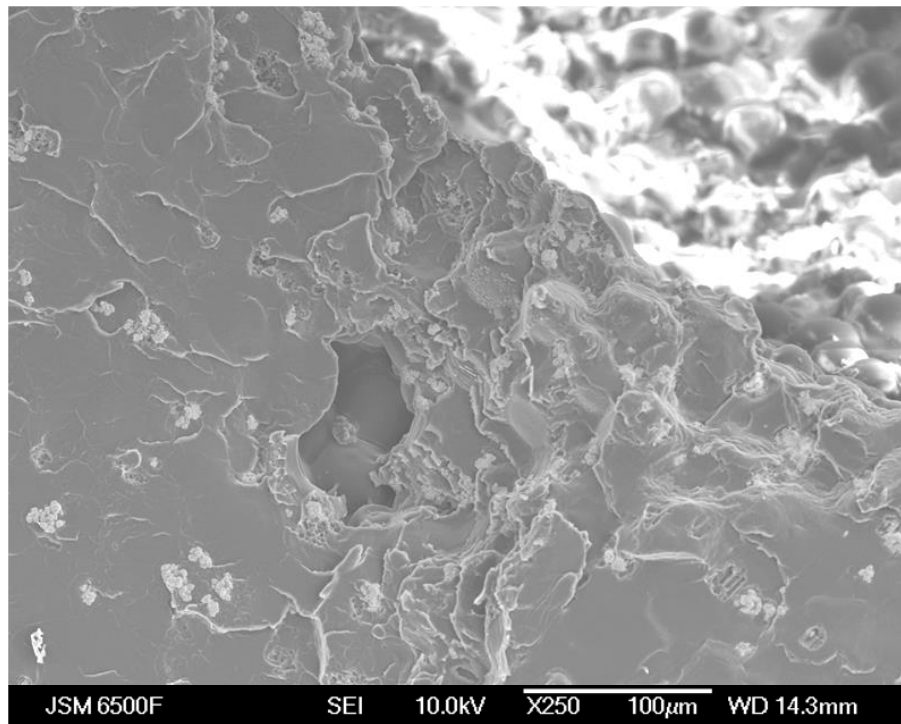


Figure 6-12: Type 1 satellite void in the vicinity of a large type 3 void in Smartset HV.

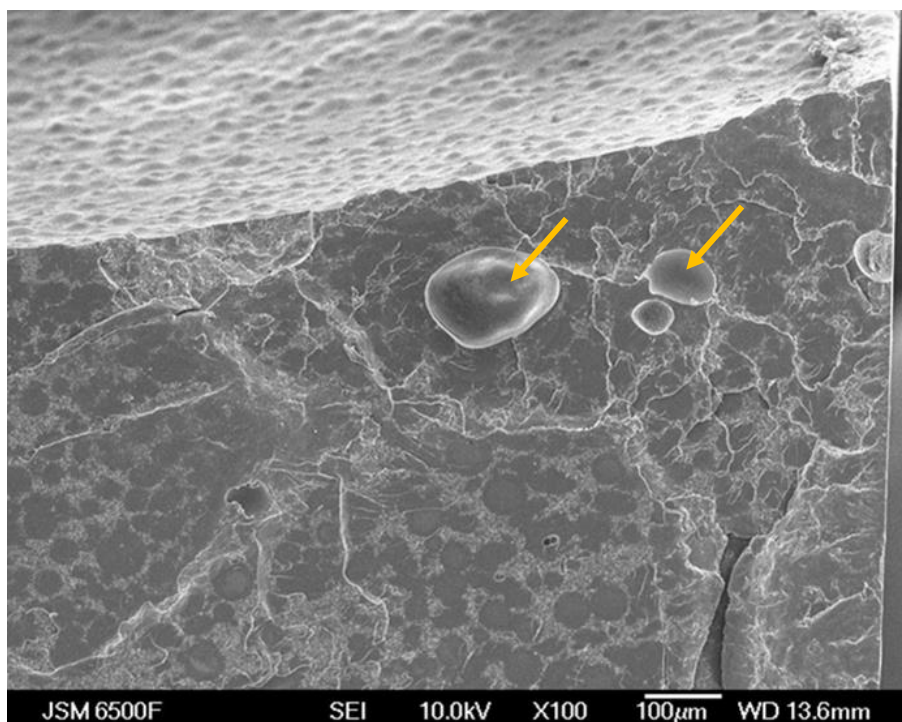


Figure 6-13: SEM micrograph showing crack initiation from type 2 satellite voids in CMW-1.

## 6.4 DISCUSSION

Mean bulk porosity values for the moulded cement specimens ranged from 0.09 to 0.60%; the highest mean porosity was found in Smartset HV cement and the lowest in Palacos R, two cements with similar formulations. These bulk porosity values are similar to the findings of Cox *et al* (2006) who measured 0.11% porosity in CMW-3 and Endurance cements using  $\mu$ -CT, but less than the 1-5% porosity reported by Hoey and Taylor (2010) in a micro-tomographic study of vacuum-mixed Simplex. In addition to variation in mixing system and operator, this difference may be due in part to the practice of polishing to remove surface porosity employed in this work: Messick (2007) identified mean area porosity of 1.4% in sectioned cemented constructs, but this was reduced to 0.8% when porosity at the interfaces was discounted.

Porosity in the moulded specimens was found to be bi-modal – specimens typically contained a few large macro-voids, and many smaller voids. Previous studies have classified bone cement porosity according to the length scale of the voids (Lewis 1997), identifying both macro-porosity (voids >1 mm diameter) and micro-porosity (voids >1mm diameter). In the present work, the size and incidence of macro-voids in the moulded cement specimens is consistent with the findings of other researchers for vacuum-mixed cement. Wang *et al.* (1993) identified 0.6-1.8 macro-voids per cm<sup>3</sup> in Palacos R with a median diameter of 1.88 mm<sup>2</sup>, while a later study by the same research team (Wang *et al.* 1996) reported 1.0±0.5 macro-voids in Palacos R mixed using the CemVac mixing system; both studies involved injection of cement into thin cylindrical moulds. Difficulty arises, however, because the largest voids occurring in the moulded specimens analysed in the present work were found to be ellipsoidal and thus, although the major axis length exceeded 1 mm, the equivalent spherical diameter of these voids was often smaller than 1 mm. The classification of these voids as macro- or micro-voids using radiography, as employed by previous researchers (Davies and Harris 1990, Wang *et al.* 1996, Lewis 1999b, Kurtz *et al.* 2005) would therefore depend on the orientation of the specimen relative to the imaging plane. As similarities exist between the largest micro-voids (> 100  $\mu$ m) and the macro-voids (> 1 mm) observed on the cement fracture surfaces and in the  $\mu$ -CT data, it is perhaps more useful to consider cement porosity in terms of both the size and morphology of the voids, using the three void types defined in the previous section.

Type 3 voids evident on the cement fracture surfaces of CMW-1 in this study are consistent with large voids on the fracture surfaces of both hand- and vacuum-mixed

Cemex Rx (Murphy and Prendergast 2000) and hand-mixed Simplex P (James *et al.* 1992, Kurtz *et al.* 2005)<sup>1</sup>. Type 3 voids on the fracture surfaces of Palacos R and Smartset HV, additionally characterized by the presence of polymer fibrils within the voids, are similar in appearance to micro- and macro-voids observed in hand- and vacuum-mixed Palacos R (Dunne *et al.* 2003). The irregular morphology of these voids at the micro-scale, with polymer beads protruding from the interior surfaces of the voids, is likely to create a geometric stress concentration that will facilitate crack initiation: the voids featured in Figure 6-11 (b)-(f) were all identified as crack-initiating defects (Chapter 5), while Murphy and Prendergast (2000) and Sinnott-Jones (2005) both reported fatigue crack initiation occurring at the interface between two or more pre-polymerised beads on the surface of a void.

Type 3 voids with equivalent spherical diameters greater than 0.5 mm were surrounded by clusters of smaller, satellite voids, which were also found to initiate fatigue cracks. If this pattern is replicated in the clinical cement mantle, the satellite voids are likely to be significant stress raisers and potential key sites for fatigue crack initiation, as they occur at distances far smaller than one radius from the surface of the primary void and may reasonably be expected to further multiply the local stress concentration around the large void. To the author's knowledge, there has been no prior reporting in the literature of the phenomenon of satellite void formation in bone cement; though a similar clustering effect can be observed in the  $\mu$ -CT data of Hoey and Taylor (2009). However, clusters of voids have been observed to facilitate fatigue crack initiation in bone cement (Murphy and Prendergast 2000, Hoey and Taylor 2009), while James *et al.* (1992) reported an increase in the number and size of fatigue cracks initiating from small voids in the vicinity of a large void, than from the large void alone.

Dunne *et al.* (2005) examined cement mixing gun stubs prepared by theatre nurses and extrapolated these findings to cement porosity in the clinical cement mantle. However, in the present work poor agreement was noted between the porosity characteristics (particularly bulk porosity and void size) of the moulded specimens and cement stubs. The porosity characteristics of residual cement extracted from mixing equipment is not considered to be a reliable indicator of the quality of the cement mantle; examination of explanted cement mantles, rather than mixing gun stubs, is therefore recommended before conclusions can be drawn regarding the effect of vacuum mixing on cement porosity *in vivo*.

---

<sup>1</sup> Cemex Rx (Tecres, Verona, Italy) and Simplex P (Stryker Orthopaedics/Howmedica, New Jersey) are both medium viscosity cement formulations, containing BaSO<sub>4</sub> as the radiopacifier phase.

The use of high resolution, three-dimensional volume assessment in this study allowed imaging of features such as satellite voids that may not have been detected using two-dimensional methods. Indeed, other researchers have measured the number of macro-voids by examination of plane radiographs (Davies and Harris 1990, Wang *et al.* 1996, Lewis 1999b, Kurtz *et al.* 2005, for example); however, in this study, macro-voids were detected in the  $\mu$ -CT data that were not apparent on a single x-ray projection, particularly if the voids were flattened in the longitudinal direction, as seen in Figure 6-2. While radiography may be useful for comparative purposes (e.g. Wang *et al.* 1996), the accuracy of this method for determining the macro-porosity of the cement mantle is therefore considered to be limited.

The bi-modal void size distribution and distinct void morphologies may be accounted for by considering the possible mechanisms of void formation in the curing cement. Several such mechanisms have been cited for the formation of voids in bone cement (Lewis 1997): air present in the constituents prior to mixing, entrapment of air during wetting of the powder, entrapment of air during the mixing phase and evaporation of the monomer. In addition, volumetric shrinkage of the cement due to polymerisation occurs during the curing process, with the amount of shrinkage being dependent on the cement formulation; Palacos R, for example, has been reported to undergo significantly higher volumetric shrinkage than CMW-1 (Kwong and Power 2006).

A void classification methodology has been described by Scheirs (2000) for industrial injection mouldings; large, non-spherical voids with rough inner surfaces (i.e. type 3 voids) were attributed to shrinkage and under-filling of moulds, while smaller, spherical voids with smooth inner surfaces (i.e. type 2 voids) were considered to have resulted from entrapment of air and/or evaporation of residual monomer. While under-filling of moulds may have been a potential source of porosity in this study, the presence of macro-voids in both the cement stubs and moulded specimens suggest that the voids were inherent in the cement dough prior to injection into the moulds. The appearance of exposed PMMA beads on the interior surfaces of the type 3 voids is consistent with fluid contraction in the surrounding matrix during the polymerisation process; furthermore, the irregular morphology and presence of fractured fibrils within some of these voids suggest tearing and shrinkage of a pre-existing defect. In this sense, the mechanism for the formation of type 3 voids may be akin to solidification cracking in metallic welds and castings (Grasso *et al.* 2002) as mentioned in the previous chapter.

It has been observed that, if the cement is cured under certain conditions of external constraint, void expansion may occur during polymerisation (Gilbert *et al.* 2000, Orr *et al.* 2003 and Muller and McCaskie 2006). The experiments of Gilbert *et al.* (2000) demonstrated that a small void in the centre of a polymer block may grow to form a much larger void, and that this phenomenon is more pronounced for vacuum-mixed cement due to the reduced void population. In the present study, the plastic nozzle of the cement gun may act to constrain the polymerising cement in a similar manner. This is evidenced by the lack of shrinkage of the cured cement away from the sides of the gun nozzle observed in the  $\mu$ -CT scans, and the absence of surface voids on the cement gun stubs despite frequently being observed on the surfaces of the moulded specimens. The very large voids and high percentage porosity found in the cement gun stubs may therefore be due to the expansion of existing smaller voids during polymerisation, as the cement cures first at the outer edge and the polymerisation front proceeds towards the centre of the stub.

The mechanism for this void growth is not fully understood. Gilbert *et al.* (2000) proposed that void expansion occurs due to volumetric polymerisation shrinkage of the cement, and correlated their experimental results with theoretical predictions based on conversion of monomer to polymer. However, Muller and McCaskie (2006) found a clear relationship between the void volume and peak polymerisation temperature. They postulated that, in a partially constrained human femoral model, the dominant force promoting void expansion is the evaporation of residual monomer across the internal interfaces of existing voids, which result in temperature dependent high peak intra-void pressures. Void expansion is further promoted by thermal expansion of trapped air and polymerisation shrinkage. According to this theory, void expansion is controlled by the pressure gradient between the void and atmosphere, and by the compliance of the polymerising cement. Regardless, void expansion due to constrained polymerisation is one possible explanation for the difference in porosity observed both between individual cement stubs, and between the moulded specimens and cement stubs prepared from the same charge of cement.

It is hypothesised that formation of satellite voids may also occur due to pressure gradients in the cement during polymerisation. When the compliance of the cement surrounding a primary void becomes too low, and further void expansion is resisted, the rapid rise in intra-void pressure may force trapped air or residual monomer into the surrounding cement to form small gas voids. This is evidenced by the occurrence of satellite voids for all primary voids exceeding a critical size, the uniform spherical

appearance of the satellite voids and the regular spacing between the primary and satellite voids. It is proposed that the mechanism of formation of satellite voids could be investigated using optical microscopy and high-resolution videography to image the process of cement polymerisation in real time. Gilbert *et al.* (2000) conducted a similar study into the effect of constraint and mixing method on the formation of shrinkage voids by taking a series of photomicrographs of the curing cement at defined time intervals. It is suggested that, for ease of imaging, a plain translucent cement formulation such as radiolucent CMW Original should be used for this study; the cement should be mixed under vacuum according to the manufacturer's instructions, and then either retained in the cement gun nozzle or injected into a rigid, translucent mould. The effect of primary void size on satellite void formation may be explored further by injecting different quantities of air into the cement during the dough phase, in order to artificially create voids.

The 'data rich' approach of this study necessitated analysis of a limited number of specimens, due to both time and machine constraints. The moulded specimens were fabricated from one batch each of CMW Original and Smartset HV cement, and two batches each of CMW-1 and Palacos R, while cement stubs were collected from two charges of CMW Original cement, one Palacos R and one Smartset HV. As such, intra-batch variation in porosity cannot be taken into account, and thus any differences in porosity noted between cement formulations, particularly with regard to the cement stubs, should be interpreted with this in mind.

The cement constituents were pre-chilled prior to mixing. This practice is recommended for vacuum-mixed Palacos R (according to the manufacturer's packaging insert), but was conducted for all cement formulations to improve the handling characteristics of the cement (i.e. reduced viscosity and increased working time). While Lewis (1999b) reported no significant difference in either porosity or fatigue life for Palacos R cement prepared with pre-chilled vs. room temperature constituents, the effect of pre-chilling on porosity in other formulations is unknown. Furthermore, the specimens were cured at room temperature in air, reducing the rate of the polymerisation reaction in comparison to the clinical scenario and eliminating the inclusion of blood and debris in the cement, which is potential source of porosity *in vivo*.

This work investigated the porosity characteristics of cement prepared with one type of vacuum-mixing system (CemVac, Depuy CMW, Blackpool, UK). Several authors have

reported differences in cement porosity when a range of mixing systems are used (Wang *et al.* 1996, Dunne *et al.* 2003, Mau *et al.* 2004, for example); further research is therefore required before firm conclusions can be drawn regard the applicability of these findings to cement prepared using all available vacuum-mixing systems.

## 6.5 CONCLUSION

This study has corroborated previous research regarding the presence and frequency of large macro-voids in vacuum-mixed bone cement. In addition, the formation of secondary satellite voids around defects exceeding 0.5 mm ESD has been noted. These satellite voids are stress raisers and potential fatigue crack initiation sites, and may therefore exacerbate the effect of macro-voids on the fatigue life of the cement. The occurrence of macro-voids in mixing gun stubs, in addition to moulded cement specimens, suggests that this porosity is inherent in the cement prior to injection; current vacuum-mixing systems may therefore be inefficient for the purpose of reducing porosity and improving the quality of the cement. Further research is needed to ascertain whether: (a) the formation of satellite voids is common to all cement formulations and mixing systems; and (b) the formation of satellite voids occurs *in vivo* and is detrimental to the longevity of the cement mantle.

---

---

## 7. FATIGUE PROCESSES IN THE *IN VIVO* CEMENT MANTLE

---

---

### 7.1 INTRODUCTION

Aseptic loosening remains the predominant cause of failure in cemented total hip arthroplasty (NJR 2012). One factor implicated in the loosening process is damage accumulation due to initiation and coalescence of fatigue micro-cracks within the cement mantle and at its interfaces with the stem and bone (Jeffers et al. 2007, Race et al. 2011, for example). A greater understanding of the micromechanical aspects of this failure process is required to enable the development of the next generation of cements and cement mixing systems, in order to improve the mechanical performance of the cement *in vivo* and thus increase the longevity of cemented constructs. In addition to *in vitro* interrogation of cement specimens, examination of *ex vivo* cement is necessary so that *in vivo* failure mechanisms can be identified with confidence. This knowledge is also vital for the validation of existing pre-clinical tests for bone cement, or the development of new test regimes that more accurately represent the clinical situation, and can identify potential weaknesses in the cement before it is adopted for clinical use.

There is limited published work on micromechanical aspects of failure in retrieved cement mantles. Existing literature is mostly aged (20 years old) and concerns hand-mixed cement (Topoleski *et al.* 1990, Jasty *et al.* 1991, Culleton *et al.* 1993), even though the use of vacuum-mixing techniques to minimise porosity has been standard clinical practice for a number of years. The effect of vacuum mixing on *in vitro* mechanical properties has been extensively researched (see Lewis 2003, Dunne *et al.* 2003, for example) but there is limited *ex vivo* data to validate these results, presumably due to the ethical and logistical difficulties associated with obtaining and examining patient-retrieved implants. This has led to controversy concerning the clinical benefits, or otherwise, of vacuum mixing to reduce porosity and improve longevity of the cement mantle (Ling and Lee 1998, Janssen *et al.* 2005a), as previously discussed in Chapter 6.

The aim of this study was to investigate the microstructural defect populations and fractographic characteristics of an *ex vivo* cement specimen using the experimental techniques developed in Chapters 4-6. The results of this analysis are compared with

the micromechanical characteristics of failure of a similar commercial cement brand (Palacos R) prepared and tested under *in vitro* fatigue loading conditions.

## 7.2 MATERIALS AND METHODS

One specimen of explanted cement was retrieved from a 51 year old female patient with hip dysplasia, undergoing revision total hip arthroplasty surgery due to pain and elevated serum metal ion concentration associated with a large diameter hybrid metal-on-metal articulation (Bolland *et al.* 2011). Time *in vivo* was 7 years. The femoral implant was a collarless, polished tapered cobalt chrome stem (CPT, Zimmer, Warsaw, Indiana), shown in Figure 7-1 (a), fixed with antibiotic radiopaque acrylic bone cement (Palacos R + G, Heraeus Medical GmbH, Hanau, Germany). No loosening of these components was reported. Permission for the collection and analysis of the retrieved cement was granted by the NRES Committee South Central – Southampton A.

The retrieved cement specimen dimensions were 10.5 mm (width) x 9.5 mm (breadth) x 21.8 mm (length) with a volume of 0.92 cm<sup>3</sup>. The location and orientation of the specimen within the cement mantle were not recorded at the time of retrieval. However, due to the thickness and curvature of the specimen, combined with the known geometry of the femoral stem, this cement fragment most likely originated in the proximo-medial region of the cement mantle, corresponding to Gruen zone 7 (Gruen *et al.* 1979), as indicated in Figure 7-1 (b). The cement-stem and cement-bone interfaces were clearly identifiable due to the presence of a smooth profile and biological debris respectively; the specimen was therefore believed to encompass the full thickness of the cement mantle.

Micro-computed tomography imaging of the retrieved cement was conducted using a 225kV HMX-ST system (Nikon Metris, Tring, UK) at a voxel size of 13 μm<sup>3</sup>. Internal (non surface-breaking) voids were segmented from the reconstructed volume using a grey value thresholding technique, as previously described (Section 3.5). Due to the irregular shape of the specimen, the boundaries of surface-breaking voids could not be reliably determined; thus only internal voids were included in the defect characterisation in this study.

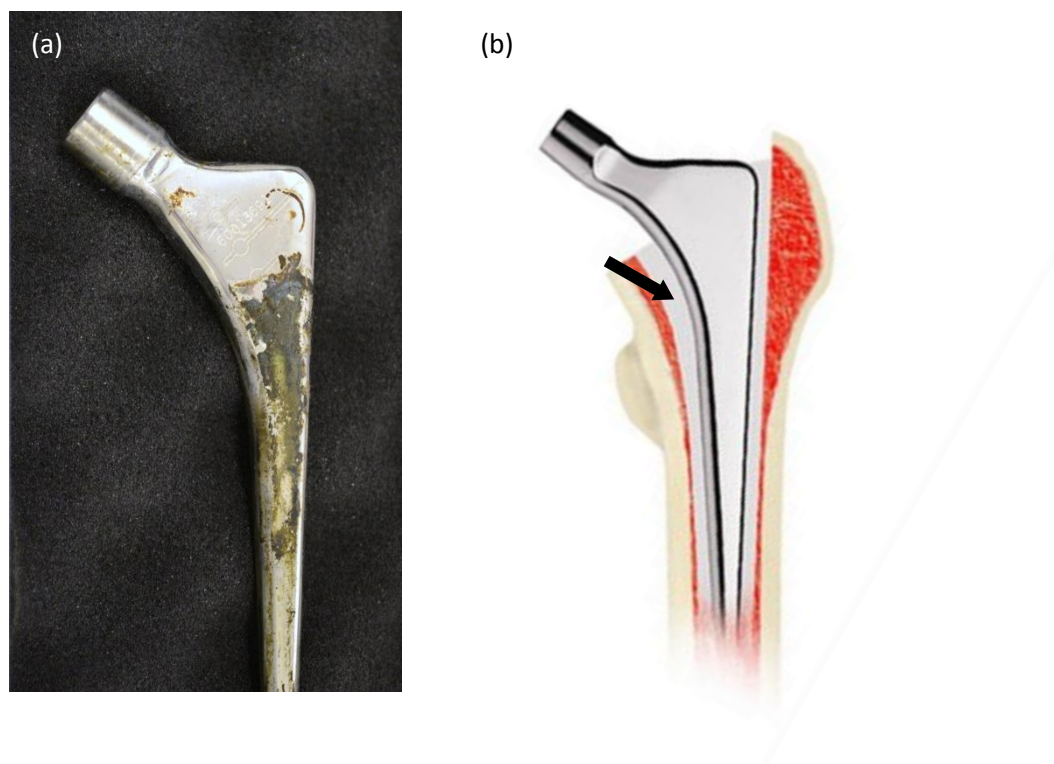


Figure 7-1: (a) Zimmer CPT® femoral stem retrieved at revision; (b) schematic diagram of a cemented Zimmer CPT® Primary Hip construct, indicating likely origin of retrieved cement specimen.

CT data indicated the presence of a major internal crack, extending lengthwise through the specimen and approximately perpendicular to the cement-stem interface, as shown (Figure 7-2). The visible length of this crack was 9 mm. To facilitate fractographic analysis, the crack was opened fully and the cement separated into two parts using the following method: first, the specimen was placed in distilled water in an ultrasonic bath at 21°C for 20 minutes to remove loose biological debris; the specimen was then cooled rapidly by immersion in liquid nitrogen for 2 minutes, removed and impacted with a sharp chisel at the surface opening of the crack, revealing the fracture surfaces. Low temperature separation was used in order to minimize the force required for crack propagation and to facilitate distinction between *in vivo*- and *ex vivo*- derived fracture surfaces.

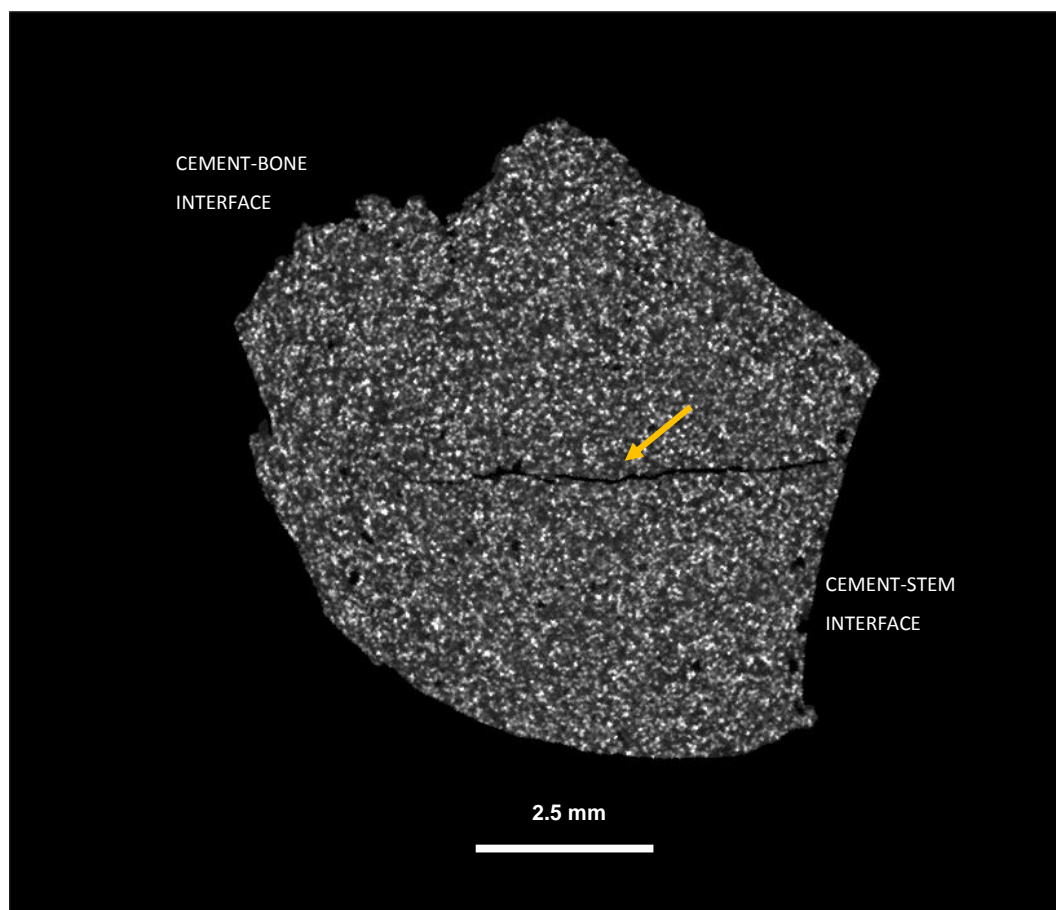


Figure 7-2: CT slice through width of retrieved cement specimen (*i.e.* transverse view). The arrow indicates the location of the main pre-existing crack.

*In vitro* fracture surfaces were prepared for comparison using Palacos R cement (Heraeus Medical GmbH, Hanau, Germany). The compositions of Palacos R and Palacos R+G are given in Table 7-1; the primary distinction between the two formulations is the addition of 2% gentamicin sulphate to Palacos R+G. The cement components were pre-chilled at 4°C prior to mixing under reduced pressure (-70 KPa) using a CemVac integrated mixing and delivery system (Depuy, Leeds, UK), according to the manufacturer's timings. Rectangular bend bars, each measuring 8 x 8 x 45 mm, were fatigue tested to failure under sinusoidal four-point bending at a peak stress of 40 MPa, R-ratio of 0.1 and frequency of 3Hz, according to the method described in Section 3.3.

Both *ex vivo* and *in vitro* fracture surfaces were sputter-coated with a thin layer (~15 nm) of gold and imaged using a JEOL JSM6500F FEG-SEM, in SEI mode at an accelerating voltage of 5-10 kV.

Table 7-1: Composition of Palacos R and Palacos R+G cements

	Palacos R*	Palacos R+G <sup>†</sup>	
<b>Powder</b>	Poly(methyl acrylate, methyl methacrylate)	84.5	82.15
	Zirconium dioxide	14.75	15.01
	Gentamicin sulphate	-	2.06
	Benzoyl peroxide	0.75	0.78
	Chlorophyll	200 ppm	0.002
<b>Liquid</b>	Methylmethacrylate	97.87	97.98
	NN-dpt	2.13	2.02
	Chlorophyll	267 ppm	0.002
	Hydroquinone	64 ppm	75 ppm

Values given as % (w/w), unless otherwise stated. \* Manufacturer's package insert; <sup>†</sup>Lewis 2009.

## 7.3 RESULTS

### 7.3.1 DEFECT POPULATION CHARACTERISATION

The retrieved cement was found to have a similar microstructure to laboratory-prepared cement specimens containing zirconium dioxide (shown in Figure 5.1); at the specified resolution ( $13 \mu\text{m}^3$ ) pre-polymerised beads were not distinct from the surrounding polymer matrix, though both large and small voids and small agglomerates of radiopacifier particles (*i.e.*  $>100 \mu\text{m}$  diameter) were evident in the CT data.

A CT reconstruction of the intact cement specimen is shown in Figure 7-3 (a), highlighting the cement-bone and cement-stem interfaces. Based on the assumed location of the retrieved cement, the width, length and breadth of the specimen are considered to correspond approximately to the dimensions along the medio-lateral, proximo-distal and antero-posterior axes respectively; the main crack bisects the specimen approximately in the coronal plane. The definitions of these anatomical terms are given in Appendix C.

Figure 7-3 (b) highlights the distribution of voids within the retrieved cement specimen. Some directional void clustering was observed along the length of the specimen. Voids were concentrated at the cement-stem interface (Figure 7-3 (c)), and appeared to be of a relatively consistent size ( $\sim 0.1 \text{ mm ESD}$ ) and even distribution along the length of this interface. Significantly larger and more elongated voids (up to  $1 \text{ mm ESD}$ ) were apparent in a cluster mid-way along the length of the specimen, towards the cement-bone interface (Figure 7-3 (a) and (b)). The major axes of these voids were oriented approximately along the proximo-distal axis, *i.e.* parallel to the cement-stem and cement-bone interfaces.

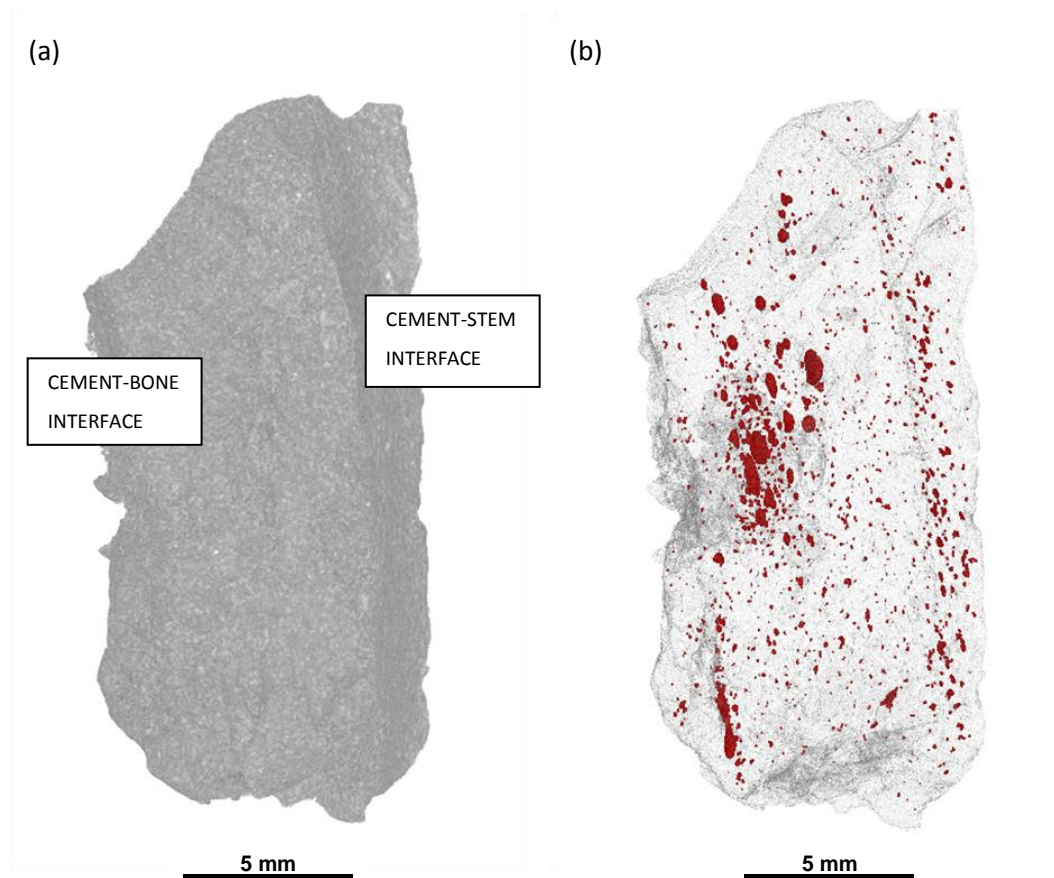
The size distribution of voids in the retrieved cement specimen is presented in Figure 7-4. The modal void size was  $0.06 - 0.10 \text{ mm ESD}$ , accounting for 48% of the total void population. Only 1% of the voids were larger than  $0.40 \text{ mm ESD}$ . The largest void was  $0.96 \text{ mm ESD}$ , accounting for 25% of the total void volume measured in this specimen. Quantitative characteristics for the total void population are detailed in Table 7-2.

The void size distribution is well-described by a generalised extreme value (GEV) distribution function given by the equation:

$$f(x) = \frac{1}{\sigma} \exp\left(-\left(1 + kz\right)^{-\frac{1}{k}}\right) \left(1 + kz\right)^{-1-1/k}$$

$$z \equiv \frac{x - \mu}{\sigma}$$

where the shape parameter  $k = 0.27$ , scale parameter  $\sigma = 0.034$  and location parameter  $\mu = 0.086$ . The P-P plot (comparing the theoretical and observed cumulative distribution functions of the void size data) for the GEV distribution function is shown in Figure 7-5. The plot is approximately linear, showing a good fit between the theoretical and observed cumulative distribution functions of the void size data. The goodness of fit of this distribution function was analysed using the Anderson-Darling normality test, in which the null hypothesis regarding the GEV distribution function is rejected if the test statistic  $A^2$  at significance level  $\alpha$  is greater than the critical value. In this case,  $A^2 = 0.96$  and the critical value (based on a sample size of 1286 voids) for  $\alpha = 0.05$  was 2.5, so the data was considered to follow the specified distribution.



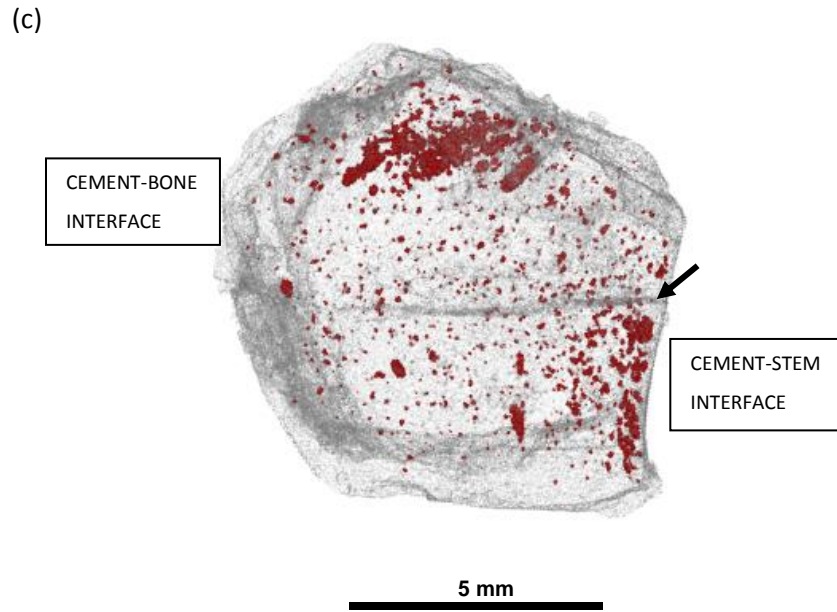


Figure 7-3: CT reconstructions of (a) coronal view of retrieved cement specimen; (b) coronal view of distribution of voids (coloured red) within specimen; (c) transverse view of distribution of voids, showing position of pre-existing crack indicated by black arrow.

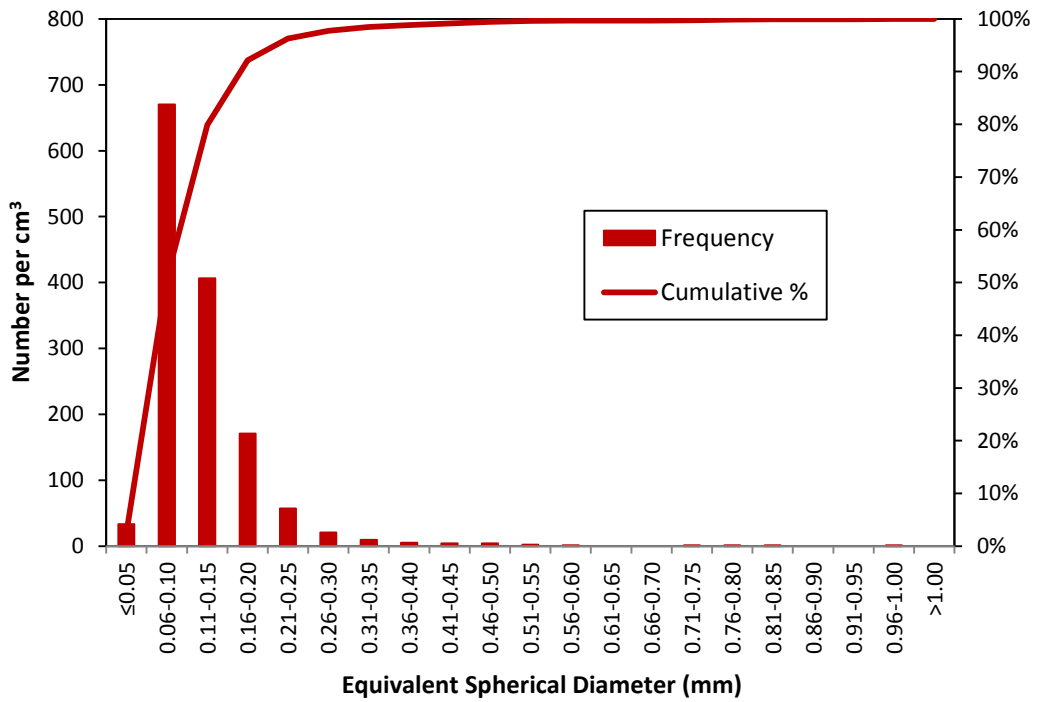


Figure 7-4: Size distribution of voids in specimen of retrieved cement

Table 7-2: Void population characteristics

Void volume (%)	0.21
No. voids per mm <sup>3</sup>	1.4
Largest void ESD (mm)	0.96
Largest void sphericity	0.64
Mean void ESD (mm)	0.14
Mean void sphericity	0.78
No. voids per mm <sup>3</sup> >0.05 mm ESD	1.4
No. voids per mm <sup>3</sup> >0.1 mm ESD	0.69

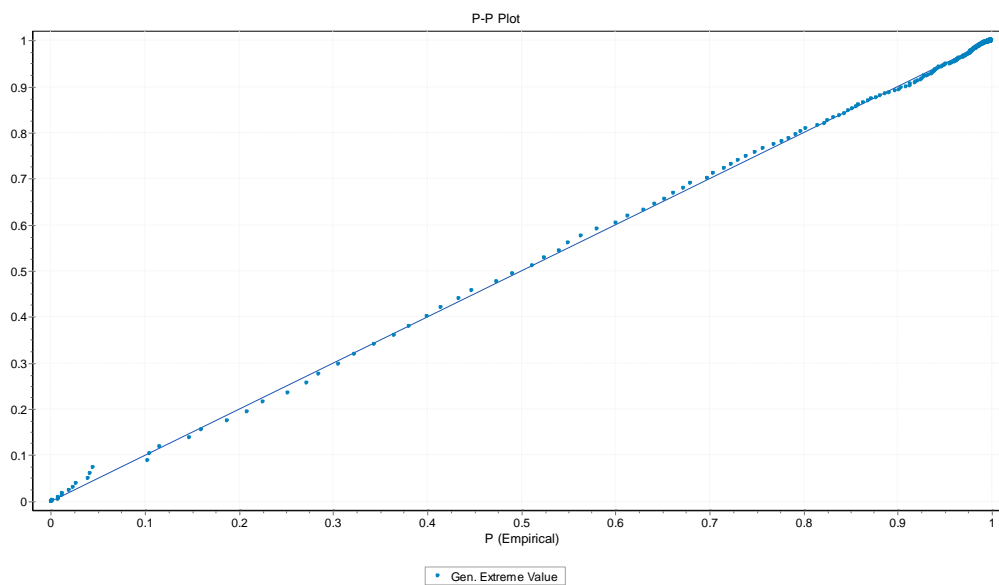


Figure 7-5: P-P plot showing the fit between the observed cumulative distribution function and the theoretical cumulative distribution predicted by the GEV distribution function.

7.3.2 FRACTOGRAPHIC ANALYSIS OF *EX VIVO* CEMENT

On visual inspection, the cement specimen was a pale green colour (Figure 7-6 (a)). Reddish-brown stains were evident on the fracture surfaces, particularly around the opening of the main crack and along the cement-bone interface, while blackening of the cement-stem interface was also observed. The shape of the fracture surface was consistent with a CT cross-section through the crack plane, as shown (Figure 7-6 (b)); the area below the dashed line in this figure indicates the approximate extent of the main pre-existing crack.

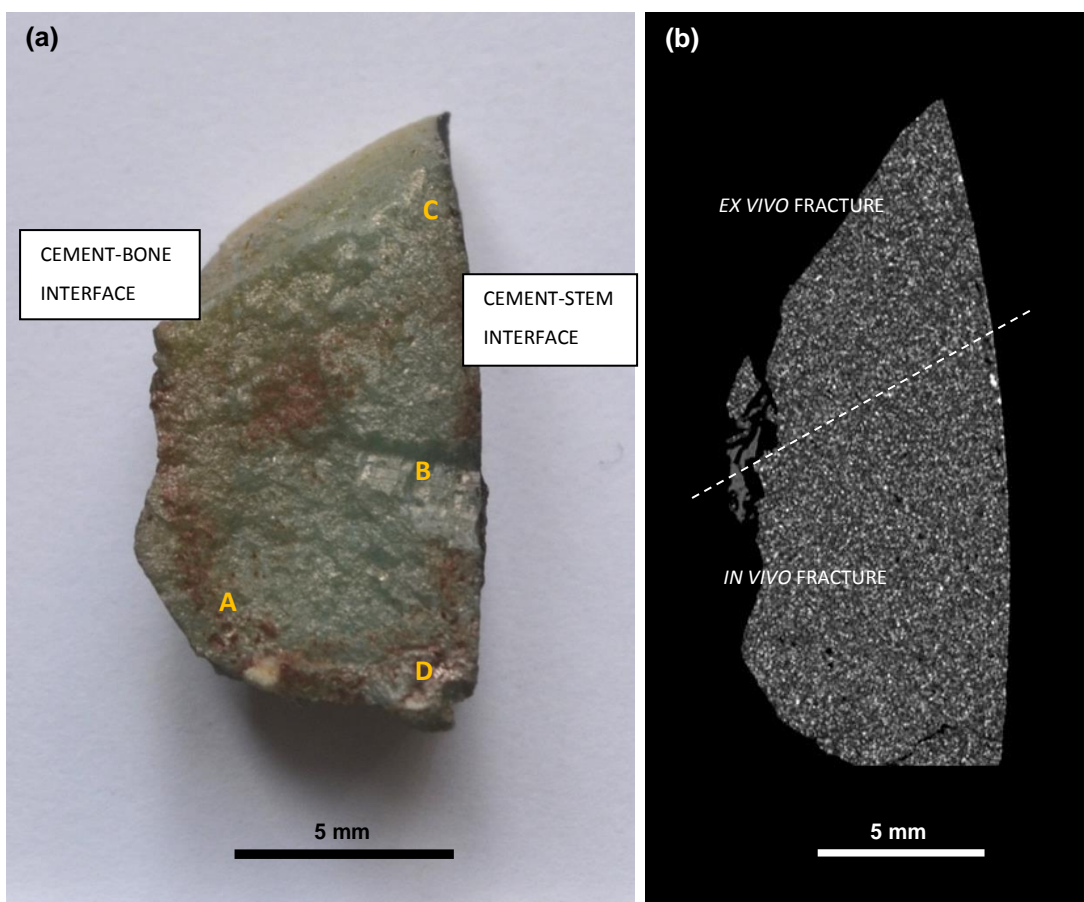


Figure 7-6: (a) Photograph showing *ex vivo* cement fracture surface – letters A-C indicate regions referred to in subsequent figures; (b) corresponding CT slice through crack plane.

Note the presence of a secondary crack in the bottom right corner of both images.

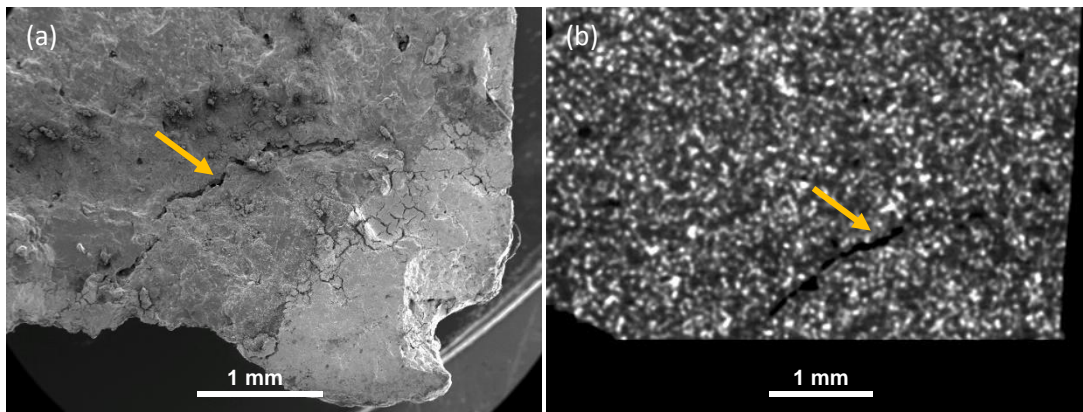


Figure 7-7: (a) SEM micrograph (x25) of region D on the cement fracture surface; (b) enlargement of corresponding CT slice through main crack plane. A secondary crack is evident in both images, indicated by yellow arrows.

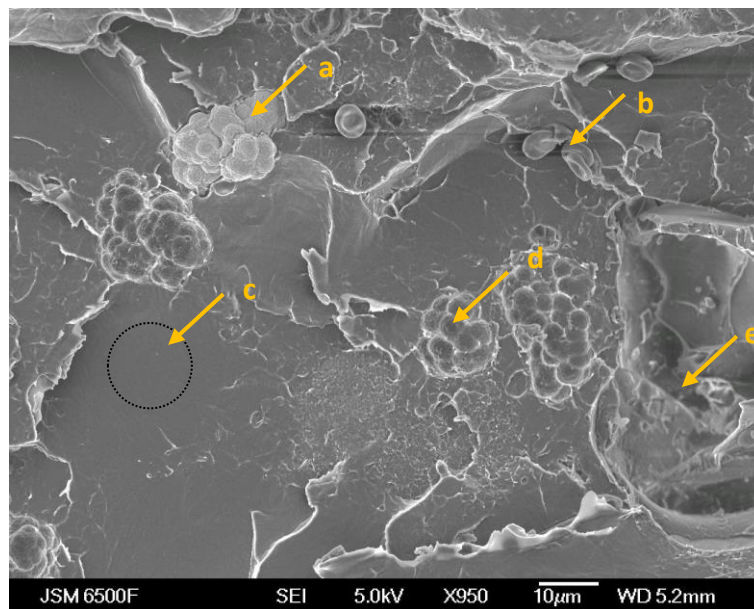


Figure 7-8: SEM micrograph (x950) of region A, showing: (a) cluster of  $ZrO_2$  radiopacifier; (b) red blood cells; (c) pre-polymerised bead; (d) indent indicating  $ZrO_2$  pull-out; (e) void.

Inspection of the fracture surfaces via SEM revealed evidence of secondary crack formation; one example is shown in Figure 7-7 (a). Cross-referencing SEM micrographs with CT data from the original, intact cement specimen (Figure 7-7 (b)) verified that this was a pre-existing secondary crack, propagating approximately perpendicular to the main crack plane (*i.e.* in the transverse plane).

SEM analysis also identified clusters of zirconium dioxide radiopacifier particles on the fracture surface (Figure 7-8 (a)), consistent with the morphology of  $ZrO_2$  identified in Chapter 5 and reported by Ginebra *et al.* (2002). This observation, combined with the green colouring due to the addition of chlorophyll, is consistent with the formulation of Palacos R+G stated by the manufacturer.

Erythrocytes (red blood cells) were visible on the fracture surface (Figure 7-8, (b)), confirming that the main crack occurred either before, or during, retrieval surgery, rather than in the laboratory. These cells do not appear to be contained within the surrounding polymer, so are not considered to result from entrapment of blood within the cement during implantation.

Several voids were observed on the *ex vivo* fracture surface. Three distinctive void morphologies were noted: type 1 was small ( $\sim 50 \mu\text{m}$  diameter) with a roughened appearance; type 2 was also small ( $< 50 \mu\text{m}$  diameter), but with a smoother, more spherical appearance; type 3 was much larger, typically several hundred  $\mu\text{m}$  in diameter, with intact pre-polymerised beads visible on the interior surface of the void. Examples of each of these void types are shown in Figure 7-9.

A clear difference in fractographic morphology was evident between the roughened surface of the main pre-existing crack, and the relatively smooth fast fracture zone resulting from brittle fracture of the specimen in the laboratory (Figure 7-11). Several features indicative of fatigue crack propagation were also evident on the fracture surface. Fatigue striations, with a spacing of  $\sim 1 \mu\text{m}$ , were visible in region B over an area of several square millimetres (Figure 7-12(a)). In addition, extensive evidence of crazing was noted; opened-up crazes, such as shown in Figure 7-13, were apparent on several regions of the fracture surface, while circular crazes were often present within and around pre-polymerised beads (*e.g.* Figure 7-8 (c)). These features are consistent with the crazing noted on fatigue fracture surfaces of radiolucent PMMA cement specimens *in vitro* (Chapter 4).

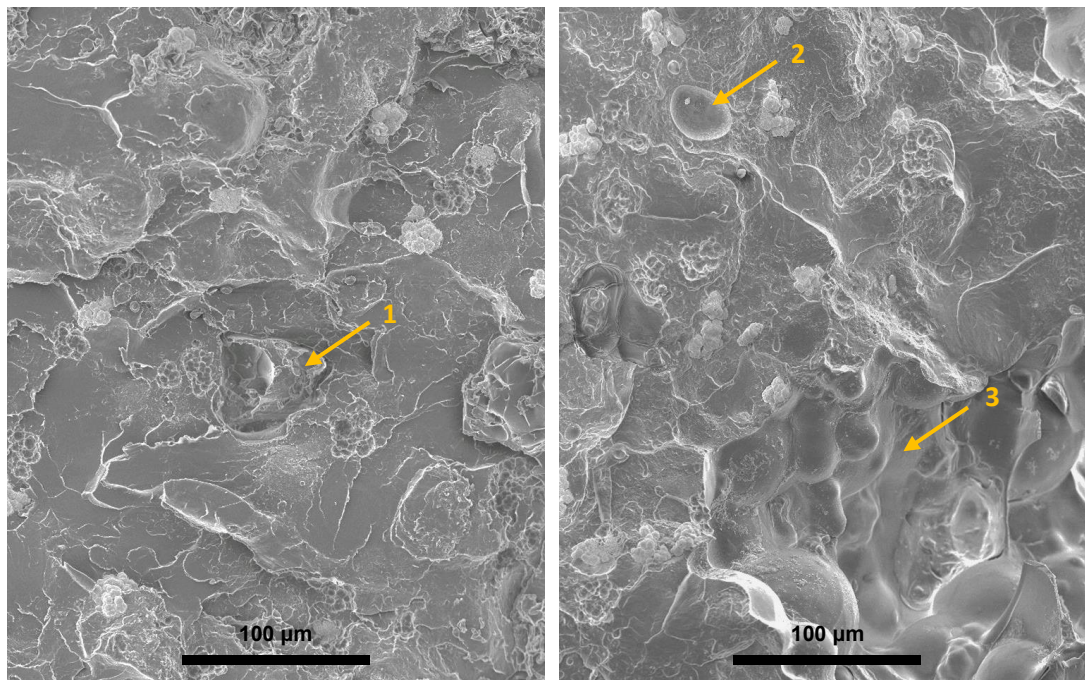


Figure 7-9: SEM micrographs (x250) indicating different void types identified on *ex vivo* fracture surface

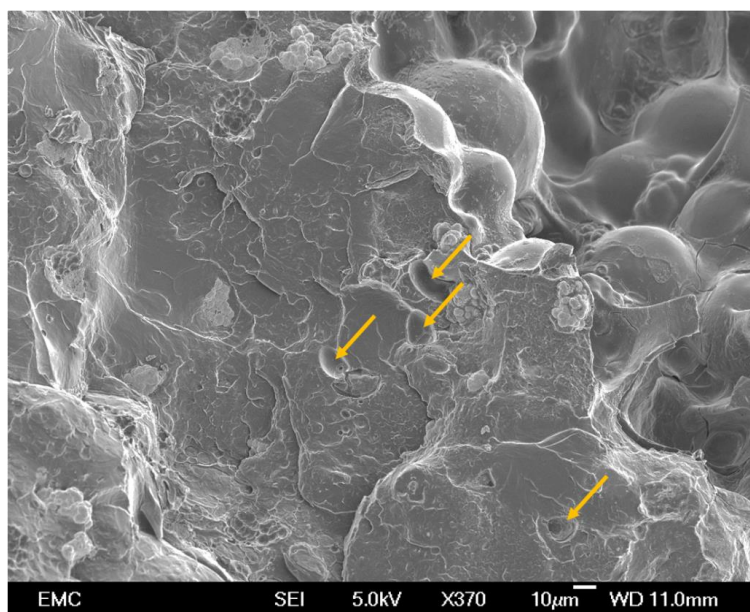


Figure 7-10: SEM micrograph (x370) of region C, showing secondary 'satellite' voids around a shrinkage void close to the cement-stem interface.

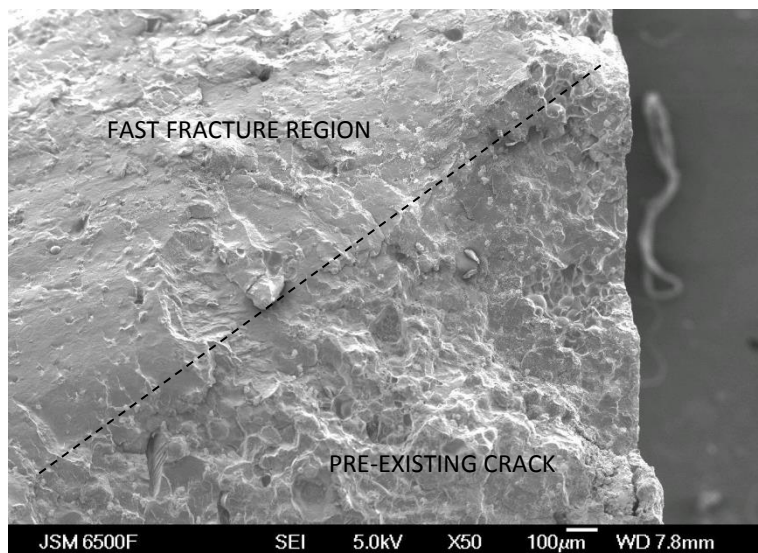


Figure 7-11: SEM micrograph (x50) of region C, highlighting different morphologies of smooth fast fracture region and roughened surface of pre-existing crack.

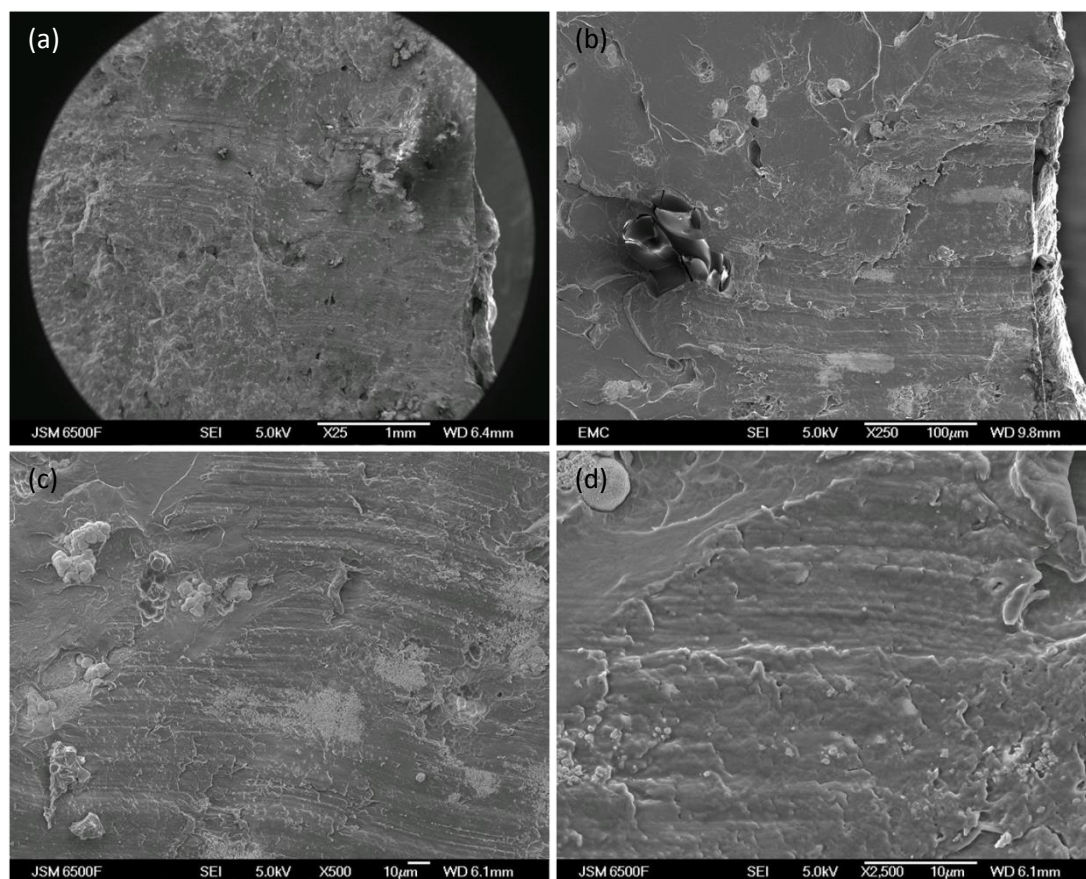


Figure 7-12: SEM Micrographs of region B, showing fatigue striations on fracture surface: (a) x25; (b) x250; (c) x500; (d) x2500.

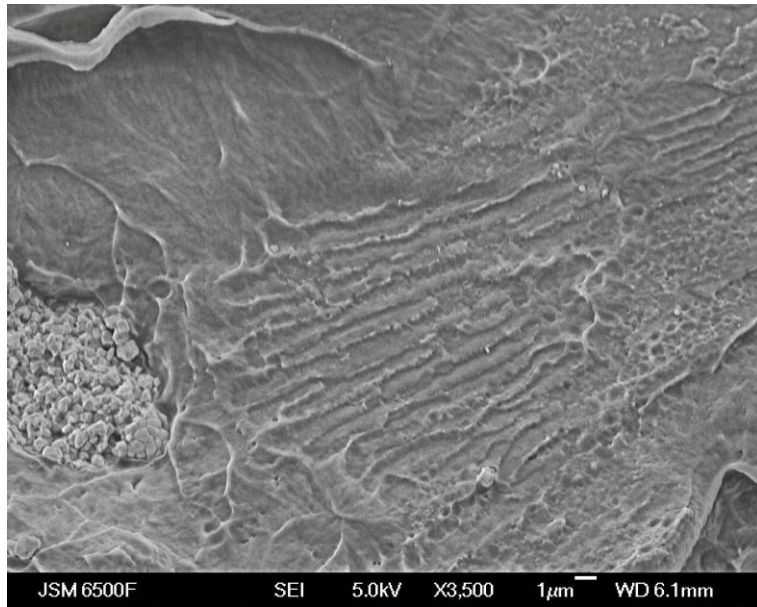


Figure 7-13: SEM Micrograph (x3,500) of region B, showing opened-up craze on fracture surface.

7.3.3 COMPARISON WITH *IN VITRO* FRACTURE SURFACE CHARACTERISTICS

SEM micrographs of the fracture surface of the retrieved cement specimen were compared with *in vitro* fracture surfaces resulting from fatigue failure of Palacos R cement under four-point bend loading. A number of similarities were identified, as detailed below.

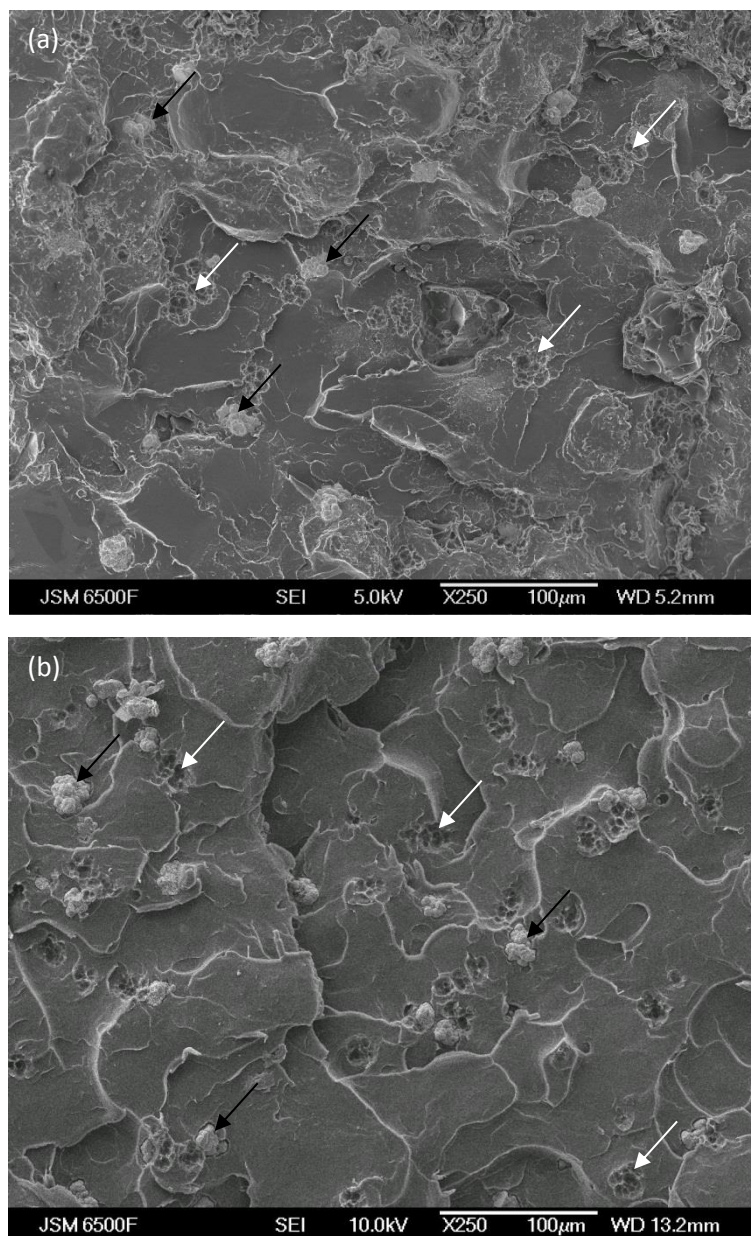


Figure 7-14: SEM Micrographs (x250) of (a) *ex vivo* region A and (b) *in vitro* fractures surfaces, highlighting stepped morphology, clusters of  $ZrO_2$  particles (black arrows) and  $ZrO_2$  pull-out (white arrows).

The fatigue striations shown in Figure 7-12 indicate the overall direction of crack propagation. These features were traced back towards the corner of the specimen, indicating the likely region of crack initiation/early crack growth on the fracture surface. Figure 7-14 (a) indicates the morphology of this region, while Figure 7-14 (b) shows the typical characteristics of the early crack growth region around the initiation site of an *in vitro* specimen. Both surfaces (Figure 7-14 (a) and (b)) show a stepped morphology, consistent with a tortuous crack path and/or the coalescence of multiple micro-cracks. On both specimens, clusters of zirconium dioxide radiopacifier particles can be seen protruding from the fracture surface, while corresponding recesses in the polymer matrix indicate where these clusters have been pulled out of the polymer matrix during fracture. Closer inspection of radiopacifier clusters (Figure 7-15) indicate limited bonding between the  $ZrO_2$  and polymer matrix, with evidence of separation of the interfaces and localized plastic deformation during fracture. The process of  $ZrO_2$  pull-out is not observed on the final failure regions of either the retrieved specimen (Figure 7-11) or *in vitro* test specimens, and is thus considered to be indicative of slow crack growth.

All three void types identified in Figure 7-9 were present on both *in vitro* and *ex vivo* fracture surfaces. In particular, the appearance of large type 3 voids observed on the surface of the retrieved cement were consistent with voids observed on the fracture surfaces of *in vitro* Palacos R specimens (Figure 7-16). Voids of this magnitude and morphology were found to initiate fatigue cracks during *in vitro* testing of Palacos R.

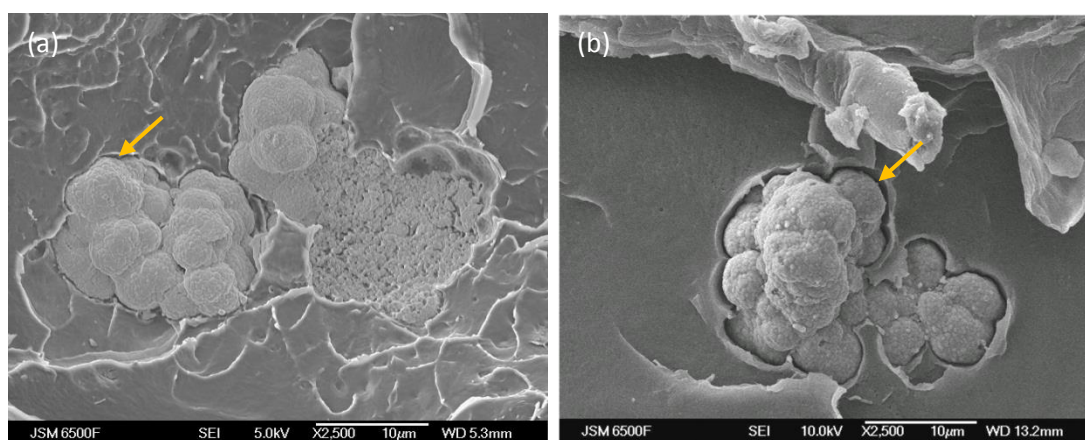


Figure 7-15: SEM micrographs (x2,500) of (a) *ex vivo* region A and (b) *in vitro* fracture surfaces, highlighting morphology of  $ZrO_2$  particles and limited bonding to surrounding polymer, with evidence of localised plastic deformation during fracture (yellow arrows).

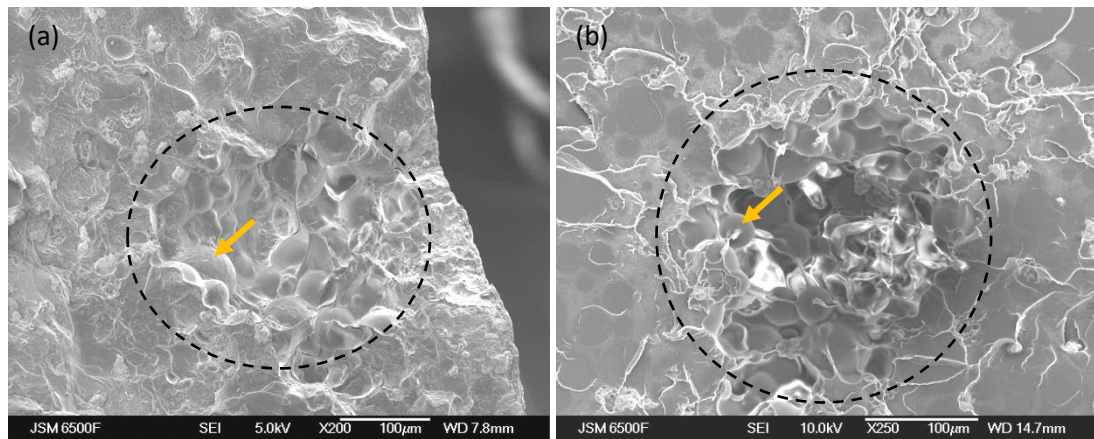


Figure 7-16: SEM Micrographs of void morphology on fracture surfaces of (a) *ex vivo* region B (x200) and (b) *in vitro* (x250) specimens. Pre-polymerised beads, identified by yellow arrows, are visible on the internal surfaces of the voids.

## 7.4 DISCUSSION

The work described has made novel use of  $\mu$ -CT for quantitative characterisation of retrieved cement. This presents a significant advantage over previous studies in this field due to the high resolution, three-dimensional and non-destructive capabilities of this technique for the imaging of high value specimens; furthermore, the detailed void analysis of a specimen of vacuum-mixed *ex vivo* acrylic bone cement presented in this study is considered to be the first of its kind.

Three distinct void morphologies were identified within the *ex vivo* cement specimen. These void types are consistent with voids observed in vacuum-mixed *in vitro* specimens, suggesting similar mechanisms of void formation in both cases. Small, smooth voids may result from entrapment of gases (*e.g.* air or residual monomer), while larger voids with protruding polymer beads may occur due to shrinkage during polymerisation and/or incomplete filling of the cement mantle, as discussed in the previous chapter (Chapter 6). Eight percent of voids in the retrieved cement (109 per  $\text{cm}^3$ ) were greater than 0.20 mm ESD, and thus in the size range previously found to initiate fatigue cracks in Palacos R cement tested *in vitro* (Chapter 5).

Bulk porosity was calculated to be 0.2% of the total specimen volume; this figure is likely to be an underestimate of the total porosity of the cement mantle, due to the exclusion of (potentially very large) surface-breaking voids, although it is comparable to bulk porosity in vacuum-mixed Palacos R prepared *in vitro* (0.33%, Chapter 5). Previous studies have reported pore fractions, assessed using two-dimensional methods, ranging from 0.1% - 27% in *ex vivo* cement (Race *et al.* 2011, Ries *et al.* 2006) mixed by hand, while Messick and co-workers (2007) measured 5.7% porosity with a number-density of 0.25 voids per  $\text{mm}^2$  in vacuum-mixed Simplex P implanted into human cadaveric femora.

The mean void size in the retrieved cement specimen was 0.14 mm ESD, approximately four times larger than the mean void size in the moulded specimens of Palacos R examined in Chapter 5. Analysis of the void size distributions for *in vitro* and *ex vivo* cement shows that the modal voids occur in the  $\leq 0.05$  mm and 0.06 - 0.10 mm ESD intervals respectively. However, the number-density of voids in the *ex vivo* cement was 1.4 per  $\text{mm}^3$ , significantly lower than the 189 voids per  $\text{mm}^3$  recorded for the *in vitro* Palacos R. In effect, the retrieved cement demonstrates a larger but sparser void population. It is hypothesised that this variation may be due to more efficient porosity reduction during cement preparation (*i.e.* superior mixing equipment and/or operator

skill); the stage at which the cement was introduced into the femoral cavity (the cement in this study was injected during the dough phase rather than the working time, in order to facilitate moulding); or the different environmental conditions in which polymerisation occurred (for example, higher temperature, aqueous environment and the potential inclusion of biological debris) which may have altered the polymerisation kinetics and inhibited void formation.

In addition to the main crack, CT imaging identified the presence of a number of smaller secondary cracks within the retrieved cement. The absence of an identifiable crack origin on the fracture surface, in addition to the variation in fracture surface morphology, suggest the main crack may have propagated as a result of coalescence of multiple smaller cracks. Damage accumulation due to the initiation and coalescence of cement micro-cracks is cited as a factor in the aseptic loosening of cemented implants, and has been replicated experimentally (McCormack and Prendergast 1999). Several authors have noted the presence of fatigue cracks in hand-mixed retrieved cement mantles (Culleton *et al.* 1993, Jasty *et al.* 1991, Topoleski *et al.* 1990), while Race *et al.* (2011) examined a number of post-mortem retrieved cement mantles and correlated the number of cracks with duration of implantation and patient BMI. However, the findings of the present study represent clear micromechanical evidence of fatigue cracking in vacuum-mixed *ex vivo* cement.

The presence of probable fatigue striations on the fracture surface of the retrieved cement signifies that crack propagation occurred under cyclic loading conditions. The slightly irregular depth and spacing of these striations may be explained by the non-uniform, discontinuous cyclic loading that would be expected to occur during normal patient activity, as described by Bergmann and co-workers (2001).

PMMA is known to exhibit either true striations or discontinuous growth bands, depending on load levels and loading history (ASM International 2003). Fatigue striations in glassy polymers typically form at higher stress levels than discontinuous growth bands, and unlike DGBs their presence does not appear to be dependent on the chemistry and molecular weight of the polymer (Skibo *et al.* 1977). Fatigue striations represent cycle-by-cycle crack growth and thus have a narrower inter-band spacing than DGBs, although the spacing of both fatigue striations and DGBs increases further from the crack origin due to increasing  $\Delta K$ .

The striations exhibited on the *ex vivo* fracture surface in this case are distinct from the discontinuous growth bands (DGBs) observed around crack initiation sites on *in vitro*

fatigue fracture surfaces in Palacos R and other bone cements (Chapters 4-5). The former are approximately parallel, with sub-micron inter-striation spacing; in contrast, the DGBs exhibit a diverging pattern, with inter-band spacing  $>2 \mu\text{m}$ . In the cements studied in this work, DGBs were frequently noted in the smooth, 'halo' region immediately surrounding the crack origin (see Figure 4-10 & Figure 5-7, for example), while the fatigue striations detected on the *ex vivo* fracture surface of Palacos R+G appeared to be situated further from the crack origin; certainly, the roughened morphology of the surrounding fracture surface was not indicative of early crack growth (Figure 7-6(a)). These findings are in agreement with the observations of Skibo and co-workers (1977) studying fatigue fracture surfaces of PMMA and other glassy polymers. The presence of fatigue striations, but not discontinuous growth bands, may be attributed to the variation in environmental and loading conditions between the *in vitro* and *ex vivo* specimens, including frequency, temperature, humidity, applied load and addition of gentamicin to the cement formulation; in particular, the variable amplitude loading of the *in vivo* cement mantle during normal daily activity may suppress the formation of DGBs.

While computational studies have predicted that the *in vivo* cement mantle is subjected to bending stress, this will be under conditions of displacement control rather than load control. Therefore, as a crack propagates, the construct will become more compliant and the load will be reduced, which may retard crack growth. Griffin *et al.* (1999) reported that the fatigue life of human cortical bone tested in a four point bend configuration was 1.5 orders of magnitude greater under displacement control than load control. The fatigue life is also known to be dependent on the type of loading, as shown in Figure 2-18; four-point bending results in a greater fatigue life than tensile testing, while fully reversed tension-compression produces the shortest fatigue life at an equivalent stress level, due to differences in the stress distribution across the cross-section of the specimen (Kuehn *et al.* 2005b).

The larger volume of a cement mantle in comparison to the critical volumes of the cement specimens tested in this work result in a greater probability of the occurrence of a defect of critical size in a region of high stress *in vivo*, according to extreme value statistics. In addition, voids and pits are likely to be present on the surface of the cement mantle, especially after a period of service due to gradual degradation of the cement mantle. It was shown in section 2.3.5 that fatigue cracks are more likely to initiate from defects occurring at or close to the specimen surface. However, the lower stresses experienced in the cement mantle, in comparison to the applied stresses

utilised in the mechanical testing in this study, may be expected to increase the sensitivity of the material to the presence of stress concentrations due to the greater dependence of the fatigue life on crack initiation.

As previously discussed, environmental conditions may also have a considerable impact on the fatigue life of the cement. In particular, creep is expected to be a more significant factor *in vivo* due higher operating temperature, longer loading duration and aqueous environment, which will act to plasticize the cement. Creep may relieve residual stresses in the cement mantle resulting from polymerisation, and reduce the damaging effect of stress concentrations such as voids and agglomerates.

Previous studies of retrieved cement have either imaged existing fracture surfaces (Topoleski *et al.* 1990, Culleton *et al.* 1993) or sectioned specimens arbitrarily (Jasty *et al.* 1991, Kawate *et al.* 1998, Race *et al.* 2011). The separation of a pre-existing crack to produce 'fresh' fracture surfaces for analysis in this study is considered to reduce the likelihood of instrument damage being introduced during retrieval and thus hindering microscopic examination of early crack growth mechanisms. Although there is a possibility that this crack was formed during revision surgery, this is considered improbable due to the following factors: (i) the cement fracture was incomplete; (ii) the cement specimen was located proximally in the cement mantle, and thus relatively easy to remove; (iii) there were a number of fractographic indications of slow, fatigue crack growth, including the surface roughness, stepped morphology, zirconium dioxide pull-out and presence of fatigue striations. It should be acknowledged, however, that this study involved the analysis of a single specimen of cement retrieved during revision surgery. The analysis of further specimens is therefore required before firm conclusions may be drawn regarding the applicability of these results to other cement brands, mixing systems and mixing personnel within the clinical scenario.

## 7.5 CONCLUSION

Preliminary imaging of the microstructure and damage within an *ex vivo* cement specimen has been conducted using  $\mu$ -CT, highlighting extensive porosity (despite vacuum-mixing), the presence of a large incomplete crack with a visible length of  $\sim 9$  mm, and multiple crack coalescence. The presence of satellite void clustering has also been observed in the vicinity of a large shrinkage void, consistent with *in vitro* findings. Fractographic analysis using SEM has identified evidence of fatigue crack propagation, and microstructural characteristics of the fracture surfaces were consistent with *in vitro* specimens of Palacos R subjected to four-point bend fatigue testing. The cracking observed can be attributed to *in vivo* fatigue failure of the cement. Analysis of further *ex vivo* specimens would be valuable to corroborate these findings and assess the effect of vacuum-mixing on porosity formation in the clinical scenario.

---

---

## 8. CONCLUSIONS AND FURTHER WORK

---

---

### 8.1 SUMMARY AND CONCLUSIONS

The aim of this investigation was to use a combination of high-resolution interrogative techniques to determine the relative effect of cement formulation and microstructural features (*i.e.* voids and radiopacifier particles) on the fatigue performance of conventional bone cements. A 'data rich' methodology has therefore been developed for the quantification of defect populations and assessment of failure mechanisms of *in vitro* and *ex vivo* cement specimens, using high-resolution  $\mu$ -CT, mechanical testing and fractographic analysis. The use of quantitative, three-dimensional volume imaging has enabled the characterisation of both global feature populations and individual crack-initiating defects in terms of size, morphology and spatial density; in addition, complex void clustering effects have been noted that may not have been identified using traditional two-dimensional imaging techniques.

Three-dimensional quantitative characterisation of microstructural features (*i.e.* voids and radiopacifier particles) in four commercial cement formulations has been conducted. In all formulations, void populations were found to be bi-modal, with many small voids and a few larger voids, up to several millimetres in diameter; the largest voids ( $> 0.5$  mm equivalent spherical diameter) were surrounded by clusters of secondary satellite voids. Extensive void formation was also noted in both moulded specimens and cement mixing gun stubs, highlighting that the formation of large voids in the cement is not entirely due to incomplete mould filling.

Barium sulphate and zirconium dioxide radiopacifiers demonstrated very different characteristics in terms of size, morphology and distribution of particles. Individual barium sulphate particles were approximately 2-5  $\mu\text{m}$  in length and therefore too small to be identified in the computed tomography data. However, large agglomerates of particles were identified in both the moulded specimens and unmixed powder, up to 0.37 mm ESD at spatial densities of up to 22 per  $\text{mm}^3$ . In contrast, the majority of zirconium dioxide particles occurred in the size range 10-30  $\mu\text{m}$  ESD; the largest particles identified were below 60  $\mu\text{m}$  ESD.

The relative influence of voids and radiopacifier particles on *in vitro* cement fatigue and failure in four commercial cement formulations has been investigated. The inclusion of barium sulphate as a radiopacifier was found to have a negative effect on the fatigue life of cement; large agglomerates of barium sulphate radiopacifier particles ( $> 100 \mu\text{m}$  ESD) were found to readily initiate fatigue cracks; furthermore, fatigue life scaled consistently with initiating defect size. In contrast, cement containing zirconium dioxide as a radiopacifier demonstrated superior fatigue performance, as evidenced by the greater peak stress required to cause failure within  $10^5$  cycles; however, greater variation in fatigue life was noted in these formulations (Palacos R in particular), which may be attributed to the dominance of large voids, present at low spatial densities, as the crack initiating defects in the  $\text{ZrO}_2$  cement formulations tested in this study. In the absence of voids, crack initiation was identified in the vicinity of zirconium dioxide particles, but only at high applied stresses ( $>50 \text{MPa}$ ).

The microstructural and fractographic characteristics of specimens of *in vitro* and *ex vivo* vacuum-mixed bone cement have been compared and contrasted. *Ex vivo* cement, retrieved at revision surgery, was analysed using  $\mu\text{-CT}$  and found to contain extensive porosity, despite the use of a vacuum-mixing technique for cement preparation. In addition, a clustering effect of small voids in the vicinity of larger ones was noted on the fracture surfaces of both *in vitro* and *ex vivo* specimens, which may act to multiply the stress concentration effect of the larger voids and initiate fatigue cracks.

The retrieved cement specimen was also found to contain a large, incomplete crack; secondary crack formation and coalescence was also noted. Consistencies were identified between the morphology of regions of the *ex vivo* fracture surface, and the early crack growth region on *in vitro* fatigue fracture surfaces. However, fractographic analysis also revealed the presence of apparent fatigue striations on the *ex vivo* fracture surface, in contrast to the discontinuous crack growth bands evident around crack initiation sites *in vitro*. While the cracking observed in *ex vivo* cement may be attributed to fatigue crack propagation, the different fatigue markings observed on *in vitro* and *ex vivo* fracture surfaces may result from the discontinuous cyclic loading and non-uniform stress distribution that is expected to occur in the clinical cement mantle.

## 8.2 FURTHER WORK

### 8.2.1 MICROSTRUCTURAL CHARACTERISATION OF BONE CEMENT

It has been acknowledged that the work conducted in this study related to a limited number of cement formulations mixed using a single vacuum-mixing device; furthermore, the effect of antibiotic addition on fatigue failure of the cement was beyond the scope of this investigation. Consequentially, further characterisation of cement microstructure and fatigue failure processes using the methodology developed herein would be beneficial. In particular, five areas have been identified for the focus of future studies:

- i. *In vitro* analysis of additional cements containing barium sulphate as the radiopacifier, to assess whether agglomeration of BaSO<sub>4</sub> particles and resulting crack initiation effects are common across all cement formulations. Paired analysis of cement brands with similar chemical compositions, such as Smartset MV (Depuy CMW, Blackpool, UK) and Simplex P (Stryker Orthopaedics, NJ, USA), would be particularly beneficial in order to identify the impact of manufacturing methods on radiopacifier agglomeration.
- ii. *In vitro* analysis of antibiotic-laden cement formulations, to assess the effect of antibiotic type and quantity on cement microstructure and fatigue crack initiation processes. The use of antibiotic cement in primary arthroplasty is becoming more prevalent; antibiotic-laden cement formulations accounted for 87% all bone cement used in total hip arthroplasty procedures conducted in England and Wales in 2011 (NJR 2012).
- iii. *In vitro* analysis of the effect of alternative cement mixing systems on cement microstructure, in particular the formation of BaSO<sub>4</sub> agglomerates and satellite voids. Current commercially available vacuum-mixing systems that could be incorporated into this study include syringe-based systems such as Palamix (Heraeus Medical, Hanau, Germany) and Summit HiVac 7 (Summit Medical, Bourton on the Water, UK), and state-of-the-art systems combining both cement constituents and mixing apparatus, such as Palacos R+G Pro (Heraeus Medical, Hanau, Germany) and Optipac (Biomet, Bridgend, UK). The mechanisms of formation of satellite voids in the cement should also be investigated using optical microscopy and videography, according to the methodology previously proposed in section 6.4.

- iv. *Ex vivo* analysis of further specimens of retrieved cement in order to characterise microstructural defect populations and failure mechanisms occurring in clinical cement mantles. Factors that should be considered include cement formulation, mixing system, mixing operator, patient characteristics and time *in vivo*. In particular, analysis of retrieved CMW-1 cement would be beneficial to assess the clinical relevance of barium sulphate agglomeration on the longevity of the cement mantle.
- v. Computational modelling of the effect of microstructural defect populations on fatigue life, in order to validate the experimental findings, particularly those shown in Figure 4-13. This could be conducted in three phases. Firstly, development of a simple mathematical model of the effect of size and location of an idealised spherical defect on the stress distribution in a four point bend bar, such as the model developed by Gao *et al.* (2004) for cylindrical tensile specimens of a cast aluminium alloy. This model should assess the effect of defect size, depth applied stress and material constants (*i.e.* to compare the relative effects of voids and agglomerates). Next, the effect of defect morphology should be evaluated using realistic void and agglomerate geometries obtained from the  $\mu$ -CT data in this study, similar to the methodology of Nicoletto *et al.* (2010). Finally,  $\mu$ -CT data should be used to create virtual models of the specimens tested in this study in order to conduct predictive finite element analysis of the effect of microstructural defect properties on the fatigue life of the cement; a similar approach has been adopted by Vanderesse *et al.* (2011).

## 8.2.2 DEVELOPMENT OF BONE CEMENT WITH IMPROVED CLINICAL LONGEVITY

The findings of this study have highlighted two microstructural features that may be of particular significance to the fatigue performance of bone cement: agglomerates of barium sulphate radiopacifier particles and the formation of clusters of satellite voids around large primary voids. In order to improve the longevity of the cement mantle, the formation of these defects should be minimised. Further work could therefore be directed in the following areas:

- i. Development of improved cement formulations, manufacturing and/or mixing methods to ensure better dispersal of the barium sulphate radiopacifier phase and prevent the formation of large agglomerates with the potential to initiate fatigue cracks.
- ii. Development of improved vacuum-mixing systems to control the formation of voids within the cement. In this study, voids exceeding  $\sim 100 \mu\text{m}$  diameter demonstrated the potential to initiate fatigue cracks, while voids exceeding 0.5 mm diameter were surrounded by clusters of satellite voids that could be expected to magnify the stress concentrating effect of the primary void. It is therefore recommended that the development of the next generation of mixing systems ideally aim to eliminate all voids greater than  $100\mu\text{m}$  diameter.



---

---

## REFERENCES

---

---

- Abdel-Kader, K.F.M., S. Allcock, D.I. Walker & S.B. Chaudhry (2001). Bone-loc bone-cement – experience in hip arthroplasty during a 3-year period. *The Journal of Arthroplasty*, 16, 811-819.
- Agarwal S. (2004). Osteolysis – basic science, incidence and diagnosis. *Current Orthopaedics*, 18, 220-231.
- Alkire, M., E. Dabezies & P. Hastings (1987). High vacuum as a method of reducing porosity of Polymethylmethacrylate. *Orthopaedics*, 10, 1533-1539.
- Ammar, H.R., A.M. Samuel & F.H. Samuel (2008). Effect of casting imperfections on the fatigue life of 319-F and A356-T6 Al-Si casting alloys. *Materials Science and Engineering A*, 473, 65-75.
- Amirzadeh-Asl, D., & Schwarz, K. H. (2010). *U.S. Patent No. 7,776,149*. Washington, DC: U.S. Patent and Trademark Office.
- AOA (2009). *Annual Report*. Australian Orthopaedic Association National Joint Replacement Registry.
- Arnold, J.C. & N.P. Venditti (2001). Effects of environment on the creep properties of a poly(methylmethacrylate) based bone cement. *Journal of Materials Science: Materials in Medicine*, 12, 707-717.
- Artola, A., M. Gurruchaga, B. Vázquez, J. San Román & I. Goñi (2003). Elimination of barium sulphate from acrylic bone cements. Use of two iodine-containing monomers. *Biomaterials*, 24, 4071-4080.
- ASM International (2003). *Characterization and failure analysis of plastics*, 414.
- Baleani, M., L. Cristofolini & A. Toni (2001). Temperature and aging condition effects on the characterization of acrylic bone cement. *Proceedings of the Institute of Mechanical Engineers: Part H*, 215, 113-118.
- Baleani, M., L. Cristofolini, C. Minari & A. Toni (2003). Fatigue strength of PMMA bone cement mixed with gentamicin and barium sulphate vs pure PMMA. *Proceedings of the Institute of Mechanical Engineers: Part H*, 217, 9-12.

- Barrs, T.J. (2006). Overview of radiopaque drugs: 1895 – 1931. *American Journal of Health-System Pharmacy*, 63, 2248-2255.
- Bauer, T.W., and J. Schils (1999). The pathology of total joint arthroplasty I. Mechanisms of implant fixation. *Skeletal Radiology*, 28, 423-432.
- Beaumont, P.W.R. (1977). The strength of acrylic bone cements and acrylic cement-stainless steel interfaces. *Journal of Materials Science*, 12, 1845-1852.
- Bellemans, J., M.D. Ries & J. Victor (2005a). *Total Knee Arthroplasty: A guide to get better performance*. Springer.
- Bellemans, J., H. Vandenuecker & J. Vanlauwe (2005b). Total Knee Replacement. *Current Orthopaedics*, 19, 446-452.
- Berger, R. A. (2001). Long-term follow up of the Miller Galante total knee replacement. *Clinical Orthopaedics and Related Research*, 388, 58-67.
- Bergmann, G., G. Deuretzbacher, M. Heller, F. Graichen, A. Rohlmann, J. Strauss & G.N. Duda (2001). Hip contact forces and gait patterns from routine activities. *Journal of Biomechanics*, 34, 859-871.
- Bergmann, G., F. Graichen & A. Rohlmann (2004). Hip joint contact forces during stumbling. *Langenbecks Archive of Surgery*, 389, 53-59.
- Bergmann, G., F. Graichen, A. Rohlmann, A. Bender, B. Heinlein & G.N. Duda (2010). Realistic loads for testing hip implants. *Biomedical Materials and Engineering*, 20, 65-75.
- Bhambri, S. K. & L. N. Gilbertson (1995). Micromechanisms of fatigue crack initiation and propagation in bone cements. *Journal of Biomedical Materials Research*, 29, 233-237.
- Bishop, N.E., M. Schönwald, P. Schultz, K. Püschel & M.M. Morlock (2009). The condition of the cement mantle in femoral hip prosthesis implantations – a post mortem retrieval study. *Hip International*, 19(2), 87-95.
- Bolland, B.J.R.F., D.J. Culliford, D.J. Langton, J.P.S. Millington, N.K. Arden & J.M. Latham (2011). High failure rates with a large-diameter hybrid metal-on-metal total hip replacement. *Journal of Bone and Joint Surgery (British)*, 93-B:5, 608-615.

- Breusch, S. & H. Malchau (2005). *The well-cemented total hip arthroplasty: theory and practice*. Springer.
- Cahir, J.G., A.P. Toms, T.J. Marshall, J. Wimhurst & J. Nolan (2007). CT and MRI of hip arthroplasty. *Clinical Radiology*, 62, 1163-1171.
- Callaghan, J. J., A. G. Rosenberg & H.E. Rubash (2007). *The Adult Hip: Volume 1*, 2<sup>nd</sup> edition. Lippincott, Williams and Wilkins.
- Chen, A., C. Gupte, K. Akhtar, P. Smith & J. Cobb (2012). The global economic cost of osteoarthritis: how the UK compares. *Arthritis*, 2012, doi:10.1155/2012/698709.
- Cheng, J., Yang, C., Mao, Z. S., & Zhao, C. (2009). CFD Modeling of nucleation, growth, aggregation, and breakage in continuous precipitation of barium sulfate in a stirred tank. *Industrial & Engineering Chemistry Research*, 48(15), 6992-7003.
- Coathup, M.J., J. Blackburn, A.E. Goodship, J.L. Cunningham, T. Smith & G.W. Blunn (2005). Role of hydroxyapatite coating in resisting wear particle migration and osteolysis around acetabular components. *Biomaterials*, 26, 4161-4169.
- Coultrup, O.J., M. Browne, C. Hunt & M. Taylor (2009). Accounting for inclusions and voids allows the prediction of tensile fatigue life of bone cement. *Journal of Biomechanical Engineering*, 131, 1-8.
- Cox, B.D., R.K. Wilcox, M.C. Levesley & R.M. Hall (2006). Assessment of a three-dimensional measurement technique for the porosity evaluation of PMMA bone cement. *Journal of Materials Science: Materials in Medicine*, 17, 553-557.
- Cristofolini, L., C. Minari & M. Viceconti (2000). A methodology and criterion for acrylic bone cement fatigue tests. *Fatigue and Fracture of Engineering Materials and Structures*, 23, 953.
- Cristofolini, L., T.A. Saponara, P. Savigni, P. Erani & M. Viceconti (2007). Preclinical assessment of the long-term endurance of cemented hip stems. Part 1: effect of daily activities – a comparison of two load histories. *Proceedings of the Institute of Mechanical Engineers: Part H*, 221, 569-584.
- Culleton, T.P., P.J. Prendergast & D. Taylor (1993). Fatigue failure in the cement mantle of an artificial hip joint. *Clinical Materials*, 12, 95-102.
- Dart, R.C. (2004). *Medical Toxicology*, 3<sup>rd</sup> edition. Lippincott Williams and Wilkins.

Davies, J.P. & W.H. Harris (1990). Optimisation and comparison of three vacuum mixing systems for porosity reduction of Simplex P cement. *Clinical Orthopaedics and Related Research*, 254, 261-269.

Dunne, N. J. & J. F. Orr (2001). Influence of mixing techniques on the physical properties of acrylic bone cement. *Biomaterials*, 22, 1819-1826.

Dunne, N. J., J. F. Orr, M. T. Mushipe & R. J. Eveleigh (2003). The relationship between porosity and fatigue characteristics of bone cements. *Biomaterials*, 24, 239-245.

Dunne, N., C. Daly, D. Beverland, J. Nixon, R. Wilson, G. Carey & J. Orr (2005). Third generation bone cement mixing systems, are they doing the job? *Journal of Bone and Joint Surgery (British)*, 87-B (SUPP III), 262-263.

Endogan, T., K. Serbetchi & N. Hasirci (2009). Effects of ingredients on thermal and mechanical properties of acrylic bone cements. *Journal of Applied Polymer Science*, 113, 4077-4084.

Espehaug, B., O. Furnes, L.I. Havelin, L.B. Engesaeter & S.E. Vollset (2002). The type of cement and failure of total hip replacements. *Journal of Bone and Joint Surgery (British)*, 84-B, 832-838.

Evans, S.L. (2006). Effects of porosity on the fatigue performance of polymethyl methacrylate bone cement: an analytical investigation. *Proceedings of the Institute of Mechanical Engineers Part H: Journal of Engineering in Medicine*, 220, 1-10.

Evans, S.L. (2007). Fatigue crack propagation under variable amplitude loading in PMMA and bone cement. *Journal of Materials Science: Materials in Medicine*, 18, 1711-1717.

Feldkamp, L.A., L.C. Davis & J.W. Kress (1984). Practical cone-beam algorithm. *Journal of the Optical Society of America A*, 1, 612-619.

Fischer C.R., J.H. Lee & W. Macaulay (2009). Patient activity after hip arthroplasty: state of the art, current knowledge, and guidelines. *Operative Techniques in Orthopaedics*, 19(3), 176-181.

Gagnon, S. (2011). *Global markets for bone cement and accessories 2012*. Millenium Research Group.

- Gao, Y.X., J.Z. Yi, P.D. Lee & T.C. Lindley (2004). The effect of porosity on the fatigue life of cast aluminium-silicon alloys. *Fatigue & Fracture of Engineering Materials & Structures*, 27(7), 559-570.
- Garellick, G., J. Kärrholm, C. Rogmark & P. Herberts (2010). *Swedish Hip Arthroplasty Register: Annual Report 2010*. Swedish Hip Arthroplasty Register.
- Gilbert, J.L., J.M. Hasenwinkel, R.L. Wixson, E.P. Lautenschlager (2000). A theoretical and experimental analysis of polymerization shrinkage of bone cement: A potential major source of porosity. *Biomedical Materials Research*, 52, 210-218.
- Ginebra, M. P., L. Albuixech, E. Fernandez-Barragan, C. Aparicio, F. J. Gil, J. San Roman, B. Vazquez & J. A. Planell (2002). Mechanical performance of acrylic bone cements containing different radiopacifying agents. *Biomaterials*, 23, 1873-1882.
- Goodman, S. (2005). Wear particulate and osteolysis. *Orthopedic Clinics of North America*, 36, 41-48.
- Graham, J., L. Pruitt, M. Ries & N. Gundiah (2000). Fracture and Fatigue Properties of Acrylic Bone Cement. The effects of mixing method, sterilization treatment and molecular weight. *The Journal of Arthroplasty*, 15, 1028-1035.
- Griffin, L.V., J.C. Gibeling, R.B. Martin, V.A. Gibson & S.M. Stover (1999). The effects of testing methods on the flexural fatigue life of human cortical bone. *Journal of biomechanics*, 32(1), 105-109.
- Gross, A.E. (2005). The role of polymethylmethacrylate bone cement in revision arthroplasty of the hip. *Orthopedic Clinics of North America*, 36, 49-54.
- Gruen, T.A., G.M. McNeice & H.C. Amstutz (1979). Modes of failure of cemented stem-type femoral components: a radiographic analysis of loosening. *Clinical Orthopaedics*, 141, 17-27.
- Hailey, J. L., J. G. Turner & A. W. Miles (1992). The effect of storage environment on the mechanical properties of acrylic bone cement. *Biomaterial-Tissue Interfaces*, 325-329.
- Hardinghaus, F., Glende, D. C., Park, J. W., & Kohler, K. (2012). *U.S. Patent No. 8,119,716*. Washington, DC: U.S. Patent and Trademark Office.

Harper, E.J., M. Braden & W. Bonfield (1997). Influence of sterilization upon a range of properties of experimental bone cements. *Journal of Materials Science: Materials in Medicine*, 8, 849-853.

Harper, E.J. & W. Bonfield (2000). Tensile characteristics of ten commercial acrylic bone cements. *Journal of Biomedical Materials Research*, 53, 605-616.

Haydon, C.M., R. Mehin, S. Burnett, C.H. Rorabeck, R.B. Bourne, R.W. McCalden & S.J. MacDonald (2004). Revision total hip arthroplasty with use of a cemented femoral component: results at a mean of ten years. *Journal of Bone & Joint Surgery (American)*, 86(6), 1179-1185.

Heraeus Medical (2008). *Palacos-R: Instructions for Use*. Heraeus Medical GmbH, Wehrheim, Germany.

Hertzberg, R.W., J.A. Manson & M. Skibo, M. (1975). Frequency sensitivity of fatigue processes in polymeric solids. *Polym Eng Sci*, 15, 252-260.

Hoey, D. & D. Taylor (2008). Fatigue in porous PMMA: The effect of stress concentrations. *International Journal of Fatigue*, 30, 989-995.

Hoey, D. & D. Taylor (2009a). Quantitative analysis of the effect of porosity on the fatigue strength of bone cement. *Acta Biomaterialia*, 5, 719-726.

Hoey, D. & D. Taylor (2009b). Statistical distribution of the fatigue strength of porous bone cement. *Biomaterials*, 30, 6309-6317.

Hoey, D. & D. Taylor (2010). The effect of mixing technique on fatigue of bone cement when stress concentrations are present. *International Journal of Nano and Biomaterials*, 3(1), 36-48.

Hua, J. & P.S. Walker (1994). Relative motion of hip stems under load. An in vitro study of symmetrical, asymmetrical and custom asymmetrical designs. *Journal of Bone and Joint Surgery (American)*, 76, 95-103.

Hubbell, J.H. & S.M. Seltzer (1996). *Tables of X-ray mass attenuation coefficients and mass energy-absorption coefficients 1 keV to 20 MeV for elements Z= 1 to 92 and 48 additional substances of dosimetric interest* (No. PB--95-220539/XAB; NISTIR--5632). Ionizing Radiation Division, National Institute of Standards and Technology-PL, Gaithersburg, USA.

---

*Human Tissue Act* (2004). Chapter 30.

<<http://www.legislation.gov.uk/ukpga/2004/30/contents>>. Accessed 14<sup>th</sup> April 2011.

Ingham, E., T. R. Green, M. H. Stone, R. Kowalski, N. Watkins & J. Fisher (2000).

Production of TNF- $\alpha$  and bone resorbing activity by macrophages in response to different types of bone cement particles. *Biomaterials*, 21, 1005-1013.

Isaac, G.H., J.R. Atkinson, D. Dowson, P.D. Kennedy & M.R. Smith (1987). The causes of femoral head roughening in explanted Charnley hip prostheses. *Engineering in Medicine*, 16(3), 167-173.

James, S. P., M. Jasty, J. Davies, H. Piehler & W. H. Harris (1992). A fractographic investigation of PMMA bone cement focusing on the relationship between porosity and increased fatigue life. *Journal of Biomedical Materials Research*, 26, 651-662.

Janssen, D., J. Stolk & N. Verdonschot (2005a). Why would cement porosity reduction be clinically irrelevant, while experimental data show the contrary. *Journal of Orthopaedic Research*, 23, 691-697.

Janssen, D., R. Aquarius, J. Stolk & N. Verdonschot (2005b). The contradictory effects of pores on fatigue cracking of bone cement. *Journal of Biomedical Materials Research Part B: Applied Biomaterials*, 74B, 747-753.

Jasty, M., J.P. Davies, D.O. O'Conner, D.W. Burke, T.P. Harrigan & W.H. Harris (1990). Porosity of various preparations of acrylic bone cements. *Clinical Orthopaedics and Related Research*, 259, 122-129.

Jasty, M., W.J. Maloney, C.R. Bragdon, D.O. O'Conner, T. Haire & W.H. Harris (1991). The initiation of failure in cemented femoral components of hip arthroplasties. *Journal of Bone and Joint Surgery (British)*, 73-B, 551-558.

Jeffers, J. R. T., M. Browne, A. Roques & M. Taylor (2005a). On the importance of considering porosity when simulating the fatigue of bone cement. *Journal of Biomechanical Engineering*, 127, 563-570.

Jeffers, J. R. T., M. Browne & M. Taylor (2005b). Damage accumulation, fatigue and creep behaviour of vacuum mixed bone cement. *Biomaterials*, 26, 5532-5541.

Jeffers, J.R.T., M. Browne, A.B. Lennon, P.J. Prendergast & M. Taylor (2007). Cement mantle fatigue failure in total hip replacement: Experimental and computational testing. *Journal of Biomechanics*, 40, 1525-1533.

- Jennings, B. R. & K. Parslow (1988). Particle Size Measurement: The Equivalent Spherical Diameter. *Proceedings of the Royal Society of London Series A*, 419, 137-149.
- Jones, R.E., B.M. Willie, H. Hayes & R.D. Bloebaum (2005). Analysis of 16 retrieved proximally cemented femoral stems. *The Journal of Arthroplasty*, 20, 84-93.
- Kawate, K., W.J. Maloney, C.R. Bragdon, S.A. Biggs, M. Jasty & W.H. Harris (1998). Importance of a thin cement mantle: autopsy study of eight hips. *Clinical Orthopaedics and Related Research*, 355, 70-76.
- Kärrholm, J., G. Garrelick, C. Rogmark & P. Herberts (2007). *Annual Report*. The Swedish Hip Arthroplasty Register, Sweden.
- Keen, C.E., G. Philip, K. Brady, J.D. Spencer & D.A. Levison (1992). Histopathological and microanalytical study of zirconium dioxide and barium sulphate in bone cement. *Journal of Clinical Pathology*, 45, 984-989.
- Ketcham, R.A. & W.D. Carlson (2001). Acquisition, optimisation and interpretation of X-ray computed tomographic imagery: applications to the geosciences. *Computers & Geosciences*, 27(4), 381-400.
- Kim, S., M. Skibo, J. Manson & R. Hertzberg (1977). Fatigue crack propagation in poly(methyl methacrylate): effect of molecular weight and internal plasticization. *Polymer Engineering Science*, 17, 194-203.
- Kitano, T., G. A. Ateshian, V. C. Mow, Y. Kadoya & Y. Yamano (2001). Constituents and pH changes in protein rich hyaluronan solution affect the biotribological properties of artificial articular joints. *Journal of Biomechanics*, 34, 1031-1037.
- Kuehn, K.D., W. Ege & U. Gopp (2005a). Acrylic bone cements: composition and properties. *Orthopedic Clinics of North America*, 36, 17-28.
- Kuehn, K.D., W. Ege & U. Gopp (2005b). Acrylic bone cements: mechanical and physical properties. *Orthopedic Clinics of North America*, 36, 29-39.
- Kurtz, S. M., M. L. Villarraga, K. Zhao & A. A. Edidin (2005). Static and fatigue mechanical behavior of bone cement with elevated barium sulfate content for treatment of vertebral compression fractures. *Biomaterials*, 26, 3699-3712.

- Kutzner, I., B. Heinlein, F. Graichen, A. Bender, A. Rohlmann, A. Halder, A. Beier & G. Bergmann (2010). Loading of the knee joint during activities of daily living measured *in vivo* in five subjects. *Journal of Biomechanics*, 43, 2164-2173.
- Kuzmychov, O., C. Koplín, R. Jaeger, H. Büchner & U. Gopp (2009). Physical aging and the creep behaviour of acrylic bone cements. *Journal of Biomedical Materials Research Part B: Applied Biomaterials*, 91B, 910-917.
- Kwong, F.N.K. & R.A. Power (2006). A comparison of the shrinkage of commercial bone cements when mixed under vacuum. *Journal of Bone and Joint Surgery (British)*, 88-B, 120-122.
- Lampman, S. (2003). *Characterization and failure analysis of plastics*. ASM International.
- Lee, A., R. Ling & S. Vangala (1978). Some clinically relevant variables affecting the mechanical behaviour of bone cement. *Archives of Orthopaedic and Trauma Surgery*, 92, 1-18.
- Lefebvre, F. (2003) Micromechanical assessment of fatigue in airframe fusion welds. PhD thesis, School of Engineering Sciences, University of Southampton.
- Lennon, A.B. & P.J. Prendergast (2002). Residual stress due to curing can initiate damage in porous bone cement: experimental and theoretical evidence. *Journal of Biomechanics*, 35, 311-321.
- Lennon, A.B., B.A.O. McCormack & P.J. Prendergast (2003). The relationship between cement fatigue damage and implant surface finish in proximal femoral prostheses. *Medical Engineering and Physics*, 25, 833-841.
- Levine B.R., S. Sporer, R.A. Poggie, C.J. Della Valle & J.J. Jacobs (2006). Experimental and clinical performance of porous tantalum. *Biomaterials*, 27, 4671-4681.
- Lewis, G. (1997). Properties of Acrylic Bone Cement: State of the Art Review. *Journal of Biomedical Materials Research*, 38, 155-182.
- Lewis, G. & S. Mladiš (1997). Effect of sterilisation method on properties of Palacos-R acrylic bone cement. *Biomaterials*, 19, 117-124.
- Lewis G. (1999a). Apparent fracture toughness of acrylic bone cement: effect of test specimen configuration and sterilization method. *Biomaterials*, 20, 69-78.

- Lewis, G. (1999b). Effect of mixing method and storage temperature of cement constituents on the fatigue and porosity of acrylic bone cement. *Journal of Biomedical Materials Research (Applied Biomaterials)*, 48, 143-149.
- Lewis, G. & S. Mladi (2000). Correlation between impact strength and fracture toughness of PMMA-based bone cements. *Biomaterials*, 21, 775-781.
- Lewis G. (2003). Fatigue testing and performance of acrylic bone-cement materials: State-of-the-art review. *Journal of Biomedical Materials Research*, 66B, 457-486.
- Lewis, G., S. Janna & A. Bhattaram (2005). Influence of the method of blending an antibiotic powder with an acrylic bone cement on physical, mechanical, and thermal properties of the cured cement. *Biomaterials*, 26, 4317-4325.
- Lewis, G. (2008). Alternative Bone Cement Formulations for Cemented Arthroplasties: Present Status, Key Issues, and Future Prospects. *Journal of Biomedical Materials Research*, 84B, 301-319.
- Lewis, G. (2009). Properties of antibiotic-loaded acrylic bone cements for use in cemented arthroplasties: A state-of-the-art review. *Journal of Biomedical Materials Research*, 89B:2, 558-574.
- Li, Y., Wang, X., Cui, Y., Ma, W., & Guo, H. (2012). High Dispersion Barium Sulfate Nanoparticles Prepared with Dodecyl Benzene Sulfonic Acid. *International Journal of Nanoscience*, 11(06).
- Lindén, U. (1988). Porosity in manually mixed bone cement. *Clinical Orthopaedics and Related Research*, 231, 110-112.
- Ling, R. S. & A. J. Lee (1998). Porosity reduction in acrylic cement is clinically irrelevant. *Clinical Orthopaedics*, 355, 249-253.
- Liu C., S.M. Green, N.D. Watkins, P.J. Gregg & A.W. McCaskie (2001). Some failure modes of four clinical bone cements. *Proceedings of the Institution of Mechanical Engineers, Part H: Journal of Engineering in Medicine*, 215, 359-366.
- Liu, C., S.M. Green, N.D. Watkins, P.J. Gregg & A.W. McCaskie (2002). Creep behaviour comparison of CMW1 and Palacos R-40 clinical bone cements. *Journal of Materials Science: Materials in Medicine*, 13, 1021-1028.

- Malchau, H., P. Herberts, P. Söderman & A. Odén (2000). *Prognosis of total hip replacement: update and validation of results from the Swedish National Hip Arthroplasty Register*. 67<sup>th</sup> Annual Meeting of the American Academy of Orthopaedic Surgeons, Orlando, USA.
- Mann, K.A., S. Gupta, A. Race, M.A. Miller, R.J. Cleary & D.C. Ayers (2004). Cement microcracks in thin-mantle regions after *in vitro* fatigue loading. *The Journal of Arthroplasty*, 19, 605-612.
- Marchisio, D. L., Barresi, A. A., & Garbero, M. (2002). Nucleation, growth, and agglomeration in barium sulfate turbulent precipitation. *AIChE journal*, 48(9), 2039-2050.
- Mau, H., K. Schelling, C. Heisel, J.S. Wang & S.J. Breusch (2004). Comparison of various vacuum mixing systems and bone cements as regards reliability, porosity and bending strength. *Acta Orthopaedica Scandinavia*, 75(2), 160-172.
- Mbuya, T.O. (2011). *Analysis of microstructure and fatigue micromechanisms in cast aluminium piston alloys*. PhD thesis, Faculty of Engineering and the Environment, University of Southampton.
- McCaskie, A.W., M. Roberts & P.J. Gregg (1995). Human tissue retrieval at post-mortem for musculoskeletal research. *British Journal of Biomedical Sciences*, 52 (3), 222-224.
- McCormack, B. A. O. & P. J. Prendergast (1999). Microdamage accumulation in the cement layer of hip replacements under flexural loading. *Journal of Biomechanics*, 32, 467-475.
- Messick, K.J., M.A. Miller, L.A. Damron, A. Race, M.T. Clarke & K.A. Mann (2007). Vacuum-mixing cement does not decrease overall porosity in cemented femoral stems. *Journal of Bone & Joint Surgery (British)*, 89-B (8), 1115-1121.
- Molino, L. N. & L. D. T. Topoleski (1996). Effect of BaSO<sub>4</sub> on the fatigue crack propagation rate of PMMA bone cement. *Journal of Biomedical Materials Research*, 31, 131-137.
- Muller, S.D. & A.W. McCaskie (2006). Dynamic void behavior in polymerizing polymethyl methacrylate cement. *The Journal of Arthroplasty*, 21(2), 279-283.
- Murakami, Y. (2002). *Metal Fatigue: Effects of Small Defects and Nonmetallic Inclusions*. Elsevier.

- Murphy, B. P. & P. J. Prendergast (2000). On the magnitude and variability of the fatigue strength of acrylic bone cement. *International Journal of Fatigue*, 22, 855-864.
- Nadot, Y., J. Mendez, N. Ranganathan & A.S. Beranger (1999). Fatigue life assessment of nodular cast iron containing casting defects. *Fatigue and Fracture of Engineering Materials and Structures (UK)*, 22(4), 289-300.
- NAR (2010). *Annual Report: June 2010*. The Norwegian Arthroplasty Register.
- NHS (2012). NHS Choices:  
<http://www.nhs.uk/Conditions/Arthritis/Pages/Introduction.aspx>. Accessed 08 April 2012.
- Nicoletto, G., G. Anzelotti & R. Konečná (2010). X-ray computed tomography vs. metallography for void sizing and fatigue of cast Al-alloys. *Procedia Engineering*, 2(1), 547-554.
- Nixon, M. & A. Aguado (2008). *Feature Extraction and Image Processing*, 2<sup>nd</sup> edition, Chapter 3. Elsevier.
- NJR (2012). *National Joint Registry: 9th Annual Report*. National Joint Registry for England and Wales.
- Orr, J. F., N. J. Dunne & J. C. Quinn (2003). Shrinkage stresses in bone cement. *Biomaterials*, 24, 2933-2940.
- Pelletier, B., K. Hughes & N. Gundiah (1999). A study of the in vivo molecular degradation of acrylic bone cements used in cemented total joint arthroplasties. In: *Transactions of the 45th Annual Meeting of the Orthopaedic Research Society*, Anaheim, California. 514.
- Pelletier, M.H., A.C.B. Lau, P.J. Smitham, G. Nielsen & W.R. Walsh (2010). Pore distribution and material properties of cement cured at different temperatures. *Acta Biomaterialia*, 6(3), 886-891.
- Pilliar, R.M. (2005). Cementless implant fixation – towards improved reliability. *Orthopedic Clinics of North America*, 36, 113-119.
- Plewes, D.B. & P.B. Dean (1981). The influence of partial volume averaging on sphere detectability in computed tomography. *Physics in Medicine and Biology*, 26, 913-919.

- Pratt C.M., S. Barton, E. McGonigle, M. Kishi & P.J.S. Foot (2006). The effect of ionising radiation on poly(methyl methacrylate) used in intraocular lenses. *Polymer Degradation and Stability*, 91, 2315-2317.
- Pulos, G. C. & W. G. Knauss (1998). Nonsteady crack and craze behaviour in PMMA under cyclical loading: II. Effect of load history on growth rate and fracture morphology. *International Journal of Fracture*, 93, 161-185.
- Race, A., M.A. Miller, D.C. Ayers & K.A. Mann (2003). Early cement damage around a femoral stem is concentrated at the cement/bone interface. *Journal of Biomechanics*, 36, 489-496.
- Race, A., M.A. Miller, T.H. Izant & K.A. Mann (2011). Direct evidence of “damage accumulation” in cement mantles surrounding femoral hip stems retrieved at autopsy: Cement damage correlates with duration of use and BMI. *Journal of Biomechanics*, 44, 2345-2350.
- Reynolds, L. A. & E.M. Tansey (2007). Early Development of Total Hip Replacement . In *Wellcome Witnesses to Twentieth Century Medicine*, 29. London: Wellcome Trust Centre for the History of Medicine at UCL.
- Rice, J., T. Prenderville, P. Murray, B. McCormack & W. Quinlan (1998). Femoral cementing techniques in total hip replacement. *International Orthopaedics*, 22 (5), 308-311.
- Riegels-Neilsen P., L. Sorenson, H.M. Andersen & S. Lindequist (1995). Bone-loc cemented total hip prostheses: Loosening in 28/43 cases after 3-38 months. *Acta Orthopaedica Scandinavica*, 66, 215-217.
- Ries, M.D., E. Young, L. Al-Marashi, P. Goldstein, A. Hetherington, T. Petrie & L. Pruitt (2006). In vivo behavior of acrylic bone cement in total hip arthroplasty. *Biomaterials*, 26, 256-261.
- Roques, A., M. Browne, A. Taylor, A. New & D. Baker (2004). Quantitative measurement of the stresses induced during polymerisation of bone cement. *Biomaterials*, 25, 4415-4424.
- Sabokbar, A., Y. Fujikawa, D.W. Murray & N.A. Athanasou (1997). Radio-opaque agents in bone cement increase bone resorption. *Journal of Bone and Joint Surgery (British)*, 79(1), 129-134.

- Scheirs, J. (2000). *Composition and failure analysis of polymers: A practical approach*. Wiley Blackwell.
- Schulze, M. (2012). Personal communication.
- Sinnett-Jones, P.E., M. Browne, W. Ludwig, J.-Y. Buffiere & I. Sinclair (2005). Microtomography assessment of failure in acrylic bone cement. *Biomaterials*, 26, 6460-6466.
- Sinnett-Jones, P. (2007). *Micromechanical aspects of fatigue failure in conventional and carbon nanotube-reinforced acrylic bone cement*. PhD thesis, School of Engineering Sciences, University of Southampton.
- Sinnett-Jones, P.E., M. Browne, A.J. Moffatt, J.R.T. Jeffers, N. Saffar, J.-Y. Buffiere & I. Sinclair (2009). Crack initiation processes in acrylic bone cement. *Journal of Biomedical Materials Research Part A*, 89, 1088-1097.
- Skibo, M.D., R.W. Hertzberg, J.A. Manson & S.L. Kim (1977). On the generality of discontinuous fatigue crack growth in glassy polymers. *Journal of Materials Science*, 12, 531-542.
- Soltész, U. (1994). The influence of loading conditions on the life-times in fatigue testing of bone cements. *Journal of Materials Science: Materials in Medicine*, 5, 654-656.
- Söderman, P. (2000). On the validity of the results from the Swedish National Hip Register. *Acta Orthopaedica Scandinavia: Supplementum*. 71 (296), 1-33.
- Stanczyk, M. & B. van Rietbergen (2004). Thermal analysis of bone cement polymerisation at the cement-bone interface. *Journal of Biomechanics*, 37, 1803-1810.
- Stolk, J., S.A. Maher, N. Verdonschot, P.J. Prendergast and R. Huiskes (2003). Can finite element models detect clinically inferior cemented hip implants? *Clinical Orthopaedics and Related Research*, 409, 138-150.
- Stolk, J., N. Verdonschot, B.P. Murphy, P.J. Prendergast & R. Huiskes (2004). Finite element simulation of anisotropic damage accumulation and creep in acrylic bone cement. *Engineering Fracture Mechanics*, 71, 513-528.
- Suresh, S. (1998). *Fatigue of Materials*. Cambridge University Press.
- Susmel, L. (2008). The theory of critical distances: a review of its applications in fatigue. *Engineering Fracture Mechanics*, 75(7), 1706-1724.

- Taylor, D. (1989). *Fatigue Thresholds*. Butterworths.
- Taylor, D. (2008). The theory of critical distances. *Engineering Fracture Mechanics*, 75(7), 1696-1705.
- Tijani, Y., A. Heinrietz, T. Bruder & H. Hanselka (2013). Quantitative Evaluation of Fatigue Life of Cast Aluminium Alloys by Non-Destructive Testing and Parameter Model. *International Journal of Fatigue*, 57, 73-78.
- Topoleski, T. L. D., P. Ducheyne & J.M. Cuckler (1990). A fractographic analysis of in vivo poly(methyl methacrylate)bone-cement failure mechanisms. *Journal of Biomedical Materials Research*, 24, 135-154.
- Topoleski, T. L. D., P. Ducheyne & J.M. Cuckler (1993). Microstructural pathway of fracture in poly(methylmethacrylate) bone-cement. *Biomaterials*, 14, 1165-1172.
- Tynnyi, A.N., S.I. Mikitishin, A.A. Velikovskii, Y.N. Khomitskii & Y.A. Kolevatov (1967). Effect of X-rays on the strength of Polymethylmethacrylate. *Journal of Materials Science*, 3, 31-33.
- Vallo, C.I. (2002a). Flexural strength distribution of a PMMA-based bone cement. *Journal of Biomedical Materials Research (Applied Biomaterials)*, 63, 226-236.
- Vallo, C.I. (2002b). Influence of load type on flexural strength of a bone cement based on PMMA. *Polymer Testing*, 21, 793-800.
- Van Hooy-Corstjens, C.S.J., L.E. Govaert, A.B. Spoelstra, S.K. Bulstra, G.M.R. Wetzels & L.H. Koole (2004). Mechanical behaviour of a new acrylic radiopaque iodine-containing bone cement. *Biomaterials*, 25, 2657-2667.
- Vanderesse, N., E. Maire, A. Chabod & J.Y. Buffiere (2011). Microtomographic study and finite element analysis of the porosity harmfulness in a cast aluminium alloy. *International Journal of Fatigue*, 33(12), 1514-1525.
- Verdonschot, N. & R. Huiskes (1997a). The effects of cement-stem debonding in THA on the long-term failure probability of cement. *Journal of Biomechanics*, 30, 795-802.
- Verdonschot, N. & R. Huiskes (1997b). Acrylic cement creeps but does not allow much subsidence of femoral stems. *Journal of Bone & Joint Surgery (British)*, 79, 665-669.

- Vidal, T. P., J. M. Letang, G. Peix & P. Cloetens (1995). Investigation of artefact sources in synchrotron microtomography via virtual X-ray imaging. *Nuclear Instruments and Methods in Physics Research B*, 234, 338-348.
- Volume Graphics (2010). *VG Studio Max 2.1 Reference Manual*. Volume Graphics GmbH, Heidelberg, Germany.
- Waanders, D., D. Janssen, K.A. Mann & N. Verdonschot (2010). The effect of cement creep and cement fatigue damage on the micromechanics of the cement-bone interface. *Journal of Biomechanics*, 43, 3028-3034.
- Walczak, J.P., J.C. D'Arcy, K.R. Ross, S.E. James, A.V. Bonnici, S.R. Koka & R.W. Morris (2000). Low-friction arthroplasty with Bone-loc bone cement: outcome at 2 to 4 years. *The Journal of Arthroplasty*, 15, 205-209.
- Wang, J.S., H. Franzén, E. Jonsson & L. Lidgren (1993). Porosity of bone cement reduced by mixing and collecting under vacuum. *Acta Orthopaedica Scandinavia*, 64(2), 143-146.
- Wang, J.S., S. Toksvig-Larsen, P. Müller-Wille & H. Franzén (1996). Is there any difference between vacuum mixing systems in reducing bone cement porosity? *Journal of Biomedical Materials Research (Applied Biomaterials)*, 33, 115-119.
- Wang, Q.G., D. Apelian & D.A. Lados (2001). Fatigue behavior of A356-T6 aluminum cast alloys. Part I. Effect of casting defects. *Journal of Light Metals*, 1(1), 73-84.
- Wang, Q.G. & P.E. Jones (2007). Prediction of fatigue performance in aluminum shape castings containing defects. *Metallurgical and Materials Transactions B*, 38(4), 615-621.
- Wang, Z. L., Liu, Y., & Zhang, Z. (Eds.). (2002). *Handbook of Nanophase and Nanostructured Materials: Synthesis/Characterization/Materials Systems and Applications I/Materials Systems and Applications II*. Springer.
- Watson, M. B., A. W. Miles & S. E. Clift (1990). The influence of curing time and environment on the fracture properties of bone cement. *Clinical Materials*, 6, 299-305.
- Williams, R.P. & D.A. McQueen (1992). A histopathologic study of late aseptic loosening of cemented total hip prostheses. *Clinical Orthopaedics and Related Research*, 275, 174-179.

- Wimhurst, J.A., R.A. Brooks & N. Rushton (2001). The effects of particulate bone cements at the bone-implant interface. *Journal of Bone and Joint Surgery (British)*, 83, 588-592.
- Wixson, R.L., E.P. Lautenschlager & M.A. Novak (1987). Vacuum mixing of acrylic bone cement. *The Journal of Arthroplasty*, 2, 141-149.
- Wroblewski, B.M., P.D. Siney & P.A. Fleming (2005). Charnley low frictional torque arthroplasty: clinical developments. *Orthopedic Clinics of North America*, 36, 11-16.
- Wolff J. (1892). *Das Gesetz der Transformation der Knochen*. Hirschwald, Berlin.
- Wolff J. (1986). *The Law of Bone Remodeling*. Berlin Heidelberg New York: Springer (translation of the German 1892 edition).
- Wong, D. C. Y., Jaworski, Z., & Nienow, A. W. (2001). Effect of ion excess on particle size and morphology during barium sulphate precipitation: an experimental study. *Chemical engineering science*, 56(3), 727-734.
- Wykman, A. & E. Olsson (1992). Walking ability after total hip replacement. *Journal of Bone & Joint Surgery (British)*, 74-B, 53-56.
- Yi, J.Z., P.D. Lee, T.C. Lindley & T. Fukui (2006). Statistical modeling of microstructure and defect population effects on the fatigue performance of cast A356-T6 automotive components. *Materials Science and Engineering: A*, 432(1), 59-68.
- Young, R.J. & P.A. Lovell (1991). *Introduction to Polymers*, 2<sup>nd</sup> edition. CRC Press.
- Zhai, T., Y. G. Xu, J. W. Martin, A. J. Wilkinson & G. A. D. Briggs (1999). A self-aligning four-point bend testing rig and sample geometry effect in four-point bend fatigue. *International Journal of Fatigue*, 21, 889-894.
- Zhu, X., J.Z. Yi, J.W. Jones & J.E. Allison (2007). A probabilistic model of fatigue strength controlled by porosity population in a 319-type cast aluminum alloy: part I. Model development. *Metallurgical and Materials Transactions A*, 38(5), 1111-1122.



---

---

## A. LIST OF PUBLICATIONS

---

---

### A.1 JOURNAL PUBLICATIONS

Shearwood-Porter, N., M. Browne & I. Sinclair (2012). Micromechanical characterisation of failure in acrylic bone cement: the effect of barium sulphate agglomerates. *Journal of Mechanical Behavior of Biomedical Materials*, 13, 85-92.

### A.2 CONFERENCE PRESENTATIONS

Shearwood-Porter, N., M. Browne & I. Sinclair (2011). *Assessing the fatigue performance of commercial bone cements*. 4<sup>th</sup> International Conference on Fatigue Design, Senlis, France.

Shearwood-Porter, N., M. Browne & I. Sinclair (2011). *Micromechanical characterisation of failure in acrylic bone cement: the effect of radiopacifier particles*. 19<sup>th</sup> Annual Meeting of the European Orthopaedic Research Society, Vienna, Austria.

Shearwood-Porter, N., M. Browne & I. Sinclair (2010). *Micromechanical characterisation of failure in acrylic bone cement due to barium sulphate agglomeration*. 23<sup>rd</sup> European Conference on Biomaterials, Tampere, Finland.



---

---

## B. VALIDATION OF PARTICLE ANALYSIS PLUG-IN

---

---

The accuracy of the particle analysis plug-in (developed by Eric Maire, Université de Lyon, INSA-Lyon, MATEIS CNRS, Villeurbanne, France) used for quantitative analysis of microstructural populations in Image J 1.4.1 (National Institutes of Health, Bethesda, USA) was checked against synthetic test images as described below.

An arbitrary image stack, produced from 7 identical SEM micrographs of ZrO<sub>2</sub> particles on the surface of a polished Palacos R cement specimen (Figure B-1(i)), was used to validate the results of the particle analysis plug-in. Each particle was plotted in Microsoft Excel 2007 using the *x* and *y* coordinates and volume (in pixels) recorded by the plug-in. The resulting graph is displayed in Figure B-2, and demonstrates very good agreement in the size and position of particles when compared to the binarised version of the original micrograph (Figure B-1(ii)). It should be noted that the data has been plotted as a series of circles of representative size, rather than as an exact fit. Despite this, on visual inspection the particle analysis plug-in was considered to provide accurate and reliable quantification of microstructural features extracted from the CT data.

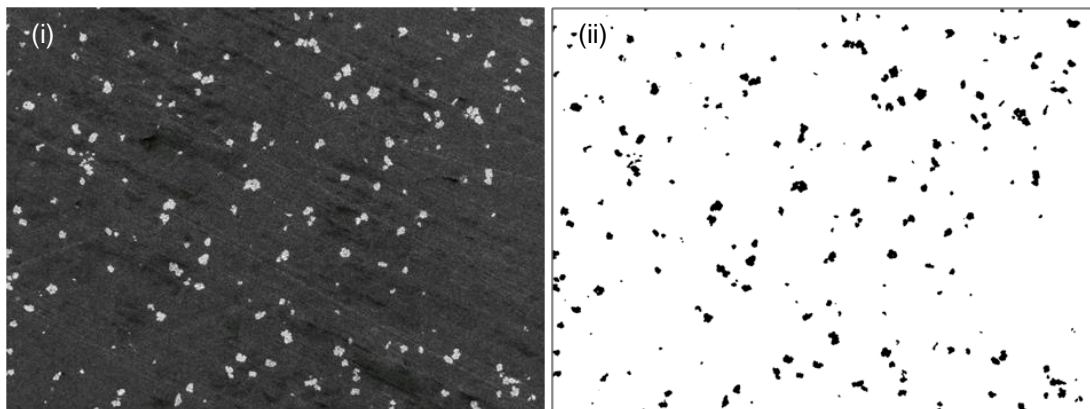


Figure B-1: Distribution of ZrO<sub>2</sub> particles on polished cement surface. (i) SEM micrograph (ii) Post-processing image

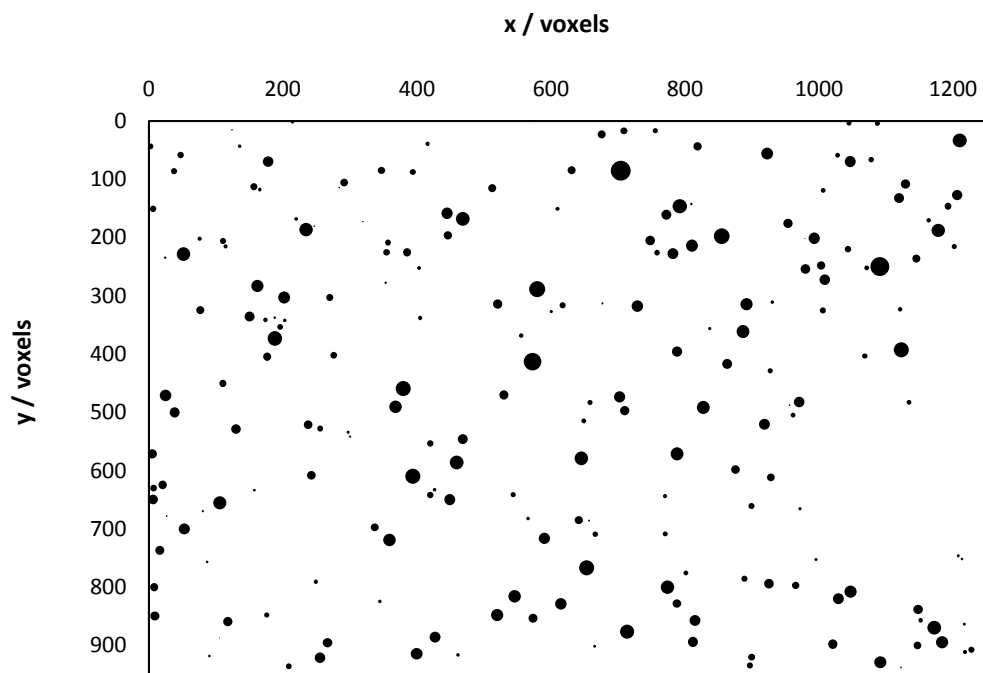


Figure B-2: Volume and position of ZrO2 particles (plotted as circles of proportional area using data returned by particle analysis plug-in).

---

## C. FURTHER CHARACTERISATION OF CEMENT MICROSTRUCTURE

---

The work described in this thesis investigated the effect of microstructure on fatigue crack initiation processes in acrylic bone cement. As such, prior understanding of the characteristics of the cement microstructure, and variation between formulations, was necessary in order to explore the micro-mechanisms of failure. Qualitative examination of polished surfaces of each of the cement formulations was conducted using SEM as previously described (Section 3.4.2). The characteristics of the cement powder components were then explored using  $\mu$ -CT (as described in Section 3.4 and Section 3.5), focusing in particular on the morphology and dispersion of the radiopacifier constituent.

### C.1 POLISHED CEMENT SURFACES

Inspection of polished cement surfaces using SEM revealed the microstructure of the cement at higher resolution (Figure C-1). On the surface of CMW-1 cement, small particles of barium sulphate ( $\sim 2 \mu\text{m}$ ) were distributed within the polymer matrix surrounding pre-polymerised beads. In contrast, pre-polymerised beads in the other cements could not be distinguished from the surrounding matrix, even at 2000 x magnification. Zirconium dioxide present on the surfaces of Palacos R and Smartset HV appeared to be somewhat larger (5 – 50  $\mu\text{m}$  across) and irregularly shaped. This variation in morphology, and the presence of matrix polymer within the zirconium dioxide, suggests the radiopacifier typically forms agglomerates composed of smaller particles. No separation or voiding was noted between the radiopacifier particles and surrounding polymer in any of the radiopaque cements.

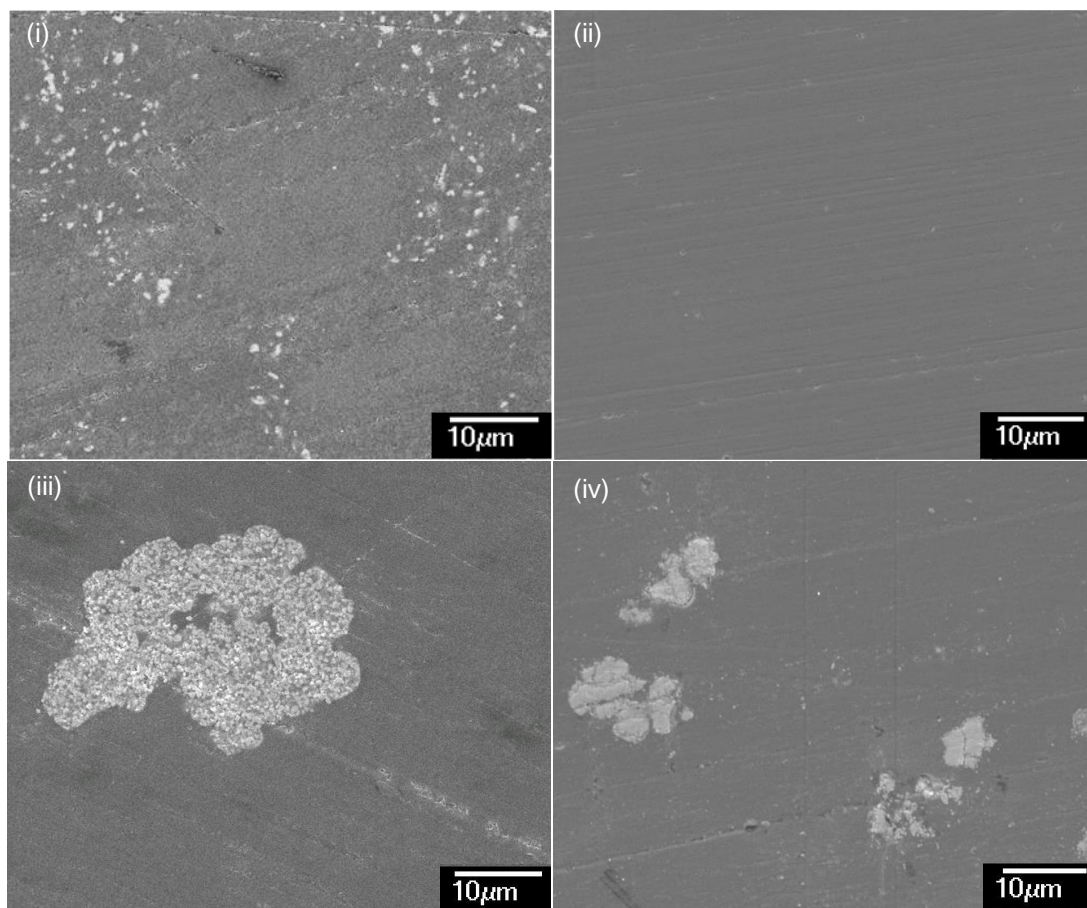


Figure C-1: SEM micrographs of polished cement surfaces, demonstrating morphology of radiopacifier particles, where applicable: (i) CMW-1, (ii) CMW Original, (iii) Palacos R and (iv) Smartset HV.

## C.2 CEMENT POWDER CHARACTERISATION

To investigate the dispersion of radiopacifier particles within the powder constituent of the radiopaque cements, specimens of unmixed cement powder (containing pre-polymerised beads, BPO and radiopacifier particles, if applicable) from each cement formulation were prepared in glass vials and CT scanned at a resolution of 9.8 microns. CMW Original (radiolucent) cement was included in this study as a control specimen. Typical CT slices for the different cement formulations are shown in Figure C-2, highlighting the variation in radiopacifier distribution.

CT images of the cement powders (Figure C-2) were remarkably similar to those of the cured cements (Figure C-3). Numerous large agglomerates of barium sulphate were evident in the CMW-1 powder. No radiopacifier particles were seen in the radiolucent control formulation (CMW Original), as expected. Smartset HV appeared to have a finer, more uniform distribution of radiopacifier particles than Palacos R; however, a few bright spots, indicating the presence of large agglomerates of zirconium dioxide within powder, were also evident in Smartset HV but did not appear in the Palacos R cement powder.

Agglomerates of radiopacifier particles that were visible at the specified resolution (i.e.  $>10\mu\text{m}^3$ ) were segmented from the reconstructed volumes, and quantified using Image J software as described in Section 3.5.3. Radiopacifier particles were defined as voxels with grayscale values  $>1000$  units higher than the darkest voxels in the matrix. The results of this analysis for each of the radiopaque cements are detailed in Table C-1. Volumes are expressed in terms of equivalent spherical diameter (ESD), i.e. the diameter of a sphere with the same volume as the particle (Jennings and Parslow 1988).

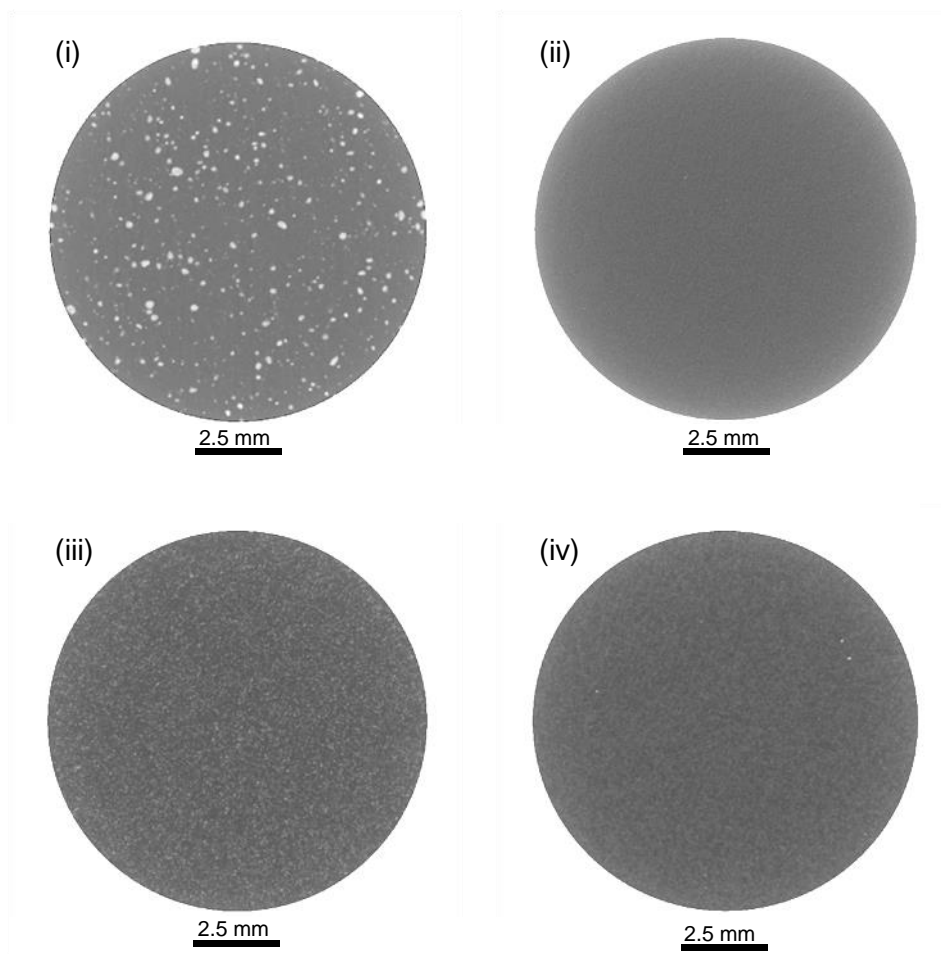


Figure C-2: Cross-sectional CT slices illustrating variation of radiopacifier dispersal in unmixed powder: (i) CMW-1, (ii) CMW Original, (iii) Palacos R, and (iv) Smartset HV.

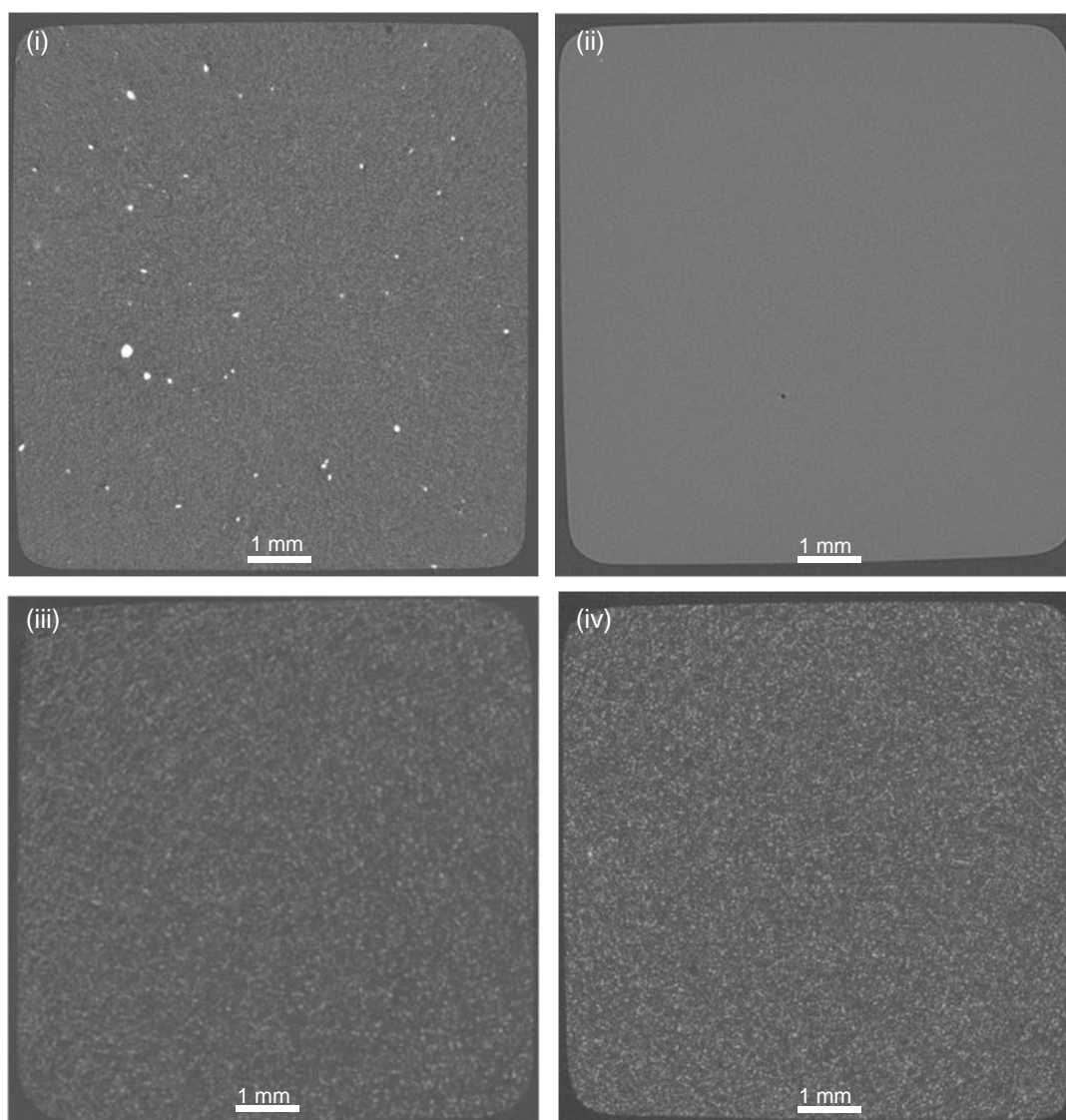


Figure C-3: Representative CT slices highlighting variation in microstructure between cement formulations: (i) CMW-1, (ii) CMW Original, (iii) Palacos R and (iv) Smartset HV. This data has been presented in Chapter 4 and Chapter 5, and is included again here for comparative purposes.

Table C-1: Characteristics of radiopacifier agglomerates in cement powder constituents.

Cement	CMW-1	Palacos R	Smartset HV
No. radiopacifier agglomerates per mm <sup>3</sup>	82.58	0.18	3.35
Volume (%)	4.76 %	0.03 %	0.01 %
Mean ESD (mm)	0.103	0.036	0.032
Largest ESD (mm)	0.364	0.078	0.116

The most significant clustering of radiopacifier particles was observed in CMW-1 cement, which demonstrated the highest spatial frequency, mean and maximum cluster size. Palacos R and Smartset HV showed a similar mean cluster size, though Smartset HV had a greater maximum cluster size, and more frequent clustering at all size intervals. Modal cluster size for both Palacos R and Smartset HV occurred in the smallest discernible size interval (0.0124 – 0.0267 mm ESD, equating to a volume of approximately 1-10 voxels), while the most frequent cluster size in CMW-1 occurred in the 0.0576 – 0.124 mm interval (~101-1000 voxels). CMW-1 was the only cement powder to contain agglomerates larger than 0.116 mm ESD (Figure C-4).

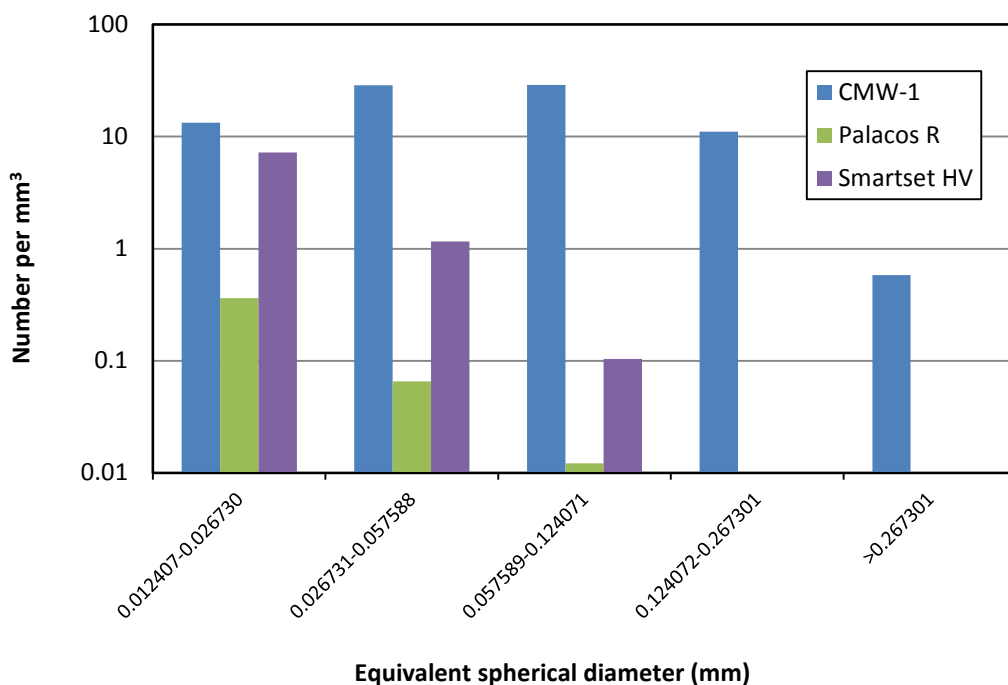


Figure C-4: Size distribution of radiopacifier particles in CMW-1, Palacos R and Smartset HV.

---



---

## D. ANATOMICAL TERMS OF LOCATION

---



---

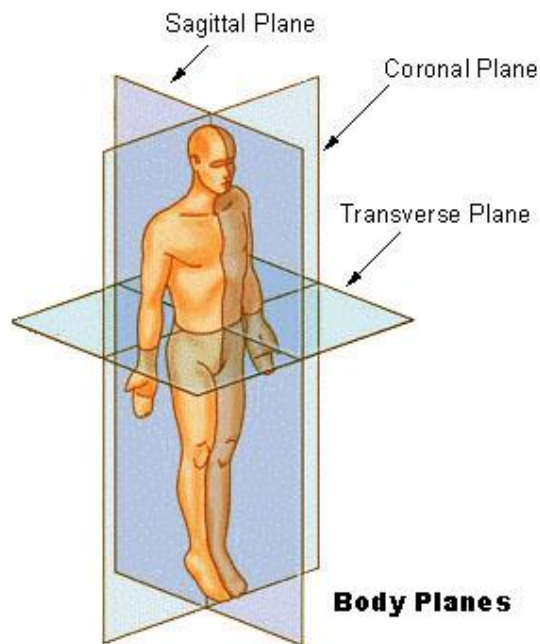


Figure D-1: Anatomical planes in the human body<sup>1</sup>

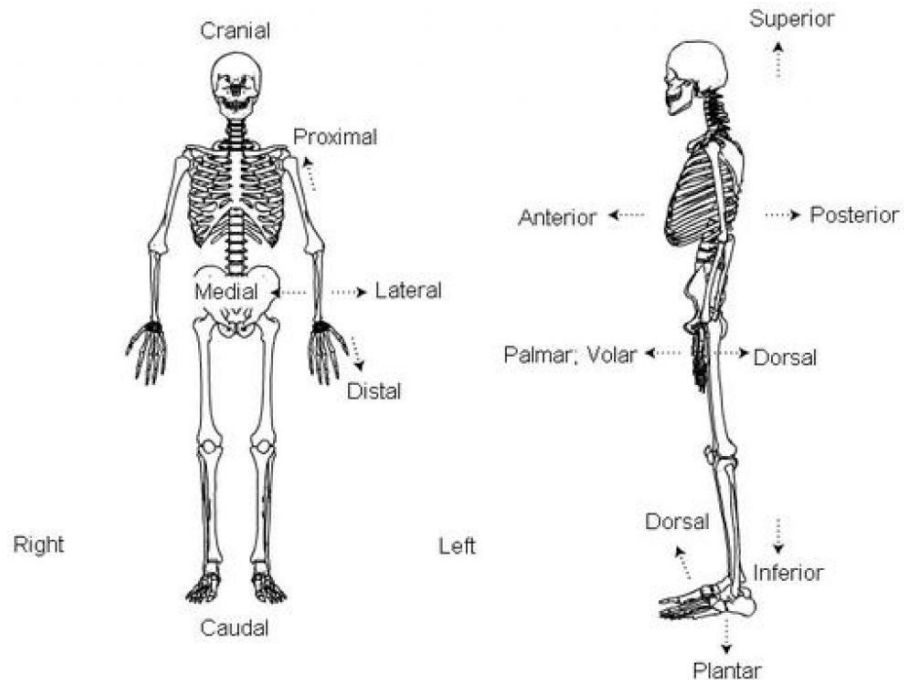


Figure D-2: Anatomical directions in the human body <sup>2</sup>

<sup>1</sup> <http://upload.wikimedia.org/wikipedia/commons/3/34/BodyPlanes.jpg>

<sup>2</sup> <http://img19.imageshack.us/img19/3883/imgpressfit10001000urlh.jpg>



---



---

## E. STATISTICAL ANALYSIS OF DEFECT SIZE DISTRIBUTIONS

---



---

### E.1 METHODOLOGY

The void and agglomerate size distributions for all four cement types, as shown in Figure 4-4 and Figure 5-4, were analysed using Microsoft Excel and a statistical distribution-fitting software package (EasyFit Professional 5.5, MathWave Technologies, Dnepropetrovsk, Ukraine). Values of equivalent spherical diameter obtained from the CT data were imported into the EasyFit software. The software compared the observed data with a number of distribution functions, including normal, two and three parameter log-normal, one and two parameter exponential, Weibull and general extreme value (GEV) functions. Cumulative distribution, probability density, probability-probability (P-P), quantile-quantile (Q-Q) and probability difference plots were generated for each distribution function, and the relevant parameters calculated. The functions were ranked in order of best fit, and analysed using Kolmogorov-Smirnov (K-S), Anderson-Darling (A-D) and Chi-Squared ( $\chi^2$ ) goodness-of-fit tests.

### E.2 CMW ORIGINAL VOIDS

The distribution of CMW Original voids was best approximated by a 3-parameter log-normal distribution described by the probability density function:

$$f(x) = \frac{\exp\left(-\frac{1}{2}\left(\frac{\ln(x-\gamma)-\mu}{\sigma}\right)^2\right)}{(x-\gamma)\sigma\sqrt{2\pi}}$$

where  $\sigma=1.058$ ,  $\mu=-4.1258$  and  $\gamma=0.0101$ . However, the fit was relatively poor. At a standard significance level of 0.05, the function passed the K-S test but failed the A-D and  $\chi^2$  tests. The probability density and P-P plots for this model are shown in Figure E-1.

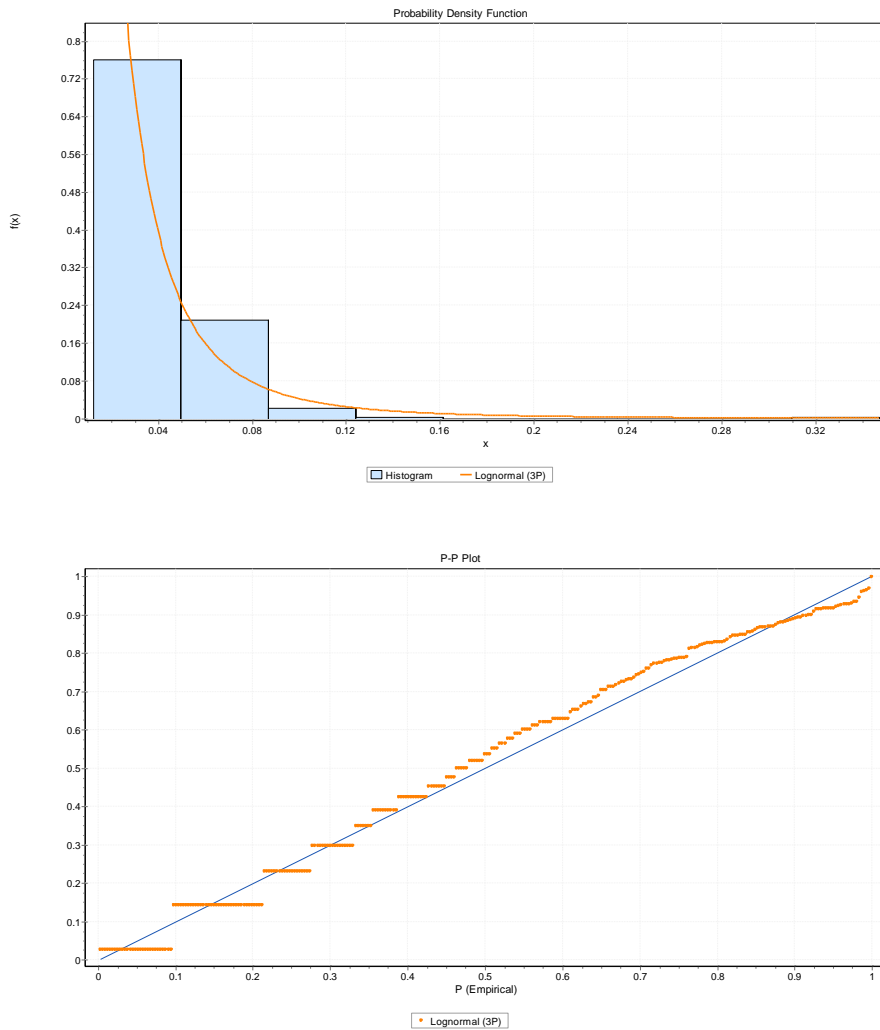


Figure E-1: Probability density function and P-P plot for 3-parameter log-normal model of CMW Original void size distribution.

### E.3 CMW-1 VOIDS

The size distribution of CMW-1 voids was not well described by any of the tested distribution functions; the 3-parameter log-normal distribution was the highest ranked but did not pass the goodness-of-fit tests at any significance level. The fit was especially poor at the lower tail of the size distribution. The data was reanalysed for all voids exceeding 0.04 mm ESD, and was found to be approximated by a 3-parameter lognormal distribution function with values  $\sigma=0.98763$ ,  $\mu=-4.8717$  and  $\gamma=0.03925$ . The probability density and P-P plots for both models are shown in Figures E-2 and E-3.

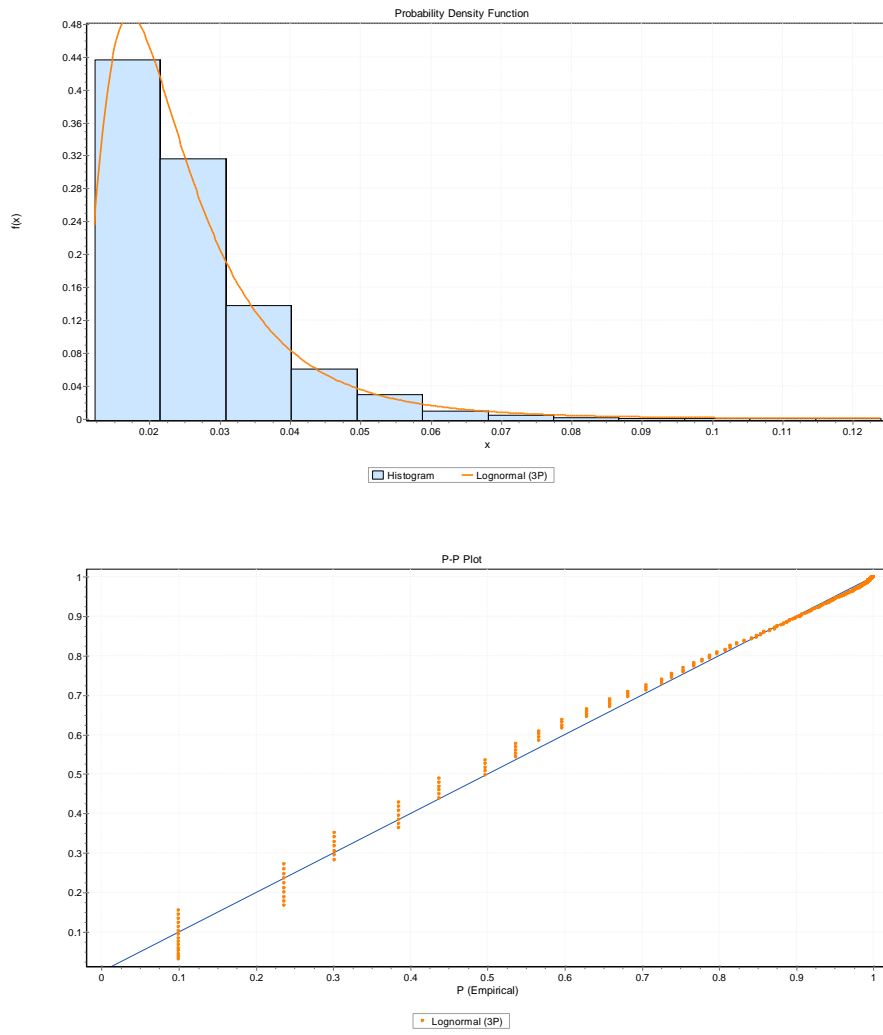
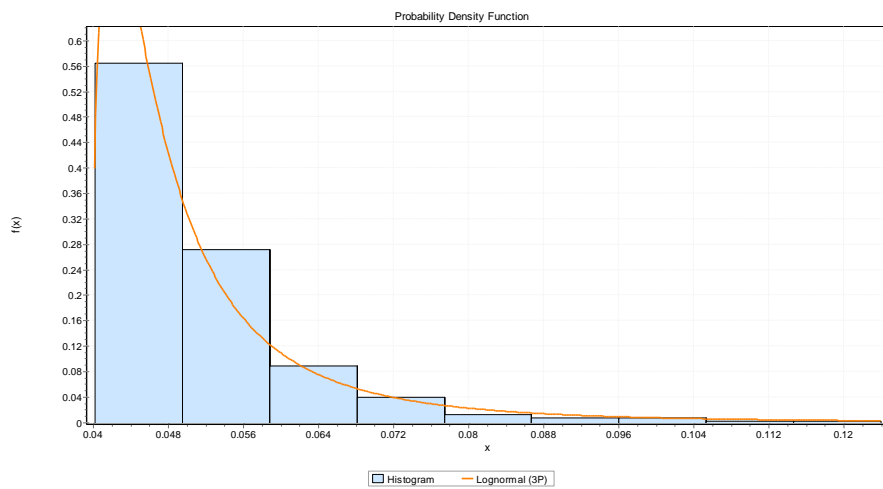


Figure E-2: Probability density function and P-P plot for 3-parameter log-normal model of CMW-1 void size distribution.



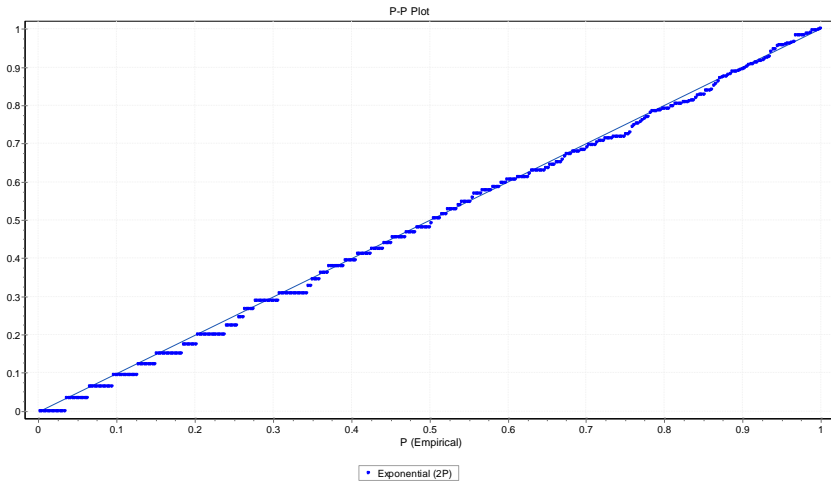


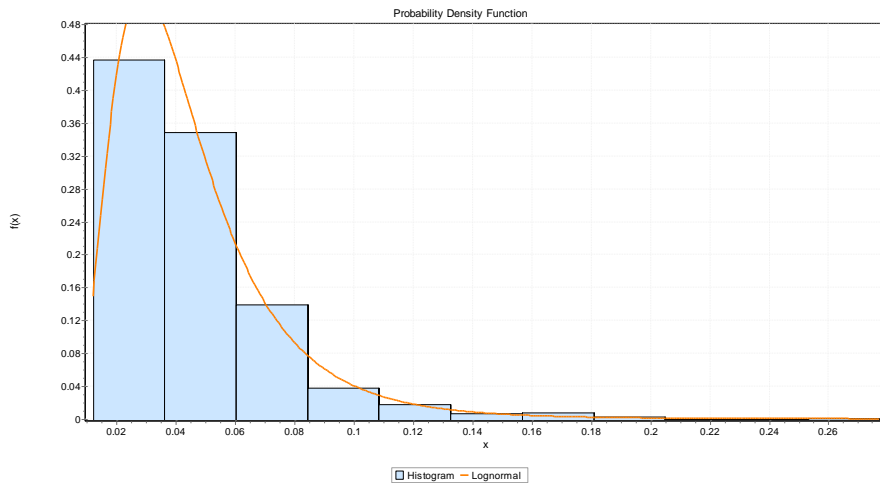
Figure E-3: Probability density function and P-P plot for 3-parameter log-normal model of CMW-1 void size distribution for voids >0.04mm ESD.

#### E.4 CMW-1 AGGLOMERATES

The size distribution of CMW-1 agglomerates was well-described by a two-parameter log-normal distribution function with probability density:

$$f(x) = \frac{\exp\left(-\frac{1}{2}\left(\frac{\ln x - \mu}{\sigma}\right)^2\right)}{x \sigma \sqrt{2\pi}}$$

where  $\sigma=0.54839$  and  $\mu=-3.2419$ . When using the A-D test, this model was considered to be a good fit at a significance level of 0.05. The probability density and P-P plots are shown in Figure E-4.



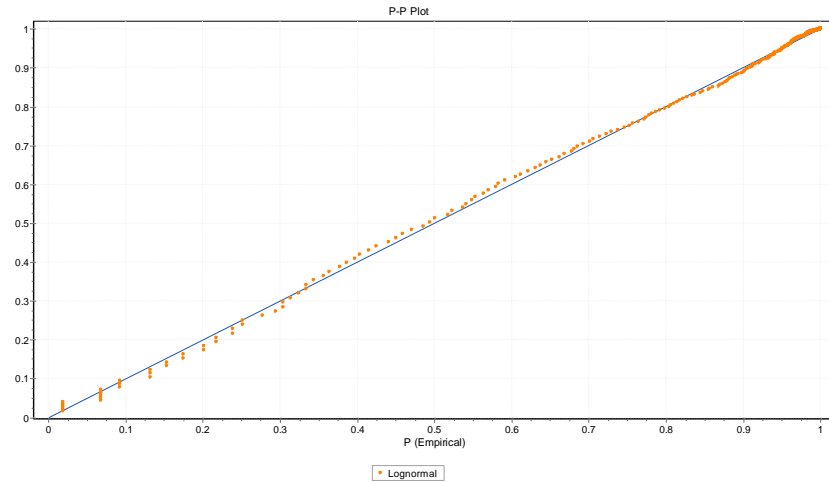


Figure E-4: Probability density function and P-P plot for 2-parameter log-normal model of CMW-1 agglomerate size distribution.

## E.5 PALACOS R VOIDS

The size distribution of Palacos R voids could not be fitted to any of the selected distribution functions. The fit was especially poor for defect sizes smaller than 0.08 mm ESD.

## E.6 PALACOS R AGGLOMERATES

The size distribution of radiopacifier agglomerates in Palacos R cement was best described by a 3-parameter log-normal distribution function with the following parameter values  $\sigma=0.49691$ ,  $\mu=-3.9815$  and  $\gamma=0.00745$ . However, this model did not pass the goodness-of-fit tests at any significance level. The probability density and P-P plots are shown in Figure E-5.

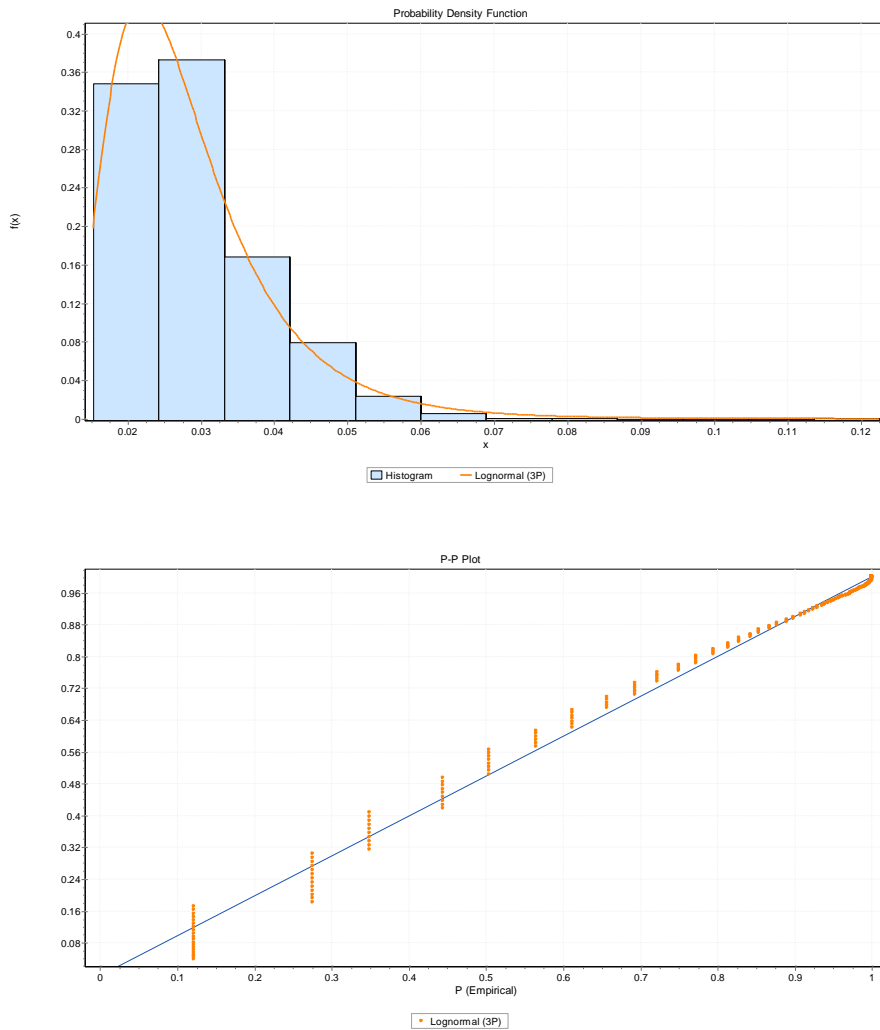


Figure E-5: Probability density function and P-P plot for 3-parameter log-normal model of Palacos R agglomerate size distribution

## E.7 SMARTSET HV VOIDS

The size distribution of Smartset HV voids could not be fitted to any of the selected distribution functions. For larger voids  $>0.04$  mm ESD, the size distribution was best described by a general extreme value (GEV) or exponential model, but neither passed goodness-of-fit tests at any significance level.

## E.8 SMARTSET HV AGGLOMERATES

The size distribution of Smartset HV agglomerates was not well-described by any of the fitted distributions. However, analysis of the probability difference plots for two and

three parameter log-normal distribution models showed higher than expected probabilities of agglomerates occurring at approximately 0.02 mm and 0.07 mm ESD, but lower than expected probability at approximately 0.04 mm ESD, as shown in Figure E-6. This finding suggests the agglomerates demonstrate a bi-modal size distribution.

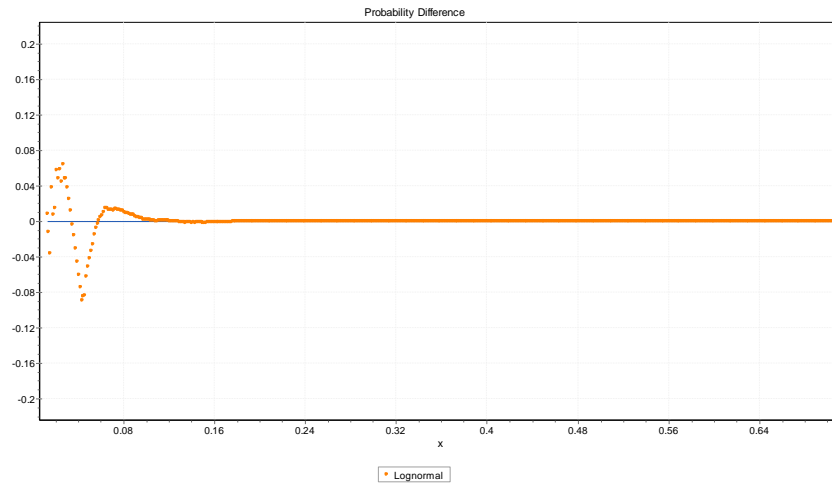


Figure E-6: Probability difference plot for 2-parameter log-normal model of Smartset HV agglomerates